CR-151497

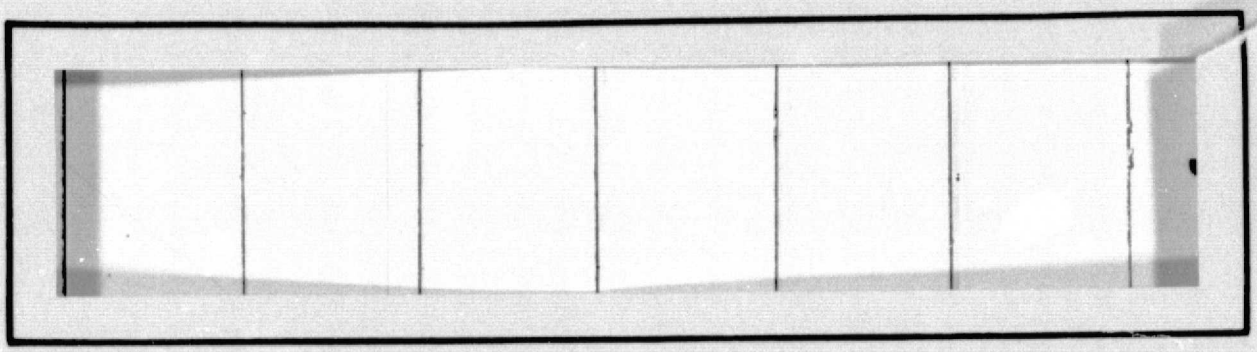

Axiomatix

Marina del Rey • California

STUDY TO INVESTIGATE AND EVALUATE MEANS OF OPTIMIZING THE KU-BAND COMBINED RADAR/COMMUNICATION FUNCTIONS FOR THE SPACE SHUTTLE

FIRST REPORT

Contract No. NAS 9-14614
Exhibit D

Prepared for

NASA Lyndon B. Johnson Space Center
Houston, Texas 77058

Prepared by

Charles L. Weber
Sergei Udalov
Waddah Alem

Axiomatix
13900 Panay Way, Suite 110M
Marina del Rey, California 90291

Axiomatix Report No. R7705-1
May 31, 1977

TABLE OF CONTENTS

LIST OF FIGURES

SUMMARY

The performance of the Space Shuttle Orbiter's Ku-Band Integrated Radar and Communications Equipment is analyzed for the radar mode of operation. The block diagram of the rendezvous radar subsystem is described. Power budgets for passive target detection are calculated, based on the estimated values of system losses. Requirements for processing of radar signals in the search and track modes are examined. Time-multiplexed, single-channel, angle tracking of passive scintillating targets is analyzed. Radar performance in the presence of main lobe ground clutter is considered and candidate techniques for clutter suppression are discussed. Principal system parameter drivers are examined for the case of stationkeeping at ranges comparable to target dimension. Candidate ranging waveforms for short range operation are analyzed and compared. The logarithmic error discriminant utilized for range, range rate and angle tracking is formulated and applied to the quantitative analysis of radar subsystem tracking loops.

1.0 INTRODUCTION AND OVERVIEW

This is the first report for the "Study to Investigate and Evaluate Means of Optimizing the Ku-Band Combined Radar/Communication Functions for Space Shuttle" (Contract NAS 9-14614, Exhibit D). The study consists of analytical tasks directed towards optimizing the design of a baseline configuration for the Ku-Band Integrated Radar and Communication Equipment. The Ku-band equipment described and analyzed in this report is being developed by Hughes Aircraft Company for the Rockwell International/Space Division, Downey, California. The equipment contractor is now proceeding with its proposed baseline design, but a number of areas of equipment function require analytical support to make the performance compatible with the requirements [1].

Although, as the description implies, the Integrated Equipment performs both the radar and the communication functions, the tasks described in this report pertain primarily to the radar mode of operation. Analysis of various facets of the optimized communication mode operation has been described in one of the recent Axiomatix reports [2]. Additional tasks pertaining to both the radar and to the communication modes of the equipment's operation, as well as the tasks dealing with the integration aspects of the equipment design will be covered during the remaining phase of this contract.

Briefly, the Ku-Band Integrated Radar and Communication Equipment time shares the two respective functions during the various phases of the Space Shuttle orbital flights. The radar is used for rendezvous with orbiting passive targets, as well as with cooperative (transponder-equipped) targets. Rendezvous requirements include initial detection of passive targets at the maximum range of 12 nmi. The active targets are to be detected at a 300 nmi maximum range.

Subsequent to detection, the radar must track the targets to a range as short as 100 feet, where the stationkeeping takes place. Target parameters measured by the radar during the tracking phase include: (1) range, (2) range rate, (3) angle, and (4) angle rate. The radar is of a coherent pulse doppler type with a peak transmitter power of 50 watts nominal. A 36-inch diameter center-fed parabolic dish is used as an antenna, whose terminals also provide the two-axis monopulse difference signals used for angle tracking. Both the transmitter, which is a TWT

amplifier, and the antenna with its associated monopulse electronics are shared with the communication mode.

In the communication mode, the Integrated Equipment is used as a spaceborne terminal to provide a Ku-band two-way link between the Shuttle Orbiter and the ground. This Ku-band link is via the TDRS. The forward link to the Shuttle consists of a 216 kbps data stream spread by a 3.03 Mcps PN code to reduce the power density incident upon the earth.

The return link consists of three independent data streams phase-multiplexed for transmission on a single carrier. The data rates of the three channels range from about 200 kbps for the lowest rate channel to as high as 50 Mbps for the wideband channel.

The forward link communication signal is received at the Shuttle on the nominal frequency of 13,775 GHz. The return link communication transmission to the TDRS is on a 15,003 MHz carrier. The radar operates in the approximate vicinity of the communication receive frequency. This permits time sharing of the receiver and the monopulse electronics between the two functions. The radar operating frequency is hopped over approximately 200 MHz to reduce target scintillation.

The baseline design proposed for the Ku-Band Integrated Radar and Communication Equipment by Hughes [3] is based upon a subdivision of the equipment into five subunits which are:

(1) Deployed Mechanism Assembly (DMA)
(2) Deployed Electronics Assembly (DEA)
(3) Electronics Assembly 1 (EA-1)
(4) Electronics Assembly 2 (EA-2)
(5) Signal Processor Assembly (SPA).

The deployed mechanism assembly (DMA) includes the antenna reflector, feed, antenna gimbals, drive motors, gyros, digital shaft encoders, rotary joints and connecting waveguides, and associated wires and cables.

The deployed electronics assembly (DEA) consists of a common receiver and transmitter, used for both radar and communication, and a common crystal-controlled exciter/LO generator, also shared by the two functions. The interconnection between the DEA and the DMA is via two rotary joints and cable wraps.

Both the DMA and the DEA are located within the Shuttle payload bay and thus have to be deployed for their operation upon the opening of the payload bay doors.

The communications electronics assembly 1 (EA-1) includes the PN despreader, the Costas loop phase-lock demodulator, the antenna servo control electronics and motor drive amplifiers, the data multiplexer/demultiplexer, and input/output buffers. As a subunit of the communication receiving equipment, the EA-1 also contributes to the TDRS signal acquisition and forward link data detection.

The electronics assembly 2 (EA-2) consists of the radar second mixer, second IF amplifier, I/Q detectors, digital Fourier transform (DFT) doppler processor, radar angle tracking circuits, radar range tracking circuits, radar range rate tracking circuits, radar timing and control, and the radar AGC detector.

The signal processing assembly (SPA) includes management logic, forward data processing, and return link data multiplexing.

Both of the electronics assemblies, as well as the signal processor assembly, are located in the avionics bay of the Shuttle. The interconnection with the two deployed assemblies is via wires and coaxial cables.

Of the five assemblies listed above, the functions performed by the EA-2 are given main consideration in this report. The functions of other assemblies are described only where necessary to explain equipment operation in the radar mode.

Section 2.0 presents the description of the radar system as configured by the appropriate assemblies. The summary of power budgets for passive radar target detection is given in Section 3.0, with the supporting analysis contained in Appendix A.

Section 4.0 summarizes radar search and track mode operations, with detailed description given in Appendix B.

Time-multiplexed single-channel angle tracking of passive targets is described briefly in Section 5.0 and in detail in Appendix C. Section 6.0 highlights the radar performance in the presence of main lobe ground clutter with supporting details given in Appendix D. The problems associated with stationkeeping and short range operation are addressed in Section 7.0. Ranging waveforms for short range operation are summarized in Section 8.0, with details in Appendix E. Section 9.0 describes the maximum likelihood estimator used for the range, range rate, angle, and angle rate estimation. Supporting analysis is given in Appendix F.

Conclusions and recommendations are presented in Section 10.0.

2.0 RADAR SYSTEM DESCRIPTION

The functional block diagram for the Integrated Ku-Band Radar/ Communication Equipment operating in the "Radar" mode is shown in Figure 1. The diagram is presented in a manner which reveals the signal flow interaction between the assemblies utilized for the radar operation. Subunits utilized for the communication function are shown in this diagram only if they are time-shared with the radar function.

The four subassemblies of the Ku-Band Integrated Equipment shown in Figure 1 are: Deployed Electronics Assembly (DEA), (2) Deployed Mechanism Assembly (DMA), (3) Electronics Assembly 2 (EA-2), and (4) Electronics Assembly 1 (EA-1). The function of each assembly, as well as that of the overall system, can be understood best by following the signal flow.

The coherent frequency synthesizer located within the DEA provides all the RF, LO, and IF signals required to generate, transmit, receive and demodulate the radar signals. The radar signal originates in the Radar Modulator located within the DEA. The modulator accepts a 651 MHz CW signal from the synthesizer and keys it in accordance with a selected transmit/receive T/R pulse modulation format. The latter is developed by the timing and control unit within the EA-2. The pulse modulated 651 MHz signal is then up-converted to the 13.8 GHz (approximate) radar operating band by mixing with the five hopped frequencies of the translation oscillator (TO) signal. This upper sideband translation is shown in Table 1.*

Table 1. Radar Transmit Frequencies Synthesis

T.O. Frequencies (MHz)	Radar Modulator Center Frequency (MHz)	Up-Converter Output (T_X Frequencies) (MHz)	
13,128	Add 651	13,779	Radar Frequencies (Upper Sideband)
13,180		13,831	
13,232		13,883	
13,284		13,935	
13,336		13,987	

*In the communication mode, only the 13,128 MHz TO signal is mixed with the 1,875 MHz communication modulator carrier, resulting in a single transmit center frequency of 15,003 MHz (15.003 GHz).

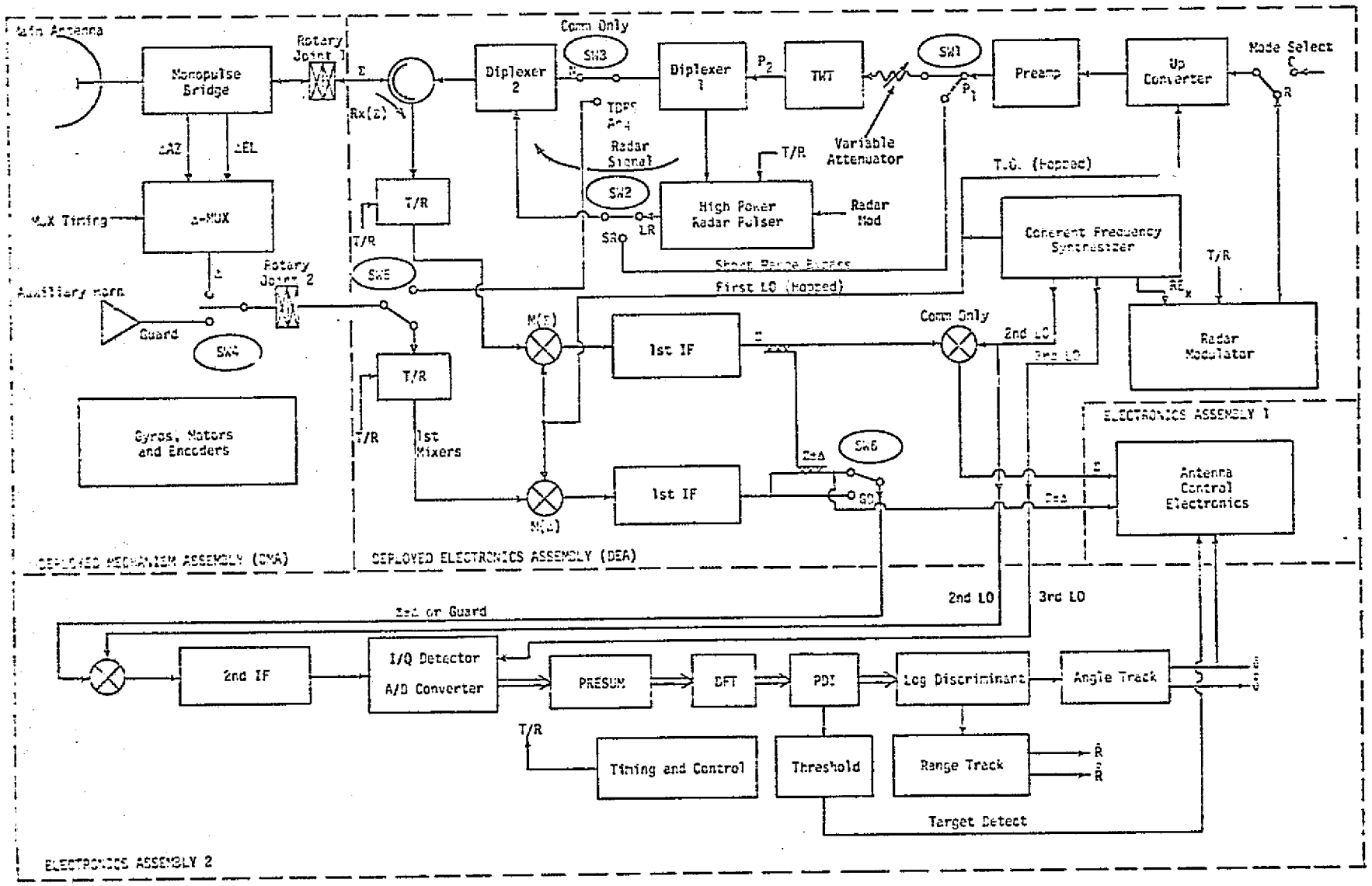

Figure 1. Functional Block Diagram for the Integrated Ku-Band Radar/Communication Equipment (Radar Mode Operation)

As shown in Table 1, the radar frequencies are spaced 52 MHz apart, resulting in a total diversity bandwidth ΔF of 208 MHz.

The output of the up-converter is applied to a preamplifier, which consists of a high frequency FET device. The preamplifier, in addition to supplying the gain, provides limiting prior to the TWT. This limiting minimizes the AM-to-PM conversion of the transmitted signal passing through the TWT. The power output P_1 of the FET limiting pre-amplifier unit is about +7 dBm.

In the search mode and the "long range" (over 3000 feet) track mode, the radar signal is amplified by the TWT. This amplification brings the drive power P_1 to the nominal 50 watts peak output power P_2. The tube gain assumed for this case is 40 dB. The function of the variable attenuator is to reduce the TWT output power for the short-range operation.

The output of the TWT is also gated in accordance with the T/R signal. Such gating prevents the tube noise from interfering with the low level signals received during the search and the long range tracking operations. Note that the TWT output is delivered to the High Power Pulser by means of Diplexer 1. This diplexer restricts the gating function only to radar region of the TWT output signal. Diplexer 2 re-inserts the gated radar signal into the main transmitter output RF line. The latter connects the transmitted signals (both radar and comm), via a circulator and a rotary joint, to the main antenna. Switch 3 is used only in the communications mode. For the initial acquisition of the TDRS, the TWT output is radiated via the auxiliary horn to facilitate spatial search for the TDRS signal by the TDRS.

In the short range radar mode, the TWT amplifier is bypassed and the preamplifier output is applied directly to Diplexer 2. Switch 1 is used to gate the low level signal and Switch 2 is in the SR position. The gated low level signal, like the TWT output, is applied to the main antenna via the circulator and the rotary joints. The position of Switch 2 therefore determines whether the TWT or the preamplifier output is applied directly to the main antenna.

The main antenna, which is a 36-inch diameter, prime-fed parabola, is a part of the deployed mechanism assembly (DMA). The antenna uses a five-element monopulse feed. Four elements are used to generate the ΔAZ

and ΔEL errors in the monopulse bridge. The fifth element is used for transmission and reception of either the radar or the communication signals. During the reception, the fifth antenna element provides the sum (Σ) channel signal. The polarization of the main antenna is selectable. For tne communication mode, it is circular (RHC) for both transmit and receive. During the radar mode, the polarization is linear and transmission is only via the main antenna.

The reception of the signal returned by either a passive or an active target is performed by both the main parabolic and auxiliary horn antennas. The purpose of the horn reception is to guard against the side-lobe lock-ons. The main antenna provides the sum (Σ) signal to the receiver. The monopulse bridge provides the two difference (Δ) signals, i.e., ΔAZ and ΔEL. The sum channel output $R_x(s)$ passes through rotary joint 1, the circulator, the transmit/receive (T/R) switch, and terminates at the input of the Σ-channel first mixer, M(Σ).

The two ΔAZ and ΔEL signals are time-multiplexed into a common channel, henceforth referred to simply as the Δ-channel. During the spatial search for the radar target, the receiver channel, which is used exclusively for Δ-signal amplification during the track mode, amplifies the output of the auxiliary horn. This is accomplished with Switch 4 in the "Guard" position. The guard signal passes through rotary joint 2, Switch 5, the T/R switch, and terminates at the input of the Δ-channel receiver first mixer M(Δ).

The first mixers translate their respective Ku-band input signals to the first IF frequency. In the radar mode, the first LO signal applied to these mixers is the same frequency-hopped signal which is used for the up-conversion in the radar transmitter. The incoming frequency-hopped signal is therefore de-hopped in the manner indicated in Table 2.

For monopulse tracking in both the radar and communication modes, a portion of the Σ-channel signal is applied to the Δ-channel, thus forming a $\Delta \pm \Delta AZ \pm \Delta EL$ signal. As shown in Figure 1, this summation is performed at the first IF. Because the guard channel is not required in the tracking mode, Switch 6 remains in the $\Sigma \pm \Delta$ position during tracking.

During the search phase, the guard channel has to be sampled periodically to prevent the lock-up onto the sidelobes. The sampled guard channel output is then compared to the main lobe, i.e., the sum

channel signal. Alternating the position of Switch 6 between the $\Sigma \pm \Delta$ and the GD (Guard) terminals permits time-sharing of the single second IF channel of the radar receiver. It must also be noted that, during search, the Δ-signals are not used and, consequently, the signal which is $\Sigma \pm \Delta$ during tracking is actually only Σ during acquisition. Furthermore, as explained in Section 4.0, the tracking of salient radar measurement parameters such as range, velocity (range rate), and angle are performed on the $\Sigma \pm \Delta AZ \pm \Delta EL$ signal, which is the only signal supplied to the third IF of electronics assembly 2 (EA-2).*

Table 2. First Conversion Frequency De-Hopping (Low Side LO Injection)

Radar Frequency (MHz)	First LO Frequency (MHz)	First Radar IF Frequency* (MHz)
13,779	13,128	
13,831	13,180	
13,883	13,232	651
13,935	13,284	
13,987	13,336	

*For communication mode only, the 13,128 MHz first LO frequency is used. The translation is then: 13,775 - 13,128 = 647 MHz for the first communication IF frequency.

The second IF radar signal is amplified and applied to a coherent processor which consists of in-phase (I) and quadrature (Q) detectors. The analog outputs of these detectors are low-pass filtered and then converted to digital data which contains both the amplitude and phase information of the received signal.

The subsequent processing of the radar signal is all digital. The processing consists of presum, digital Fourier transform (DFT), post-detection integration (PDI), and logarithmic discriminant formatter. During the search mode, the output of the PDI is applied to the threshold detector which stops the antenna search pattern when the target is

*For the communication mode only, the Σ-channel is translated to the third IF located in EA-1. The recovery of the angle tracking information is performed by envelope detection of the $\Sigma \pm \Delta AZ \pm \Delta EL$ signal at the first IF and by subsequent demultiplexing.

detected. Subsequently, the angle and range tracking units take over and the system is switched from the "track" mode to the "search" mode. Descriptions of the search and track modes are presented in Section 4.0 and Appendix B of this report.

3.0 POWER BUDGET FOR RADAR PASSIVE TARGET DETECTION

The initial detection of the passive 1 m^2 target at the 12 nmi range is the driving requirement for the radar system's power budget. Appendix A of this report presents a detailed description of the pertinent factors contributing to the power budget for the Ku-band radar in the passive target mode. Based on these factors, power budgets are calculated. The following two specific cases are considered: (1) the improvement due to the use of frequency diversity is negligible (slow fading), and (2) the improvement due to the use of frequency diversity is ideal (fast fading).

Table 3 shows the power budgets for these two cases. As can be seen from this table, the design margin for the slow fading case is negative, specifically -6 dB. In comparison, the fast fading case assumption results in a positive design margin of +2 dB. The latter is a more realistic case.

An alternate set of power budgets, which incorporate recent changes in system parameters, is also considered. Although these changes were incorporated into the system design to decrease implementation complexity, the penalty paid turns out to be the performance degradation for the passive search mode. Table 4 shows the updated power budgets. As is shown in Table 4, the design margin for the slow fading case is lowered to -8.5 dB and the margin for the fast fading case is reduced to -0.54 dB.

Conservative assumptions used for the updated power budgets may account for the negative margins. It is therefore anticipated that performance in some cases will be improved and the design margins will be increased accordingly over those presented here. There are various alternatives to improve the design margin to a more satisfactory value, namely, 6 to 10 dB for the passive mode.

In all cases considered, the gain of the main antenna was assumed to be G = 38.5 dB, which is the most recently known value [4]. Furthermore, all of the budget estimates presented in this report assume that two scans of the volume to be illuminated can be accomplished in 1 minute. At 12 nmi, the two-sided cone angle that must be searched is 40 degrees. It has been shown in [5,6] that, at these values of cone angle and range, two scans can be completed in 1 minute with an antenna spatial dwell time of 36 msec. This value of spatial dwell time is used in this report for power budget estimation.

Table 3. Power Budget for Passive Search at 12 nmi Without Range Designated

Item	Term	Section Number in This Report	Value	Budget #1 Case #1 (Slow Fade) (dB)	Budget #2 Case #2 (Fast Fade) (dB)
1	R_p	3.1	Required Peak SNR	18.2	11.7
2	G^2	3.4	G = 38.5 dB	-77.0	-77.0
3	λ^2	3.3	λ = 0.0218 m	33.24	33.24
4	$\bar{\sigma}$	3.2	1 m^2	0	0
5	$(4\pi)^3$			33	33
6	R^4	3.6	R = 12 nmi = 22.2 km	173.9	173.9
7	k	3.7	1.38×10^{-23}	-228.6	-228.6
8	T_s	3.7	1500°K	31.76	31.76
9	Coherent Addition Time τ_f	3.5	1.195 msec	29.23	29.23
10		2.0	2	-3	-3
	Losses	3.8			
11	Transmit Losses	3.8.1	RFP	3.5	3.5
12	Beam Shape	3.8.2	Scan Alignment - Lateral Scan	3.2	3.2
13	Threshold	3.8.3	Constant FAP	1.0	0.5
14	Processor Loss	3.8.4		1.7	1.0
15	Range Gate Straddling Loss	3.8.5		0	0
16	Doppler	3.8.6	Mismatch	1.0	0.7
17	PDI		Postdetection Integration BEF [5]	1.25	1.25
18	Pre-Sum Mismatch	3.8.7	Due to Doppler	0.6	0.6
19	P_p	3.5	Required Peak Power	22.98 dB (198.6 w)	14.98 dB (31.5 w)
20	d_t	3.5	Duty Factor = 0.2	-7.0	-7.0
21	P_{avg}		Required Average Power	15.99 dB (39.7 w)	7.99 dB (6.3 w)
22	P_p Design		Reference [5]	50 w	50 w
23	P_{avg} Design		Reference [5]	10 w	10 w
24	Design Margin			-6.0 dB	+2.0 dB

Table 4. Alternate Power Budget for Passive Search at 12 nmi Without Range Designated

Item	Term	Section Number in This Report	Value	Budget #3 Case #1 (Slow Fade) (dB)	Budget #4 Case #2 (Fast Fade) (dB)
1	R_p	3.1	Required Peak SNR	18.2	11.7
2	G^2	3.4	G = 38.5 dB	-77.0	-77.0
3	λ^2	3.3	λ = 0.02161 m	33.31	33.31
4	$\bar{\sigma}$	3.2	1 m^2	0	0
5	$(4\pi)^3$			33	33
6	R^4	3.6	R = 12 nmi = 22.2 km	173.9	173.9
7	k	3.7	1.38×10^{-23}	-228.6	-228.6
8	T_s	3.7	1500°K	31.76	31.76
9	Coherent Addition Time τ_f	3.5	1.062 msec	29.74	29.74
10		2.0	2	-3	-3
	Losses	3.8			
11	Transmit Losses	3.8.1	RFP	3.5	3.5
12	Beam Shape	3.8.2	Scan Alignment · Lateral Scan	3.2	3.2
13	Threshold	3.8.3	Constant FAP	1.0	0.5
14	Processor Loss	3.8.4		1.7	1.0
15	Range Gate Straddling Loss	3.8.5		2.0	2.0
16	Doppler	3.8.6	Mismatch	1.0	0.7
17	PDI		Postdetection Integration Ref. [5]	1.25	1.25
18	Pre-Sum Mismatch	3.8.7	Due to Doppler	0.57	0.57
19	P_p	3.5	Required Peak Power	25.53 dB (357.3 w)	17.53 dB (56.6 w)
20	d_t	3.5	Duty Factor = 0.2	-7.0	-7.0
21	P_{avg}		Required Average Power	18.54 dB (71.5 w)	10.54 dB (11.3 w)
22	P_p Design		Reference [5]	50 w	50 w
23	P_{avg} Design		Reference [5]	10 w	10 w
24	Design Margin			-8.5 dB	-0.54 dB

4.0 RADAR SEARCH AND TRACK MODES

The objective of the Ku-band radar system on the Shuttle Orbiter is to detect the presence of a target and then obtain continous accurate estimates of the various target parameters, namely, its range, range rate (velocity), azimuth angle, elevation angle, and angle rates. The target is first detected when the radar is in the search mode; then the accurate estimates are obtained in the track mode.

The radar employs coherent processing over each RF frequency transmitted and noncoherent postdetection integration (PDI). Following the intermediate amplifiers, in-phase and quadrature phase signals are sampled and digitized (A/D converted), providing target amplitude and phase information. For longer range search and acquisition ($R > 3000$ ft), 16 doppler filters are formed, covering the doppler interval defined by the repetition rate. This is an ambiguous doppler interval; this ambiguity is removed via differentiation of the range estimates.

Following the filters, the target magnitude is determined, summed over the number of RF frequencies (noncoherent postdetection integration) and compared to a threshold. The threshold is set from noise measurements, so as to maintain a constant false alarm probability (CFAP). This can be implemented by any of several methods.

In the search mode, only the sum channel data is processed. When the threshold is exceeded and target detection is declared, the auxiliary antenna signal is processed and its magnitude is compared with that of the main antenna to eliminate sidelobe detected targets. The auxiliary antenna has a peak gain which is approximately 20 dB less than that of the main antenna. Also, the sidelobes of the main antenna are approximately 20 dB down from the main lobe. This provides roughly a 20 dB main lobe/guard antenna ratio to detect and eliminate sidelobe targets.

In the modes for which angle tracking is required, namely, GPC acquisition and autotrack, the sum-plus-angle error channels are processed. The azimuth and elevation error signals are time-multiplexed, thereby eliminating the need for a second and third matched processing channel.

The Shuttle Ku-band radar signal flow block diagram is shown in Figure 2. The antenna assembly consists of a main antenna and an auxiliary antenna, which are subunits of the deployed mechanism assembly (DMA). Further processing of antenna signals takes place in the deployed

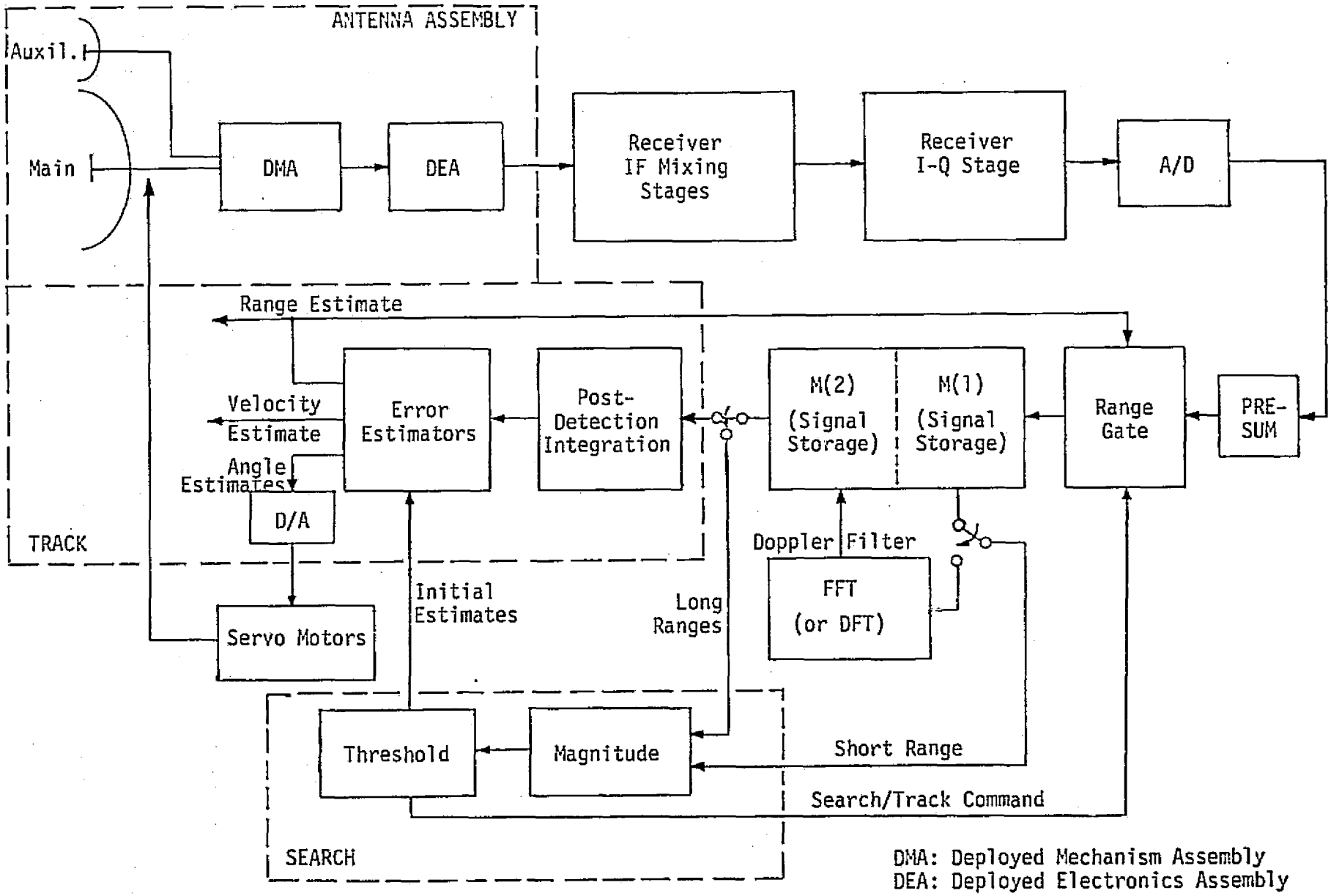

Figure 2. Radar Block Diagram

electronics assembly (DEA), where various switching and filtering operations take place. The antenna assembly is followed by several IF mixing stages to bring the carrier frequency down to a stable IF of $f_0 = 78.143$ MHz. The output of the I-Q stage that follows is a pair of baseband signals which are in phase and in quadrature with the input signal.

The available information is converted by an A/D converter to digital data which samples both channels at a rate of $f_s = 480$ kHz, which is slightly larger than the Nyquist rate of the baseband signals at the output of the I-Q stage. (The LPF bandwidth in both the I and Q channels is equal to 237 kHz.) The output of the A/D converter is a set of complex numbers which undergo various stages of digital processing before estimates of the target parameters (range, velocity, azimuth angle, elevation angle) are obtained. The first processing stage is a presumming stage, followed by a set of range gates and doppler filters consecutively. The arrangement of the gates is varied for the two modes of operation. In the search mode, where range designation is not present, there are four range gates per pulse, while in the track mode there are only two non-overlapping gates: an early gate and a late gate.

For long ranges, the magnitudes of the outputs of the doppler filters are summed over the RF frequencies and compared to a threshold to detect the existence of a target. For short ranges ($R < 3000$ ft), the detection takes place without using any doppler filtering.

Once a target is detected, the radar is switched to a track mode and the digital signals undergo postdetection integration, followed by an error estimation unit which is initiated by a crude estimate obtained by the search mode operation. The final estimates of the various parameters are:

(1) Fed as inputs to the servo motors for angle track.

(2) Used to adjust the position of the early and late gates for range track.

(3) Displayed for the astronauts for visual reading (all variables being tracked).

(4) Utilized to update the state of the error estimators to obtain new estimates.

Frequency diversity, using five RF frequencies, is employed in both the search and track modes. Table 1 (page 4) lists these frequencies.

The radar modulation parameters are summarized in Table 5.

Table 5. Radar Modulation Parameters as a Function of Range

Designated Range (nmi)	τ (μsec)	PRF (Hz)	Search Mode	
			Frequency Dwell Time (msec)	Spatial Dwell Time (msec)
8-22	66.3	2987	5.3	31.8
4-8	33.2	7177	2.2	13.4
2-4	16.6	7177	2.2	13.4
1-2	8.3	7177	2.2	13.4
0.5-1	4.1	7177	2.2	13.4

In explaining the search mode operation, low range signal format is chosen for demonstration. All other ranges follow identical processing except for the short range (<0.5 nmi) which does not utilize the doppler filters.

Sixteen pulses are transmitted at each RF frequency. The duration of each pulse is 66.3 μsec, while the time between consecutive pulses is 335 μsec, as shown in Figure 3. Four range gates (R_1 through R_4) are used to cover the designated range. It is important to note that no doppler correction is used at the presummer in the search mode. For each RF frequency, 64 complex numbers are stored in a memory designated at M(1), as shown in Figure 4. The output of each range gate at every RF frequency is passed through a bank of 16 doppler filters, implemented as discrete Fourier transforms (DFT) or fast Fourier transforms (FFT), and the magnitudes of the outputs of these filters are calculated and compared to precalculated thresholds. The target is detected when the magnitude of one or two outputs of adjacent doppler filters pertaining to one or two range gates is exceeded. An initial estimate of the range and the range rate of the target are calculated from the knowledge of the doppler filters and range gates whose outputs have exceeded the threshold. These initial estimates are fed into the error estimators as initial conditions to start the successive estimation process in the track mode. Thresholds are calculated to produce an error alarm rate of one false alarm per hour.

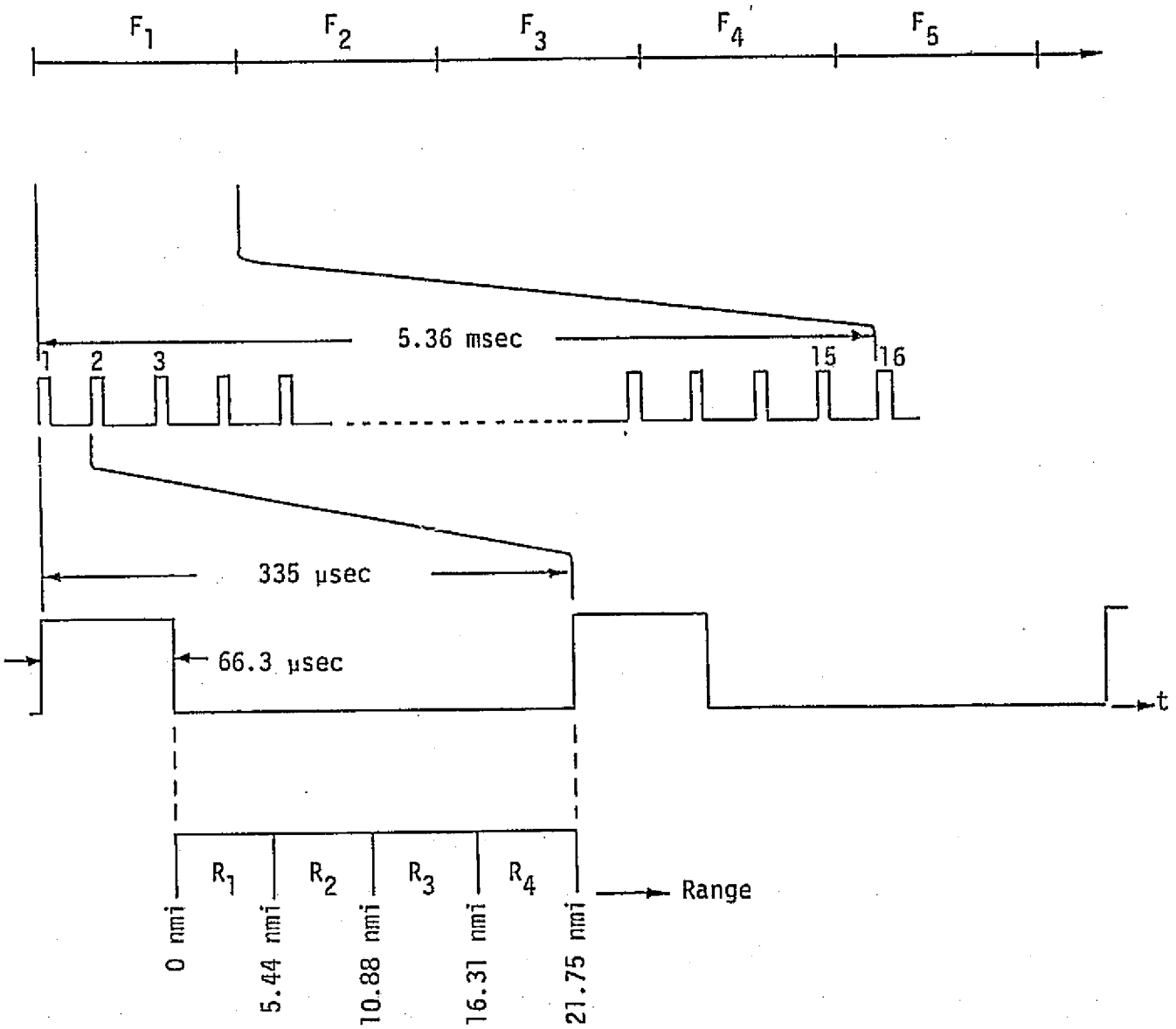

Figure 3. Long Range Search Signals

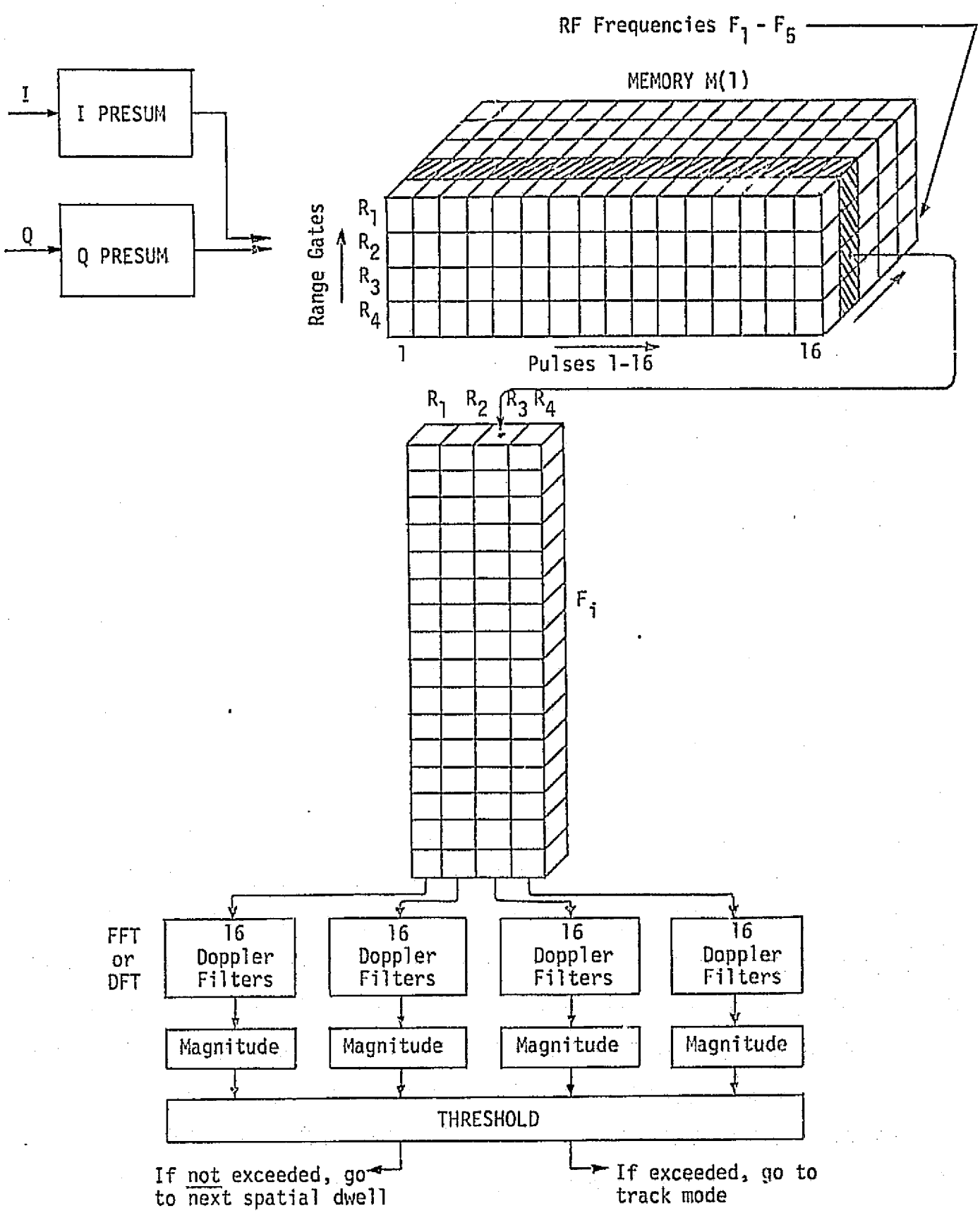

Figure 4. Search Mode Signal Processing

Figure 5 illustrates the signal format in the track mode. As shown in the figure, the signal in the track mode consists of 64 pulses for each RF frequency, instead of the 16 pulses of the search mode. For long range tracking, the frequency dwell time is equal to 21.44 msec. Each frequency dwell time is divided into four time slots by the switching combination of SW1 and the phase encoder switch in the antenna assembly. The signals in the succeeding time slots are $\Sigma + \Delta AZ$, $\Sigma - \Delta AZ$, $\Sigma + \Delta AZ$, and $\Sigma - \Delta EL$, respectively. The time slots are arranged so that the first two are used to measure the azimuth angle, while the last two are used for the elevation angle. Each one of the previous time slots consists of 16 pulses. The pulses are passed through an early gate and a late gate, which are located around a predicted estimate of the range, $R_p(n)$, from the processor timing unit. The width of each gate is equal to the pulse width. The output of each range gate is a complex number $z(I,J,L,K)$, which is a function of four parameters (I, J, L, K):

I denotes the RF frequency being transmitted; $I = 1,2,\ldots,5$.

J denotes the time slot in each frequency such that

$J = 1$ corresponds to $\Sigma + \Delta AZ$

$J = 2$ corresponds to $\Sigma - \Delta AZ$

$J = 3$ corresponds to $\Sigma + \Delta EL$

$J = 4$ corresponds to $\Sigma - \Delta EL$.

K denotes a particular pulse in each time slot; $K = 1,\ldots,16$.

L denotes the range gate under consideration:

$L = -1$ corresponds to Early Gate

$L = +1$ corresponds to Late Gate.

The detailed description of signal processing involved in the search and track modes is presented in Appendix B.

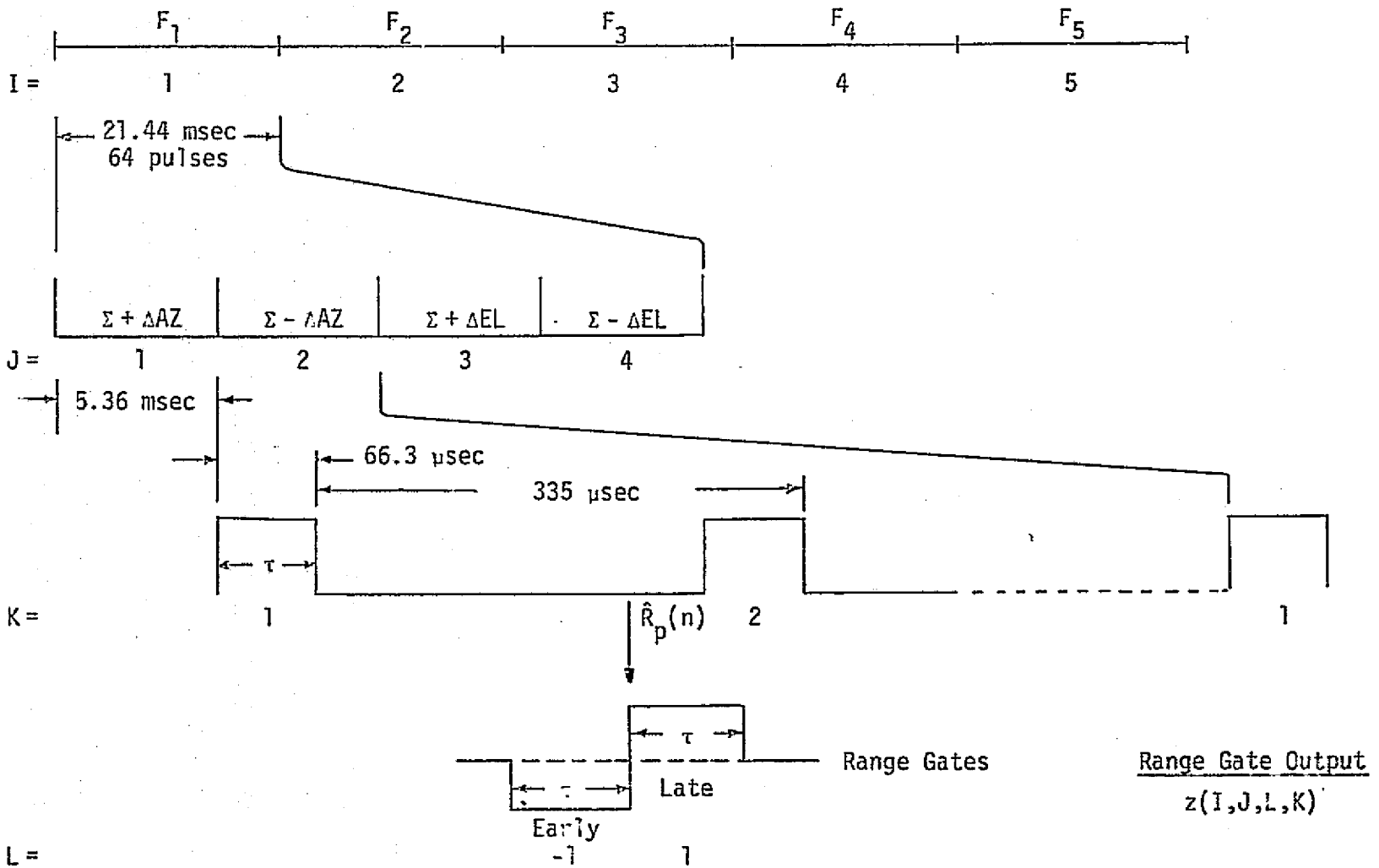

Figure 5. Track Mode Signal Format

5.0 TIME-MULTIPLEXED SINGLE-CHANNEL ANGLE TRACKING OF PASSIVE TARGETS

In the Ku-band integrated radar and communications for the Orbiter, the angle tracking subsystem, when operating in the communications mode, has received extensive attention [7]. In Appendix C of this report, the radar angle tracking of passive targets is studied. Both thermal noise and target scintillation are taken into account. It is shown that the performance requirements for the angle tracking of passive targets meets the specification requirements with a design margin of greater than 10 dB at 10 nmi and closer. The angle rate estimation requirements were not included in this report.

A block diagram of the single channel* monopulse angle tracking loop is shown in Figure 6. All of the operations pertinent to the angle tracking functions are as shown in this figure. In particular, the pre-sum operation assumes that the range gate tracking loop is also tracking satisfactorily. Degradations in signal-to-noise ratio due to errors in the range gate tracking loop would not seriously affect the operation of the angle tracking loop unless these degradations were very significant. This is because of the ample design margin of the angle tracking loops.

The same comments can also be made about the doppler tracking loop, which sets the centers of the doppler filters.

The performance of the angle tracking loop is shown in Figure 7, where the RMS tracking error due to thermal noise and target scintillation is plotted against range in nautical miles. For all ranges less than 18 nmi, the RMS error is below the specification value of 0.153 deg, and naturally improves as the range decreases.

In summary, there appears to be no difficulty in angle tracking capability of the radar for passive targets from the standpoint of the thermal noise. The passive mode was chosen for this detailed study since it imposes the most severe requirements on signal-to-noise ratio.

---

*Single channels implies multiplexing of three information channels (Σ, ΔAZ and ΔEL) into a single channel.

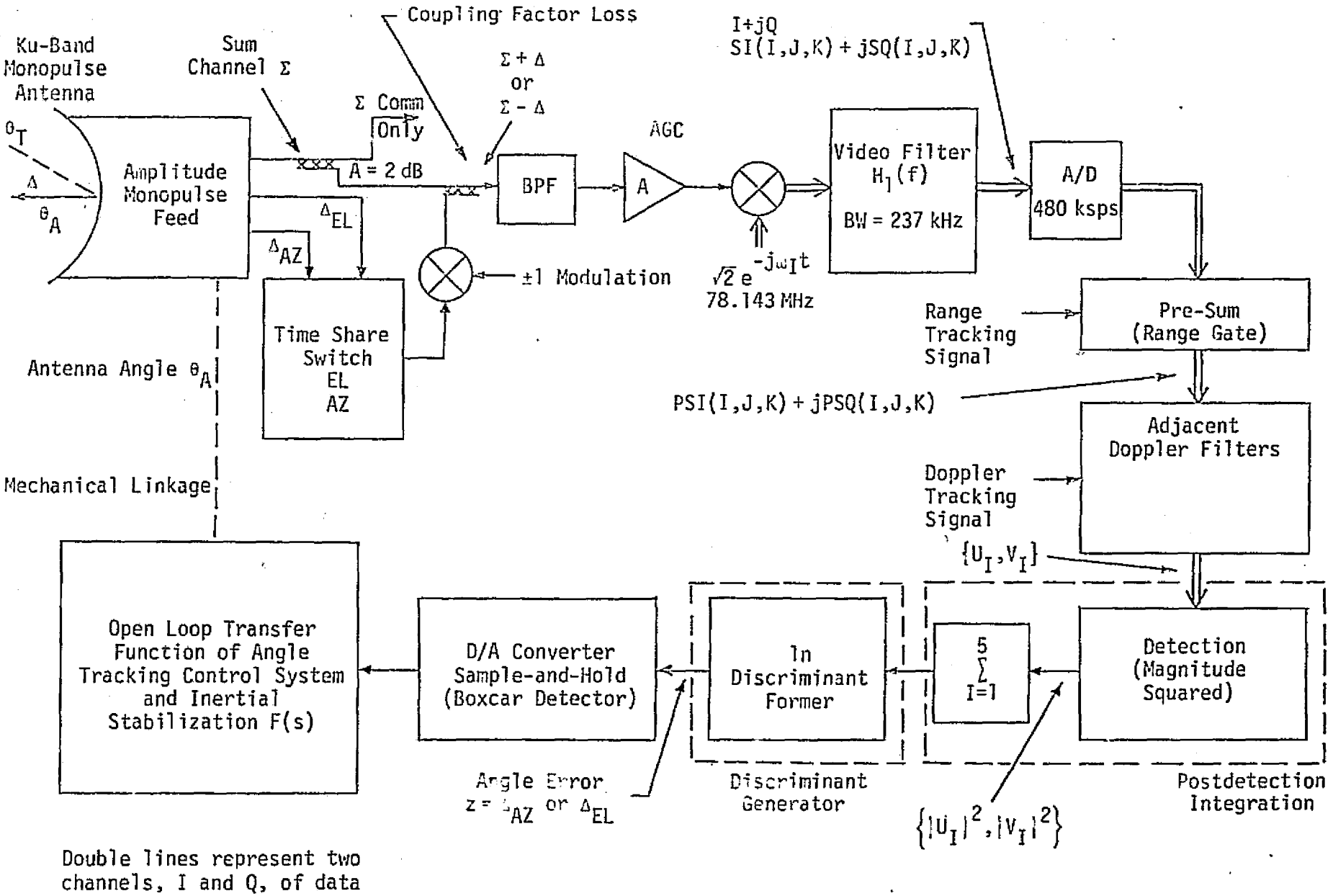

Figure 6. Block Diagram of Single Channel Monopulse Angle Tracking Loop

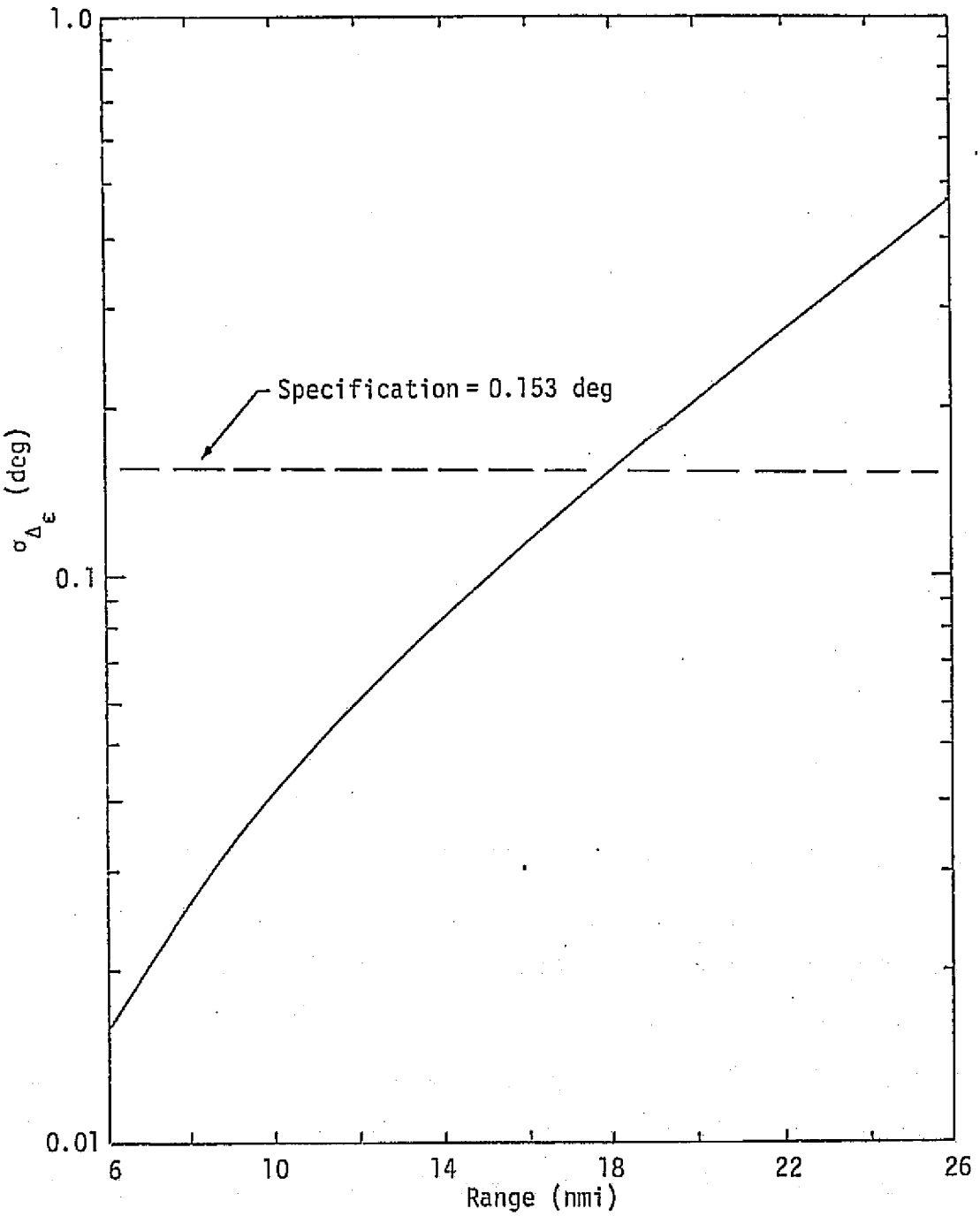

Figure 7. RMS Angle Tracking Error of Passive Radar Versus Range (nmi)

6.0 RADAR PERFORMANCE IN PRESENCE OF MAIN LOBE GROUND CLUTTER

The possibility of main lobe ground clutter interference arises when the Shuttle radar is working with a target which is in a position requiring the radar antenna to be pointed in the direction of the earth and close to vertical. The geometry characteristic of this case is shown in Figure 8. In addition to the geometrical causes for ground interference, the signal structure utilized by the radar may be such that clutter discrimination is not easily implemented. For example, a radar system whose parameters are optimized for operation at ranges of 12 nmi or less, such as the Shuttle Ku-band system, will typically employ PRF in the range of 3000 to 8000 kHz, i.e., just low enough to provide nonambiguous acquisition of range. Such high PRFs, however, will cause the ground return at orbit altitudes ranging from 100 nmi to 500 nmi to appear as a target "blip" within the same range interval as the desired target. In other words, with PRFs matched to target range (specifically passive target) clutter discrimination in time is not possible.

Furthermore, the magnitude of the clutter return itself, at a minimum orbit altitude of 100 nmi, may be such that the passive target signal is masked by clutter at ranges far shorter than the maximum specified acquisition range of 12 nmi.

The detailed quantitative analysis of the ground clutter return is given in Appendix D. It is shown there that, at vertical incidence, the ground return is of a beamwidth limited type for all pulse widths greater than 1 μsec and for orbit altitudes ranging from 100 nmi to 500 nmi. Figure 9 illustrates this fact. The nature of beamwidth limitation is evident by the fact that the ground return, even for h = 500 nmi, approaches its asymptotic maximum value with "response times" less than 1 μsec.* Because the long range tracking and acquisition mode pulse length of the system are above 2 μsec beamwidth, limited operation is assumed for the case of main lobe nadir return.)

Utilizing the analytical techniques described in Appendix D, we have calculated the relative power (in dBm) of the desired passive target

---

*Response time is arbitrarily defined here as the time required for the main lobe nadir clutter return to reach 90% of its maximum power value.

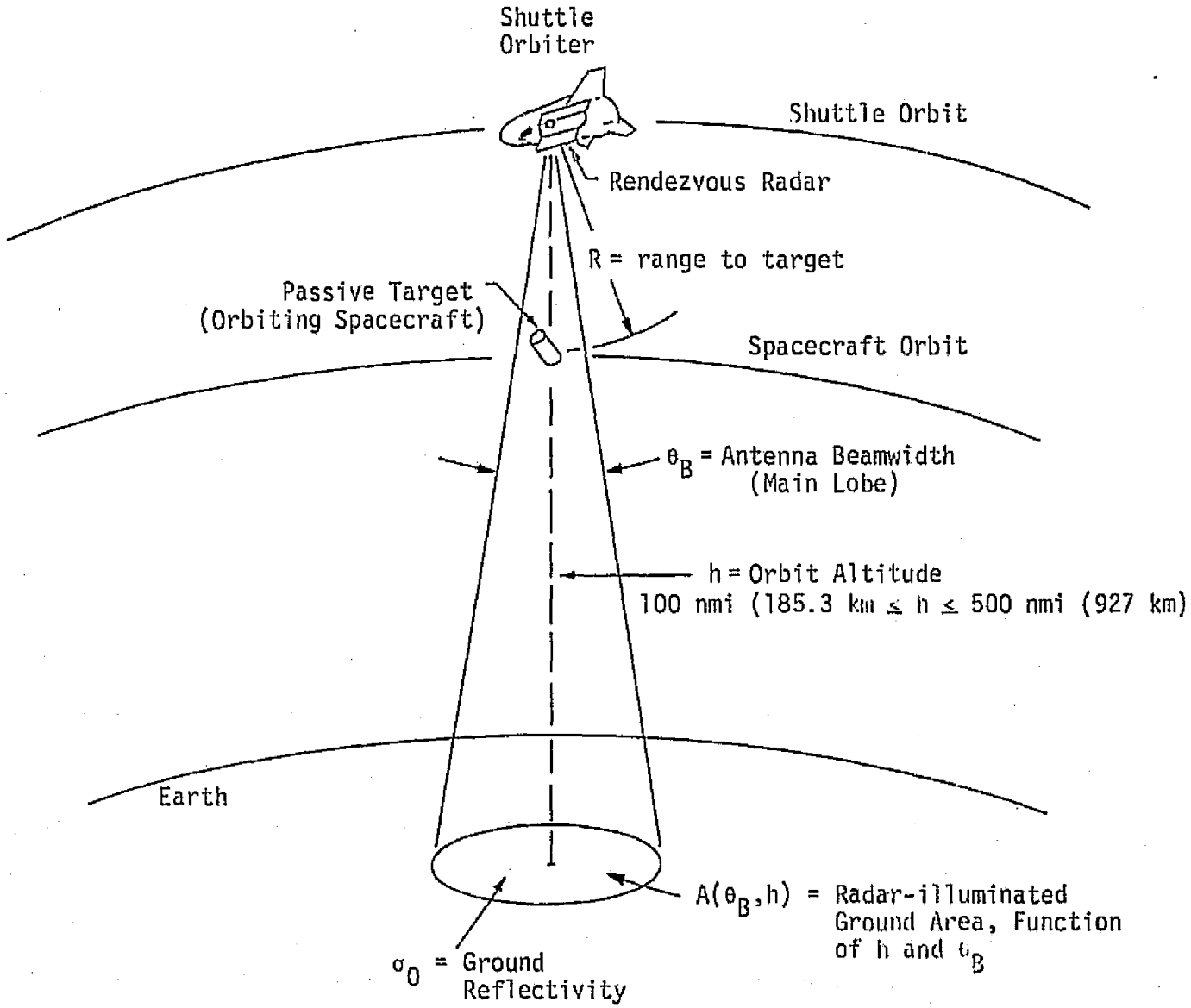

Figure 8. Rendezvous Geometry* With Ground Clutter Return in Main Lobe

*Not to scale

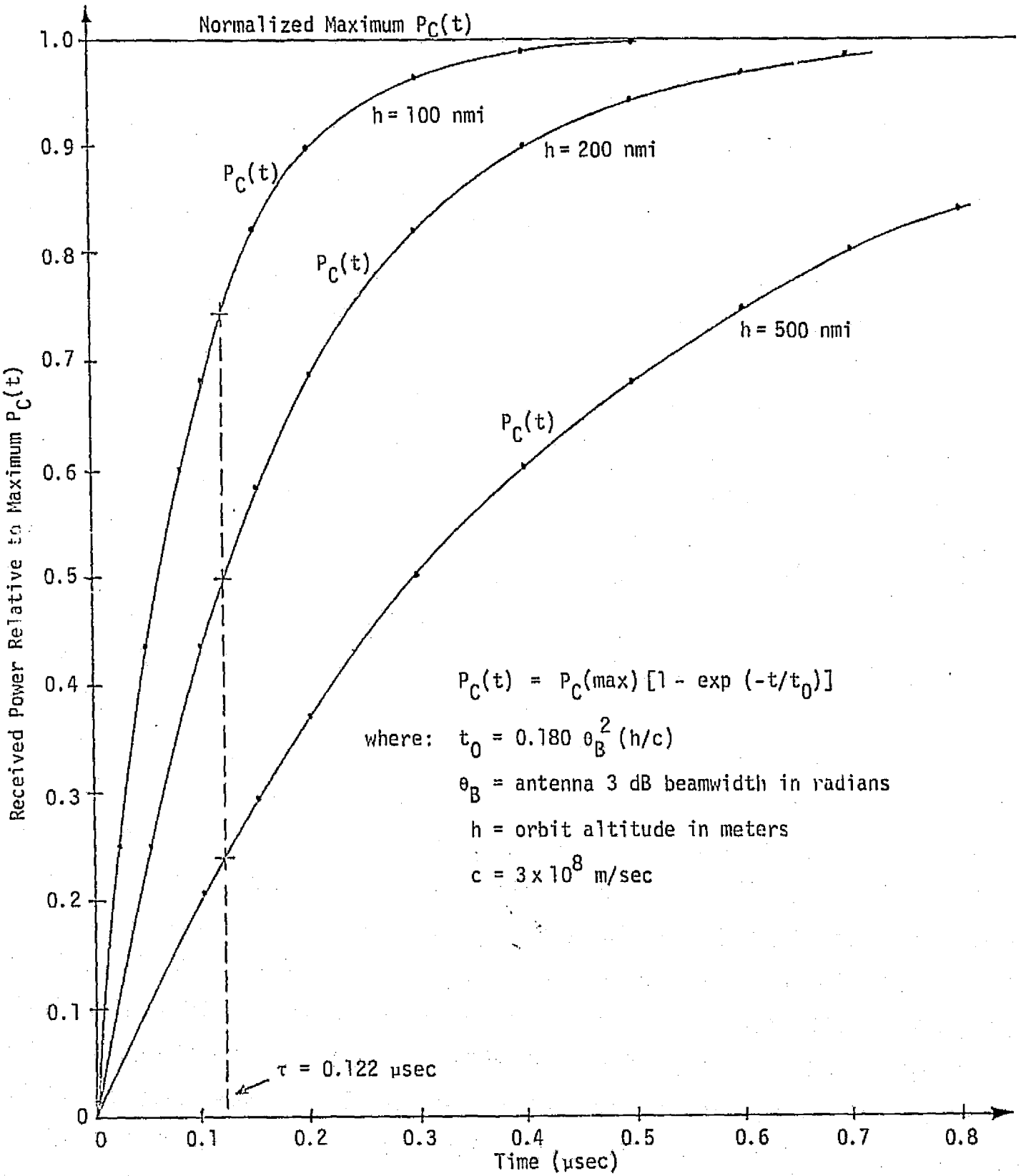

Figure 9. Effect of the Orbit Altitude on the Rise Time of Main Lobe Nadir Ground Return

return(s), P_S, and the power of the nadir clutter return at various altitudes. Figure 10 presents the pertinent information. Note that all power levels shown are referred to presum output. This reference point is chosen because beyond it analytical comparison becomes nearly impossible, due to extremely complex time-frequency relationship of the ground clutter return.

From Figure 10, it is evident that, if one accepts the criteria of $P_S/P_C \geq 20$ dB (at presum output) and all radar modes functional, the system range at h = 100 nmi is limited to 1 km for a 1 m^2 target and to about 1.8 km for a 10 m^2 target. This is a significant reduction from the specified maximum range of 12 nmi (22.2 km) for a 1 m^2 target. Note, however, that at 0.5 nmi (0.927 km) and with $\sigma = 10$ m^2, parameters typical of a Skylab reboost mission, $P_S/P_C \cong 30$ dB, even at h = 100 nmi. This makes the radar system under consideration acceptable for the Skylab reboost mission without requiring special modifications or parameter changes.

From the standpoint of improving the performance of the Ku-band radar system for targets other than the Skylab, one should consider "fixes" available to the system. One such fix, which is actually a built-in one, is the frequency agility employed by the radar for combating target fluctuations. Figure 11 depicts the altitude versus incidence angle diagram of the clutter interference region for the two PRFs currently employed by the Ku-band radar for the search and track modes. According to Figure 11, PRFs of 7177 kps and 2987 kps result in "clutter-free" orbit altitudes of 192 nmi and 460 nmi, respectively. The 192 nmi orbit may be acceptable for the Skylab reboost mission, but the 460 nmi orbit altitude, although within the 500 nmi maximum specification, may be too high to be associated with clutter-related problems. Nevertheless, the intrinsic ability of the Ku-band system to reject clutter by frequency agility may be of benefit to some of the Shuttle missions.

Suppose now that one considers a frequency agility pattern which eliminates first-time ground returns up to 500 nmi. The region of direct (i.e., first-time-around) interference would then be as shown in Figure 12. This is a highly desirable result, because it provides a "clear" operation at all altitudes of up to 500 nmi. At 500 nmi, however, the ground return will be at least 14 dB down from the 100 nmi return. The penalty paid

Figure 10. Power Received From a Passive Target Relative to Range, Ground Clutter, and System Noise (All power refers to pre-sum output)

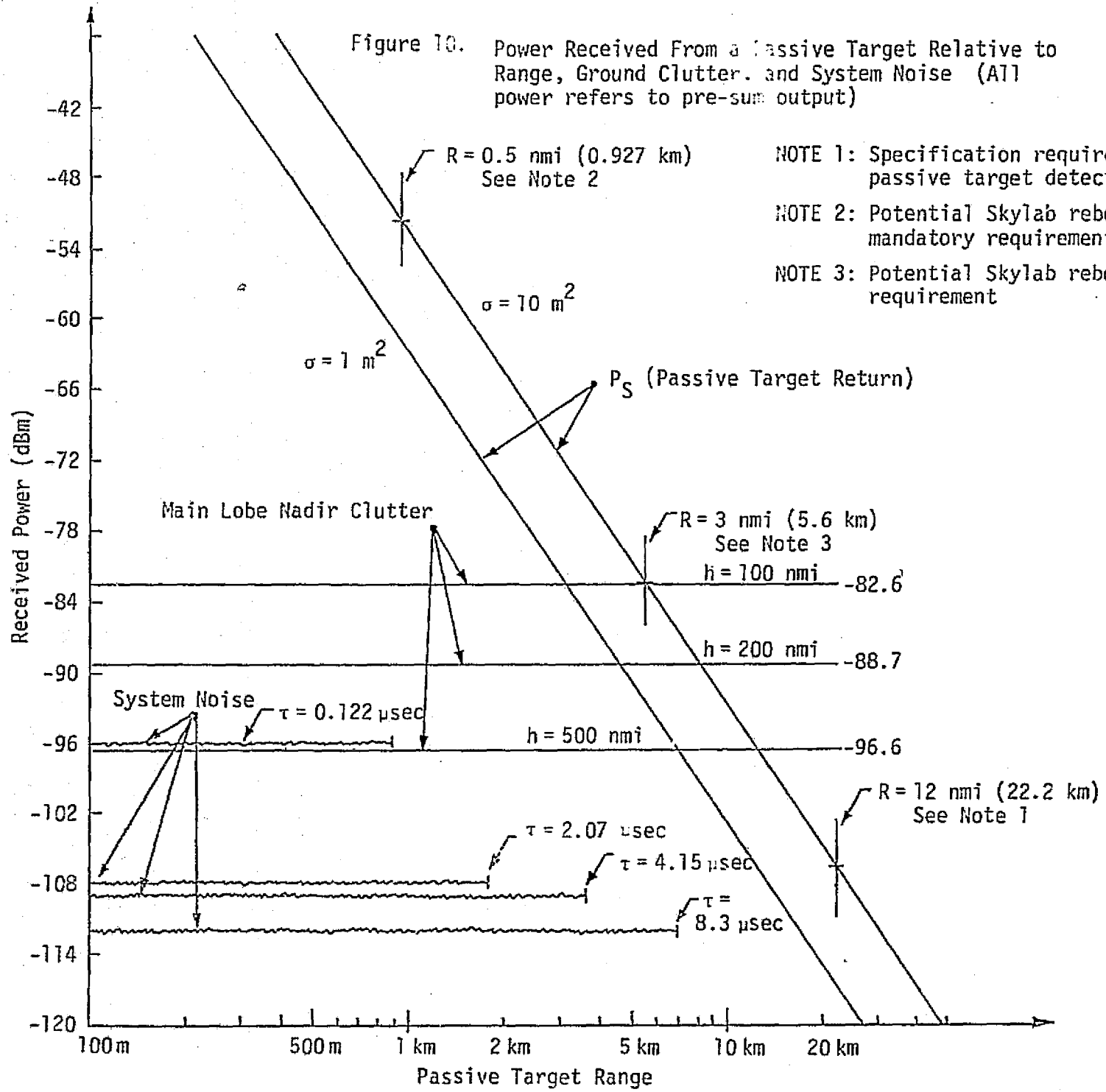

NOTE 1: Specification requirement for passive target detection

NOTE 2: Potential Skylab reboost mission mandatory requirement

NOTE 3: Potential Skylab reboost goal requirement

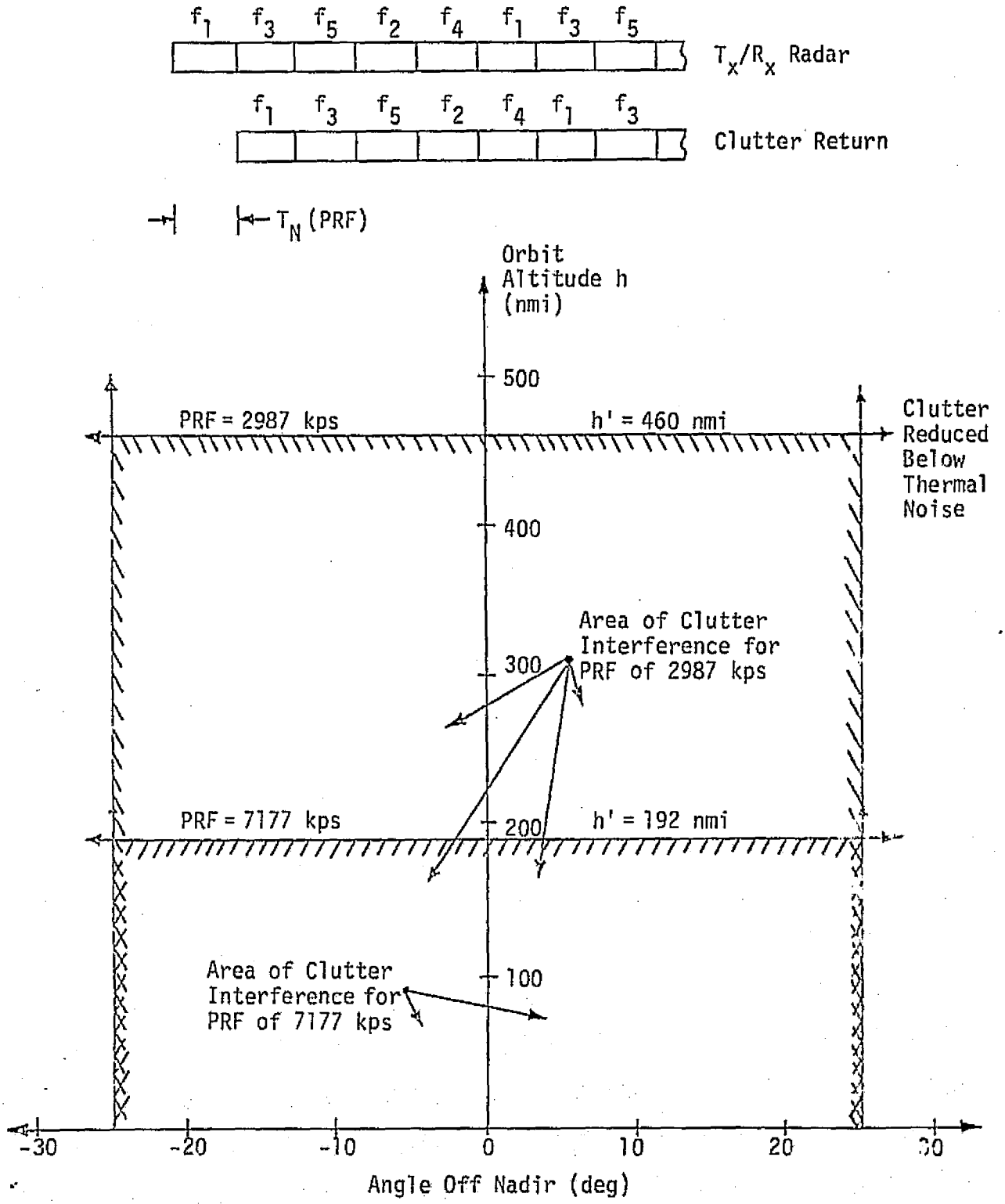

Figure 11. Typical Time-Frequency Pattern of Radar and Corresponding Areas of Clutter Interference

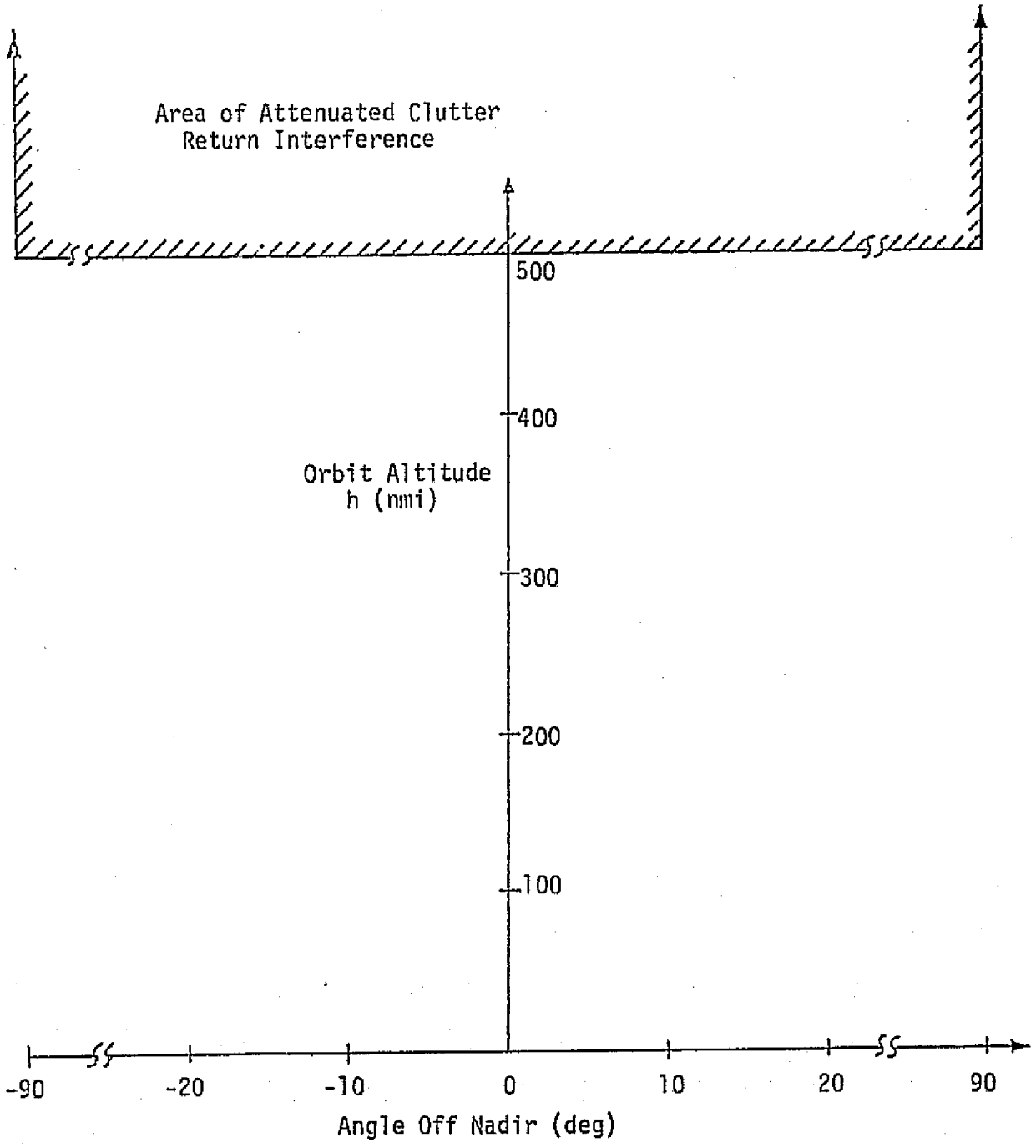

Figure 12. Changing Frequency at Intervals Equal to Radar Time for 100 nmi Clears the 500 nmi Altitude Range of Primary Clutter Interference (5 frequencies used)

for achieving the clutter-free operation at altitudes between 100 nmi and 500 nmi is the shortening of the coherent frequency dwell time. For a PRF of 2987 kps, this means that only about 4 pulses are available for coherent integration at any one frequency.

Thus, a 16-point Fourier transform cannot be implemented with "fast" hops (1.24 msec) commensurate with the 100 nmi ground return time. On the other hand, if one considers a possibility of coherently summing up consecutive 4-pulse groups to form a 16-point transform, the clutter-free region operation depicted by Figure 12 may be achieved. The factors to consider are: (1) transmitter coherency over several discrete frequency dwells, (2) target coherency over these dwells, and (3) the effect of time-multiplexed F-transformation on the memory storage requirements.

7.0 STATIONKEEPING CONSIDERATIONS FOR THE KU-BAND RADAR

One of the most difficult requirements for the Ku-band radar is the capability of establishing a stationkeeping environment for the target at approximately 35 feet from the Orbiter. Because of the operational planning of the Skylab reboost, the Ku-band radar will have to be able to maintain stationkeeping when looking into the earth clutter background.

As the operation is presently envisioned [8], there will be a ground-controlled sequence of maneuvers to get the Orbiter within 300 nmi of an active target and within 10-20 nmi of a passive target. The Ku-band radar will then acquire and track the target down to a braking or initial stationkeeping region which will be at a range of 1000-3000 feet. The final approach will then be carried out to a range of 35 feet, where it can be retrieved by the 50-foot boom.

The geometry of the braking, initial stationkeeping, and final approach is shown in Figure 13, which is similar to that shown in [8]. Four positions are shown. Although it is not pertinent to the radar considerations, from an energy consumption point of view, stationkeeping will be significantly easier in positions V_1 and V_2 than in positions R_1 and R_2. What is important from the radar point of view is that some targets (primarily military) will be at low altitudes, thereby possibly requiring an approach from above, with an initial stationkeeping position at $\bar{R}_2$. In this position, the earth clutter problem must be addressed. It is envisioned also that the requirements on range and range rate estimates will be more accurate in the initial stationkeeping positions R_1 and R_2.

The radar operation at these close ranges have been broken down into three modes:

(a)	Short mode	300 to 3000 feet
(b)	Short-short mode	100 to 300 feet
(c)	Short-short-short mode	35 to 100 feet

Whether these modes can be consolidated will depend on which implementation is chosen. Preliminary comments concerning the choice of implementation are given below. The approach taken is as follows:

(1) What needs to be done to modify the existing radar structure so as to meet all requirements in the Short mode of operation without an

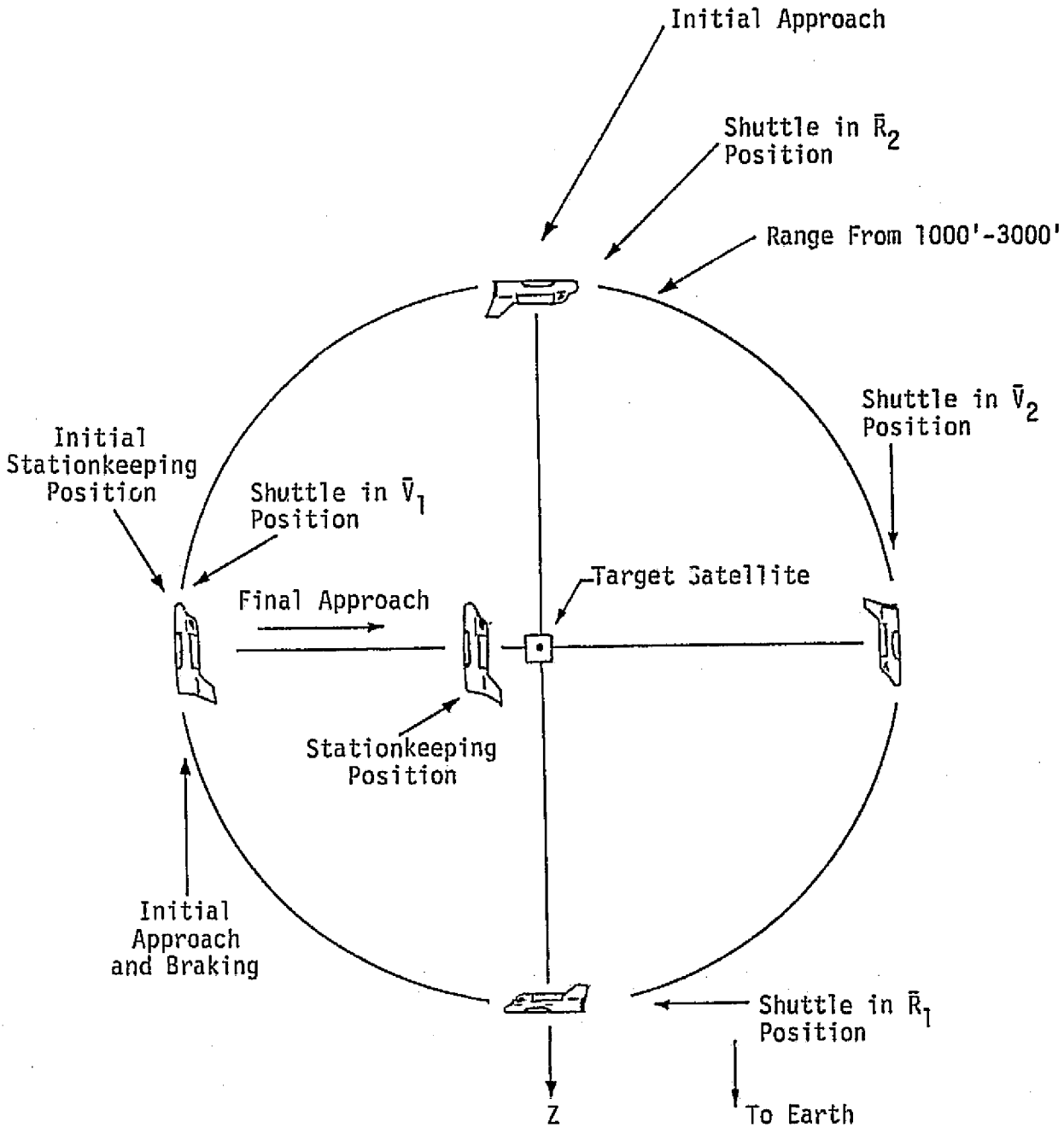

Figure 13. Geometry of Approach and Braking

undue amount of additional hardware?

(2) If a separate unit is employed for the Short modes, what are the candidates and which positions of the existing RF sections could also be used by this unit?

It is our understanding that search and track capability is required for the Short-Short mode and that it is highly desirable for the Short-Short-Short mode. One of the first problems is to evaluate exactly what it means to track in angle, range and range rate at ranges as short as 35 feet. Figure 14 illustrates the point. With a 36-inch (D = 0.91 meter) diameter antenna, the near field region extends to about 76 meters, or about 250 feet. This means that, at the distance of 35 feet, the main antenna beams are not well defined and the monopulse capability must be questioned. The target reference point to which the radar parameters (range, range rate, angle and angle rate) are to be measured also needs to be established.

On the positive side, signal-to-noise ratio should not be a problem. In fact, to protect targets from high levels of electromagnetic radiation, the TWT may be bypassed, thereby obtaining a 44 dB reduction in transmitted peak power. In addition, to protect the receiver from saturation, additional attenuators (ferrite attenuators have been proposed) can be inserted in the receiver front end. Implementation difficulties center around the rise and fall times of the RF switches, particularly since the pulse widths will be between 30 and 122 msec.

For the existing 36-inch Ku-band antenna, as it applies to the Short range modes of operation, it has already been pointed out that the near field extends to approximately 76 meters. Therefore, the Short-Short and Short-Short-Short modes are entirely within the near field of the existing antenna. This probably precludes any monopulse capability in these modes.

One fix is to defocus the antenna at short ranges so that the target would be entirely within the main beam. The present antenna cannot be defocused sufficiently to permit an 18-meter target to be entirely within the main beam. A dipole antenna would provide a sufficiently wide beam, but would not provide any monopulse capability.

A candidate which could provide monopulse capability is to use the monopulse feed of the existing antenna, either by physically rotating

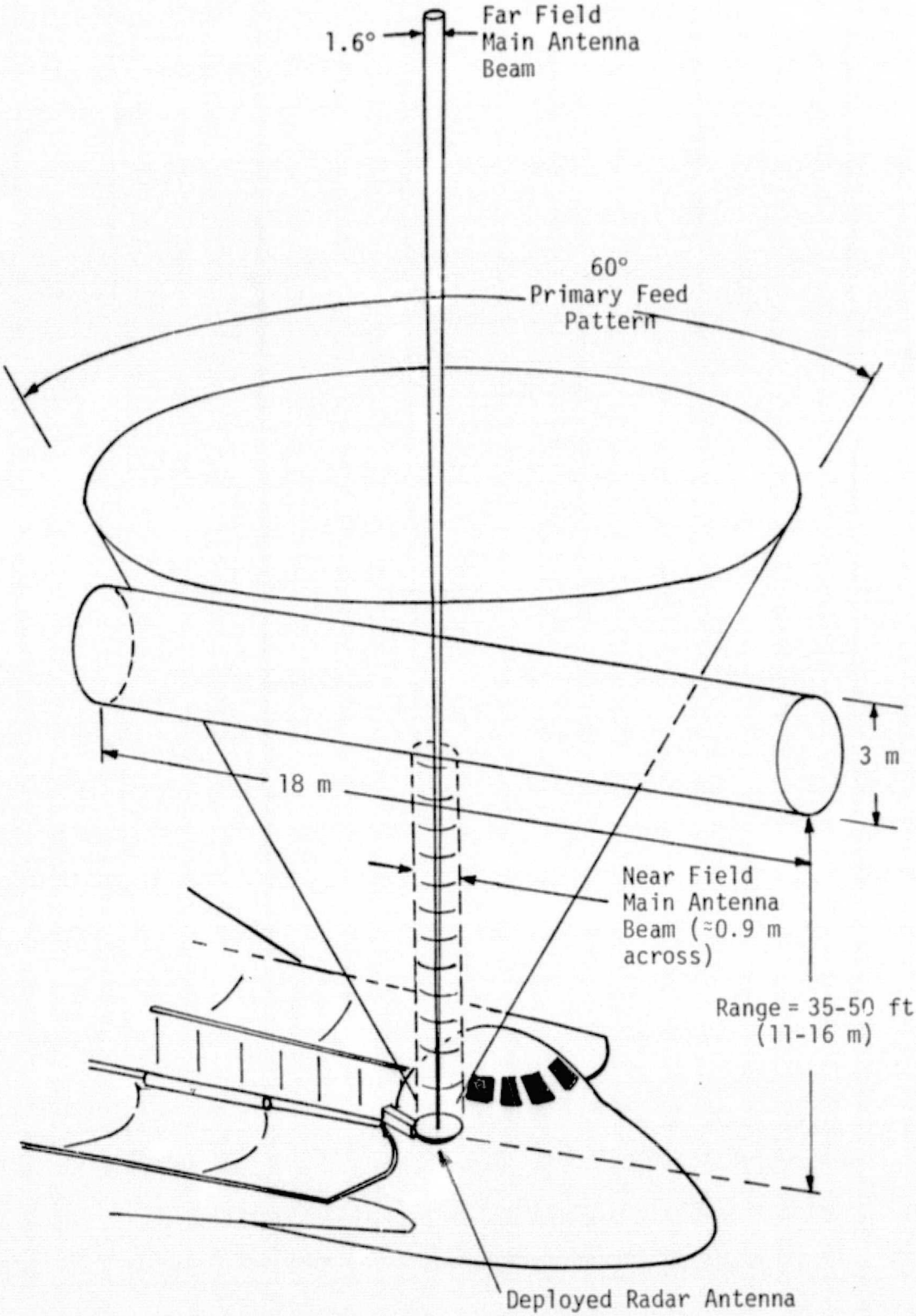

Figure 14. Antenna Directivities for Radar Tracking of a Passive Target at Stationkeeping Ranges

the horn by 180°, as shown in Figure 15a, or to switch to a second horn mounted behind the main horn, as shown in Figure 15b. The antenna patterns of these feeds are ±30° or, equivalently, a 60° beamwidth. In Figure 15a, the concept is conveyed of using the same horn for all modes of operation, but rotating it 180°, thus eliminating the dish for short range operation. Figure 15b illustrates an equivalent fix, only using two horns, switching from one to the other for short range operation. This, of course, also bypasses the dish. With a 60° beamwidth, even an 18-meter target can fit within the main beam out to a range of 18 meters. The gain drops to 3 dB, but that appears to be adequate at these short ranges.

It is recommended that this and other modifications of the existing antenna subsystem be examined as candidate solutions for the short range modes.

At these short ranges (as low as 35 feet), in order to transmit and receive a complete pulse, the pulse must be less than 70 nsec. In order to compensate for switching times and finite rise and fall times, the pulse width must be substantially less than 70 nsec. If the transmitted pulse is kept larger than that, then the receiver gate can be opened only for the last part of the pulse. This suggests that the trailing edge be used for range tracking. The problem is more intricate than this, however, since for an 18-meter target, a pulse of any width substantially less than 120 nsec will be spread in time to at least 120 nsec, due to time dispersion by the target. For a point target, of course, the pulse will return with little or no time dispersion. For large targets, therefore, the concept of range from a tracking point of view is not so immediate. The most satisfying range from an operational point of view is to have the closest range to the target.

It is recommended that the various candidate modifications of the existing Ku-band radar to accommodate the specifications at short range be examined carefully with particular emphasis on those suggested in [9]. It is apparent from this discussion that the modifications will involve all aspects of the system.

(a) One Horn - Rotated Mechanically

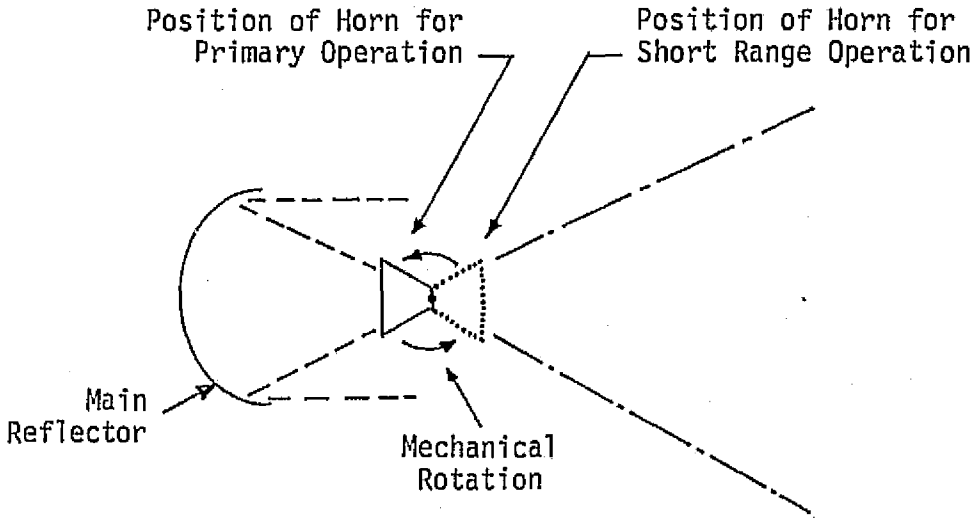

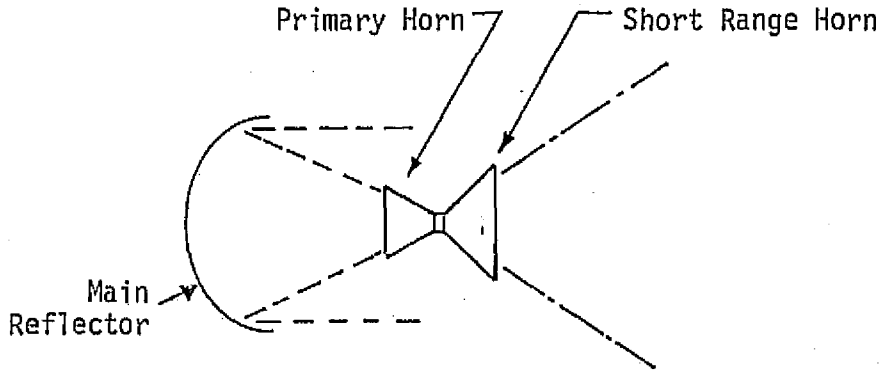

(b) Two Horns - No Mechanical Rotation

Figure 15. Candidate Short Mode Antenna Configurations

8.0 RANGING WAVEFORM CANDIDATES FOR SHORT RANGE OPERATION

The latest trend towards defining the short range operation of the Ku-band system is to consider two intervals: 3000 to 300 feet and 300 to 30 feet. Because the target return power at these ranges is more than adequate, signal-to-noise ratio is not a limiting factor. On the other hand, accuracy of the range and range rate (velocity) measurements becomes of paramount importance. In view of these requirements, one should consider possibilities of using waveforms other than conventional pulse for short range operation.

In Appendix E, several alternate (to pulse) candidate waveforms for short range ($R < 3000$ ft) radar are introduced. The basic requirement in choosing any one of these waveforms is the high range resolution accuracy, preferably combined with high range rate estimation accuracy. The latter can be achieved by the use of a bank of doppler filters or via the α-β estimator at these short ranges.

The ranging waveforms under consideration are: (1) linear FM signal, (2) short pulse signal, (3) tone ranging signal, and (4) pulse coded signal. The resolution capabilities, as well as the ambiguity functions, of these waveforms are presented and compared in Appendix E.

However, in order to choose the best ranging waveform for close range tracking, further rigorous analysis of all the candidates is required. This analysis should take into consideration all resulting implementation losses, as well as the added complexity (if any) of the transmitter and the receiver. These factors should be weighed against the performance capability of the existing pulse system.

9.0 MAXIMUM LIKELIHOOD ESTIMATOR DESCRIPTION

In the radar tracking mode, a logarithmic error discriminant is used [10] to obtain error signals for the various parameters of interest, namely, range, range rate, azimuth angle, and elevation angle. All of these parameters are mathematical duals of each other and a single model can apply to all of them. In each case, the information is imbedded in a pair of voltages $\underline{U}$ and $\underline{V}$, whose difference is approximately proportional to the target parameter under consideration.

Both $\underline{U}$ and $\underline{V}$ can be assumed to be narrowband processes and a maximum likelihood estimate of any desired parameter can be deduced by taking the logarithm of the powers of the two vectors; thus,

$$z = \log (\underline{U}^T\underline{U}/\underline{V}^T\underline{V}) .$$

In Appendix F, the maximum likelihood (M.L.) estimate of the ratio of the power in two narrowband processes is considered. These processes are assumed to be Gaussian and, in general, will be correlated. The in-phase and quadrature phase components of each process are sampled N times, where the time between samples is assumed to be large enough so that the samples are statistically independent. Numerical computation of the standard deviation formula (31) in Appendix F is shown in Figure 16 for N = 2,5,10. In the figure, ρ is the normalized correlation coefficient between the two processes. The results agree closely with those derived from an empirical formula in [10].

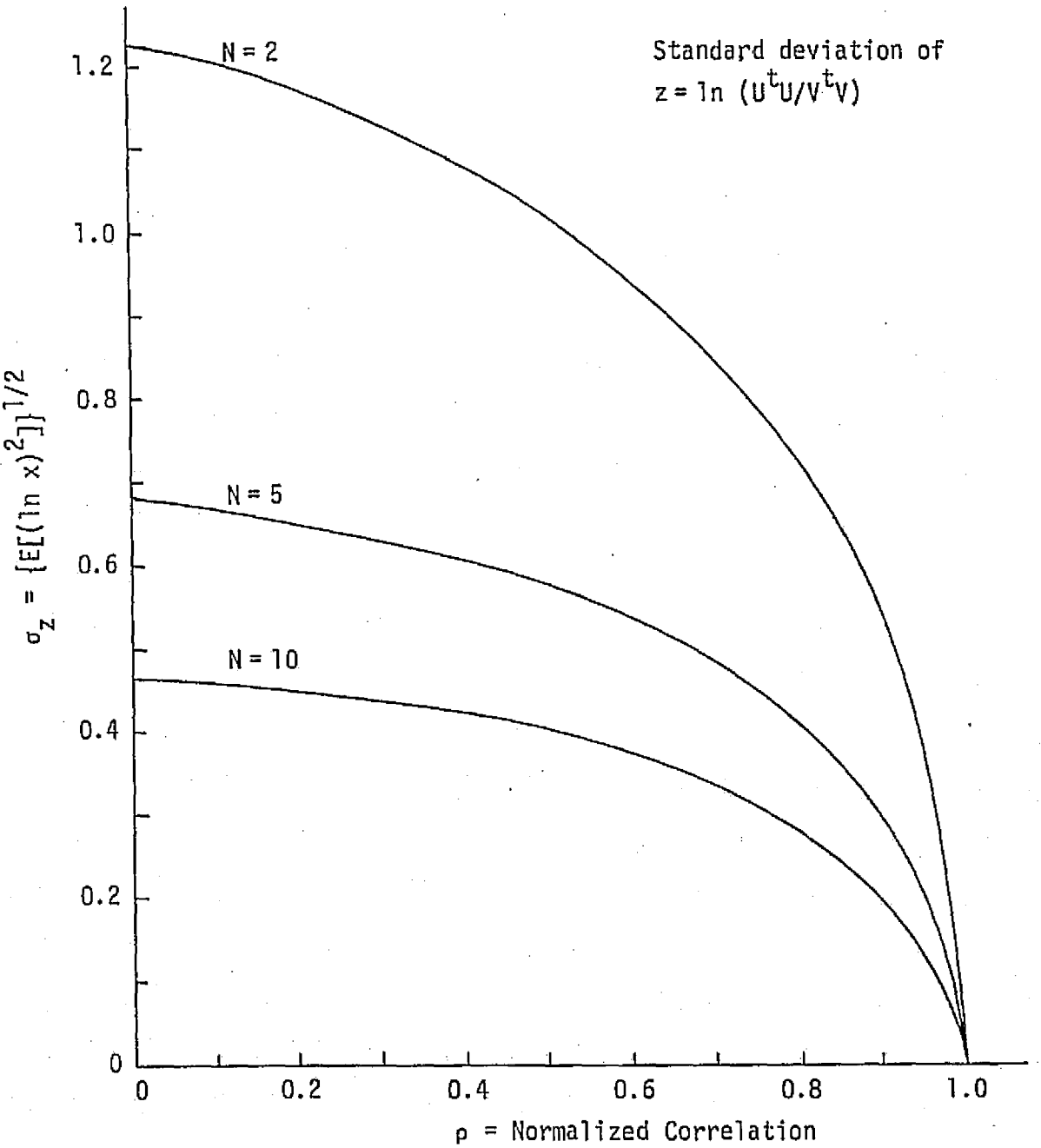

Figure 16. Standard Deviation of the Random Variable z as a Function of Correlation

10.0 CONCLUSIONS AND RECOMMENDATIONS

10.1 Power Budgets

It has been shown that, with the present set of system parameters (as of April 1977), when the radar is searching for a 1 m^2 passive target in the "Autotrack" mode at 12 nmi, the design margin is -0.5 dB. This is a reduction of 2.5 dB in design margin from the previous set of system parameters. Most of the loss is due to the significant increase of range gate straddling loss for the new set of system parameters. This may not be a serious situation in that the power budgets were performed at 12 nmi, and all radar tracking loops and estimators must be operating by the time range is reduced to 10 nmi. This is a time period corresponding to 2 nmi to initiate track. For a coherent radar, with digital signal processing, it is expected that this can be carried out in much less time. A gain of 2.3 dB in design margin is obtained by carrying out the power budget at 10.5 nmi. This is due to range reduction alone. There is also a 1+ dB gain in range gate straddling loss at 10.5 nmi.

Therefore, even though the design margin is still not very large, it is at least a couple of dB on the positive side.

It is recommended that further power budgets be carried out for the GPC-ACQ mode at 10-12 nmi to correctly assess the effect of range designate errors on search and track performance. Also, at short ranges ($R < 2$ nmi), similar power budgets are recommended in both modes with particular emphasis on the effect of errors in range designate.

10.2 Angle Track

A thorough analysis of the Ku-band radar which is angle tracking a passive target is presented in Appendix C. The analysis is applicable to all modes of operation which require angle tracking, namely, GPC-ACQ, GPC-DES, and Autotrack. At all ranges of interest ($R < 10$ nmi) for passive targets, the angle tracking system has a design margin of at least 70 dB. The crosscoupling errors into the angle tracking loops from the range and doppler tracking loops were described but not evaluated. With the present design margin and the fact that range and doppler crosstalk tracking errors may not be significant, it is expected that the design margin for the angle tracking loop will remain adequate.

10.3 Range and Doppler Tracking

It is recommended that the range tracking loop and doppler tracking loop be analytically developed in a manner similar to that of the angle tracking loop presented in this report. It is anticipated that both the range and doppler tracking loops will not have a design margin as satisfactory as the angle tracking loop.

In addition, it is recommended that the α-β tracking loop in the range tracking loop and the angle rate estimator be similarly developed. This would then clarify the performance capability of all aspects of the Ku-band radar when tracking a passive target in all modes in which tracking is required.

10.4 Stationkeeping

Preliminary considerations concerning the stationkeeping requirements of the Ku-band radar are presented in Section 7.0. Some suggestions are given as to how the presently configured system could be altered to meet the stationkeeping requirements, both in the presence and absence of clutter. The geometry of the Skylab reboost and the military satellites are such that it will be necessary to provide stationkeeping in the presence of earth clutter.

There are several areas that are deserving of significant effort. In the Short-Short mode (100-300 feet) and the Short-Short-Short mode (35-100 feet), the present antenna is operating in the near field. This has significant implications on the received signal and in monopulse tracking. One potential solution is the use of the feed-only part of the Ku-band antenna when in these modes. Preliminary studies show that this candidate configuration has promise. It is recommended that this potential modification, as well as other candidates, be carefully evaluated.

The other major area is the radar signal processing in the Short mode, Short-Short mode, and Short-Short-Short mode. One particular implementation is presently being evaluated, which totally eliminates clutter for all ranges to the earth up to 500 nmi. Other implementations have been proposed for these modes and are also under investigation.

10.5 Ground Clutter

Analysis of radar operation in the presence of main lobe ground clutter indicates that both acquisition and tracking requirements can be met for Skylab reboost missions with the present system configuration. This applies even to the case of nadir return. Meeting the general specifications, that is, of acquiring and tracking a 1 m^2 passive target at 12 nmi may not be possible unless either the radar modulation formats are modified from their present configuration or angles of incidence close to vertical are avoided. The investigation of methods for altering the modulation formats without impacting considerably the existing design is recommended. The goal of such an investigation will be to provide the required radar mode capability regardless of incidence angle and of the magnitude of the ground return.

The areas requiring further analysis, as outlined above, will be included with the remaining tasks of the program.

REFERENCES

1. "Procurement Specification MC409-0025, Ku-Band Integrated Radar and Communications Equipment," Vol. II, Space Division/Rockwell International, March 15, 1976.

2. M. K. Simon, S. Udalov, and G. K. Huth, "Study to Investigate and Evaluate Means of Optimizing the Ku-Band Communication Function for the Space Shuttle," Axiomatix Report No. R7703-2 (under NASA Contract NAS 9-14614), March 31, 1977.

3. "Proposal for Ku-Band Integrated Radar and Communication Equipment for the Space Shuttle Orbiter Vehicle," Vol. II, Hughes Aircraft Company, Ref. No. D7768/SCG 60176P, May 1976.

4. C. L. Weber, "Optimization of Proposed Radar for the Integrated Ku-Band Radar Communication System," Axiomatix Report No. R7408-5, August 1974.

5. "Ku-Band Integrated Radar and Communication Equipment for the Space Shuttle Orbiter Vehicle," Hughes Aircraft Co., Ref. No. D7738-SCG76075V, HS237-202, Conceptual Design Review, January 31, 1977.

6. S. Udalov, "Power Budgets for Passive Target Detection - Pulse Doppler Radar," Appendix N in "Study to Investigate and Evaluate Means of Optimizing the Radar Function for the Space Shuttle," Axiomatix Report No. R7607-4, July 1976.

7. "Study to Investigate and Evaluate Means of Optimizing the Radar Function for the Space Shuttle," Axiomatix Report No. R7607-4 (under NASA Contract NAS 9-14614), July 31, 1976.

8. R. Becker, "Rendezvous Profile Summary," Ku-Band Monthly Report, April 15, 1977.

9. "Ku-Band Integrated Radar and Communication Equipment for the Space Shuttle Orbiter Vehicle," Hughes Aircraft Company Monthly Program Status Report, May 24, 1976.

10. "Space Shuttle Ku-Band Integrated Rendezvous Radar/Communications System Study," Hughes Aircraft Co., Report No. D4148 SCG60041R, for NASA-JSC under Contract NAS 9-14595, March 1976.

APPENDIX A

POWER BUDGETS FOR THE KU-BAND RADAR FOR THE SPACE SHUTTLE ORBITER VEHICLE OPERATING IN THE AUTOTRACK MODE

APPENDIX A

POWER BUDGETS FOR THE KU-BAND RADAR FOR THE SPACE SHUTTLE ORBITER VEHICLE OPERATING IN THE AUTOTRACK MODE

by

Charles L. Weber

SUMMARY

Power budgets are developed for the Ku-band radar in the "Autotrack" search mode for a passive target at 12 nmi. Two cases are considered: (1) the improvement due to the use of frequency diversity is negligible (slow fading), and (2) the improvement due to the use of frequency diversity is ideal (fast fading).

For the slow fading case, the design margin is -6.0 dB, while for the fast fading case, the design margin is +2.0 dB. The latter is the more realistic case.

An alternate set of power budgets is also presented which incorporates recent changes in system parameters. Although these changes were instituted to decrease implementation complexity, there is a degradation in radar search performance in the passive mode. For the slow fading case, the design margin is lowered to -8.5 dB and in the fast fading case, the design margin is reduced to -0.54 dB.

Some of the cases presented are rather conservative. It is therefore anticipated that performance in some cases will be improved and that the design margins will be improved over those presented.

There are various alternatives to improve the design margin to a more satisfactory value, namely, 6 to 10 dB for passive radar.

In all cases considered, the gain of the main antenna was assumed to be G = 38.5 dB, which is the most recently known value [9].

Furthermore, all of the results in this report assume that two scans of the column to be illuminated can be accomplished in 1 minute. At 12 nmi, the two-sided cone angle that must be illuminated is 40 degrees. It has been shown [1,2] that, at these values of cone angle and range, two scans can be completed in 1 minute with a spatial dwell time of 36 msec. This is the spatial dwell time used in this report.

POWER BUDGETS FOR THE KU-BAND RADAR FOR THE SPACE SHUTTLE ORBITER VEHICLE

by

Charles L. Weber

1.0 INTRODUCTION

Sample power budgets are presented for the Orbiter Ku-band radar described in [1]. Most of the hardware losses predicted in [1] are used in the budget computations in this report. The passive automatic search-and-detect mode only is considered. This mode is the most critical from the required transmitted power point of view. Each of the parameters is considered individually before the composite power budgets are assembled.

2.0 THE RADAR EQUATION

The radar equation that is appropriate for passive mode detection of a pulse doppler radar which is essentially using an optimal receiver [2-4] is given by

$$\bar{R}_p = \frac{2E_p}{N_0} = \frac{[G^2 \bar{\sigma} \lambda^2][2 P_p \tau_f]}{[(4\pi)^3 R^4][k T_s][L]}$$

where

$\bar{R}_p$ = ensemble averaged peak SNR required per pulse for a given probability of detection, P_d, and false alarm probability, P_{fa}. In the case of an optimal radar which employs frequency diversity, the time of the pulse corresponds to the total time during which coherent addition takes place during one frequency dwell time.

E_p = peak signal energy received during the time in which coherent addition takes place

N_0 = equivalent one-sided noise power spectral density of the entire receiver system = $k T_s$

$\bar{\sigma}$ = average target cross section

λ = radar RF wavelength

G = peak antenna power gain

P_p = peak transmit power = P_{avg}/d_t

d_t = transmitter duty factor

P_{avg} = average transmit power

τ_f = total time of coherent addition at one RF = τM

τ = transmitted pulse width

M = number of transmitted pulses per RF frequency

R = range

k = Boltzmann constant = 1.38×10^{-23} Joules/°K

T_s = system noise temperature, °K

L = total system losses.

3.0 SEARCH RADAR SYSTEM PARAMETERS

Each of the above parameters is now considered in regard to the Ku-band radar for the Space Shuttle Orbiter Vehicle described in [1]. The reasoning and/or source of the choice of each parameter value is indicated.

3.1 Required Peak Signal-to-Noise Ratio Per Pulse

$$\bar{R}_p = \frac{2E_p}{N_0}$$

This value is dependent on the assumptions made about the mode of detection. The assumptions to be used in these power budgets are among the following cases. The overall probability of detection is 0.99 and the false alarm probability is 10^{-6}. The 0.99 value is a specification requirement, and the $\alpha = 10^{-6}$ value is approximately equivalent to one false alarm per hour, which is the specified value. The value of R_p is relatively insensitive to the choice of α. Hence, the choice is not critical. The cases shown in Table 1 all assume two scans, so that the probability of detection per scan is 0.9. The following definitions are used in Table 1:

N = number of pulses, noncoherently added

P_d = probability of detection per scan

n' = false alarm number

$\alpha = 0.693/n'$.

The table takes into account target fluctuation loss in both the slow and fast fading cases.

Table 1. Required Value of Signal-to-Noise Ratio to Meet the Indicated Performance Levels Under the Indicated Assumptions

Case	Requirements				SNR Needed	
	Description	N	P_d**	n'	R_p (dB)	E_p/N_0 (dB)
1	Swerling I (Slow Fading)*	6	0.9	10^6	18.2	15.2
2	Swerling II (Fast Fading)*	6	0.9	10^6	11.7	8.7
3	Swerling I	1	0.9	10^6	24.2	21.2
4	Nonfluctuating Target	1	0.9	10^6	16.3	13.3
5	Nonfluctuating Target	6	0.9	10^6	10.1	7.1
6	Swerling II	5	0.9	10^6	12.6	9.6

*The phraseology being adopted (somewhat incorrectly) is that the Swerling I model corresponds to slow fading and Swerling II to fast fading. The interpretation is based on the following assumptions, namely, that frequency diversity is being employed and that the target is initially modeled by Swerling I fluctuations. If the frequency diversity is not effective so that the Swerling I model still applies, then the term "slow fading" is used. If the frequency diversity is completely effective, and independent samples are being received upon changes in RF, then Swerling II applies, and it is called "fast fading."

**The cumulative probability of detection is specified at 0.99. With two scans of the column in 60 seconds, each scan then has a probability of detection of $P_d = 0.9$.

3.2 Average Target Cross Section

$$\bar{\sigma} = 1 \text{ m}^2, \text{ as per specification}$$

$$= 0 \text{ dB}.$$

3.3 Radar RF Wavelength

The RF for the radar is 13.775 GHz. This corresponds to

$$\lambda = 0.0218 \text{ meters}$$

$$\lambda^2 = -33.24 \text{ dB}.$$

3.4 Peak Antenna Power Gain

The antenna diameter has been specified as d = 36" = 0.914 m. Based on the rule of thumb,

$$\theta_B \text{ (deg)} \approx (180/\pi)(d/\lambda),$$

the 3 dB beamwidth is $\theta_B \approx 1.32$ deg. The 3 dB beamwidth quoted in [1] is 1.6 deg. Based on the rule of thumb [8],

$$G \approx \frac{32{,}000}{(\theta_B)^2} \qquad (\theta_B \text{ in deg}),$$

the peak power gain of the antenna is

$$G \approx 41 \text{ dB}.$$

The peak power gain in [1] is 38.9 dB, so that

$$G^2 = 77.8 \text{ dB}.$$

More recently, however, the peak power gain is given as 38.5 dB [9], so that

$$G^2 = 77.0 \text{ dB}.$$

The latter value is used in the power budgets in this report.

3.5 Transmitted Signal Characteristics

$$P_p = \text{peak transmitter power}$$

Given all other parameters and assumptions in the radar equation, the required peak transmitter power will then be obtained.

For the automatic search mode of a passive target, the PRF is presently set at 2666, so that the pulse repetition interval (PRI) is

$$\text{PRI} \triangleq T_p = 375 \ \mu\text{sec}.$$

Also, the pulse width is

$$\tau = 74.7 \ \mu\text{sec},$$

so that the transmitter duty factor is

$$d_t = 0.20$$

and the maximum unambiguous range is 30.4 nmi. The spatial dwell time, T_d, based on the algorithm described in [1] is

$$T_d = 36 \ \text{msec}.$$

This also agrees with that developed by Udalov [5] for the Ku-band radar search mode of a passive target.

The timing of the RF signal during one spatial dwell time is as shown in Table 2, where the frequency dwell time is seen to be 6 msec over each of the five RFs.

Table 2. One Spatial Dwell Time

RF	F_1	F_2	F_3	F_4	F_5	F_6	Total
Number of RF Pulses	16	16	16	16	16	16	96
msec	6	6	6	6	6	6	36

There are 16 RF pulses during each RF frequency dwell time. These are coherently added in the digital implementation, since the bandwidth of each of the doppler filters is matched to that associated with 16 pulses at one RF.

This is not a centerline radar, since there is no centerline filter, and since wideband sampling is performed at IF. This allows the coherent addition of all coherent lines in the receiver RF spectrum over the entire IF bandwidth.

The total time of coherent addition at one RF is

$$\tau_f = \tau M ,$$

where $\tau = 74.7$ sec

$M = 16$ pulses .

Therefore,

τ_f = total time of coherent addition

= 1195.2 μsec

= -29.2 dB .

3.6 Range

The specification calls for meeting the above requirements for a ($\bar{\sigma} = m^2$) passive target at 12 nmi = 22.236 km. Hence,

$$R = 22.236 \times 10^3 \text{ meters}$$

$$R^4 = 173.9 \text{ dB} .$$

3.7 Receiver Noise Parameters

The equivalent one-sided power spectral density of the receiver noise is

$$N_0 = kT_s \text{ watts/Hz} ,$$

where k = Boltzmann constant = 1.38×10^{-23} Joules/°K

= -228.6 dB

T_s = overall system noise temperature

The components in the overall system noise temperature can be computed from the diagram shown in Figure 1.

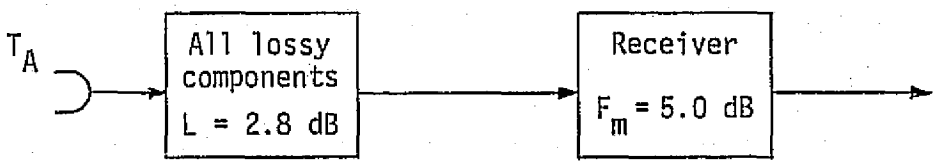

Figure 1. Simplified Diagram of Losses for Ku-Band Radar Receiver

The receiver is assumed to have a noise figure of 5 dB. All component losses [1] between the antenna and the receiver add to 2.8 dB.

When the first stage of a receiver is an attenuator, as is the case here, it can be shown [6] that the system noise temperature, computed at the antenna, is

$$T_s = T_A + T_c + (L-1)T_0 + L T_e ,$$

where T_A = antenna temperature

T_c = additional antenna temperature due to clutter

L = total attenuation from all lossy components between the antenna and receiver input

T_e = receiver noise temperature = $(F_n - 1)T_0$

F_n = receiver noise figure

T_0 = standard room temperature = 290°K.

The design in [1] assumes the receiver noise figure is $F_n = 5.0$ dB or, equivalently, $T_e = 627$°K, and the attenuation from all lossy components between the antenna and receiver front end is $L = 2.8$ dB. The antenna temperature is assumed to be $T_A = 5.5$°K and the additional antenna temperature due to earth clutter when looking horizontally is $T_c = 36.5$°K. Then

$$\begin{aligned} T_s &= T_A + T_c + (L-1)T_0 + L T_e \\ &= 5.5 + 36.5 + 263 + 1195 \\ &= 1500\text{°K} \\ &= 31.76 \text{ dB}. \end{aligned}$$

This is increased somewhat as the look angle increases. When looking directly towards the earth, the clutter temperature increases to 263.5°K, and T_s increases to

$$T_s = 1727\text{°K} = 32.37 \text{ dB}.$$

3.8 Losses

In this section, the pertinent losses are listed, along with the references where the values were derived or where the losses were specified.

3.8.1 Transmit Losses

The RFP and the response [1] have specified the transmit losses at 3.5 dB. At this point, no attempt is being made to dispute this value, so it is accepted and used in the computations.

3.8.2 Scan Alignment Loss and Lateral Scan Loss

The specification calls for a total beam shape loss of 2 dB. In [3], it is shown that the scan alignment loss is 1.03 dB each way and the lateral scan loss is 0.58 dB each way, when the antenna movement from one circle to the next in the spiral scan is 0.6 θ_B. The spiral scan described in [1] and [5] calls for an antenna movement of 0.7 θ_B. The difference in scan alignment loss and lateral scan loss between adjacent antenna paths of 0.6 θ_B and 0.7 θ_B is negligible. Thus, the two-way loss due to beam shape which includes scan alignment loss and lateral scan loss is set at $2(1.03 + 0.58) = 3.2$ dB.

3.8.3 Threshold Loss (Constant FAP)

The specification calls for a threshold loss of 1 dB due to maintaining a constant false-alarm probability by monitoring the system noise level. This value is used in the computation, realizing that it should be possible to reduce this value to a few tenths of a dB.

3.8.4 Processor Loss

It is estimated that the algorithms in the radar digital signal processor will result in approximately 1.7 dB loss [1]. This value is also used in the power budget, while anticipating that it may be possible to reduce it.

3.8.5 Range Gate Straddling

The present implementation calls for four range gates when the initial range to the target is not designated by GPC [1], as shown in Figure 2. Each range gate is of the same width as the transmitted pulse. The corresponding values of range are shown at the beginning of each range gate which corresponds to zero straddling loss. For example, at 12 nmi, the received pulse will show up exactly in Range Bin 2. As the range decreases, straddling loss increases, but not as fast as the R^4 factor increases signal power. The net effect is that, at 12 nmi, there is

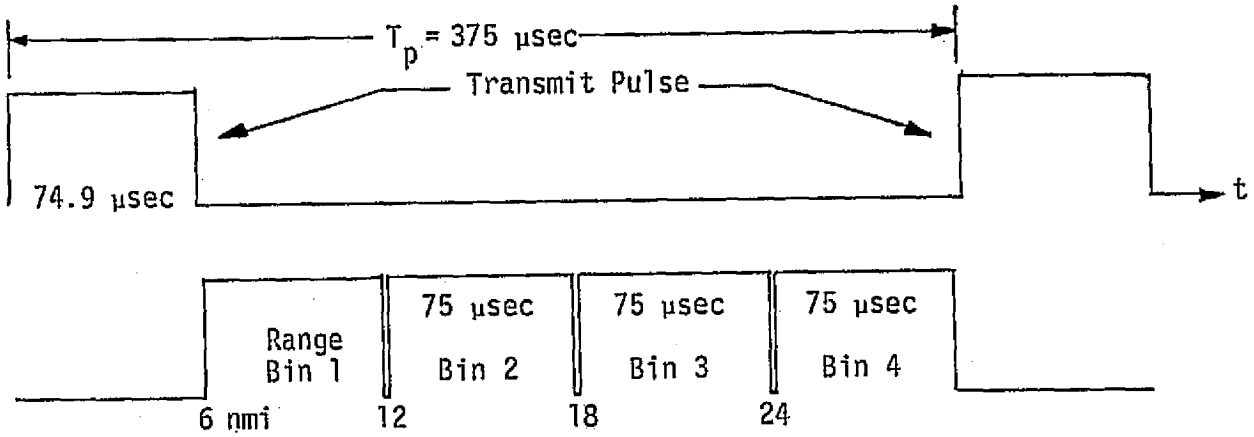

Figure 2. Range Gate Diagram

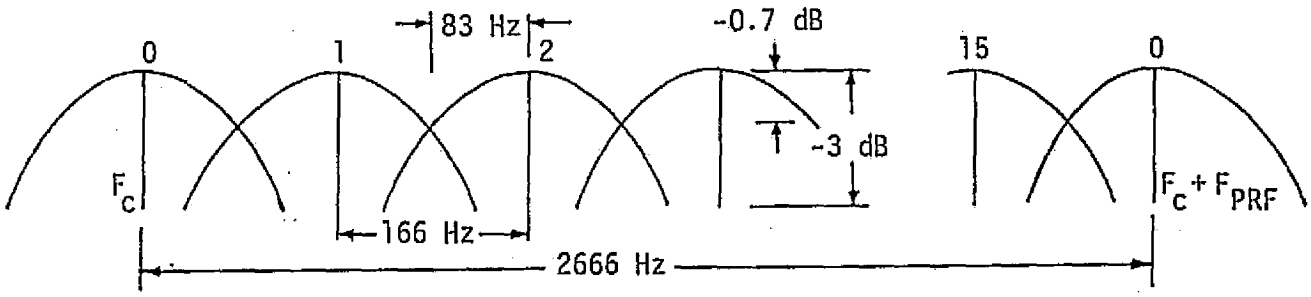

Figure 3. Description of Bank of Doppler Filters

no range gate straddling loss and, at all shorter ranges, the SNR increases. As a result, the range gate straddling loss is set to zero. Straddling loss and eclipsing loss are analyzed in detail in [7].

3.8.6 Doppler Filter Loss

Following each of the four range bins is a bank of 16 doppler filters, as shown in the block diagram of Figure 3. These filters are uniformly spaced over the frequency range $[f_c, f_c + f_{PRF}]$. For passive search and detection at 12 nmi, the PRF is 2666 Hz, so that the frequency difference between the center of adjancent filters is 166 Hz, as shown in Figure 3. If the 3 dB (one-sided) is set at $F_{PRF}/16$, then at the points where the adjacent filter gains cross (at ±83 Hz about the center of the filter), the gain is down approximately 1 dB for a first order Butterworth filter, and down approximately 0.7 dB for a $[(\sin x)/x]^2$ filter. This loss is classified as mismatch due to doppler. In our pessimistic power budget, we use -1 dB, and, in the more realistic budget, -0.7 dB is used.

There may be additional loss due to the lack of a proper match between the pulse bandwidth, the PRF, and the bandwidth of the FFT.

3.8.7 Pre-Sum Mismatch

There is an additional loss due to doppler in the pre-sum. The pre-sum adds all samples over the width of one range bin from a transmitted pulse. There is no doppler compensation in the pre-sum. If there is no doppler, then this coherent addition is ideal and there is no loss. As the doppler frequency increases, the pre-sum loss increases. This loss is in both the I and Q channels and can be described in terms of the following integral and is shown in Figure 4.

$$L_{PRE\text{-}SUM} = \left| \frac{1}{\tau_p} \int_0^{\tau_p} e^{j2\pi f_D t} \, dt \right|^2$$

where τ_p is the transmitted pulse width and f_D is the doppler frequency. This is a very close approximation to the actual pre-sum loss, since the sampling rate is high. The pre-sum loss becomes

$$L_{PRE\text{-}SUM} = \left| \frac{\sin(\pi f_D \tau_p)}{\pi f_D \tau_p} \right|^2 ,$$

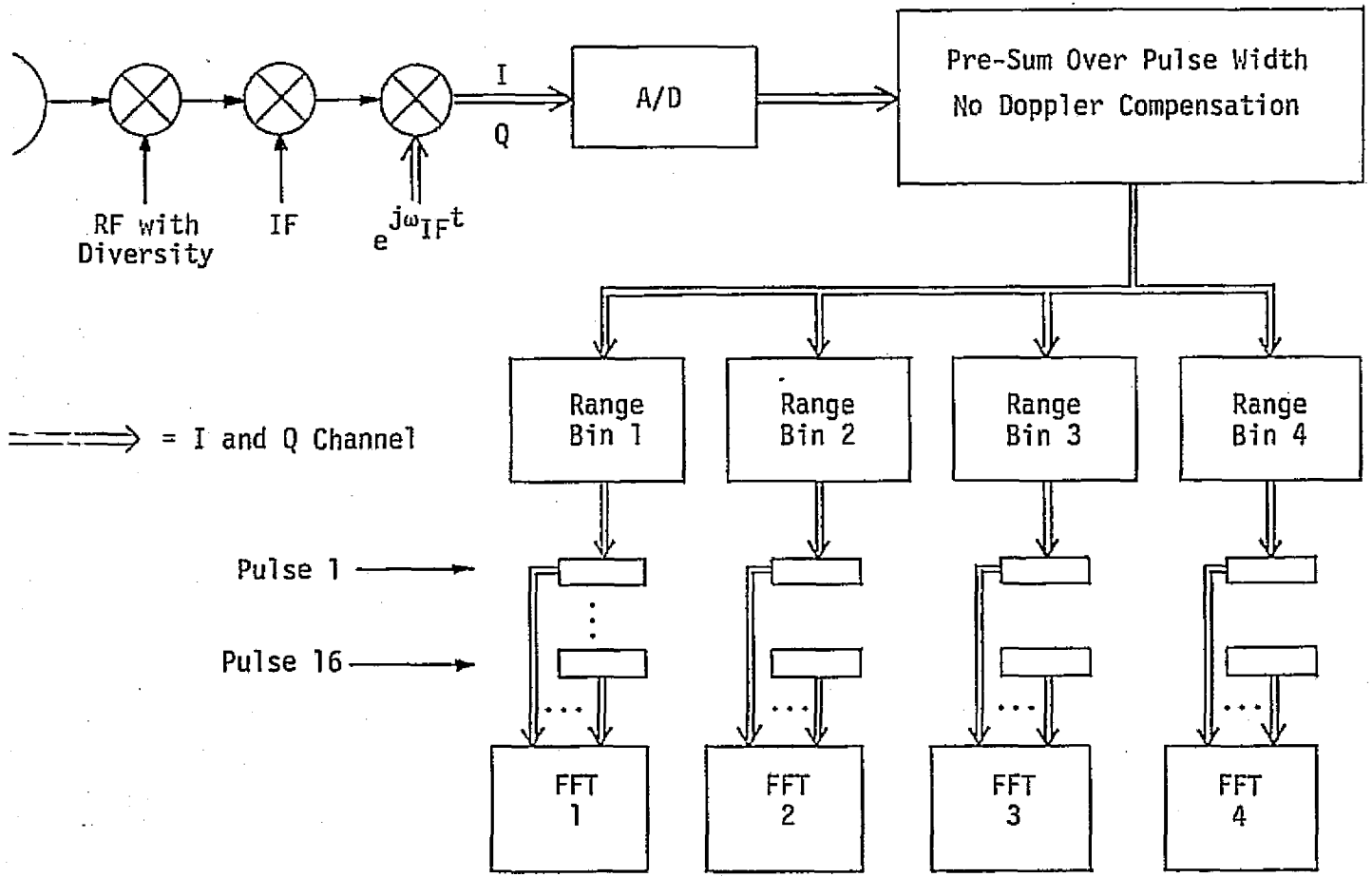

Figure 4. Block Diagram of Digital Pulse Doppler Detection

which is plotted in Figure 5. For the radar in [1], $\tau_p = 75$ μsec. The range rate varies over -75 fps to +148 fps. At $f_c = 13.775$ GHz, each fps is equal to approximately 28 Hz, so that the doppler frequency is within the range

$$F_D \in [-2100, +4144 \text{ Hz}].$$

Ambiguity clearly exists, since the PRF = 2666 Hz. This ambiguity is being resolved by filtering and differentiating the range measurements. The maximum pre-sum loss therefore occurs at $F_D = 2666$ Hz. Then,

$$\tau_p F_D = (75 \text{ μsec})(2666 \text{ Hz}) = 0.2.$$

This is shown as the dot in Figure 5, and the resulting maximum pre-sum loss is 0.6 dB.

4.0 POWER BUDGETS FOR PASSIVE SEARCH

In Table 3, the results of the previous sections are summarized for the slow and fast fading cases. The assumptions that the target range is not designated and that detection must be accomplished at R = 12 nmi are maintained.

Budget #1, the slow fading case, assumes frequency diversity is present but totally ineffective and that independent samples are not obtained when the RF frequency is switched. As a result, we have a Swerling I target. The postdetection integration is still noncoherent from frequency to frequency.

With all of the assumptions listed in Table 3, the required <u>average</u> power in Budget #1 is 39.7 watts, which is higher than the design value of 10 watts [1] by 6.0 dB. The corresponding peak power is 198.6 watts when the duty factor is $d_t = 0.2$.

With Budget #2, the fast fading derived from the use of frequency diversity is assumed to be ideal. This is somewhat optimistic since one of the RF frequencies is used twice over the spatial dwell time. An underestimate of the power required would be to set the number of RF frequencies to N = 5, and the spatial dwell time to 30 msec.

For Budget #2, the required average power is 6.3 watts, and the required peak power is 31.5 watts. Both of these values are below the average TWT power required for the Ku-band communication system. Based

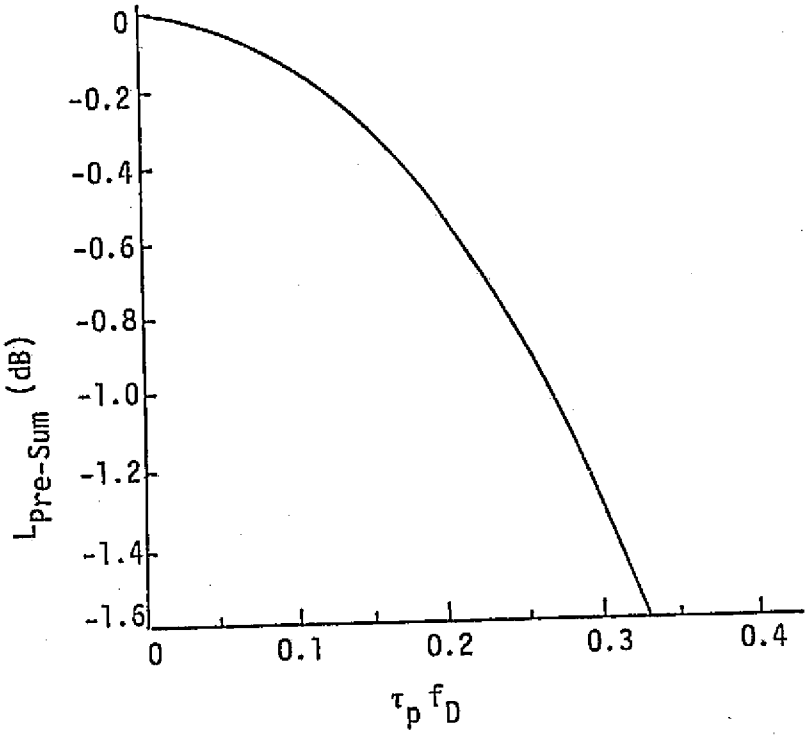

Figure 5. Pre-Sum Loss as a Function of the Pulse Width-Doppler Frequency Product

Table 3. Power Budget for Passive Search at 12 nmi Without Range Designated

Item	Term	Section Number in This Report	Value	Budget #1 Case #1 (Slow Fade) (dB)	Budget #2 Case #2 (Fast Fade) (dB)
1	R_p	3.1	Required Peak SNR	18.2	11.7
2	G^2	3.4	G = 38.5 dB	-77.0	-77.0
3	λ^2	3.3	λ = 0.0218 m	33.24	33.24
4	$\bar{\sigma}$	3.2	1 m^2	0	0
5	$(4\pi)^3$			33	33
6	R^4	3.6	R = 12 nmi = 22.2 km	173.9	173.9
7	k	3.7	1.38×10^{-23}	-228.6	-228.6
8	T_s	3.7	1500°K	31.76	31.76
9	Coherent Addition Time τ_f	3.5	1.195 msec	29.23	29.23
10		2.0	2	-3	-3
	Losses	3.8			
11	Transmit Losses	3.8.1	RFP	3.5	3.5
12	Beam Shape	3.8.2	Scan Alignment - Lateral Scan	3.2	3.2
13	Threshold	3.8.3	Constant FAP	1.0	0.5
14	Processor Loss	3.8.4		1.7	1.0
15	Range Gate Straddling Loss	3.8.5		0	0
16	Doppler	3.8.6	Mismatch	1.0	0.7
17	PDI		Postdetection Integration BEF [1]	1.25	1.25
18	Pre-Sum Mismatch	3.8.7	Due to Doppler	0.6	0.6
19	P_p	3.5	Required Peak Power	22.98 dB (198.6 w)	14.98 dB (31.5 w)
20	d_t	3.5	Duty Factor = 0.2	-7.0	-7.0
21	P_{avg}		Required Average Power	15.99 dB (39.7 w)	7.99 dB (6.3 w)
22	P_p Design		Reference [1]	50 w	50 w
23	P_{avg} Design		Reference [1]	10 w	10 w
24	Design Margin			-6.0 dB	+2.0 dB

on a peak power of 50 watts and an average power of 10 watts, the design margin is 2.0 dB. Without the advantage of frequency diversity, as described by Budget #1, the design margin is -6.0 dB.

The more realistic power budget is Budget #2, where there is a positive design margin. It is also expected that some of the losses can be improved so that the design margin improves over that presented.

5.0 ALTERNATE POWER BUDGETS FOR PASSIVE SEARCH

In Table 4, alternate power budgets for passive search at 12 nmi are presented. The assumption that the target range is not designated is kept. In Table 4, the values which have altered from those in Table 3 are designated with an asterisk. The new values are a result of changes suggested in [9]. The altered values are now considered.

Item 3. A new set of RF frequencies for the Ku-band radar have been specified, and are:

13.779 GHz
13.831 GHz
13.883 GHz
13.935 GHz
13.987 GHz .

Using the center of these RFs, the value of the wavelength is
$\lambda = 0.02161$ m.

Item 9. The updated value of PRF for target ranges greater than 7.2 nmi is 2987 Hz and the updated value of pulse width is 66.4 μsec. Therefore,

$$\text{PRI} = 335 \text{ μsec}$$
$$\text{Maximum unambiguous range} = 21.8 \text{ nmi}$$
$$\text{Duty factor} = 0.20 \text{ (unchanged)}$$

Sixteen pulses are still assumed to be transmitted at each RF during search, so that the frequency dwell time is

$$\tau_t = (16)(335 \text{ μsec}) = 5.36 \text{ msec}$$

and the coherent addition time is

$$\tau_f = (16)(66.4 \text{ μsec}) = 1.062 \text{ msec}.$$

Number of Independent Observations of the Target. If the spatial dwell time of 36 msec is unchanged (which is assumed), then 6.72 RF frequencies illuminate the target during each spatial observation.

Table 4. Alternate Power Budget for Passive Search at 12 nmi Without Range Designated

Item	Term	Section Number in This Report	Value	Budget #3 Case #1 (Slow Fade) (dB)	Budget #4 Case #2 (Fast Fade) (dB)
1	R_p	3.1	Required Peak SNR	18.2	11.7
2	G^2	3.4	G = 38.5 dB	-77.0	-77.0
3	λ^2	3.3*	λ = 0.02161 m	33.31	33.31
4	$\bar{\sigma}$	3.2	1 m^2	0	0
5	$(4\pi)^3$			33	33
6	R^4	3.6	R = 12 nmi = 22.2 km	173.9	173.9
7	k	3.7	1.38×10^{-23}	-228.6	-228.6
8	T_s	3.7	1500°K	31.76	31.76
9	Coherent Addition Time τ_f	3.5*	1.062 msec	29.74	29.74
10		2.0	2	-3	-3
	Losses	3.8			
11	Transmit Losses	3.8.1	RFP	3.5	3.5
12	Beam Shape	3.8.2	Scan Alignment - Lateral Scan	3.2	3.2
13	Threshold	3.8.3	Constant FAP	1.0	0.5
14	Processor Loss	3.8.4		1.7	1.0
15	Range Gate Straddling Loss	3.8.5*		2.0	2.0
16	Doppler	3.8.6	Mismatch	1.0	0.7
17	PDI		Postdetection Integration Ref. [1]	1.25	1.25
18	Pre-Sum Mismatch	3.8.7*	Due to Doppler	0.57	0.57
19	P_p	3.5	Required Peak Power	25.53 dB (357.3 w)	17.53 dB (56.6 w)
20	d_t	3.5	Duty Factor = 0.2	-7.0	-7.0
21	P_{avg}		Required Average Power	18.54 dB (71.5 w)	10.54 dB (11.3 w)
22	P_p Design		Reference [1]	50 w	50 w
23	P_{avg} Design		Reference [1]	10 w	10 w
24	Design Margin			-8.5 dB	-0.54 dB

Since there are 5 RFs in the frequency diversity algorithm, there are 1.72 repeats during each spatial observation. Under the realistic assumption that, on the average, the repeated frequencies are only 50% as effective as new frequencies would be, the value of N = 6 independent observations of the target is used in the budgets of Table 4.

Item 15. With the new set of values proposed in [9], there is a range gate straddling loss. At 12 nmi, the pulse is received as shown in Figure 6, where four range gates are used in the search mode and range is not designated. The loss of received (coherently added) energy in Range Gate 2 is

$$\left(\frac{5.45 - 11}{5.45}\right)^2 = -2 \text{ dB}.$$

The square results from the fact that the received signal is being coherently (predetection) integrated. The straddling loss would be linear in the noncoherent case.

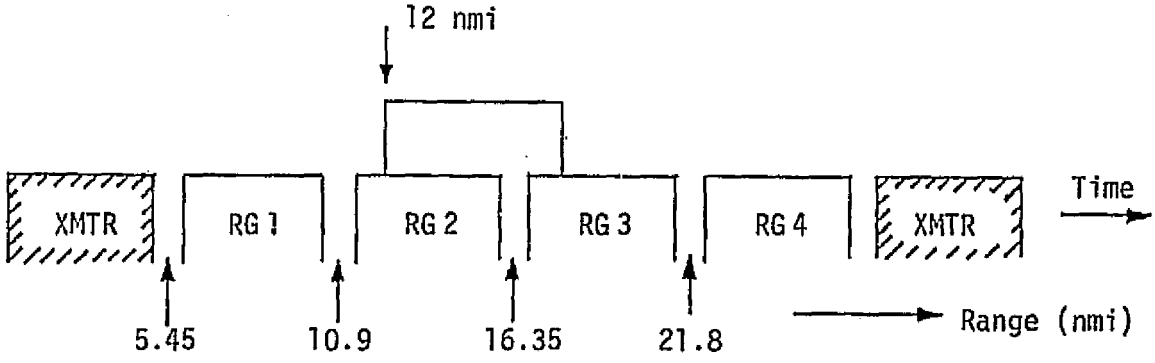

Figure 6. Range Gate Straddling Loss at 12 nmi

Item 18. There is an almost negligible change in the pre-sum mismatch due to doppler. From Figure 4, when $\tau_p = 66.4$ μsec and $f_d = 2987$ pps, the pre-sum loss is 0.57 dB.

All remaining entries in the budgets in Table 4 are carried forward from Table 3. For the passive search mode, it is noted that the new parameters deteriorate performance with respect to the former values in Table 3. When frequency diversity is totally ineffective on a Swerling I target (Budget #3), the design margin drops from -6.0 dB to -8.5 dB. When the

frequency diversity is assumed to operate ideally (Budget #4) and the various other loss improvements are used as described previously, then the design margin drops from +2.0 dB to -0.54 dB.

By allowing 2 nmi (12 to 10) to initiate all track modes of operation and get all RMS errors within specification, the detection must meet specification at 12 nmi. For coherent radar, it is most likely that this time is substantially less. For example, if these power budgets were computed at 11 nmi instead of 12 nmi, +1.5 dB of design margin is gained, and if they were performed at 10.2 nmi, +2.8 dB is gained in the design margin.

REFERENCES

1. Hughes Aircraft Co., "Ku-Band Integrated Radar and Communication Equipment for the Space Shuttle Orbiter Vehicle," Ref. No. D7738-SCG76075V, HS237-202, Conceptual Design Review, January 31, 1977.

2. S. Udalov, "Power Budgets for Passive Target Detection - Pulse Doppler Radar," Appendix N in "Study to Investigate and Evaluate Means of Optimizing the Radar Function for the Space Shuttle," Axiomatix Report No. R7607-4, July 1976.

3. C. L. Weber, "Optimization of Proposed Radar for the Integrated Ku-Band Radar Communication System," Axiomatix Report No. R7408-5, August 1974.

4. J. V. DiFranco and W. L. Rubin, Radar Detection, Prentice-Hall, 1968.

5. S. Udalov, "Spiral Scan Analysis," Appendix M in "Study to Investigate and Evaluate Means of Optimizing the Radar Function for the Space Shuttle," Axiomatix Report No. R7607-4, July 1976.

6. A. B. Carlson, Communication Systems, An Introduction to Signals and Noise in Electrical Communication, McGraw-Hill, 1968.

7. C. L. Weber, "Analysis of a Center Line Pulsed Doppler Radar Operating in the Search Mode," Axiomatix Report No. R7407-1, July 1974.

8. M. Skolnik, Radar Handbook, McGraw-Hill, 1970.

9. Hughes Aircraft Co., "Ku-Band Integrated Radar and Communication System for the Space Shuttle Orbiter Vehicle," Monthly Review, April 20, 1977.

APPENDIX B

RADAR SEARCH AND TRACK MODES DESCRIPTION

APPENDIX B

RADAR SEARCH AND TRACK MODES DESCRIPTION

by

Waddah Alem

1.0 INTRODUCTION

The objective of the Ku-band radar system on the Shuttle Orbiter is to detect the presence of a target and then obtain continuous accurate estimates of the various target parameters, namely, its range, range rate (velocity), azimuth, elevation angle, and angle rates. The target is usually detected when the radar is in the search mode, while the accurate estimates are obtained in the track mode. It is the objective of this appendix to clarify the overall radar block diagram and to explain its operation in both the search and track modes.

The radar employs coherent processing over each RF frequency transmitted, and noncoherent postdetection integration (PDI). Following the intermediate amplifiers, in-phase and quadrature phase signals are sampled and digitized (A/D converted), providing target amplitude and phase information. For longer range search and acquisition ($R > 3000$ ft), 16 doppler filters are formed, covering the doppler interval defined by the repetition rate. This is an ambiguous doppler interval; this ambiguity is removed via differentiation of the range estimates.

Following the filters, the target magnitude is determined, summed over the number of RF frequencies (noncoherent postdetection integration) and compared to a threshold. The threshold is set from noise measurements, so as to maintain a constant false alarm probability (CFAP). This can be implemented by any of several methods.

In the search mode, only the sum channel is processed. When the threshold is exceeded and target detection is declared, the auxiliary antenna signal is processed and its magnitude is compared with that of the main antenna to eliminate sidelobe detected targets. The auxiliary antenna has a peak gain which is approximately 20 dB less than that of the main antenna. Also, the sidelobes of the main antenna are approximately 20 dB down from the main lobe. This provides roughly a 20 dB main lobe/guard antenna ratio to detect and eliminate sidelobe targets.

In the modes for which angle tracking is required, namely, GPC acquisition and autotrack, the sum plus angle error channels are processed. The azimuth and elevation error signals are time-multiplexed, thereby eliminating the need for a second and third matched processing channel.

In Section 2.0, a general block diagram is drawn and explained in more detail; the functions of the individual blocks are described in the subsequent sections.

2.0 RADAR BLOCK DIAGRAM

The Shuttle Ku-band radar block diagram is shown in Figure 1. The antenna assembly consists of a main antenna and an auxiliary antenna, followed by the deployed mechanism assembly (DMA) and the deployed electrical assembly (DEA), where various switching and filtering operations take place, as explained in Section 3.0. The antenna assembly is followed by several IF mixing stages to bring the carrier frequency down to a stable IF of $f_0 = 78.143$ MHz. The output of the I-Q stage that follows is a pair of baseband signals which are in phase and in quadrature with the input signal. The operation of the previous two stages is discussed in Section 4.0. The available information is converted by an A/D converter to digital data which samples both channels at a rate of $f_s = 480$ kHz, which is slightly larger than the Nyquist rate of the baseband signals at the output of the I-Q stage. (The LPF bandwidth in both the I and Q channels is equal to 237 kHz.) The output of the A/D converter is a set of complex numbers which undergo various stages of digital processing before estimates of the target parameters (range, velocity, azimuth angle, elevation angle) are obtained. The first processing stage is a presumming stage, followed by a set of range gates and doppler filters consecutively. The arrangement of the gates is varied for the two modes of operation. In the search mode, where range designation is not present, there are four range gates per pulse, while in the track mode, there are only two nonoverlapping gates: an early gate and a late gate.

For long ranges, the magnitudes of the outputs of the doppler filters are summed over the RF frequencies and compared to a threshold to detect the existence of a target. For short ranges ($R < 3000$ ft), the detection takes place without using any doppler filtering.

Once a target is detected, the radar is switched to a track mode and the digital signals undergo postdetection integration, followed by

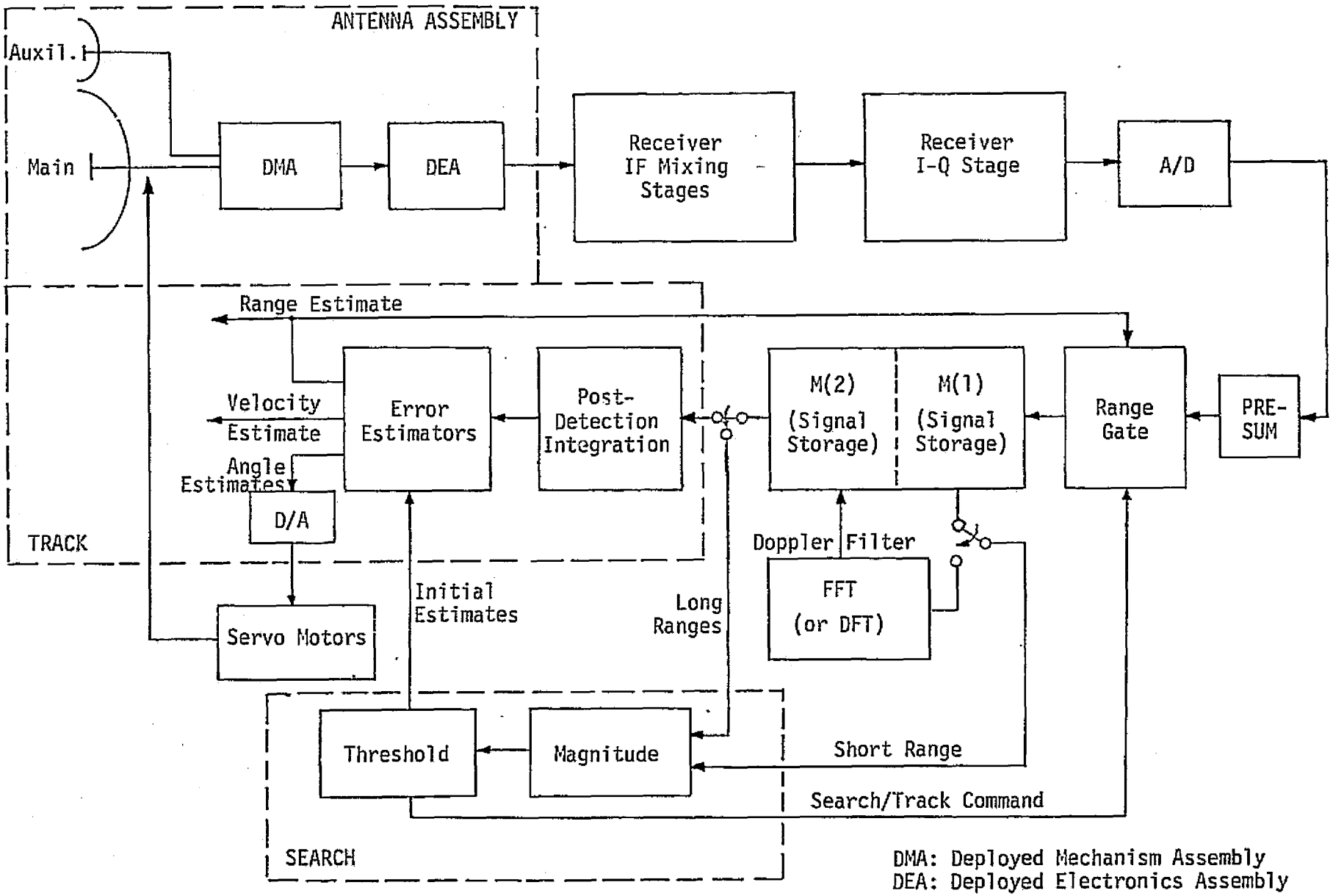

Figure 1. Radar Block Diagram

an error estimation unit which is initiated by a crude estimate obtained by the search mode operation. The final estimates of the various parameters are:

(1) Fed as inputs to the servo motors for angle track.

(2) Used to adjust the position of the early and late gates for range track.

(3) Displayed for the astronauts for visual reading (all variables being tracked).

(4) Utilized to update the state of the error estimators to obtain new estimates.

In the following sections, a detailed discussion of the various stages in the block diagram is presented, along with an analysis of the signal timing in both the search mode and the track mode.

3.0 ANTENNA ASSEMBLY

The antenna assembly is illustrated in Figure 2. The main antenna has a gain G = 38.5 dB. There is also an auxiliary antenna whose gain is G = 20 dB, which is used to guard against target effect on the sidelobes of the main antenna. Three signals emerge from the antenna, namely, the sum signal (Σ) which carries the received signal, and two angle signals (ΔAZ and ΔEL) which supply the azimuth and elevation angle information. The Σ signal is passed through a bandpass filter (BPF), whose center frequency can be adjusted, by a centralized frequency synthesizer, to be one of the five frequencies (13.779, 13.831, 13.883, 13.935, 13.987 GHz). The angle signals ΔAZ and ΔEL are passed through a selecting switch which selects one of the signals at a time at a rate of 93 Hz. The output of the switch is then passed through a phase encoder whose rate is twice that of the selecting switch. A typical sequence of signals out of the encoder is shown in Figure 3. The encoded angle signal is then passed through a matching BPF to that of the Σ signal. The two signals are then passed through the T/R switch to the receiver IF mixing stage.

When angle track is operating, there are four antenna error dwell periods at each RF, during which the azimuth and elevation error signals are processed. During each error dwell period, 16 doppler filter outputs (via DFT or FFT) are computed.

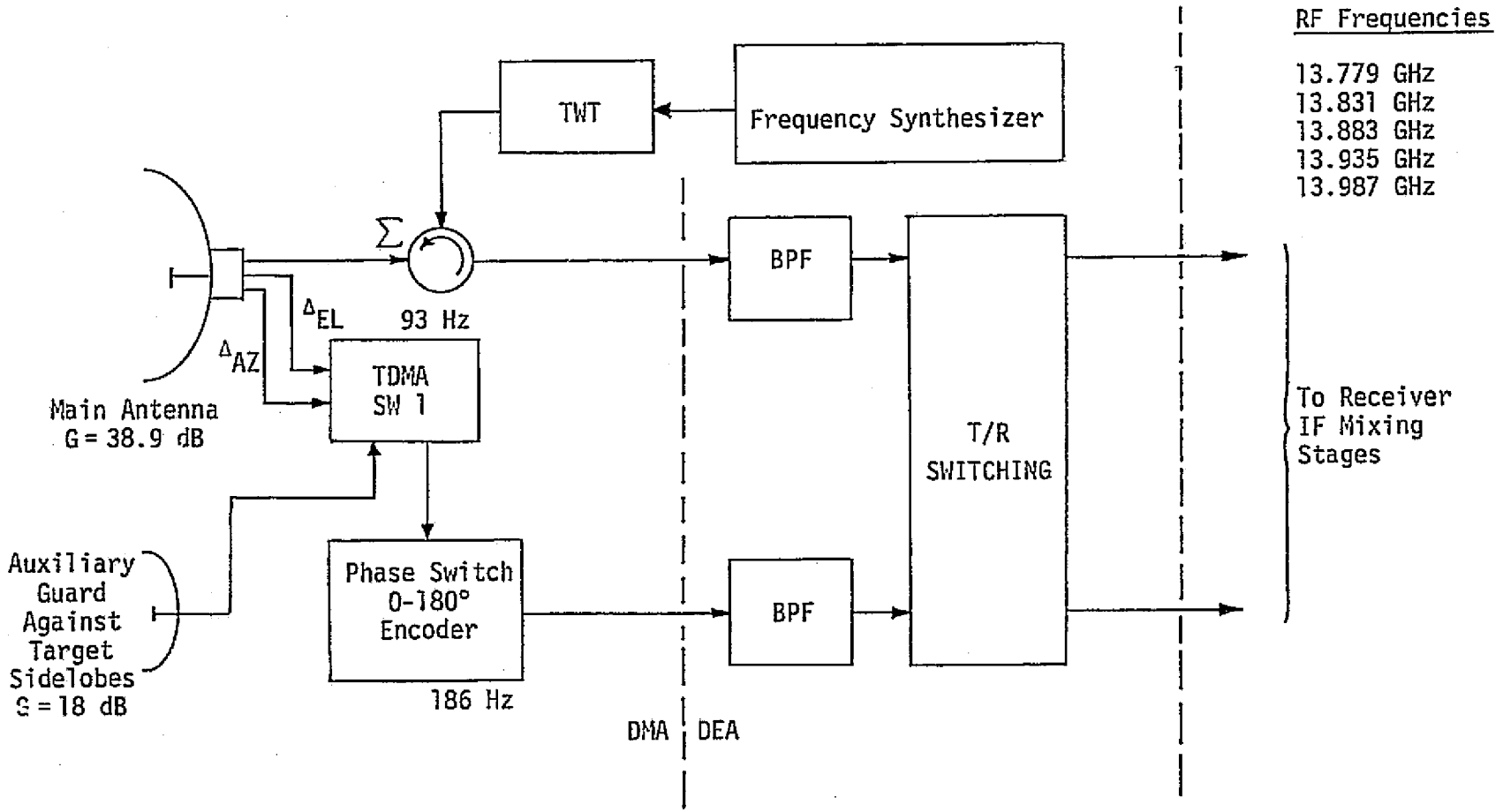

Figure 2. Antenna Assembly

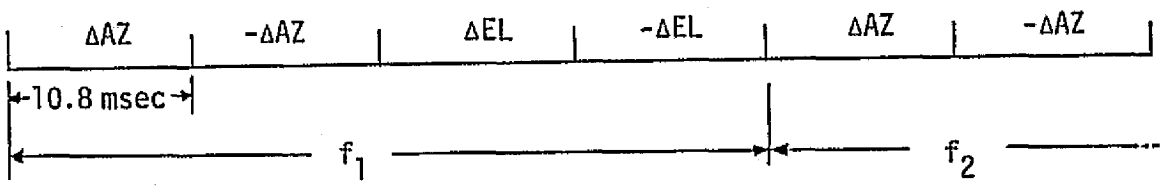

Figure 3. TDMA and Phase Encoder Output of Angle Error Information, During Angle Track

4.0 IF MIXING AND I-Q STAGES

The antenna assembly is followed by two stages of intermediate amplifiers and IF filters, where the frequency of the signal is beaten down to a stable 78.143 MHz, as shown in Figure 4. This, in turn, is followed by an in-phase and quadrature detectors (I-Q), where the signal is converted to two baseband signals. The two signals are converted to digital data using an A/D converter whose sampling frequency is slightly higher than twice the bandwidth of the signal to reduce the aliasing error to less than 0.5 dB.

The A/D converter supplies 32 samples/pulse from each channel of the I-Q detector for each range gate period. These samples are summed at the PRESUM stage to give a complex number that represents every received pulse.*

5.0 SIGNAL FORMAT

Before explaining the different modes of operation, it is important to discuss the signals that are being used. The signals are RF pulses with a duration (τ) and a pulse repetition frequency (PRF) that are functions of the designated range. Frequency diversity, using five RF frequencies, is used in both the search and track modes. Table 1 lists these frequencies which are cycled in a given pattern which is convenient for the manual operation mode [1]. The various signal timings are summarized in Table 2.

---

*The 32 samples/pulse number applies to the search mode only, where the pulse width is 66.3 μsec.

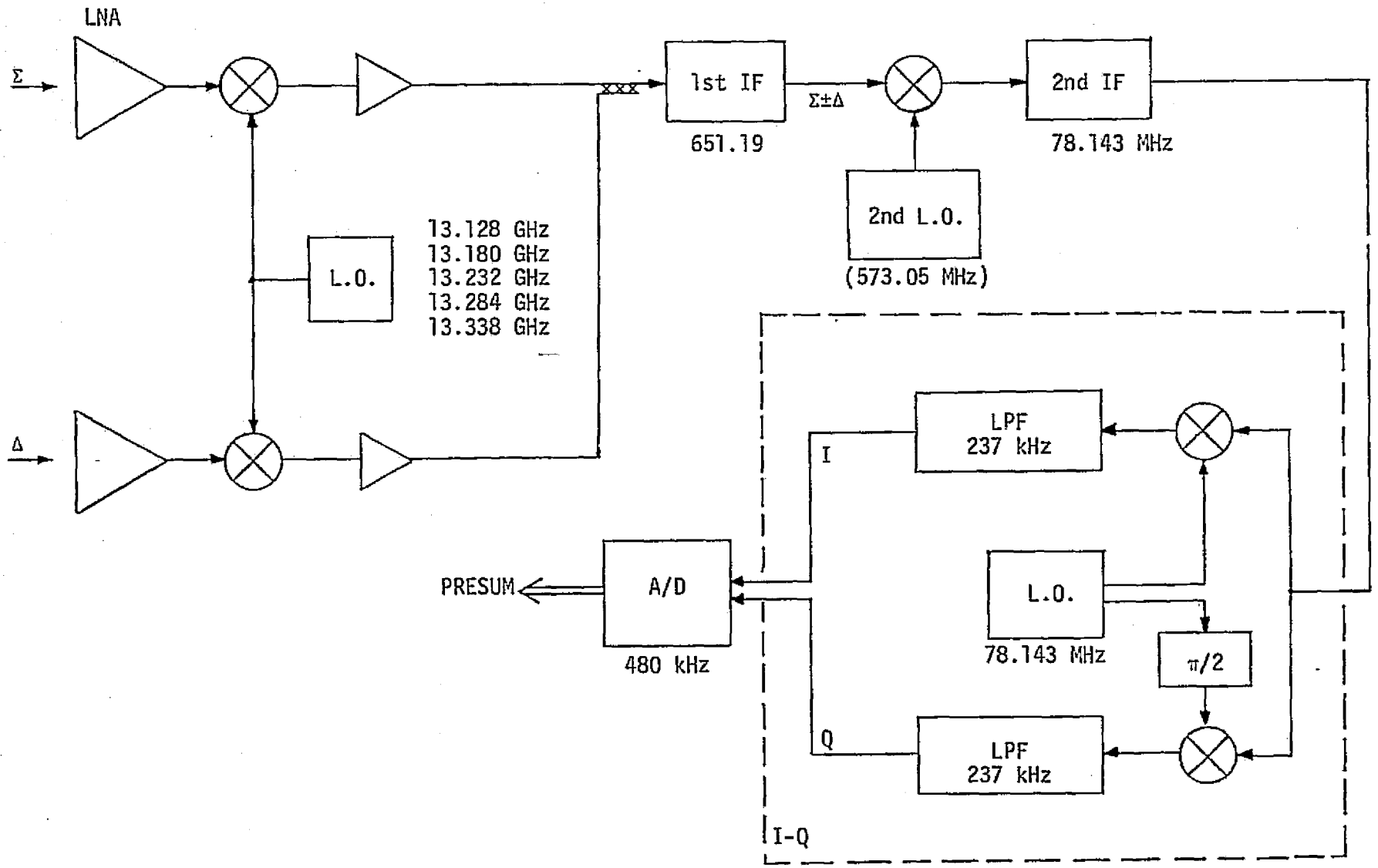

Figure 4. IF Mixing and I-Q Stages

Table 1. Frequency Synthesizer Frequencies for the First IF Mixing L.O. (in GHz)

F_1	F_2	F_3	F_4	F_5
13.128	13.180	13.232	13.284	13.336

Table 2. Dwell Times for Various Designated Ranges

			Search Mode	
Designated Range (nmi)	τ (μsec)	PRF (Hz)	Frequency Dwell Time (msec)	Spatial Dwell Time (msec)
8-22	66.3	2987	5.3	31.8
4-8	33.2	7177	2.2	13.4
2-4	16.6	7177	2.2	13.4
1-2	8.3	7177	2.2	13.4
0.5-1	4.1	7177	2.2	13.4

6.0 THE SEARCH MODE

In explaining the search mode operation, long range signal format is chosen for demonstration. All other ranges follow identical processing except for the short range (<0.5 nmi) which does not utilize the doppler filters.

Sixteen pulses are transmitted at each RF frequency. The duration of each pulse is 66.3 μsec, while the time between consecutive pulses is 335 μsec, as shown in Figure 5. Four range gates (R_1, R_2, R_3, R_4) are used to cover the designated range. It is important to note that no doppler correction is used at the presummer in the search mode. For each RF frequency, 64 complex numbers are stored in a memory designated as M(1), as shown in Figure 6. The output of each range gate at every RF frequency is passed through a bank of 16 doppler filters—implemented as discrete Fourier transforms (DFT) or fast Fourier transforms (FFT)—and the magnitudes of the outputs of these filters are calculated and compared to precalculated thresholds. The target is detected when the magnitude of one or two outputs of adjacent doppler filters pertaining to one or two range gates is exceeded. An initial estimate of the range and the range rate of the target are calculated from the knowledge of the doppler filters and range gates whose outputs have exceeded the threshold. These initial estimates are fed into the error estimators as initial conditions to start the successive estimation process in the track mode. The thresholds are calculated to produce an error alarm rate of one false alarm per hour.

7. THE TRACK MODE

7.1 Signal Format

The signal in the track mode consists of 64 pulses for each RF frequency, instead of the 16 pulses in the search mode, as shown in Figure 7 [1,2]. For long range tracking, the frequency dwell time is equal to 21.44 msec. Each frequency dwell time is divided into four time slots by the switching combination of SW1 and the phase encoder switch in the antenna assembly. The signals in the succeeding time slots are $\Sigma + \Delta AZ$, $\Sigma - \Delta AZ$, $\Sigma + \Delta EL$, and $\Sigma - \Delta EL$, respectively. The time slots are arranged so that the first two are used to measure the azimuth angle, while the last two are used for the elevation angle. Each one of the

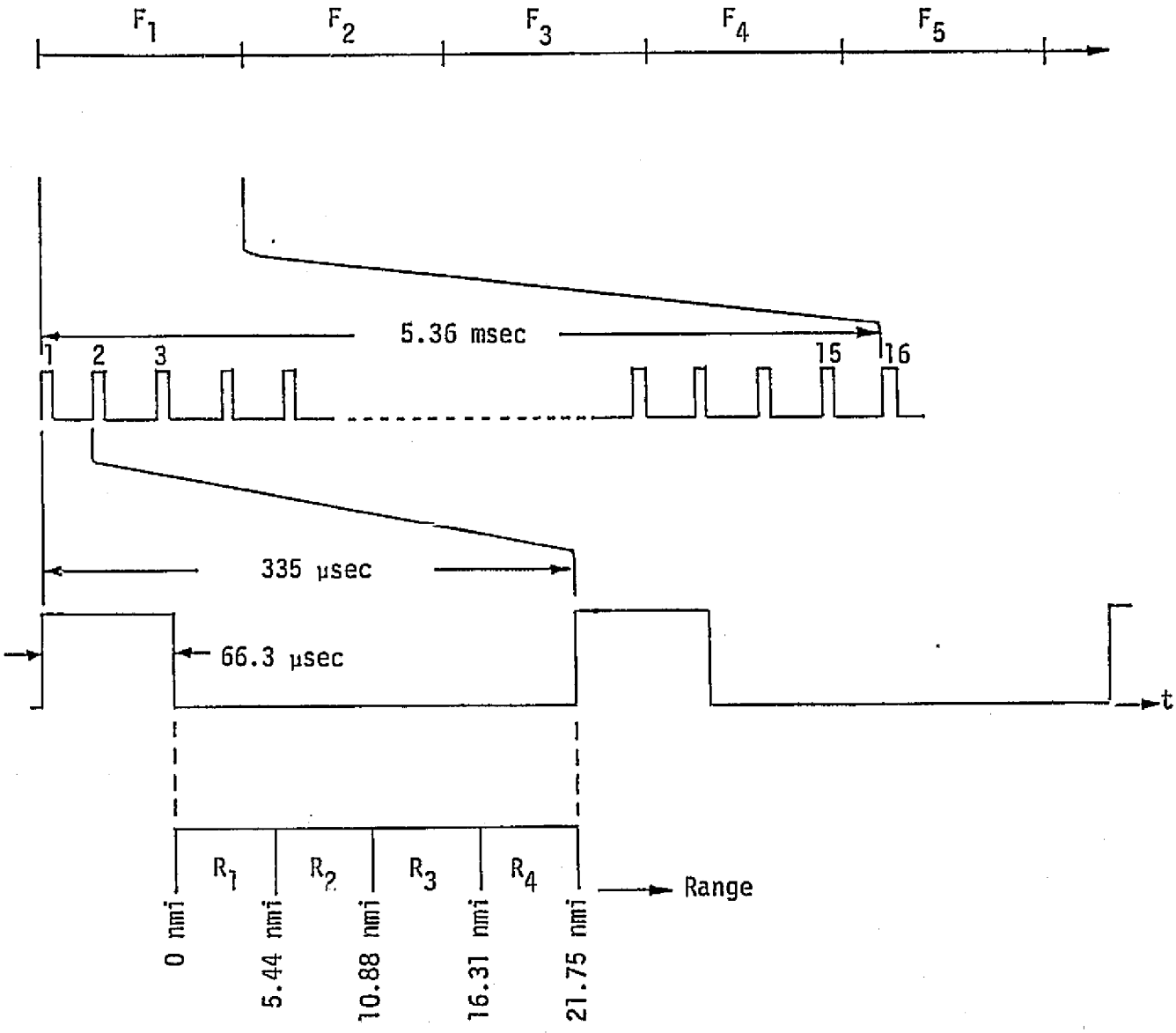

Figure 5. Long Range Search Signals

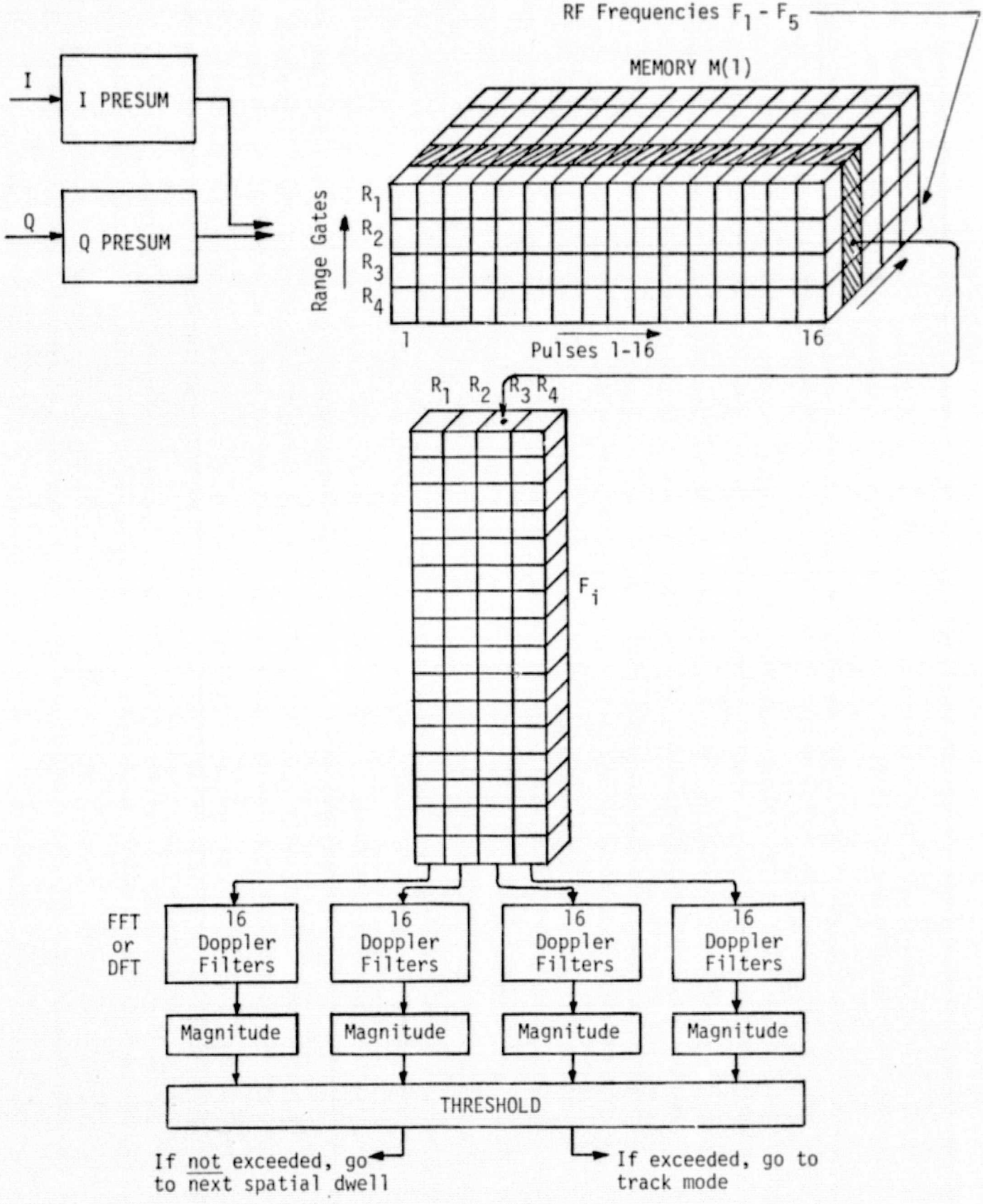

Figure 6. Search Mode Signal Processing

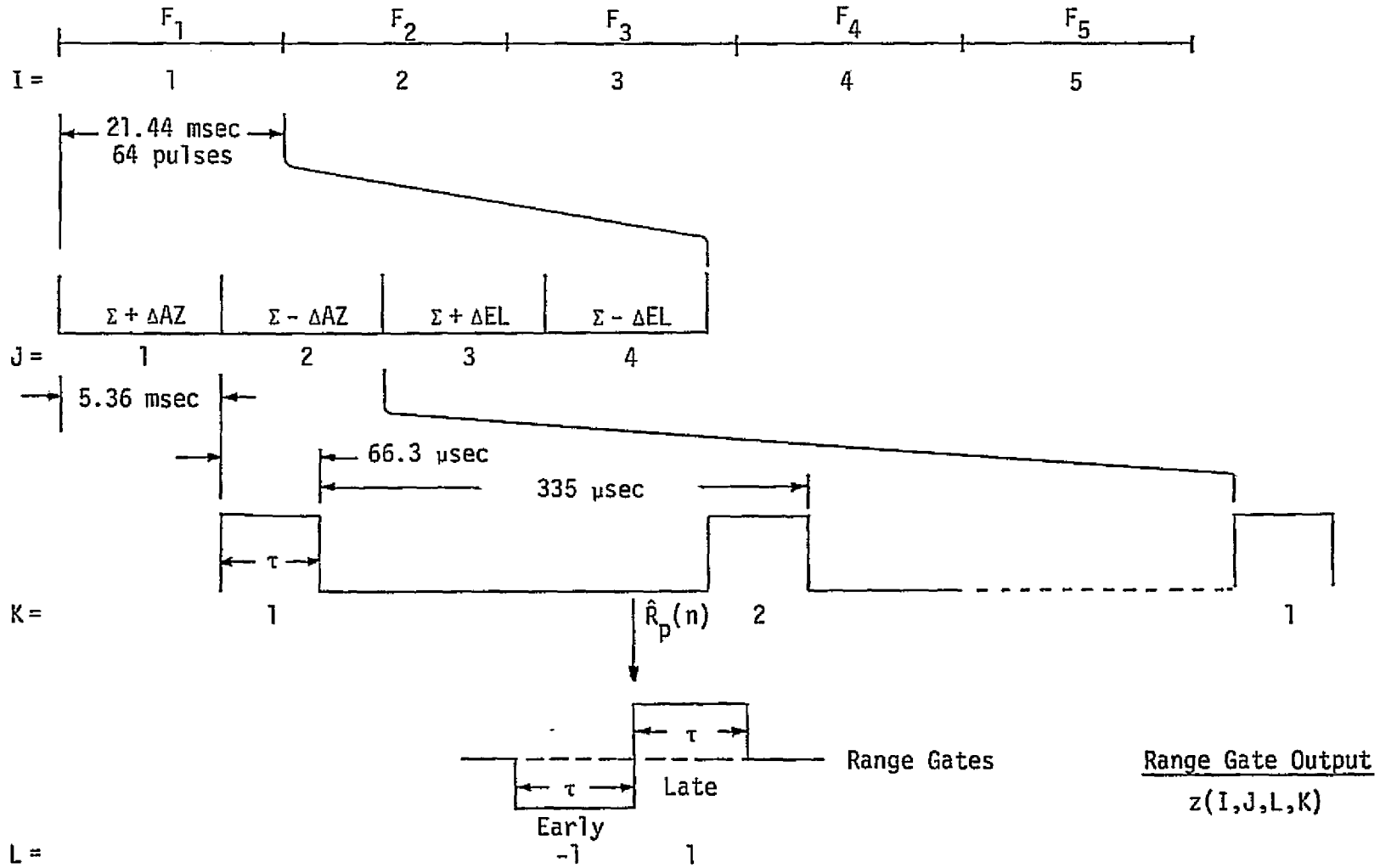

Figure 7. Track Mode Signal Format

previous time slots consists of 16 pulses. The pulses are passed through an early gate and a late gate, which are located around a predicted estimate of the range [$R_p(n)$] from the processor timing unit. The width of each gate is equal to the pulse width. The output of each range gate is a complex number z(I, J, L, K), which is a function of four parameters (I, J, L, K):

I denotes the RF frequency being transmitted; I = 1,2,...,5.

J denotes the time slot in each frequency such that

J = 1 corresponds to $\Sigma + \Delta AZ$

J = 2 corresponds to $\Sigma - \Delta AZ$

J = 3 corresponds to $\Sigma + \Delta EL$

J = 4 corresponds to $\Sigma - \Delta EL$.

K denotes a particular pulse in each time slot; K = 1,...,16.

L denotes the range gate under consideration:

L = -1 corresponds to Early Gate

L = +1 corresponds to Late Gate.

Figure 7 illustrates the signal format in the track mode.

7.2 Doppler Filtering

The outputs of the range gates are stored in a memory bank designated for illustration as M(1). For all combinations of I, J, and L, the series of 16 pulses (K = 1,...,16) are passed through a bank of 16 doppler filters, as shown in Figure 8 [1,5]. The doppler filters are uniformly spread over f_c, $f_c + f_{PRF}$. The overlapping of adjacent filters results in doppler filter loss, which has to be taken into consideration. The outputs of the doppler filters are designated as ω(I, J, L, M), where M denotes a particular filter (M = 1,...,16). I, J, and L represent the RF frequency, the time slot, and the range gate, respectively. Since doppler filtering is accomplished by digital Fourier transforms (DFT), ω(I, J, L, M) is given by

$$\omega(I,J,L,M) = \sum_{K=1}^{16} z(I,J,L,K)\, e^{-(j2\pi KM)/16}. \qquad (1)$$

Implementing doppler filters using FFT might result in losses due to the lack of proper match between the pulse bandwidth, the PRF, and the bandwidth of the FFT.

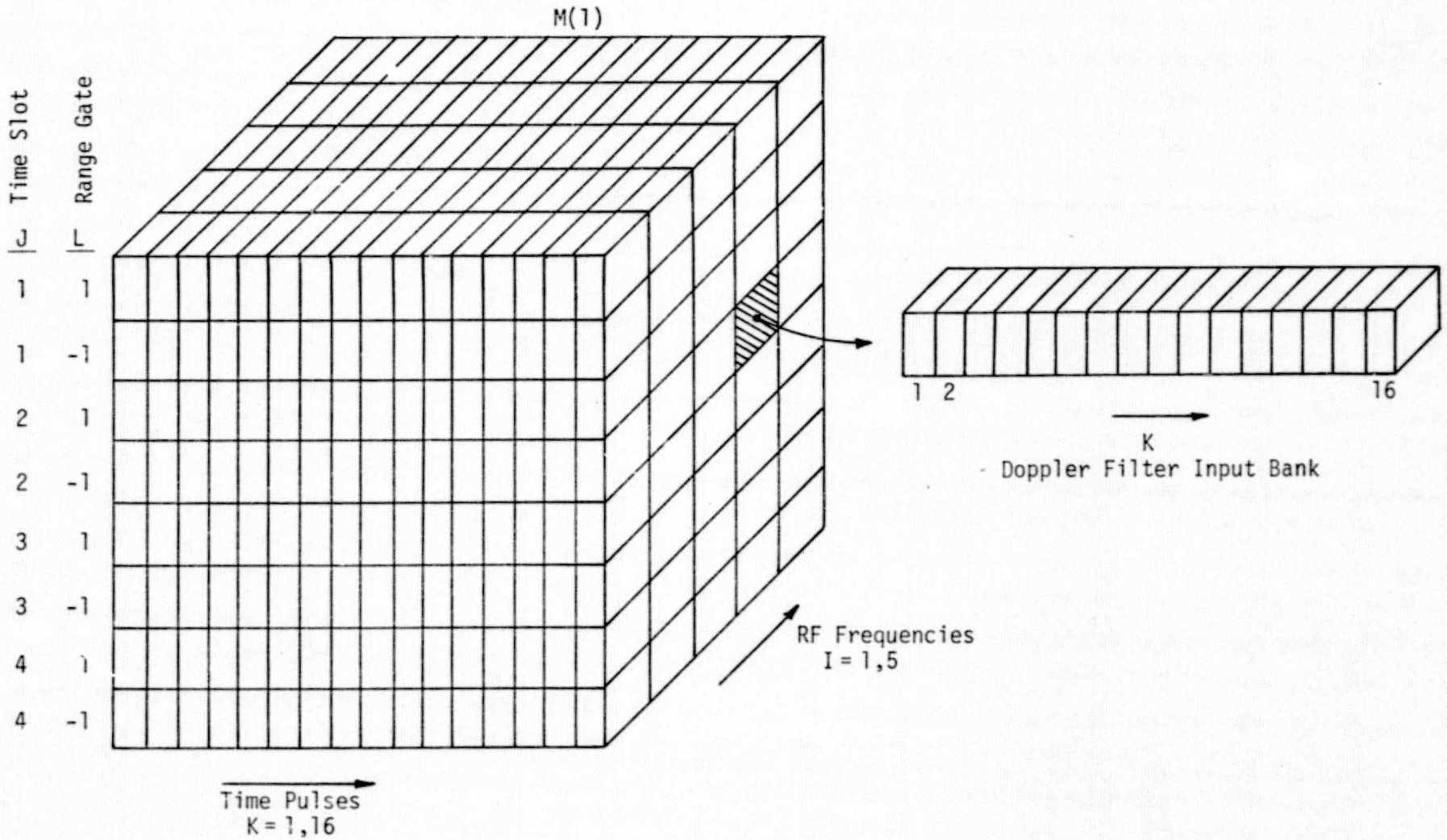

Figure 8. Pictorial Illustration of Memory Bank M(1)

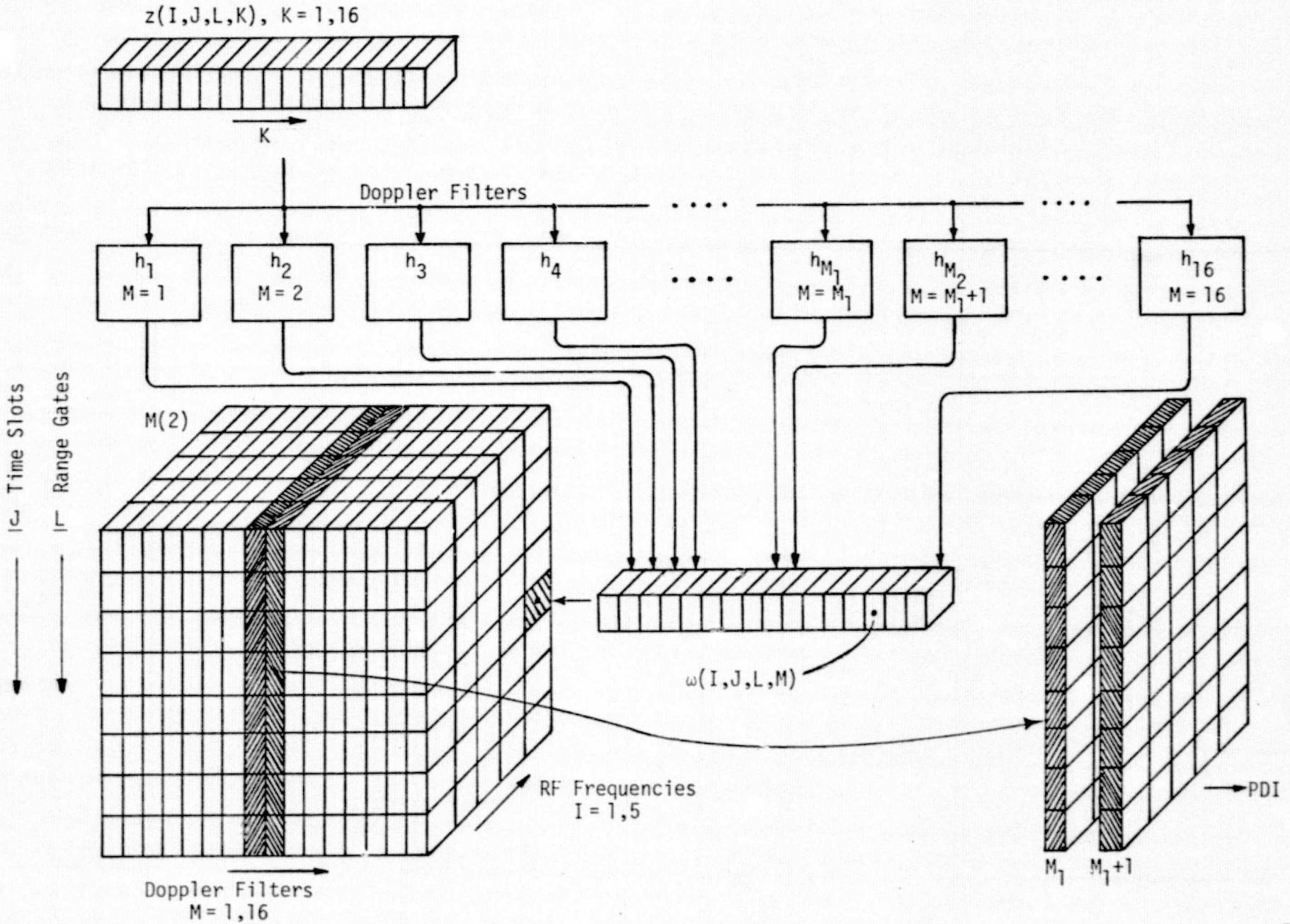

Figure 9. Pictorial Illustration of Memory Bank M(2)

The outputs of the doppler filters are stored in a memory bank designated as M(2), as shown in Figure 9. Two possibilities might occur:

(1) Two adjacent filter outputs exceed a prespecified threshold. All their values for various RF frequencies (I), time slots (J), and range gates (L) are then postintegrated.

(2) Only one filter's output exceeds the threshold; then the outputs of the filter along with one of the adjacent filters are postintegrated.

For illustration, it is supposed that the outputs of the filters $M = M_1, M_1+1$ are processed.

7.3 Postintegration

The outputs of the two doppler filters that have exceeded the threshold consist of 40 memory cells from the memory M(2), as shown in Figure 9. The 40 cells correspond to five RF frequencies ($I = 1,5$), two range gates ($L = \pm 1$), and four time slots ($J = 1,4$). Each one of these cells carries a complex number $\omega(I, J, L, M)$, whose magnitude is found by multiplying it with its conjugate. The squares of these magnitudes are added in different manners to form the postdetection integration (PDI) outputs. To be able to demonstrate the logical procedure for adding these magnitudes, the memory cells under consideration are redrawn for a given RF frequency F_i in Figure 10.

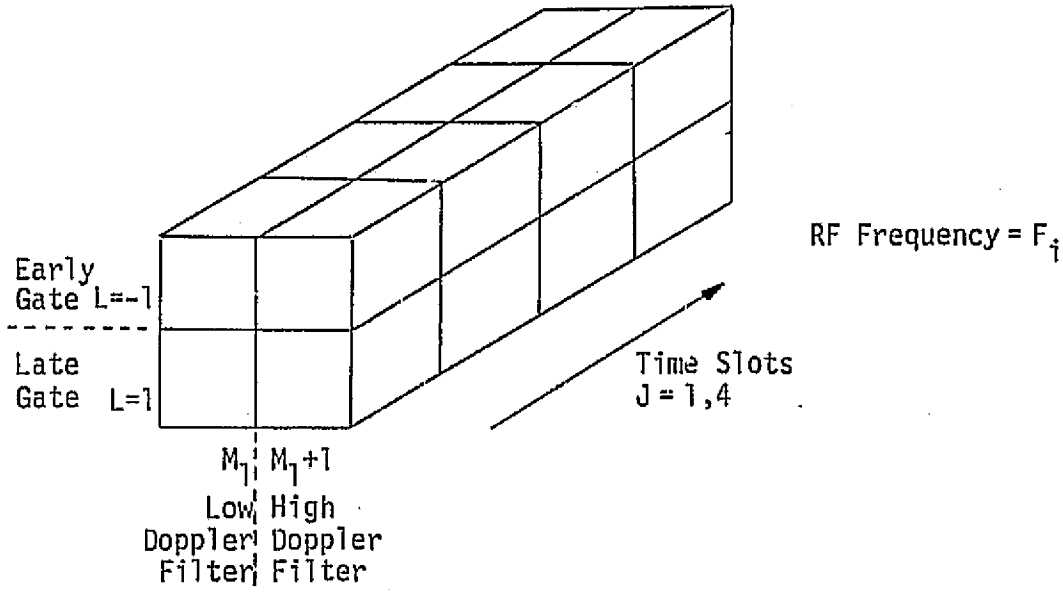

Figure 10. Memory Cells Storing $\omega(I,J,L,M)$ for a Given RF

Eight sums are formed at the output of the postdetection integrator—two corresponding to each of the four parameters of interest, namely, range, range gate, azimuth angle, and elevation angle.

7.3.1 Range PDI Outputs

The two range outputs are denoted $S_R(L=-1)$ and $S_R(L=+1)$. The R denotes the range and the L denotes the early or late gate. Thus, to obtain $S_R(L=-1)$, the square of all the complex numbers pertaining to the early gate are added over all the RF frequencies. $S_R(L=+1)$ is obtained in a similar fashion, using the late gate; hence,

$$S_R(L=-1) = \sum_{i=1}^{5} \sum_{j=1}^{4} |\omega(i,j,-1,M_1)|^2 + |\omega(i,j,-1,M_1+1)|^2 \qquad (2)$$

$$S_R(L=+1) = \sum_{i=1}^{5} \sum_{j=1}^{4} |\omega(i,j,1,M_1)|^2 + |\omega(i,j,1,M_1+1)|^2 . \qquad (3)$$

7.3.2 Range Rate (Doppler) PDI Outputs

The doppler PDI outputs $S_D(M=M_1)$ and $S_D(M=M_1+1)$ are obtained by summing the square of the magnitudes of the numbers out of the doppler filters M_1 and M_1+1, respectively, rather than the outputs of the early and late gates, as was done for the range computations. Therefore,

$$S_D(M=M_1) = \sum_{i=1}^{5} \sum_{j=1}^{4} |\omega(i,j,-1,M_1)|^2 + |\omega(i,j,1,M_1)|^2 \qquad (4)$$

$$S_D(M=M_1+1) = \sum_{i=1}^{5} \sum_{j=1}^{4} |\omega(i,j,-1,M_1+1)|^2 + |\omega(i,j,1,M_1+1)|^2 . \qquad (5)$$

7.3.3 Angle PDI Outputs

To obtain the two PDI outputs for the azimuth (elevation) angle information, the squares of the magnitudes of the first (last) two time slots corresponding to $\Sigma + \Delta AZ$ and $\Sigma - \Delta AZ$ ($\Sigma + \Delta EL$ and $\Sigma - \Delta EL$) are added over all RF frequencies to give $S_{AZ}(J=1)$ and $S_{AZ}(J=2)$ [$S_{EL}(J=3)$ and $S_{EL}(J=4)$], respectively. The various angle PDI outputs are shown in equations (6) through (9).

$$S_{AZ}(J=1) = \sum_{i=1}^{4} \sum_{m=M_1}^{M_1+1} |\omega(i,1,-1,m)|^2 + |\omega(i,1,+1,m)|^2 \quad (6)$$

$$S_{AZ}(J=2) = \sum_{i=1}^{4} \sum_{m=M_1}^{M_1+1} |\omega(i,2,-1,m)|^2 + |\omega(i,2,+1,m)|^2 \quad (7)$$

$$S_{EL}(J=3) = \sum_{i=1}^{4} \sum_{m=M_1}^{M_1+1} |\omega(i,3,-1,m)|^2 + |\omega(i,3,+1,m)|^2 \quad (8)$$

$$S_{EL}(J=4) = \sum_{i=1}^{4} \sum_{m=M_1}^{M_1+1} |\omega(i,4,-1,m)|^2 + |\omega(i,4,+1,m)|^2 . \quad (9)$$

7.4 Logarithm Discriminant Formation

The purpose of the logarithm discriminant is to obtain an estimate of the error (error signal) including sign of the various parameters under consideration. The idea is best explained by using the well known Taylor series expansion of $\ln[(1+x)/(1-x)]$.

$$\ln \frac{1+x}{1-x} = 2x + \frac{x^3}{3} + \frac{x^5}{5} + \ldots \quad ; \quad |x| < 1 . \quad (10)$$

For small x, the following approximation is valid:

$$\ln \frac{1+x}{1-x} \simeq 2x ; \qquad x \ll 1 . \quad (11)$$

Thus, if x represents the errors in the parameters under consideration, then forming the logarithm of $(1+x)/(1-x)$, this error can be computed. The mathematical derivation of the variance of the logarithmic estimator is formed in [3], where the maximum likelihood estimator of the form

$$\ell = \log \frac{\sum_i |U_i|^2}{\sum_i |V_i|^2} \quad (12)$$

is analyzed. U_i and V_i represent a pair of voltages whose difference is proportional to the target parameter being measured. Since the target range, range rate, and orientation angles are mathematical duals of each

other, it is the objective of the following discussion to relate $|U_i|^2$ and $|V_i|^2$, shown in (12), to the various outputs of the PDI.

7.4.1 Range Discriminant

In the formation of the range discriminant, a sum signal (S) and a difference signal (D) are formed such that

$$S = S_R(L=-1) + S_R(L=+1) \tag{13}$$

$$D = S_R(L=-1) - S_R(L=+1) \tag{14}$$

where $S_R(\ )$ is defined in equations (2) and (3).

Since the output of the early gate is a measure of $R-\Delta R$, where ΔR is an absolute error in the range, and the output of the late gate is a measure of $R+\Delta R$, then S is a measure of the range R and D is a measure of the absolute range error. Then, replacing S by R and D by ΔR, it can be stated that

$$S_R(L=-1) \propto R-\Delta R \tag{15}$$

$$S_R(L=+1) \propto R+\Delta R. \tag{16}$$

(A proportionality constant might be added; however, this coefficient will drop when taking the logarithms.)

Letting

$$S_R(L=-1) \equiv \sum_{i=1}^{20} |U_i|^2 \tag{17}$$

$$S_R(L=+1) \equiv \sum_{i=1}^{20} |V_i|^2, \tag{18}$$

it is easy to see that, using (15) through (18),

$$\ln \frac{\sum_i |U_i|^2}{\sum_i |V_i|^2} = \frac{2\Delta R}{R} \triangleq 2R_\varepsilon, \tag{19}$$

where R_ε is the required range error signal. The procedure is illustrated in Figure 11.

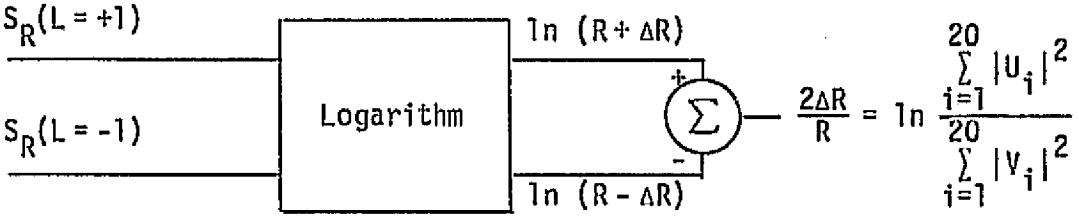

Figure 11. Range Discriminant

7.4.2 Doppler Discriminant

A similar argument can be stated for the doppler discriminant. In this case, from (4) and (5),

$$\sum_{i=1}^{20} |U_i|^2 = S_D(M=M_1)$$

$$\sum_{i=1}^{20} |V_i|^2 = S_D(M=M_1+1),$$

from which

$$\ln \frac{\sum_{i=1}^{20} |U_i|^2}{\sum_{i=1}^{20} |V_i|^2} \simeq 2 \frac{S_D(M=M_1) + S_D(M=M_1+1)}{S_D(M=M_1) - S_D(M=M_1+1)} \simeq 2\hat{R}_\epsilon . \qquad (20)$$

7.4.3 Angle Discriminants

As has already been noted, the data from the DFT representing the early and late range gates are summed to form an on-target gate, and then integrated over the transmitter frequency cycle. The sum and difference samples of angle error are then log-converted and subtracted to form the

normalized angle errors for the elevation and azimuth channels. The error signals are then D/A converted and sent to the servo filters and finally to the servo motors.

In particular, for the azimuth angle, the estimation vectors U_i and V_i satisfy [from (6) and (7)]:

$$\sum_{i=1}^{20} |U_i|^2 = S_{AZ}(J=1)$$

$$\sum_{i=1}^{20} |V_i|^2 = S_{AZ}(J=2) .$$

Similarly, for the elevation angle [from (8) and (9)]:

$$\sum_{i=1}^{20} |U_i|^2 = S_{EL}(J=3)$$

$$\sum_{i=1}^{20} |V_i|^2 = S_{EL}(J=4) ,$$

from which the error signals become

$$2\Delta_\varepsilon AZ \triangleq \ln \frac{S_{AZ}(J=1)}{S_{AZ}(J=2)} = \frac{2\Delta AZ}{\Sigma} \tag{21}$$

$$2\Delta_\varepsilon EL \triangleq \ln \frac{S_{EL}(J=3)}{S_{EL}(J=4)} = \frac{2\Delta EL}{\Sigma} . \tag{22}$$

The error signals in (19) through (22) are used to obtain the various required estimates pertaining to the parameters under consideration.

Since the error signals are obtained successively as new readings are processed, they will be denoted by $R_\varepsilon(n)$, $\dot{R}_\varepsilon(n)$, $\Delta_\varepsilon AZ(n)$, and $\Delta_\varepsilon EL(n)$, where (n) denotes the nth error signal being processed.

The angle error signals $\Delta_\varepsilon AZ$ and $\Delta_\varepsilon EL$ are fed into loop filters as shown in Figure 12 to obtain two sets of estimates:

(1) Angle estimates $\hat{\Delta}AZ$ and $\hat{\Delta}EL$, which are fed back to the servo motors.

(2) Angle rate estimates $\hat{\dot{\Delta}}AZ$ and $\hat{\dot{\Delta}}EL$, which are displayed for the astronauts for visual reading.

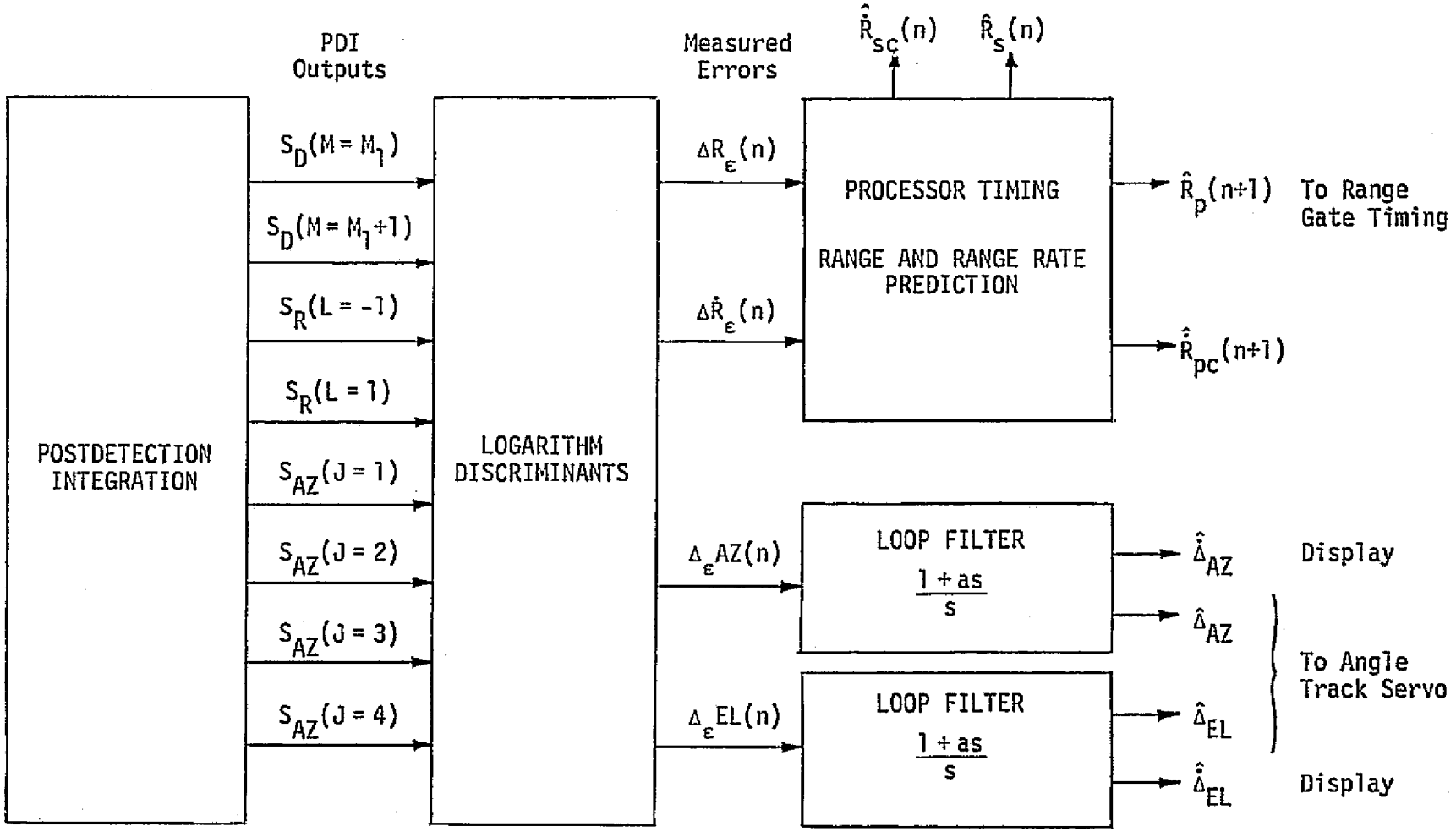

Figure 12. PDI and Parameter Estimators

The range and range rate error signals, however, are fed into the processor timing unit to obtain various required estimates, as discussed in the following section.

7.5 Processor Timing, Range and Range Rate Prediction

The processor timing stage consists of two substages. The first is called the α-β tracker [4] and the second is designated as the ambiguous doppler resolver and corrector, as shown in Figure 13. The α-β tracker is employed to give a smoothed estimate of the current range $\hat{R}_s(n)$, a predicted estimate of the next range reading $\hat{R}_p(n+1)$, and a smoothed estimate of the range rate $\hat{\dot{R}}_s(n)$. This latter value is used along with the range rate error signal $\dot{R}_\varepsilon(n)$ as inputs to the ambiguous doppler resolver and corrector to produce a smoothed corrected doppler estimate $\hat{\dot{R}}_{sc}(n)$ and a predicted corrected doppler estimate $\hat{\dot{R}}_{pc}(n+1)$. The previous estimates are used for various purposes as summarized in Table 3.

Table 3. Processor Timing Stage Outputs

Estimate	$\hat{R}_p(n+1)$	$\hat{R}_s(n)$	$\hat{\dot{R}}_{sc}(n)$	$\hat{\dot{R}}_{pc}(n+1)$
Use	Adjust early and late gates location	Display	Display	Adjust doppler filters

The one-step prediction and smoothing equations of the α-β tracker, as well as a block diagram of a possible implementation of the tracker are shown in Figure 14. The equations were derived in [3,4], along with the variances of these estimates. The initial conditions R(0) and $\dot{R}(0)$, which are necessary to start the α-β tracker operation, are supplied by the search mode operation after the target is detected.

The operation of the ambiguous doppler resolver and corrector is explained in Section 7.6.

7.6 Doppler Ambiguity Resolution

The doppler discriminant and resulting estimation will give a value between [0,PRF]. The maximum closing velocity is +148 fps, and

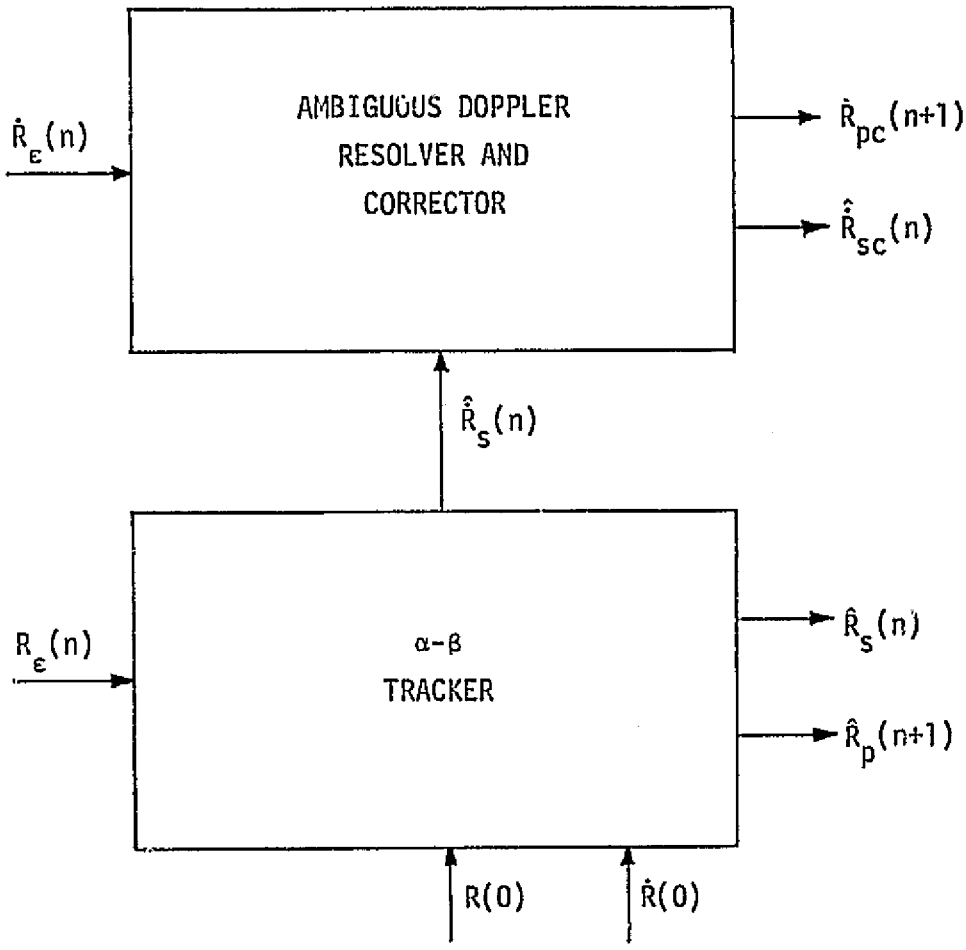

Figure 13. Processor Timing Stage

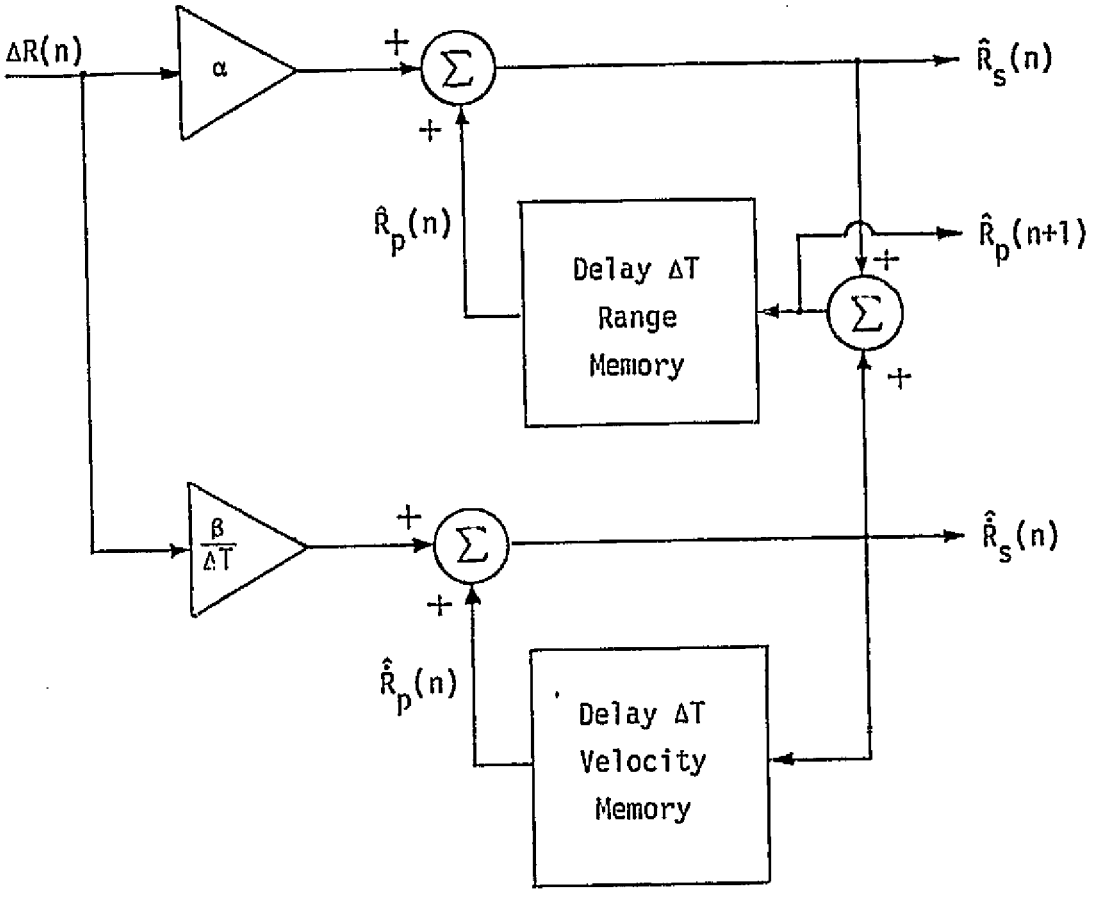

Prediction Formula

$$\hat{R}_p(n+1) = \hat{R}_s(n) + \Delta T\, \hat{\dot{R}}_s(n)$$

$$\hat{\dot{R}}_p(n+1) = \hat{\dot{R}}_s(n)$$

Smoothing Formula

$$\hat{R}_s(n) = \hat{R}_p(n) + \alpha\, \Delta R(n)$$

$$\hat{\dot{R}}_s(n) = \hat{\dot{R}}_p(n) + \frac{\beta}{\Delta T} \Delta R(n)$$

$$R_e(n) \equiv R_{(n)} - \hat{R}_p(n)$$

$\Delta T \equiv$ time between two computation steps

Figure 14. α-β Tracker for Range Tracking and Coarse Velocity Estimation

the maximum opening velocity is -75 fps. At 13.9 GHz, this corresponds to approximately 28 Hz/fps doppler. The maximum opening doppler is therefore -2100 Hz and maximum closing doppler is +4144 Hz, as shown in Figure 15.

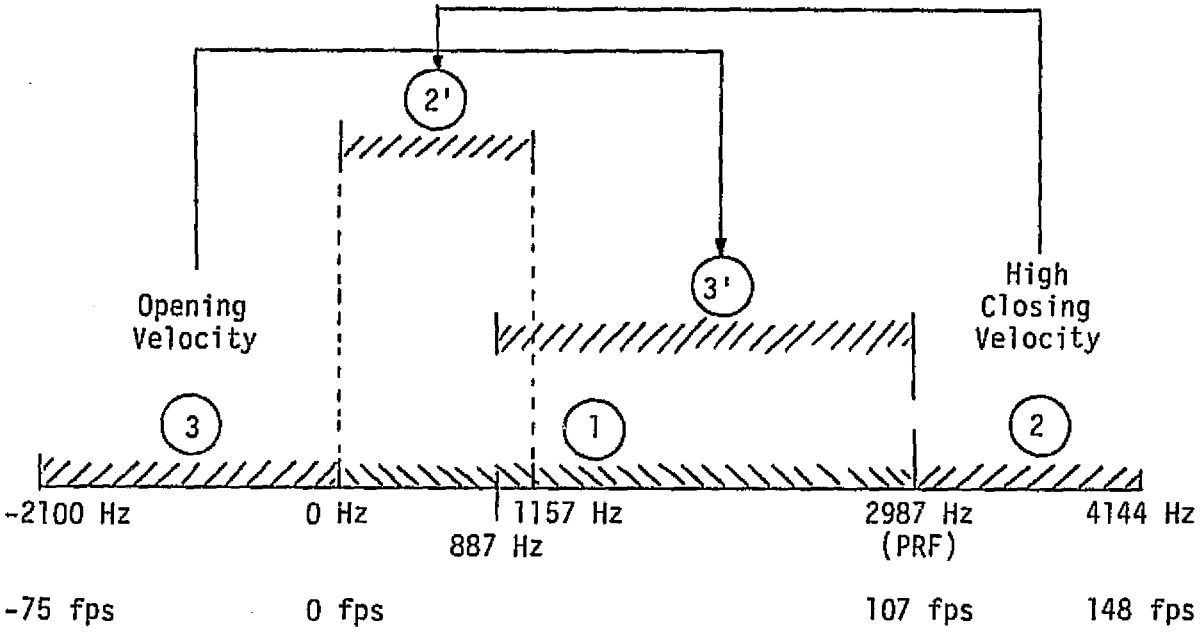

Figure 15. Resolution of Doppler Ambiguity

When the high PRF of 7177 is used, there is no doppler ambiguity from the doppler estimation from the α-β tracker. For the low PRF at longer ranges, namely, 2987, there is a doppler ambiguity as indicated in Figure 15. The resolution is easily resolved from the more coarse estimation of range rate from the α-β tracker by noting the following.

(a) If the coarse $\hat{R}_s(n) > 0$ (opening), then the fine estimation $\hat{R}_{sc}(n)$ will be in Region 3', whereas the actual estimate should be in Region 3. In this case $\hat{R}_{sc}(n)$ is adjusted by subtracting the PRF equal to 2987 Hz.

(b) If the coarse $\hat{R}_s(n)$ is longer than 2987 Hz (high closing velocity), the estimate $\hat{R}_{sc}(n)$ will be in Region 2'. In this case, $\hat{R}_{sc}(n)$ is adjusted by adding the PRF.

(c) If the coarse estimate is between 0 and 2987 Hz, the fine estimate is not altered.

It is assumed that the resolution of the ambiguity is carried out ideally, so that it does not contribute to the RMS tracking error.

REFERENCES

1. Hughes Aircraft Co., "Ku-Band Integrated Radar and Communication Equipment for the Space Shuttle Orbiter Vehicle," Ref. D7738-SCG 76075V, HS237-202, Conceptual Design Review, January 31, 1977.

2. Hughes Aircraft Co., "Ku-Band Integrated Radar and Communication System for the Space Shuttle Orbiter Vehicle," Monthly Review, April 20, 1977.

3. C. L. Weber, "Maximum Likelihood Estimation of the Ratio of Powers in Two Narrowband Processes," Axiomatix Report No. R7701-3, January 31, 1977.

4. C. L. Weber, "Study to Investigate and Evaluate Means of Optimizing the Radar Function," Axiomatix Report No. R7511-3, Appendix D, November 24, 1975.

5. Hughes Aircraft Co., "Proposal for Ku-Band Integrated Radar and Communication Equipment for the Space Shuttle Orbiter Vehicle," Vol. II, Technical Proposal, Ref. D7768.60176P, May 1976.

6. D. Barton and H. Ward. Handbook of Radar Measurement. Prentice-Hall, Inc., 1969.

7. M. Skolnik. Radar Handbook. McGraw-Hill, 1970.

APPENDIX C

TIME MULTIPLEXED SINGLE CHANNEL ANGLE TRACKING OF PASSIVE TARGETS

APPENDIX C

TIME MULTIPLEXED SINGLE CHANNEL ANGLE TRACKING OF PASSIVE TARGETS

by
Charles L. Weber

1.0 INTRODUCTION

Angle tracking is carried out by sequential processing of monopulse signals. The angle error signals are derived by sequentially processing the monopulse error signals. Angle tracking is potentially more critical than range or range rate tracking since angle monopulse signals are subject to angular (glint) and amplitude (scintillation) variations due to the target motions. The easiest method to reduce these effects is by postdetection integration over the RF frequencies before the tracking error signals are generated.

In the angle tracking loop analyzed in this appendix and described in [1], single channel processing is used for generation of the angle error signals. The single channel is time-division-multiplexed between the $\Sigma + \Delta_{AZ}$, $\Sigma - \Delta_{AZ}$, $\Sigma + \Delta_{EL}$, and $\Sigma - \Delta_{EL}$ error signals. The alternative is a two- or three-channel monopulse system. The primary advantage of the three-channel monopulse is that it allows angle error measurements to be derived from a single pulse. To reduce the effects of angular glint, however, several pulses are averaged to obtain smoothed data. The primary disadvantage of the three-channel monopulse system is the requirement that the two additional channels be phase and gain balanced to the first channel. Alternatively, the advantage of the single channel monopulse system is the simplicity in implementation and the noncriticality of phase and gain, at the expense of a 3 to 6 dB reduction in performance. A disadvantage is that it may be more suspect to target scintillation. As mentioned previously, this can be circumvented by frequency diversity.

In the next section, the single channel monopulse system under consideration will be described, followed in subsequent sections by a performance analysis.

2.0 SINGLE CHANNEL AMPLITUDE MONOPULSE

A single channel monopulse system is described, where the channel is time shared by the various error signals. The description of the

various radar tracking functions has already been presented in the Appendix B. From that description a block diagram of the single channel monopulse is shown in Figure 1. Familiarity of the previous appendix is assumed. Only those components of the radar that are pertinent to the angle tracking function are shown in Figure 1.

2.1 Ku-Band Amplitude Monopulse Antenna

Referring to Figure 1, the Ku-band monopulse antenna outputs a sum channel and two angle error signals, which are designated Δ_{AZ} and Δ_{EL} for the azimuth and elevation signals, respectively. With respect to the amplitude monopulse feed, sum and difference patterns of a monopulse antenna network are usually determined experimentally in order to account for the effects of coupling between horns and of introduction of high-order transmission modes at the mouth of the horn assembly.

Studies of the actual parabolic antenna patterns [2-4] have shown that the normalized sum (voltage) pattern can be represented very closely by

$$E_s = \cos^2 (1.18\, \Delta_\epsilon/\theta_B), \tag{1a}$$

where Δ_ϵ is the angle off the boresight axis, azimuth or elevation, and θ_B is the 3 dB beamwidth. It is assumed that Δ_ϵ and θ_B are given in the same units. This representation of the normalized sum pattern is excellent to well below 3 dB from the boresight axis of the main lobe and is therefore a convenient representation when evaluating antenna tracking performance. At the lower gain portions of the main lobe and over the sidelobe, the above representation is not useful.

The measured difference (voltage) pattern for the same type parabolic antenna is well represented by

$$E_\Delta = 0.707 \sin (2.36\, \Delta_\epsilon/\theta_B), \tag{1b}$$

where the same comments given above apply. Significant differences between these approximations and actual patterns appear only at the edges of the main beam, well beyond the 3 dB beamwidth.

In the angle tracking monopulse system under consideration, as well as in most cases, only the variation within the 3 dB beamwidth is of interest, in which case, the above approximations are very satisfactory.

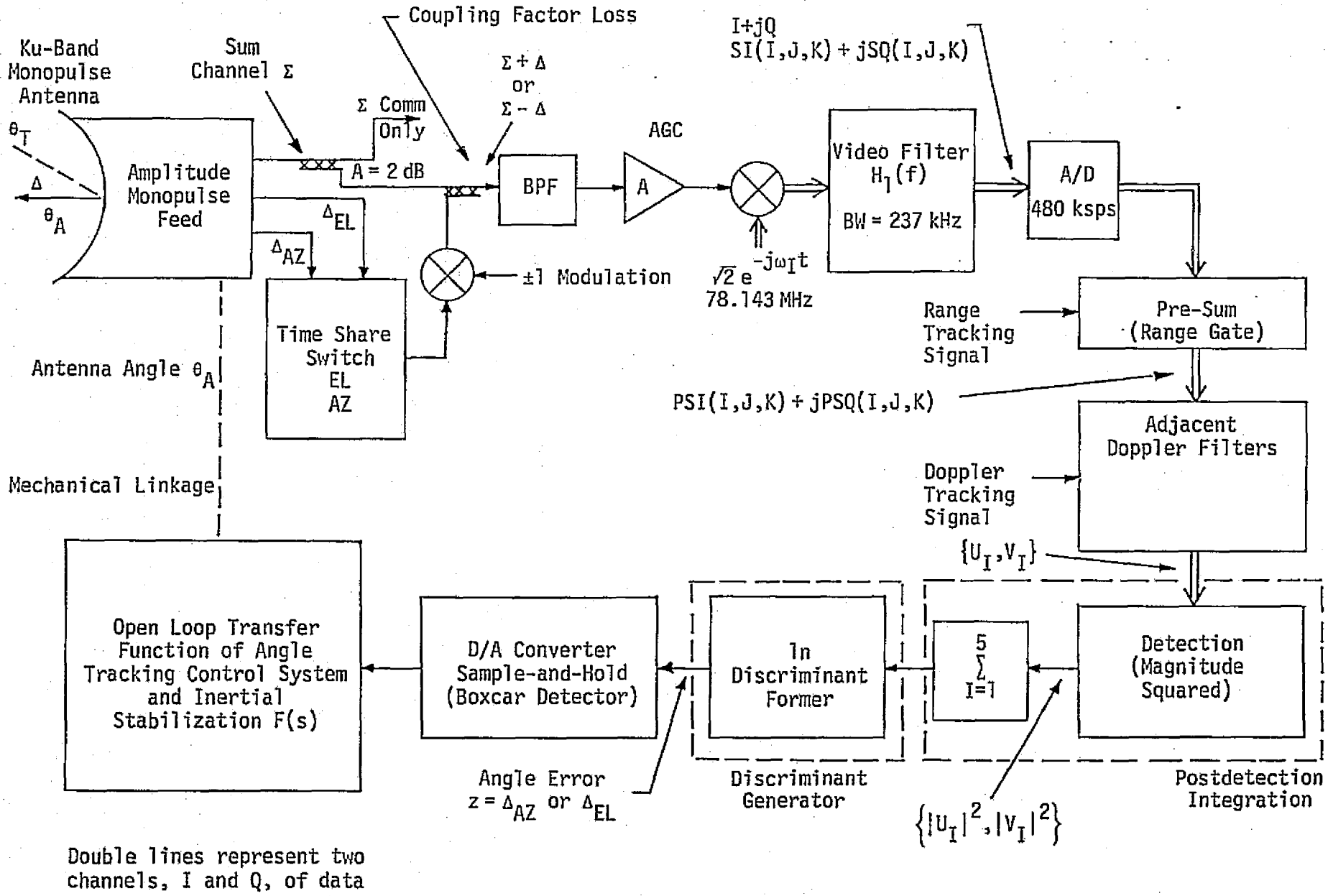

Figure 1. Block Diagram of Single Channel Monopulse Angle Tracking Loop

The actual error pattern is approximately linear to at least one-third of the beamwidth off the boresight. The normalized error pattern E_Δ/E_s which approximately results from the AGC and logarithmic discriminant operation in the receiver system (Figure 1) is linear over more than 0.6 of the beamwidth. The slope increases as the direction of the received signal approaches the half power point of the sum channel beam. The antenna error slope is designated as k_m and is approximately 1.67 for the representations given above. This can be seen by observing that

$$\frac{E_\Delta}{E_s} = \sqrt{2} \tan\left(1.18 \frac{\Delta_\varepsilon}{\theta_B}\right) \approx 1.67\, \Delta_\varepsilon/\theta_B$$

for small Δ_ε. Within the linear region, the error voltage is

$$\text{Error Voltage} = \frac{E_\Delta}{E_s} = k_m(\Delta_\varepsilon/\theta_B) \tag{2a}$$

or, equivalently,

$$\Delta_\varepsilon\big|_{\text{deg}} = \theta_B\big|_{\text{deg}}\, k_m^{-1}\, \frac{E_\Delta}{E_s} . \tag{2b}$$

The actual value of the antenna error slope, k_m, varies over different monopulse antenna designs. A conservative interval is

$$1.0 \le k_m \le 1.9 , \tag{3}$$

with typical values being 1.2 to 1.7.

The connection between $\Sigma \pm \Delta$ and (E_s, E_Δ) is that $\Sigma + \Delta$ is proportional to $E_s + E_\Delta$ and $\Sigma - \Delta$ is proportional to $E_s - E_\Delta$, where the proportionality constant is the same in both cases.

Since the antenna gain patterns discussed above have been normalized to 1, there is no loss in generality in equating

$$\Sigma + \Delta = E_s + E_\Delta \tag{4a}$$

and

$$\Sigma - \Delta = E_s - E_\Delta . \tag{4b}$$

Hence,

$$\frac{\Sigma + \Delta}{\Sigma - \Delta} = \frac{E_s + E_\Delta}{E_s - E_\Delta} . \tag{5}$$

This will be used in the discriminant function to relate $\frac{\Sigma + \Delta}{\Sigma - \Delta}$ to E_Δ/E_s.

3.0 Description of Single Channel Monopulse

The amplitude monopulse feed of the Ku-band antenna system outputs three channels of data—the sum channel Σ, the azimuth error channel Δ_{AZ}, and the elevation error channel Δ_{EL}, as shown in Figure 1. As described in more detail in the previous appendixes of this report, the elevation and azimuth error channels time-share the single signal processing channel. The modulation by ±1 either passes the error signal unchanged or inverts the RF phase. After recombining the error channel with the sum channel, the time-sharing is as shown in Figure 2.

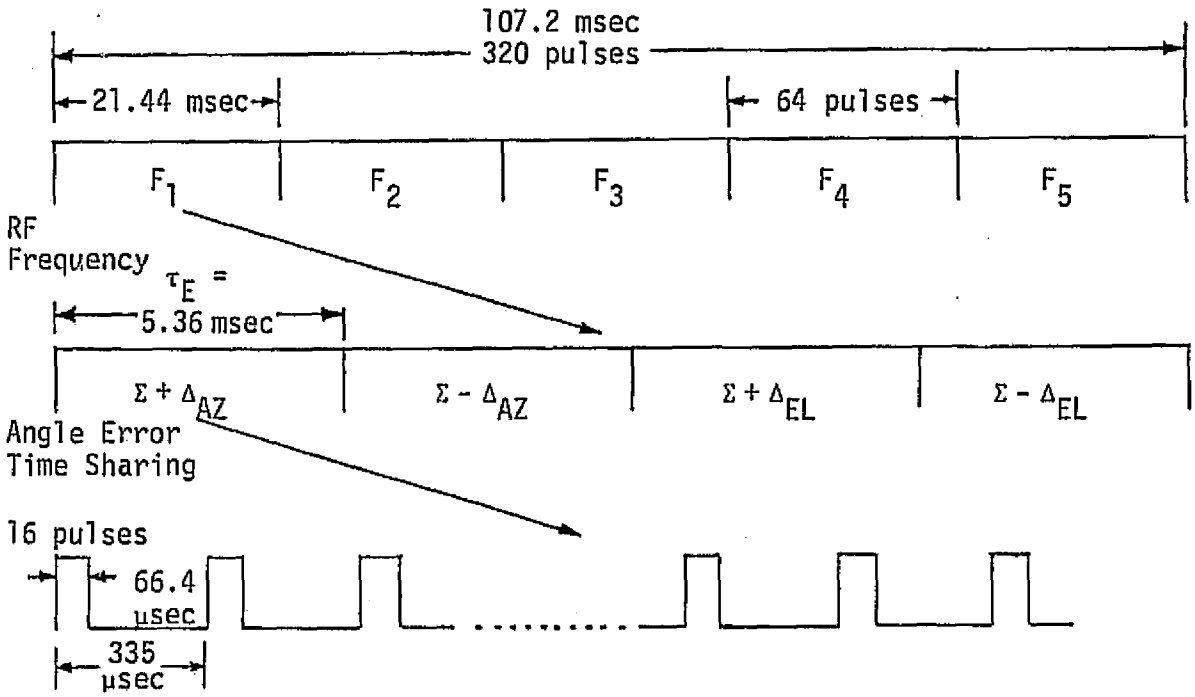

Figure 2. Timing for Single-Channel Time-Shared Monopulse Tracking

During the track mode of operation, the frequency diversity consists of 5 RF's, each of which operates for 21.44 msec. During each RF frequency, the single channel processing is equally time-shared among the four signals—$\Sigma + \Delta_{AZ}$, $\Sigma - \Delta_{AZ}$, $\Sigma + \Delta_{EL}$, $\Sigma - \Delta_{EL}$—in the four time slots. Each of these is processed for 5.36 msec, during which time 16 pulses are transmitted and received. Throughout this description, the system parameters corresponding to the largest range interval of interest are being employed. In particular [7],

PRI = T_p = pulse repetition interval = 335 μsec

PRF = 2987

Pulse Width = τ = 66.4 μsec

Frequency Dwell Time = τ_F = 21.44 msec/RF

τ_E is the dwell time of $\Sigma + \Delta_{AZ}$, which is one of four time slots for each frequency dwell, and the range interval is 7.2 to 18.9 nmi.

Referring again to Figure 1, the various stages of IF and AGC are simplified and consolidated into one bandpass filter (BPF) and AGC. The AGC is shown but not taken into account in the angle track performance analysis, since for angle tracking purposes, the logarmithmic discriminant is already self-normalizing. The primary purpose of the AGC is to maintain satisfactory signal level in the receiver and avoid receiver saturation. The AGC is herein assumed to be performing its operation, so that all normalization can be accounted for in the discriminant.

The final stage of IF converts the sum plus error narrowband signals to I and Q (complex) baseband waveforms. The video filter before the A/D is a 2-pole Butterworth with transfer function

$$|H_1(f)|^2 = \left[1 + \left(\frac{f}{f_c}\right)^4\right]^{-1}, \qquad (6)$$

where f_c = 237 kHz. At these longer ranges, R > 7.2 nmi, where the pulse width is 66.4 μsec, the signal can be assumed to be undistorted by $H_1(f)$.

The sampling frequency of the A/D is 480 ksps, which corresponds to 32 samples over each pulse width τ. This is a sufficiently large number so that the pre-sum can be accurately approximated by analog integration.

The notation developed in the previous appendixes is maintained. In particular,

I = 1,...,5 corresponds to RF frequency

J = 1,...,4 corresponds to time slot;

- J = 1 implies $\Sigma + \Delta_{AZ}$
- J = 2 implies $\Sigma - \Delta_{AZ}$
- J = 3 implies $\Sigma + \Delta_{EL}$
- J = 4 implies $\Sigma - \Delta_{EL}$

K = 1,...,16 corresponds to the pulse number for a given I and J.

Now consider the complex baseband waveforms before the pre-sum and restrict attention to the azimuth channel. The I and Q wave forms are

$$SI(I,J,K) = \{\sqrt{2}\,(\Sigma \pm \Delta_{AZ})\,A_I\,P(t - kT_p)\cos[(\omega_I + \omega_d)t + \theta_I] + n(t)\}\sqrt{2}\cos(\omega_I t) \quad (7a)$$

and

$$SQ(I,J,K) = \{\sqrt{2}\,(\Sigma \pm \Delta_{AZ})\,A_I\,P(t - kT_p)\cos[(\omega_I + \omega_d)t + \theta_I] + n(t)\}\sqrt{2}\sin(\omega_I t) \quad (7b)$$

for the I channel and Q channel, respectively. The peak <u>received</u> signal power is given by

$$P_{pr} = E[A_I^2] ,$$

where it is assumed that $\Sigma \pm \Delta$ (which are the factors representing antenna processing) are normalized to 1. The average received power is

$$P_{avg\ r} = d_t P_{pr} ,$$

where d_t is the duty factor of the radar pulse train. When J = 1, the amplitude is proportional to $\Sigma + \Delta_{AZ}$, and when J = 2, the amplitude is proporational to $\Sigma - \Delta_{AZ}$. The amplitudes A_I are assumed to be Rayleigh random variables, since the target is assumed to be Swerling I. The random phase θ_I is assumed to be uniformly distributed over $(0,2\pi)$. The Rayleigh and uniform random variables A_I and θ_I, respectively, are independent. The pulse P(t) has magnitude of unity over the transmitted pulse width $\tau = 66.4$ μsec. The doppler frequency shift is represented by ω_d.

The receiver system noise n(t) after the bandpass filter has the narrowband representation

$$n(t) = \sqrt{2}\,[N_c(t)\cos\omega_I t - N_s(t)\sin\omega_I t] , \quad (8)$$

where N_c and N_s are independent zero mean narrowband Gaussian processes with one-sided power spectral density of N_0 watts/Hz, and one-sided noise bandwidth approximately equal to f_c ($f_c = 237$ kHz), which is the 3 dB

bandwidth of $H_1(f)$. The total noise power of $n(t)$ is $2N_0 f_c$, and the power in $N_c(t)$ and $N_s(t)$ is $N_0 f_c$ each.

Before the A/D, the complex waveform is given by

$$SI + jSQ = \left[\sqrt{2}\,(\Sigma \pm \Delta_{AZ})\,A_I\,P(t - kT_p)\cos\left[(\omega_I + \omega_d)t + \theta_I\right] + n(t)\right]\sqrt{2}\,e^{-j\omega_I t}$$

$$= (\Sigma \pm \Delta_{AZ})\,A_I\,P(t - kT_p)\,e^{j[\omega_d t + \theta_I]} + N_c(t) + jN_s(t)\,. \qquad (9)$$

3.1 Pre-Sum (Range Gate)

After the A/D, each received pulse is pre-summed over the pulse width. The timing of this pre-sum is dependent on the setting of the range gate in the range tracking loop. The range tracking loop is presently assumed to be tracking ideally. Variations in tracking errors will be taken into account subsequently when design margins are considered.

With ideal range tracking, the pre-sum output is

$$PSI(I,J,K) + jPSQ(I,J,K) = \int_{kT_p}^{kT_p+\tau} [SI(t) + jSQ(t)]\,dt. \qquad (10)$$

Errors in range gate tracking would be accounted for by errors in the limits of integration in (10), where again, the digital sum of the pre-sum is being approximated by analog integration.

3.2 Doppler Filters (Range Rate Tracking)

Adjacent doppler filters are being used for accurate range rate tracking, as described in Appendix B. The frequency midway between the correct two adjacent doppler filters in the DFT is assumed to be at the frequency $\omega_d + \Delta\omega_d$, where $\Delta\omega_d$ represents the error in doppler tracking. The effect of this DFT filtering can be approximated by multiplying $SI + jSQ$ by $\exp[-j(\omega_d - \Delta\omega_d)t]$ before the pre-sum integration and extending the equivalent integration of the pre-sum and DFT from $\tau = 66.4$ μsec to $\tau_E = 5.36$ msec. This corresponds to the $\Sigma + \Delta_{AZ}$ dwell time at one RF and also corresponds to the bandwidth of each of the doppler filters of approximately $\tau_E^{-1} = 187$ Hz.

3.3 Statistical Parameters of Doppler Filter Outputs

The output of the doppler filters can then be represented by

$$\begin{bmatrix} U_I \\ V_I \end{bmatrix} = \begin{bmatrix} \Sigma + \Delta_{AZ} \\ \Sigma - \Delta_{AZ} \end{bmatrix} A_I \frac{1}{\tau_E} \int_0^{\tau_E} e^{j(\Delta\omega_d t + \theta_I)}\, dt + \begin{bmatrix} N_{UI} \\ N_{VI} \end{bmatrix}. \qquad (11)$$

The equivalent noise term for U_I is given by

$$N_{UI} = \frac{1}{\tau_E} \int_0^{\tau_E} [N_c(t) + jN_s(t)]\, dt \qquad (12a)$$

and the equivalent noise term for V_I is given by

$$N_{VI} = \frac{1}{\tau_E} \int_{\tau_E}^{2\tau_E} [N_c(t) + jN_s(t)]\, dt\,. \qquad (12b)$$

For the signal part of V_I in (11), the integral actually is over $(\tau_E, 2\tau_E)$, but the result is exactly identical to the integral over $(0, \tau_E)$ since coherent processing is being carried out over the entire RF dwell time. This is not the case for the noise, since the noise at this point is wideband with respect to τ_E^{-1} and therefore the noise contribution to U_I is independent from that of V_I.

It is also important to note that, since the processing time of the DFT is taken to be the entire elapsed time of the 16 pulses, namely, $\tau_E = (16)T_p = 5.36$ msec, then the corresponding signal power is average signal power over that same period, as opposed to peak signal power. Additional comments concerning the filter response of the DFT to a range gated coherent pulse train are given in Section 6.0.

The noise terms are identically distributed and independent.

At this point, the signal and noise have both been accounted for during both the $\Sigma + \Delta_{AZ}$ time slot for the Ith RF, which is designated as U_I, and during the $\Sigma - \Delta_{AZ}$ time slot for the Ith RF, which is designated as V_I. This is because the desired signal portions of U_I and V_I are correlated. The noise contributions remain uncorrelated.

Carrying out the indicated integral, the representation in (11) can be expressed as

$$\begin{bmatrix} U_I \\ V_I \end{bmatrix} = \begin{bmatrix} \Sigma + \Delta_{AZ} \\ \Sigma - \Delta_{AZ} \end{bmatrix} A_I \, e^{j\theta_I} \exp\left(\frac{j\Delta\omega_d \tau_E}{2}\right)\left(\frac{\sin\,(\Delta\omega_d \tau_E/2)}{(\Delta\omega_d \tau_E/2)}\right) + \begin{bmatrix} N_{UI} \\ N_{VI} \end{bmatrix}. \tag{13}$$

From the signal standpoint, the effect of nonideal range rate tracking can be seen to be an attenuation of signal strength by the factor

$$\left[\frac{\sin\,(\Delta\omega_d \tau_E/2)}{(\Delta\omega_d \tau_E/2)}\right]^2 \tag{14}$$

in power, and a phase shift of $\Delta\omega_d\tau_E/2$. The phase shift is inconsequential since θ_I is already uniform and independent of A_I.

For the present, the doppler tracking loop is assumed to be working ideally, so that $\Delta\omega_d \equiv 0$.

In (13),

$$N_{UI} = N_{cUI} + j\, N_{sUI} \tag{15a}$$

and

$$N_{VI} = N_{cVI} + j\, N_{sVI}\,. \tag{15b}$$

All of these random variables are Gaussian with zero mean and variance

$$\sigma^2 = E[N_{cUI}^2] = E[N_{sUI}^2] = E[N_{cVI}^2] = E[N_{sVI}^2] = N_0 B_F \tag{16}$$

where B_F is the one-sided bandwidth of the DFT filters, namely, $B_F = 187$ Hz. These random variables are all mutually independent.

With this information, the statistical parameters of the doppler filter outputs can be determined for a given RF. In particular, the power in U_I is

$$P_U \triangleq E\left[|U_I|^2\right] = d_t(\Sigma + \Delta_{AZ})^2 E(A_I)^2 \left[\frac{\sin\,(\Delta\omega_d \tau_E/2)}{(\Delta\omega_d \tau_E/2)}\right]^2 + 2N_0 B_F\,. \tag{17a}$$

The power in V_I is

$$P_V \triangleq E\left[|V_I|^2\right] = d_t(\Sigma - \Delta_{AZ})^2 E(A_I)^2 \left[\frac{\sin(\Delta\omega_d \tau_E/2)}{(\Delta\omega_d \tau_E/2)}\right]^2 + 2N_0 B_F \quad (17b)$$

and the correlation (unnormalized) is

$$P_{UV} = E[U_I V_I^*] = P_{VU}^*$$

$$= d_t(\Sigma + \Delta_{AZ})(\Sigma - \Delta_{AZ}) E(A_I^2) \left[\frac{\sin(\Delta\omega_d \tau_E/2)}{(\Delta\omega_d \tau_E/2)}\right]^2 \quad (17c)$$

where $(^*)$ means complex conjugate and d_t is the duty factor of the signal.

In general, P_{UV} would be complex. If there were an unaccounted RF phase shift in the antenna, DMA or DEA, then the angle error channels would not be exactly in phase with the sum channel when they are recombined into one channel (Figure 1). When this occurs, P_{UV} becomes a complex correlation. In this development, no RF phase difference between the sum and angle error channels is assumed. The effects of such errors on angle tracking performance is examined in [6].

If the doppler tracking loop is assumed to be working ideally, then $\Delta\omega_d = 0$. Recalling that the peak received signal power is given by

$$P_{pr} = E(A_I^2) \quad (18)$$

when, when $\Delta\omega_d = 0$,

$$P_U = d_t(\Sigma + \Delta_{AZ})^2 P_{pr} + 2N_0 B_F \quad (19a)$$

$$P_V = d_t(\Sigma - \Delta_{AZ})^2 P_{pr} + 2N_0 B_F \quad (19b)$$

and

$$P_{UV} = d_t(\Sigma + \Delta_{AZ})(\Sigma - \Delta_{AZ}) P_{pr} . \quad (19c)$$

Define the normalized correlation coefficient between U and V as

$$\rho^2 \triangleq \frac{|P_{UV}|^2}{P_U P_V} . \quad (20)$$

When $\Delta\omega_d = 0$, ρ^2 is given by

$$\rho^2 = \left\{\left[1 + \frac{2N_0B_F}{P_{avg\,r}(\Sigma+\Delta_{AZ})^2}\right]\left[1 + \frac{2N_0B_F}{P_{avg\,r}(\Sigma-\Delta_{AZ})^2}\right]\right\}^{-1} . \qquad (21)$$

From an average power point of view, $(\Sigma \pm \Delta)^2$ is normalized to unity, particularly for small angle errors, so that

$$\rho = \frac{1}{1 + \frac{2N_0B_F}{P_{avg\,r}}} = \frac{1}{1 + \frac{2N_0}{P_{avg\,r}\tau_E}} . \qquad (22)$$

The signal-to-noise ratio (SNR) $P_{avg\,r}\tau_E/(2N_0)$ is the signal-energy-to-noise-spectral-density over the time slot τ_E, which is the dwell time of $\Sigma + \Delta_{AZ}$. Equivalently, this is the SNR in the doppler signal bandwidth.

The significant observation is that the normalized correlation coefficient is dependent on SNR, as given by (22). Note that, as

$$\text{SNR} \to \infty, \text{ then } \rho \to 1$$

and, as

$$\text{SNR} \to 0, \text{ then } \rho \to 0 . \qquad (23)$$

This will subsequently be related to the performance of the monopulse angle tracking loop.

With these statistical parameters of U_I and V_I now determined, the remainder of the angle tracking loop can be described and the performance analyzed.

3.4 Angle Tracking Discriminant Generator

Referring to Figure 1, the detector forms the magnitude squared:

$$|U_I|^2; \quad I = 1,\ldots,5 \qquad (24a)$$

$$|V_I|^2; \quad I = 1,\ldots,5 \qquad (24b)$$

where I represents the Ith RF. The only correlation that exists is between U_I and V_I for each I. As noted in the previous section, the statistical parameters of the complex Gaussian random variable $\{U_I, V_I\}$ are independent of I.

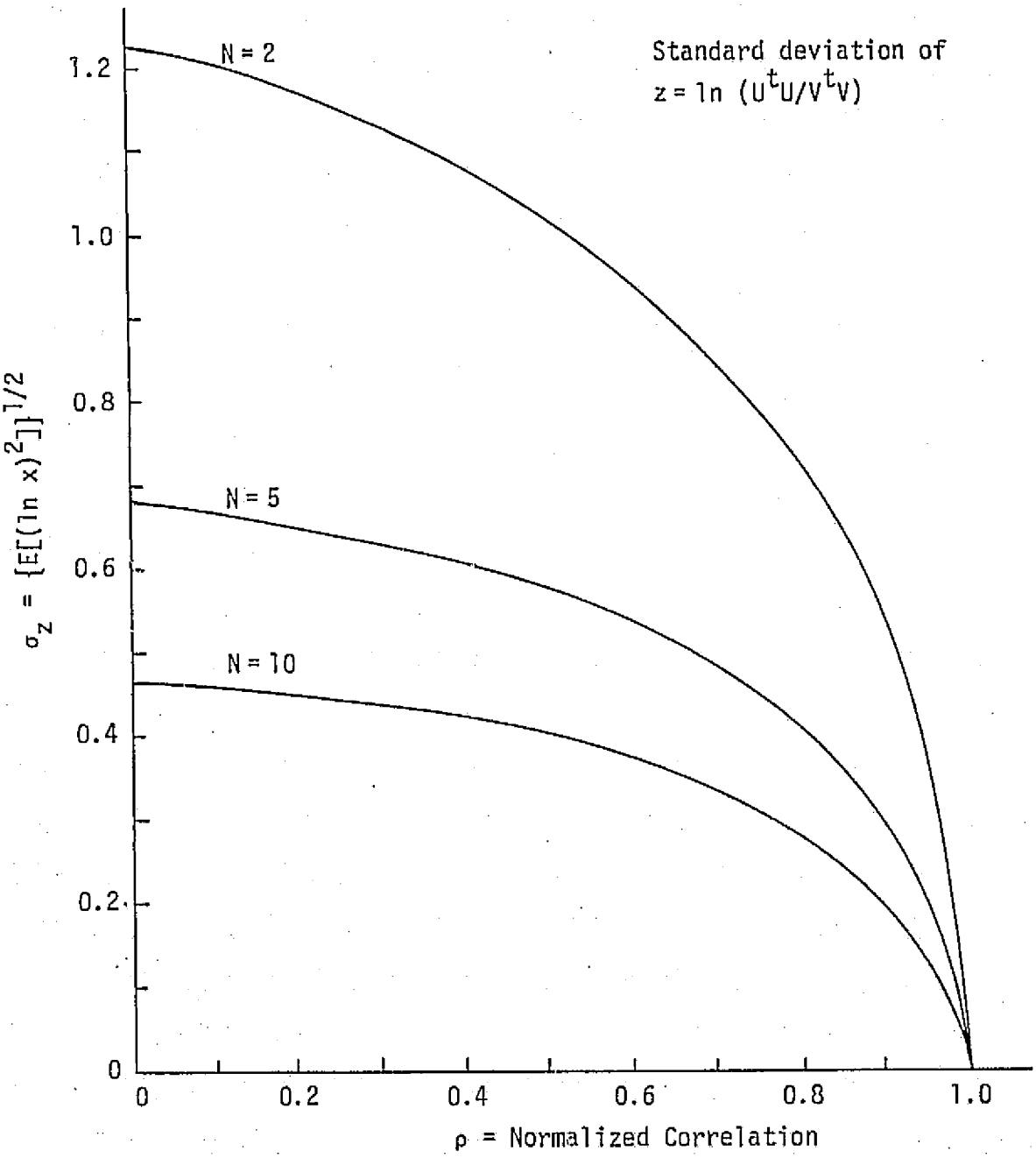

Figure 3. Standard Deviation of the Random Variable z as a Function of Correlation

The postdetection integration forms

$$\sum_{I=1}^{N} |U_I|^2 \quad , \quad \sum_{I=1}^{N} |V_I|^2 \tag{25}$$

where, in this instance, N = 5.

Finally, the logarithm discriminant former generates

$$z = \widehat{\Delta_{AZ}} = \ln \left[\sum_{I=1}^{N} |U_I|^2 \Big/ \sum_{I=1}^{N} |V_I|^2 \right] \tag{26}$$

as shown in Figure 1. The computation techniques for generating z are considered in Appendix B.

The random variable z is the maximum likelihood (M.L.) estimate [5] of th logarithm of the ratio of the power in U_I to the power in V_I, i.e.,

$$z = \widehat{\ln [P_U/P_V]} \tag{27}$$

where (^) means maximum likelihood estimate.

It has been shown in [5] that z is the M.L. estimate of $\ln (P_U/P_V)$ whether or not there exists correlation between U_I and V_I.

In order to see how z forms a measure of antenna angle error, note first that z is an unbiased estimate of $\ln (P_U/P_V)$ [8], namely,

$$z = \ln [P_U/P_V] + x \, , \tag{28}$$

where [5]:

$$E(x) = 0 \tag{29}$$

where $\sigma_x^2 = \sigma_z^2$ is the variance of the estimate of P_U/P_V. Equivalently stated,

$$E(z) = \ln (P_U/P_V) \tag{30}$$

The RMS error of z, namely σ_x, has been derived and numerically presented in [5], and the performance curves are shown here in Figure 3. The RMS error is dependent only on the number of frequency dwells (N) and the normalized correlation coefficient (ρ) between U_I and V_I, as given in equations (20), (21), and (22). It can be seen that, as the normalized correlation coefficient increases, the RMS error decreases and, in the limit, as $\rho \to 1$, the RMS error $\to 0$.

The improvement in performance due to increases in signal-to-noise ratio is related to RMS error through the correlation coefficient. As indicated in (22) and plotted in Figure 4, the normalized correlation coefficient increases as the signal-to-noise ratio increases.

In Figure 5, the results of Figures 3 and 4 are combined. The RMS error of the maximum likelihood estimate is shown as a function of the SNR = $P_{avg\ r}/(2N_0 B_F)$ for various values of N. In this system, the pertinent value of N is 5, since there are 5 RF's in the frequency diversity.

The second step is to obtain the appropriate understanding of $\ln (P_U/P_V)$, which is the quantity being estimated in the maximum likelihood sense by z. Upon substitution of (19) into (30),

$$\ln (P_U/P_V) = \ln \left[\frac{(\Sigma+\Delta)^2 P_{avg\ r} + 2N_0 B_F}{(\Sigma-\Delta)^2 P_{avg\ r} + 2N_0 B_F} \right]$$

$$= \ln \left[\frac{(1+\frac{\Delta}{\Sigma})^2 + \frac{2N_0 B_F}{\Sigma^2 P_{avg\ r}}}{(1-\frac{\Delta}{\Sigma})^2 + \frac{2N_0 B_F}{\Sigma^2 P_{avg\ r}}} \right] . \qquad (31)$$

Inspection of (31) indicates that the output of the discriminant generator is a function of the signal-to-noise ratio, as well as the normalized measure of the angle error Δ/Σ.

As indicated in Section 2.0, when the monopulse angle error is small, so that the error voltage is in the linear region, then the desired error voltage is given by

$$\text{Error Voltage} = \frac{E_\Delta}{E_s} = \frac{\Delta}{\Sigma} = k_m(\Delta_\varepsilon/\theta_B) \qquad (32a)$$

or, equivalently, the actual angular error is

$$\Delta_\varepsilon = \theta_B k_m^{-1} \frac{E_\Delta}{E_s} = \theta_B k_m^{-1} \left(\frac{\Delta}{\Sigma}\right) . \qquad (32b)$$

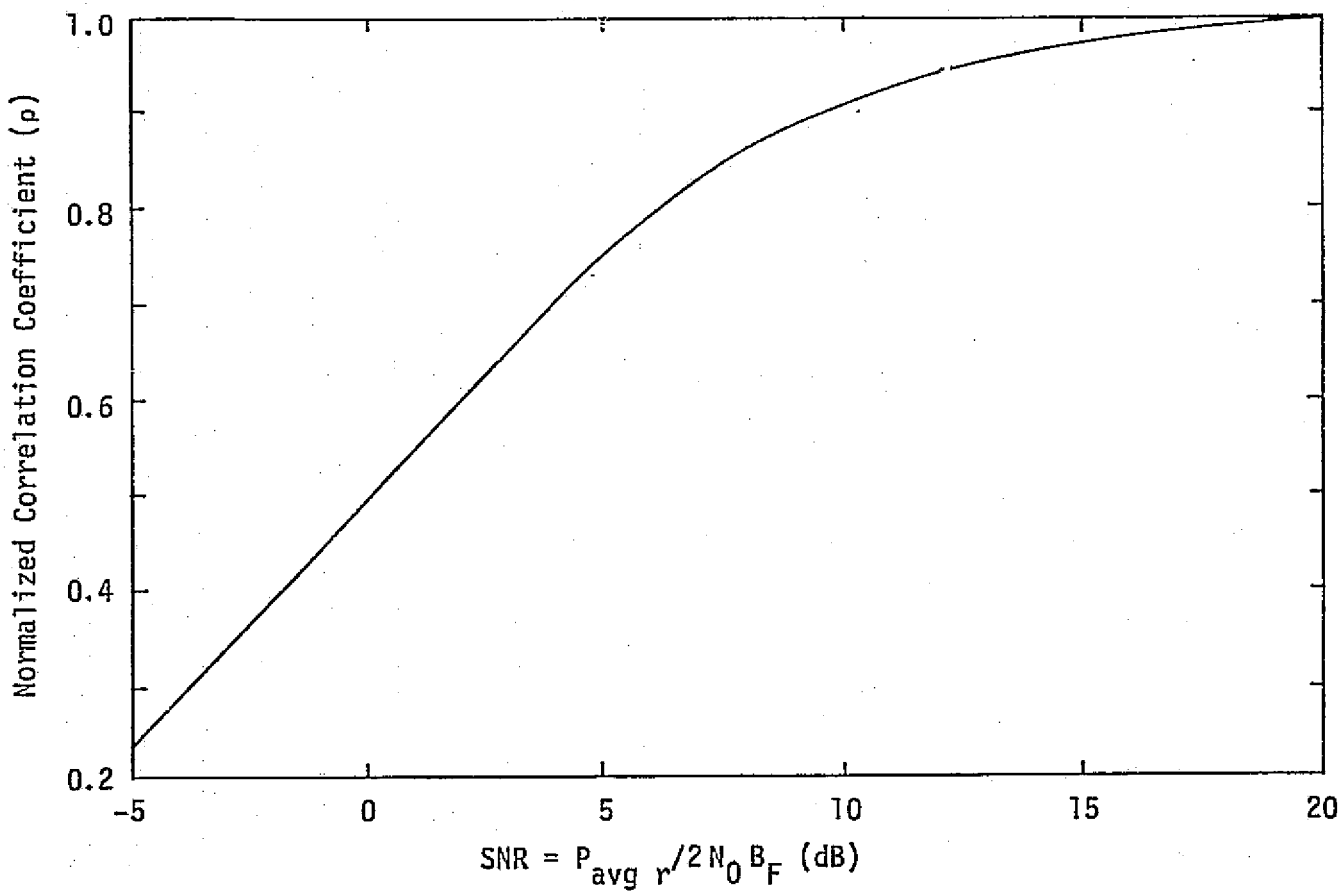

Figure 4. Normalized Correlation Coefficient ρ Versus Signal-to-Noise Ratio $P_{avg\ r}/2N_0B_F$

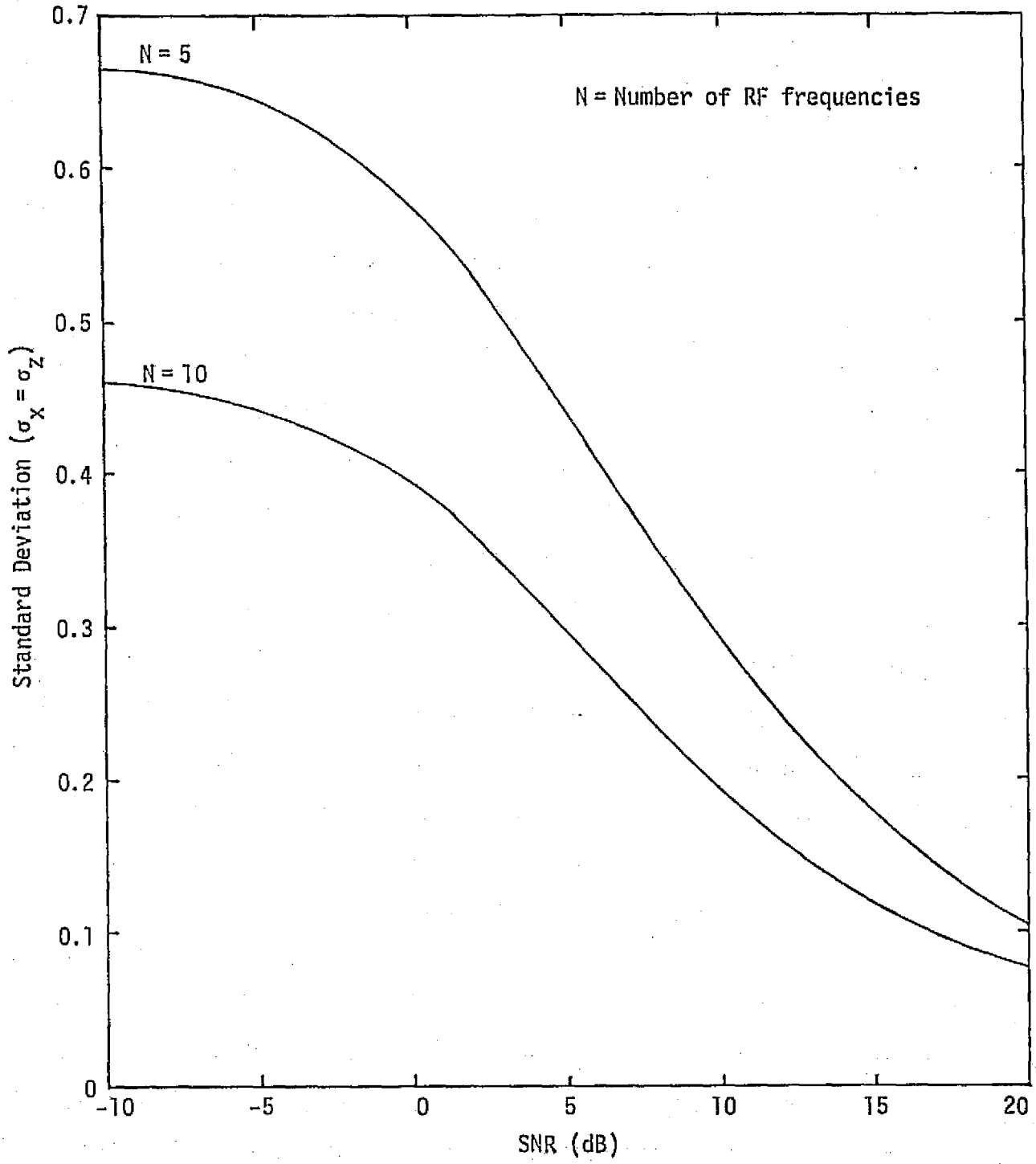

Figure 5. Standard Deviation of the Output of the Logarithm Discriminant Generator Versus Signal-to-Noise Ratio for Certain Values of N

For small values of (Δ/Σ), corresponding to small values of antenna angular error Δ_ε, $\ln (P_U/P_V)$ as described in (31) can be expressed as

$$\ln (P_U/P_V) = \ln \left[\frac{1 + \frac{2(\Delta/\Sigma)}{1+(SNR)^{-1}} + \frac{(\Delta/\Sigma)^2}{1+(SNR)^{-1}}}{1 - \frac{2(\Delta/\Sigma)}{1+(SNR)^{-1}} + \frac{(\Delta/\Sigma)^2}{1+(SNR)^{-1}}} \right]$$

$$\approx 4\left(\frac{\Delta}{\Sigma}\right)\left[\frac{1}{1+(SNR)^{-1}}\right] = 4\rho\left(\frac{\Delta}{\Sigma}\right), \qquad (33)$$

where

$$SNR \triangleq \frac{P_{avg}\, r}{2 N_0 B_F}, \qquad (34)$$

Σ^2 is already normalized to unity, and the approximation $\ln (1+\gamma) \approx \gamma$ for small γ has been employed.

The first moment of the output of the log discriminant generator $\ln (P_U/P_V)$ without the above approximation is shown in Figure 6. It can be observed that, for small values of Δ/Σ, the value of $\ln (P_U/P_V)$ varies almost linearly in Δ/Σ, and that the slope is dependent on SNR. The more drastic variations in $\ln (P_U/P_V)$ occur at larger values of Δ/Σ where the reduction in loop gain is more significant. It is henceforth assumed that the approximation in (33) is satisfactory, and that the effect of SNR on $\ln (P_U/P_V)$ is through the multiplication of (Δ/Σ) by ρ, thus corresponding to a reduction in loop gain.

4.0 PERFORMANCE OF THE AMPLITUDE MONOPULSE ANGLE TRACKING LOOP

The results of the previous sections can now be combined to provide the RMS angle error due to thermal noise and target scintillation when the target is in the linear region of the antenna angle error channels. Only one of the angle errors is considered.

A block diagram of the equivalent model of the antenna tracking loop is shown in Figure 7. The result is a system whose angle tracking performance is identical to that in Figure 1 when the antenna is in the linear region. In Figure 7,

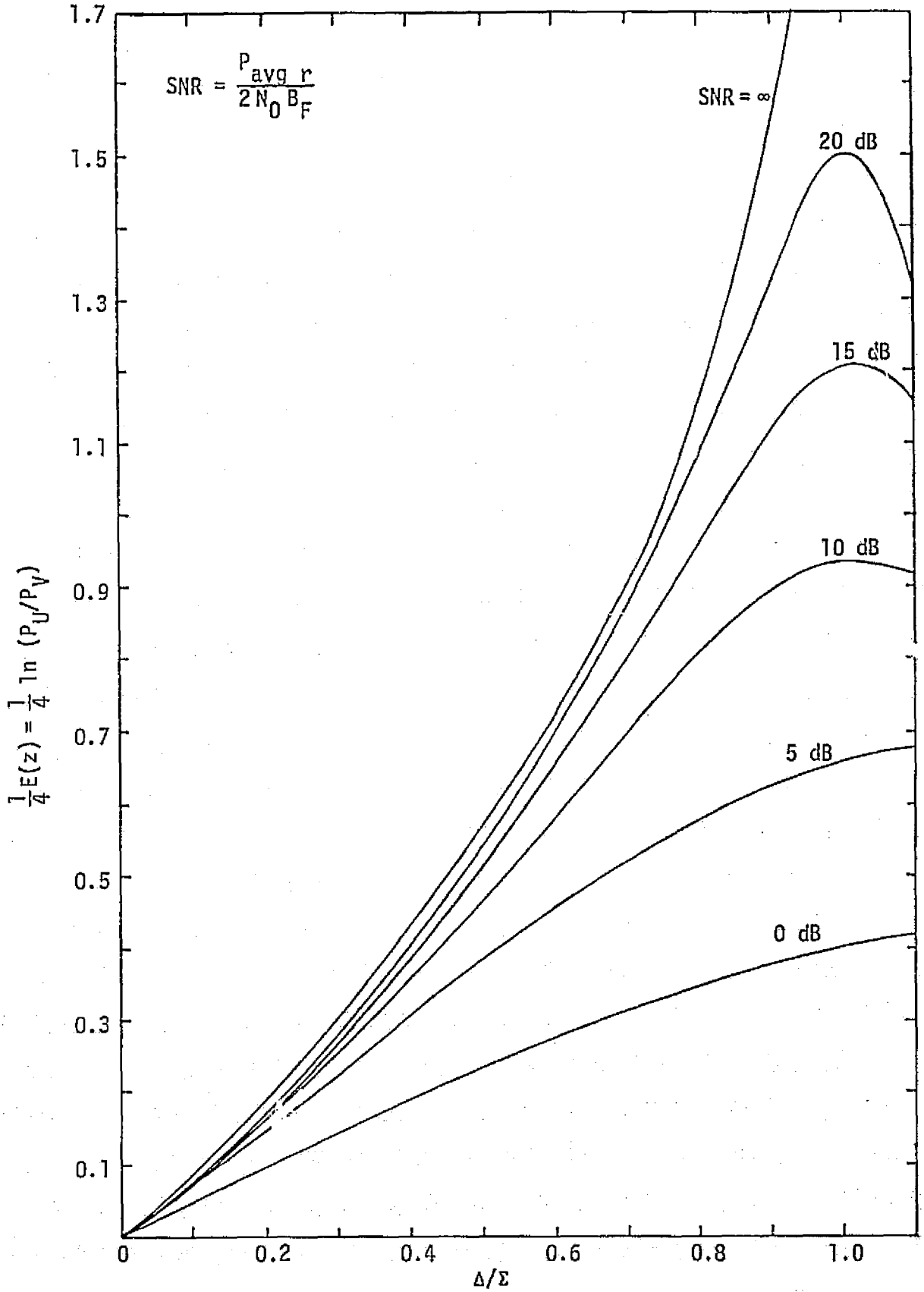

Figure 6. First Moment of Output of Angle Tracking Discriminant Generator as a Function of Normalized Angle Error for Various Signal-to-Noise Ratios

θ_T = relative angle of the target with respect to an arbitrary inertial reference

θ_A = relative angle of the antenna boresight in either the azimuth or elevation direction

$\Delta_\varepsilon = \theta_T - \theta_A$ = angular error in either the azimuth or elevation directions

k_m/θ_B = scale factor necessary to convert angular error to antenna amplitude monopulse output voltage

4ρ = scale factor in (33) necessary to give $\ln (P_U/P_V)$

x = equivalent noise of the system, taking into account the effects of thermal noise and target scintillation as described in this report and in [5]

$z = \ln (P_U/P_V) + x$ is the output of the log discriminant generator, as given in (28) and diagrammed in Figure 1

K_{eq} = equivalent loop gain of the antenna tracking loop, which takes into account all of the various contributing gains

$F(s)$ = open loop antenna angle control system and inertial stabilization transfer function. A discussion of such transfer functions is given in [6].

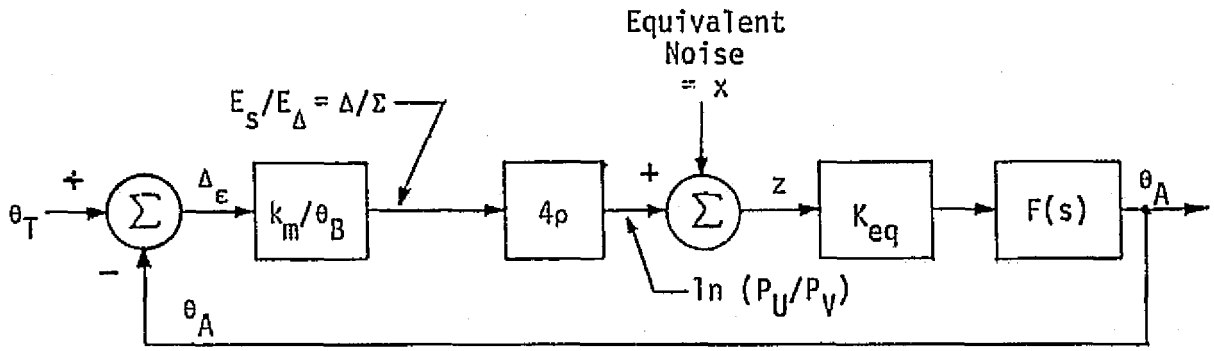

Figure 7. Block Diagram of the Equivalent Model of the Antenna Tracking Loop

Since a transient analysis and a study of the dynamic characteristics of the antenna tracking loop are not a part of this development, the effects of the loop gain and open loop transfer functions are taken into account through the noise loop bandwidth B_N (Hz).

Referring to Figure 7, the closed loop transfer function from θ_T to θ_A is equal to

$$H(j2\pi f) = \frac{\left(\frac{4\rho\, k_m}{\theta_B}\right) K_{eq}\, F(j2\pi f)}{1 + \left(\frac{4\rho\, k_m}{\theta_B}\right) K_{eq}\, F(j2\pi f)} \tag{35}$$

and the corresponding noise bandwidth is defined as

$$B_N(\rho) = \int_0^\infty |H(j2\pi f)|^2\, df\,. \tag{36}$$

The dependence of B_N on ρ has been explicitly indicated to emphasize the dependence of noise bandwidth on the signal-to-noise ratio by way of the normalized correlation coefficient ρ. For intermediate and high gain tracking loops, the dependence of B_N on ρ is approximately given by

$$B_N(\rho) \approx \rho\, B_N(\sigma = 1) \tag{37}$$

where $\rho = 1$ corresponds to the infinite SNR case. This is the case since loop gain varies linearly with SNR. In addition, a high values of loop gain, the noise bandwidth varies approximately linearly in loop gain and therefore SNR. This is indeed the case for all loop transfer functions that are anticipated for F(s).

The transfer function from the equivalent noise input x to the angle tracking error Δ_ε is given by

$$\Delta_\varepsilon = \left(\frac{\theta_B}{4\rho\, k_m}\right) H(s)\, x\,, \tag{38}$$

so that the variance of the angle tracking error is given by

$$\sigma^2_{\Delta_\varepsilon} = \left(\frac{\theta_B}{4\rho\, k_m}\right)^2 B_N\, T_s'\, \sigma_x^2(N,\rho)\,, \tag{39}$$

where

$\sigma_x^2(N,\rho) = \sigma_x^2$ is the variance of the maximum likelihood estimate of $\ln (P_U/P_V)$, which is also the variance per sample of the noise in the equivalent block diagram of the angle tracking loop. The dependence on the correlation coefficient ρ and the number of RF frequencies N is emphasized in (39)

T_s' = time per sample of the random sequence x by the D/A converter and succeeding boxcar detector in Figure 1. In this system,

$T_s' = T_p(16)(4)(N)$, where (40)

N = 5 is the number of RF frequencies. The noise samples x are assumed to be statistically independent from frequency to frequency

16 = number of pulses during which $\Sigma + \Delta$ is observed (see Figure 2)

4 = factor corresponding to the number of different angular error measurements per frequency dwell time, namely, $\Sigma + \Delta_{AZ}$, $\Sigma - \Delta_{AZ}$, $\Sigma + \Delta_{EL}$, and $\Sigma - \Delta_{EL}$

T_p = pulse repetition interval = 335 μsec.

Upon substitution of these values into (40),

$$T_s' = 320\, T_p = 107.2 \text{ msec}. \tag{41}$$

Upon substitution, the RMS angle tracking error is then given by

$$\sigma_{\Delta_\varepsilon}\Big|_{\text{deg}} = \frac{\theta_B}{4\rho\, k_m} \left[B_N(\rho=1)\, T_s'\right]^{1/2} \sigma_x(N,\rho) \tag{42}$$

or, equivalently,

$$\sigma_{\Delta_\varepsilon}\Big|_{\text{deg}} = \frac{\theta_B}{4k_m} \left\{1 + \left(\frac{P_{avg}\, r}{2N_0 B_F}\right)^{-1}\right\} \left[B_N(\rho=1)\, T_s'\right]^{1/2} \sigma_x\left(N, P_{avg}\, r/(2N_0 B_F)\right) \tag{43}$$

where θ_B = 3 dB antenna beamwidth in degrees.

5.0 PERFORMANCE COMPUTATIONS

For the Ku-band Integrated Radar and Communication Equipment for the Space Shuttle Orbiter Vehicle proposal [1], the radar parameters needed to compute the RMS angle error in (43) are given as

$$\theta_B = 1.6°$$

$$k_m = 1 \text{ ([1], p. 3-47)}$$

$$B_N = 1 \text{ Hz ([1], p. 3-47)}$$

$$T_s' = 107.2 \text{ msec [eq. (41)]} .$$

For these values of the system parameters, the performance of the angle tracking loop is shown in Figure 8. The RMS angle tracking error is plotted against the signal-to-noise ratio $P_{avg\ r}/(2N_0 B_F)$, which is the SNR at the output of the doppler filter (see Figure 1). The specification value for the Ku-band radar system is shown in Table 1 as

$$\sigma_{SPEC} = 0.153 \text{ deg} . \tag{44}$$

This is shown as the dashed line in Figure 8. It is seen that the specification value is met for

$$\frac{P_{avg\ r}}{2N_0 B_F} > 0 \text{ dB} . \tag{45}$$

Table 1. Specification Radar Parameter Allowable Measurement Errors

	Random 3σ	Bias 3σ
Angle Rate Error Including Target Effects		
LOS Pitch	0.8 mrad 0.458 deg	±2°
LOS Azimuth	0.8 mrad 0.458 deg	±2°
Angle Rate Error Not Including Target Effects		
LOS Pitch	0.14 mrad/sec 0.008 deg/sec	±0.14 mrad/sec
LOS Azimuth	0.14 mrad/sec 0.008 deg/sec	±0.14 mrad/sec

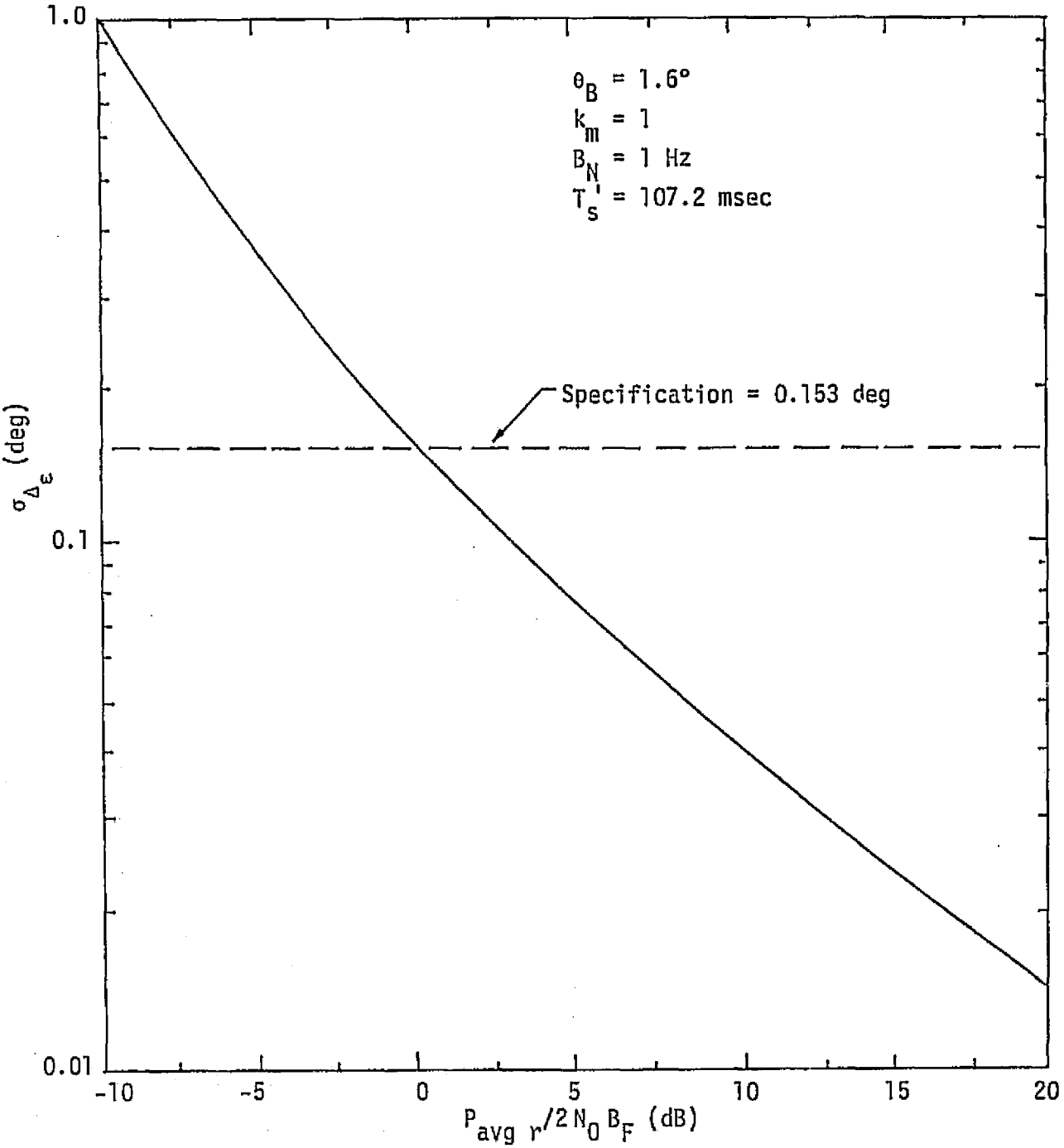

Figure 8. RMS Angle Tracking Error of Passive Targets Versus Signal-to-Noise Ratio at the Output of the Doppler Tracking Filter

In order to obtain angle track performance as a function of range, the following radar equation is used to determine $P_{avg\ r}/(2N_0 B_F)$

$$\frac{P_{avg\ r}}{2N_0 B_F} = \frac{[G^2 \bar{\sigma} \lambda^2][d_t P_p \tau_E]}{2(4\pi)^3 L [k T_s] R^4}, \qquad (46)$$

where all of the parameters are defined in Appendix A of this report. The values used in the computation correspond to those in Table 3, Budget #2, of Appendix A, namely,

G = peak antenna gain = 38.5 dB

$\bar{\sigma}$ = radar cross-section = 1 m^2

λ = wavelength = 0.0218 m

d_t = duty factor = 0.2

P_p = peak transmitted power = 50 watts

τ_E = dwell time corresponding to one computation of the DFT $= B_F^{-1}$ = 5.36 msec

k = Boltzmann's constant = 1.38×10^{-23} w/Hz-K

T_s = system noise temperature = 1500°K

R = range, in meters

L = losses, itemized as follows for angle track; see Appendix A for more details

Transmit	3.5 dB
Scan alignment	0
Lateral scan	0
Threshold	0.5
Processor loss	1.0
Range gate straddling	0
Doppler mismatch	0
PDI	1.25
Pre-sum	0.6
Signal loss due to coupling (see Section 7.0)	2.0
Noise increase due to combining of Σ and Δ channels (see Section 7.0)	2.1
Total Losses	10.95 dB

With these parameters, the RMS angle tracking error is shown in Figure 9 versus range in nautical miles. For all ranges below 18 nmi, the RMS angle error is below the specification value, where the effects

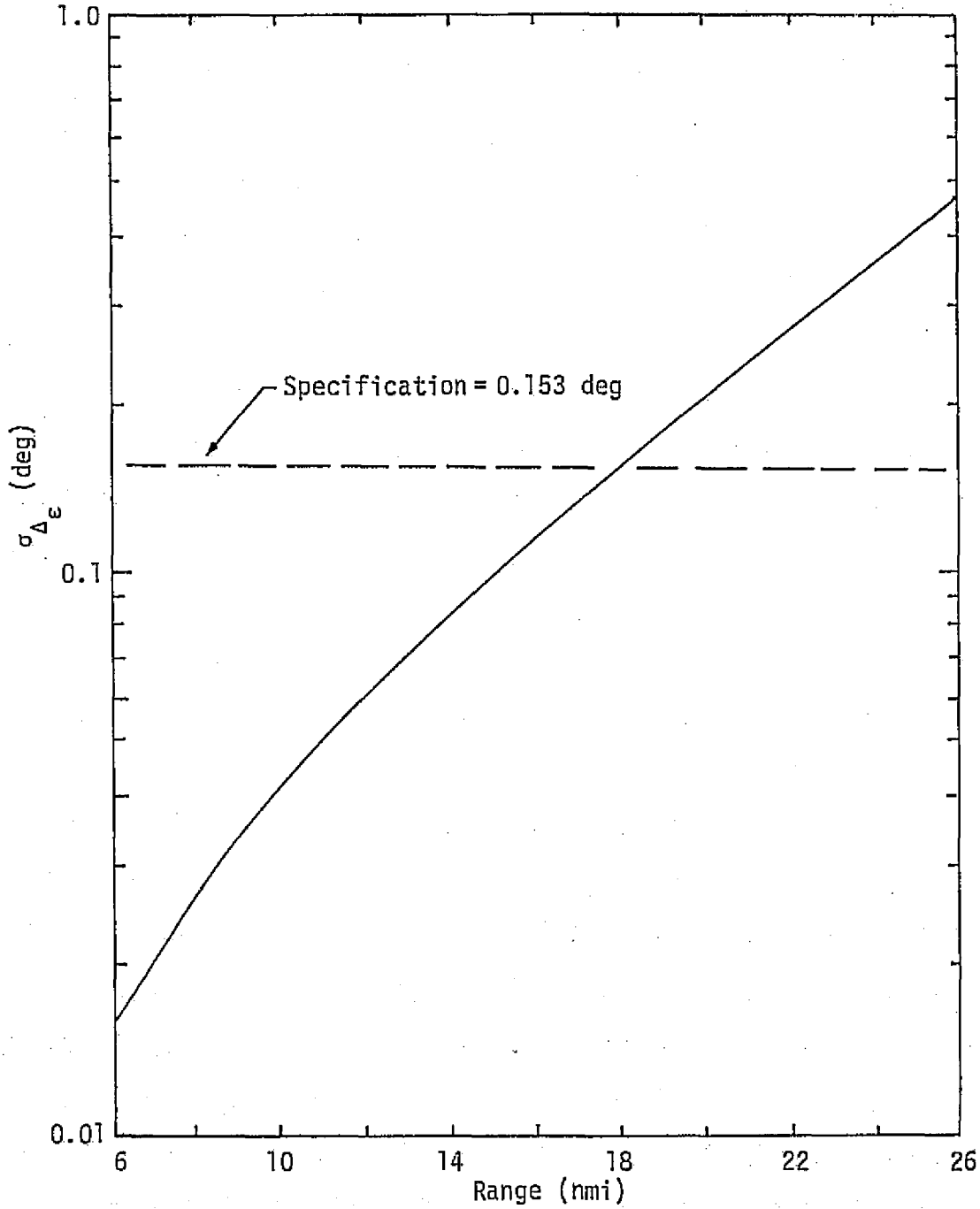

Figure 9. RMS Angle Tracking Error of Passive Radar Versus Range (nmi)

of both thermal noise and target scintillation have been taken into account. The performance curves do not take into account any degradation in the angle tracking loops due to errors in the range tracking and doppler tracking loops. With the SNR design margin for angle tracking of passive targets at approximately 10 dB, there is room to allow degradations for these errors.

In summary, the angle tracking specification for passive targets is met with ample design margin (≈10 dB) by the Ku-band system.

The other angle tracking specification is the estimation of angular rate. Note that the angular rate specification does not require that target effects be taken into account. Therefore, a nonfluctuating target can be assumed, thereby greatly increasing the average signal-to-noise ratio. The performance of angular rate estimation is not taken into account in this report.

6.0 COMMENTS CONCERNING THE FILTER RESPONSE OF THE DISCRETE FOURIER TRANSFORM

In this section, certain additional comments are made concerning the response of a DFT to a coherent pulse train. The particular waveform under discussion is shown in Figure 10. It is a complex baseband signal which is assumed to be ideally range gated as shown. It corresponds to the signal $I + jQ$ in Figure 1. The signal is sampled and presummed to form the complex numbers $s_1,\ldots,s_N$ where $N = 16$. These are the inputs to the DFT.

The time of pre-sum is equal to the pulse width, which is equal to the width of the range gate. During the remainder of the time, the signal does not exist, although implicitly it does, since coherence is maintained from pulse to pulse.

In the frequency domain, the picture is as shown in Figure 11. In the upper part of the figure is the spectrum of the coherent pulse train. The bandwidth to the first crossover is $1/\tau$. The "needles" of the spectrum are spaced by the PRF. The one-sided width of each "needle" is $(NT_p)^{-1}$, where N is the number of pulses observed.

The number of "needles" within the bandwidth $1/\tau$ is d_t^{-1}, where $d_t = \tau/T_p$ is the duty factor. The shift of the entire spectrum due to a doppler frequency shift is also indicated.

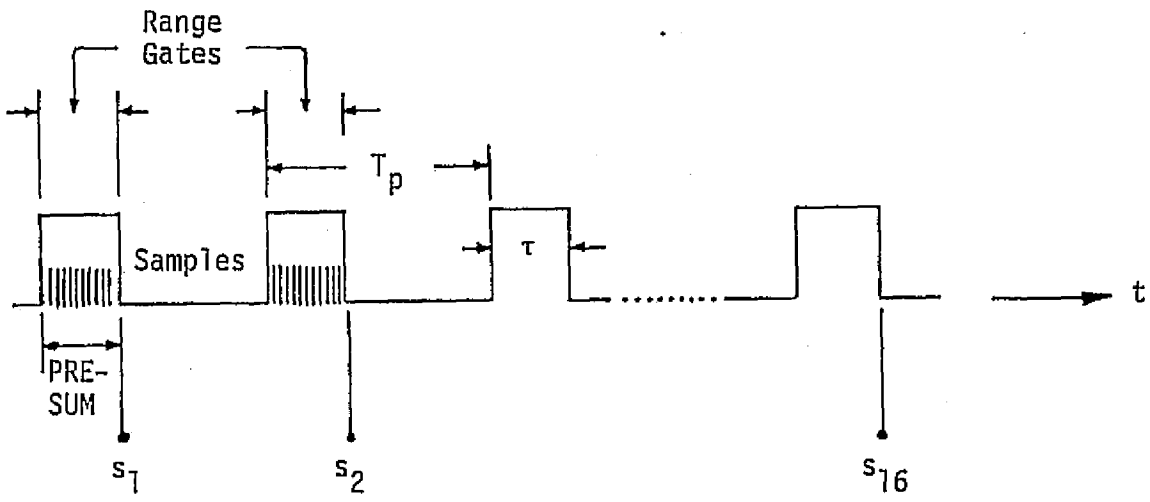

Figure 10. Coherent Pulse Train with Pre-Sum

In the lower part of Figure 11 is the location of each of the filters in the DFT filter bank. In this instance, the fact that digital filters have periodic frequency domain responses is an advantage and all "needles" in the signal spectrum will fall within one of the filters.

The bandwidth of each filter is $(NT_p)^{-1}$. If the pulse width remains constant and T_p varies, then

(a) The bandwidth of the signal, $1/\tau$, remains unchanged.

(b) The bandwidth of each needle varies.

(c) The bandwidth of each filter varies exactly as that of the needle in the signal spectrum.

Since the filter bandwidth is matched to the bandwidth of each needle in the signal spectrum, the output signal-to-noise ratio at the end of the observation period is approximately optimized. This is what is done, since the samples are made at the end of the observation interval.

Whether in a search or track mode, a coherent radar can extract the maximum energy from the signal by use of the optimal receiver shown in Figure 12. All of the necessary ideal assumptions have been made, namely, doppler is assumed known, the range to the target is assumed known, and ideal coherence is maintained. The digital signal processor, which is a slightly suboptimal implementation of the above, is shown in Figure 13. The only difference is the reversal of order of the integrator over the range gate, and the mixing by the doppler frequency. In most coherent radars, the resulting loss is negligible (in the hundredths of

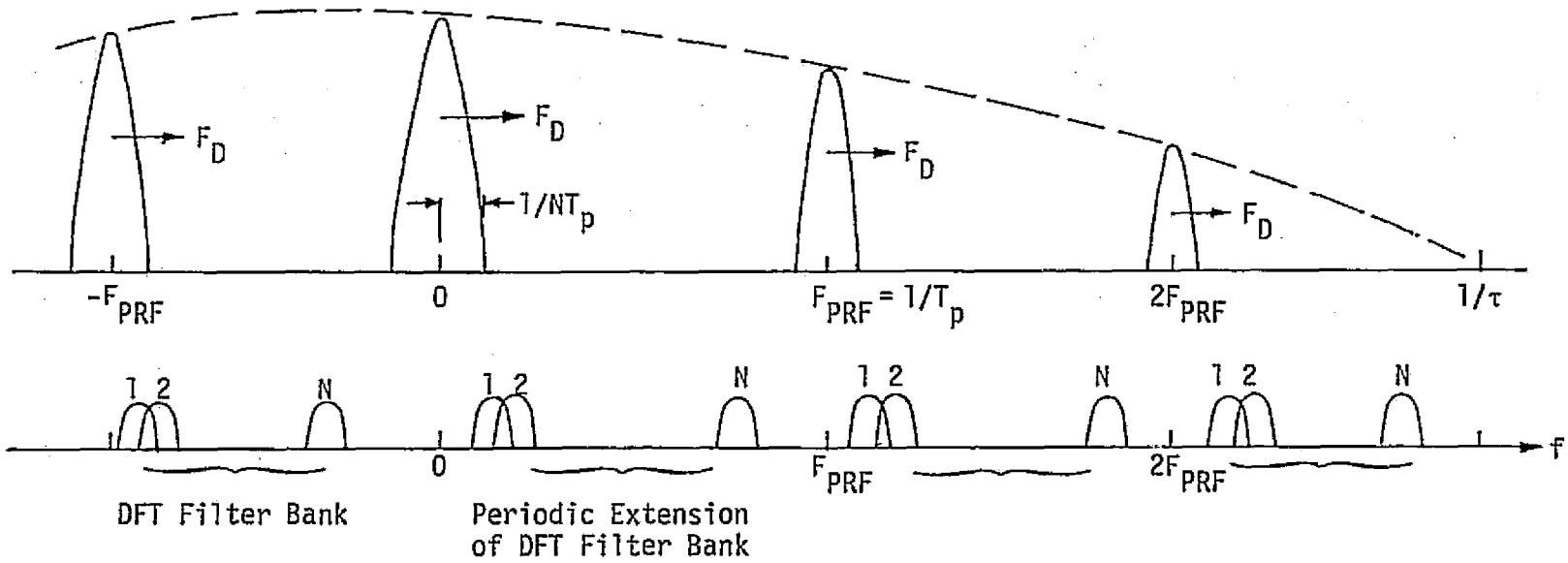

Figure 11. Spectrum of Transmitted Pulse Train and the Bank of Filters Formed by the DFT

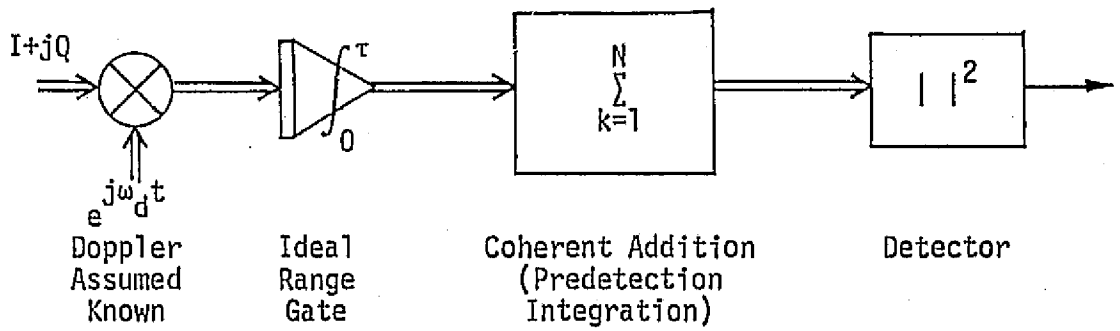

Figure 12. Block Diagram of Optional Coherent Radar Receiver

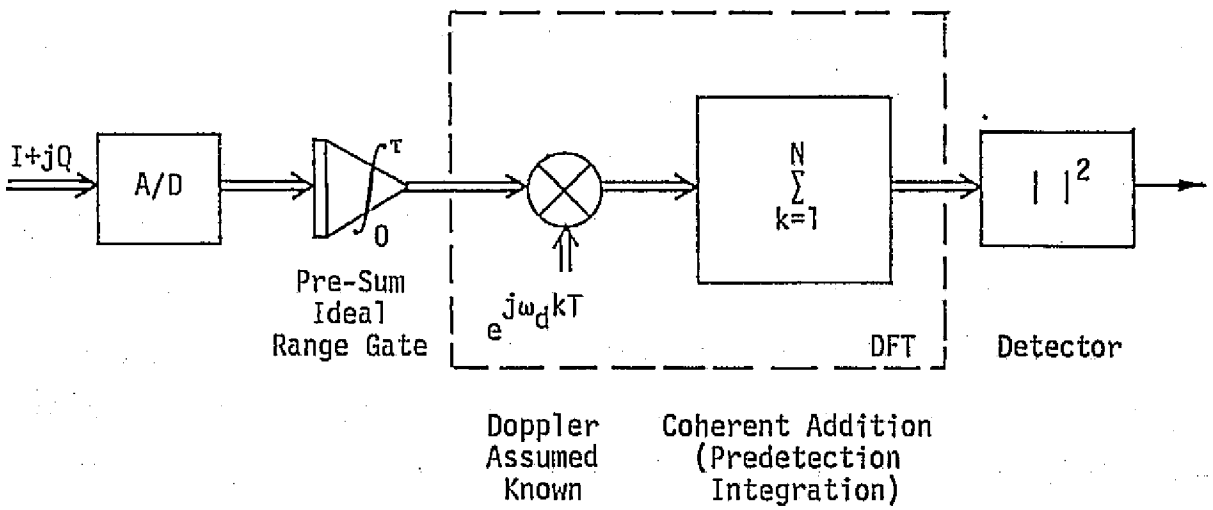

Figure 13. Digital Signal Processor Implementation of the Coherent Radar Receiver

a dB). In this radar, it is shown in Appendix A that the loss is approximately 0.6 dB. The purpose for making the change is that the doppler mixing and predetection integration are then most conveniently carried out by the DFT. The digital implementation is thus essentially the same as the optimal implementation. The time domain representation and the frequency domain representation have the same appearance for both implementations.

7.0 ANGLE TRACKING COUPLING LOSSES

In the power budget of Section 5.0, two coupling losses are noted. These are determined as follows. In Figure 14, the power divide and power combiner for the sum and angle error channels are shown. In the power divide, the signal and noise powers decrease by the coupling factor A = -2 dB. The overall power in the $\Sigma + \Delta$ or $\Sigma - \Delta$ combined signal is therefore reduced by 2 dB, since the signal power in the angle error channel is very small. This is the signal loss due to coupling.

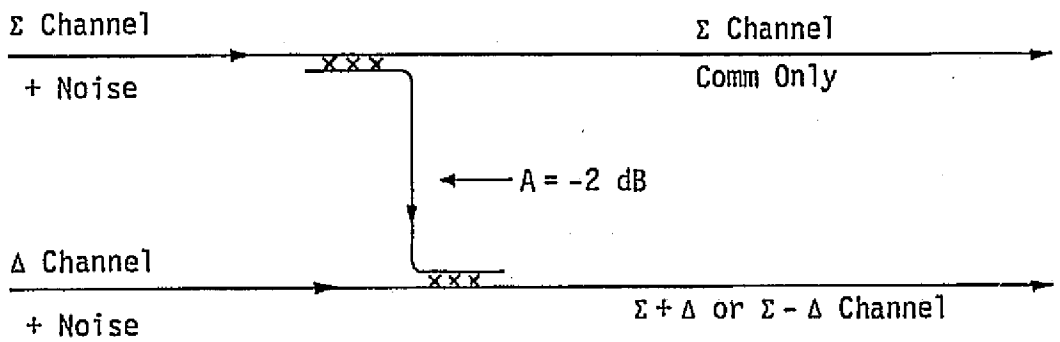

Figure 14. Block Diagram of Coupling Losses

For the noise, the thermal noise spectral density level in the sum and angle error channels are the same. These two noises are also statistically independent and their spectral density levels can therefore be added. Therefore, the overall noise level is

$$N_0\big|_{\Sigma+\Delta} = A\, N_0\big|_{\Sigma} + N_0\big|_{\Delta} = 1.63\, N_0,$$

which is an increase in noise spectral density of 2.1 dB. This is the noise increase due to the thermal noise in the difference channel being combined with that in the sum channel.

REFERENCES

1. Hughes Aircraft Co., "Proposal for Ku-Band Integrated Radar and Communication Equipment for the Space Shuttler Orbiter Vehicle," Volume II, May 1976.

2. D. K. Barton. Radar System Analysis. Prentice-Hall, 1964.

3. P. W. Hannan, "Optimum Feed for All Three Modes of a Monopulse Antenna," IRE Trans. Ant. Prop., Vol. AP-9, No. 5, September 1961, pp. 441-461.

4. S. F. George and A. S. Zannamaker, "Multiple Target Resolution of Monopulse Versus Scanning Radars," Proc. NEC, No. 15, 1959, pp. 814-823.

5. C. L. Weber, "Maximum Likelihood Estimation of the Ratio of Powers in Two Narrowband Processes," Axiomatix Report No. R7701-3, January 31, 1977. Also see Hughes Aircraft Co., "Space Shuttle Ku-Band Integrated Rendezvous Radar/Communications System Study Final Report," No. D4148 SCG 60041R, March 1976, Appendix C.

6. C. L. Weber, "The Orbiter Monopulse Antenna Angular Control System," Axiomatix Report No. R76C7-4, July 1976.

7. Hughes Aircraft Co., "Ku-Band Integrated Radar and Communication Equipment for the Space Shuttle Orbiter Vehicle," Monthly Progress Meeting, April 20, 1977.

8. N. E. Nahi. Estimation Theory and Applications. R. E. Kreiger, 1976.

APPENDIX D

RADAR PERFORMANCE IN PRESENCE OF MAIN LOBE GROUND CLUTTER

APPENDIX D

RADAR PERFORMANCE IN PRESENCE OF MAIN LOBE GROUND CLUTTER

by
Sergei Udalov

1.0 MOTIVATION FOR GROUND RETURN CONSIDERATIONS

The possibility of the ground return interfering with the Shuttle rendezvous radar operation arises when the target is in such a position that the radar antenna points towards the earth at an angle close to vertical. Figure 1 depicts such geometry.

In addition to the geometry shown, i.e., the target being in the line-of-sight (LOS) to ground, the conditions which results in a potentially troublesome ground clutter are:

(1) The ranging waveform repeating at a period shorter than the round trip time to ground, thus precluding the rejection of the ground clutter in real time.

(2) The radar operating at the same frequency for a time interval longer than the round trip time to ground, thus precluding clutter rejection in the frequency domain.

(3) The clutter return being of the same order of magnitude as (or possibly higher than) the signal, thus precluding clutter rejection by magnitude discrimination.

If the system interpulse period exceeds the radar time to ground, receiver gating can be used to prevent clutter from interfering with radar operation. Also, if the operating frequency of the radar is changed so that the ground return arrives when the receiver has been already switched to the next frequency, the clutter interference is eliminated. Consequently, if either one of these clutter suppression techniques is available to the radar system, the clutter magnitude is irrelevant, except for the receiver front end saturation consideration.

However, if the radar system is designed to operate at a relatively high PRF* and if the signal processing is such that the radar is required to dwell at each of the operating frequencies for a time which

---

*Such is the case of the Ku-band rendezvous radar system, which is limited to peak transmitter power of 50 watts.

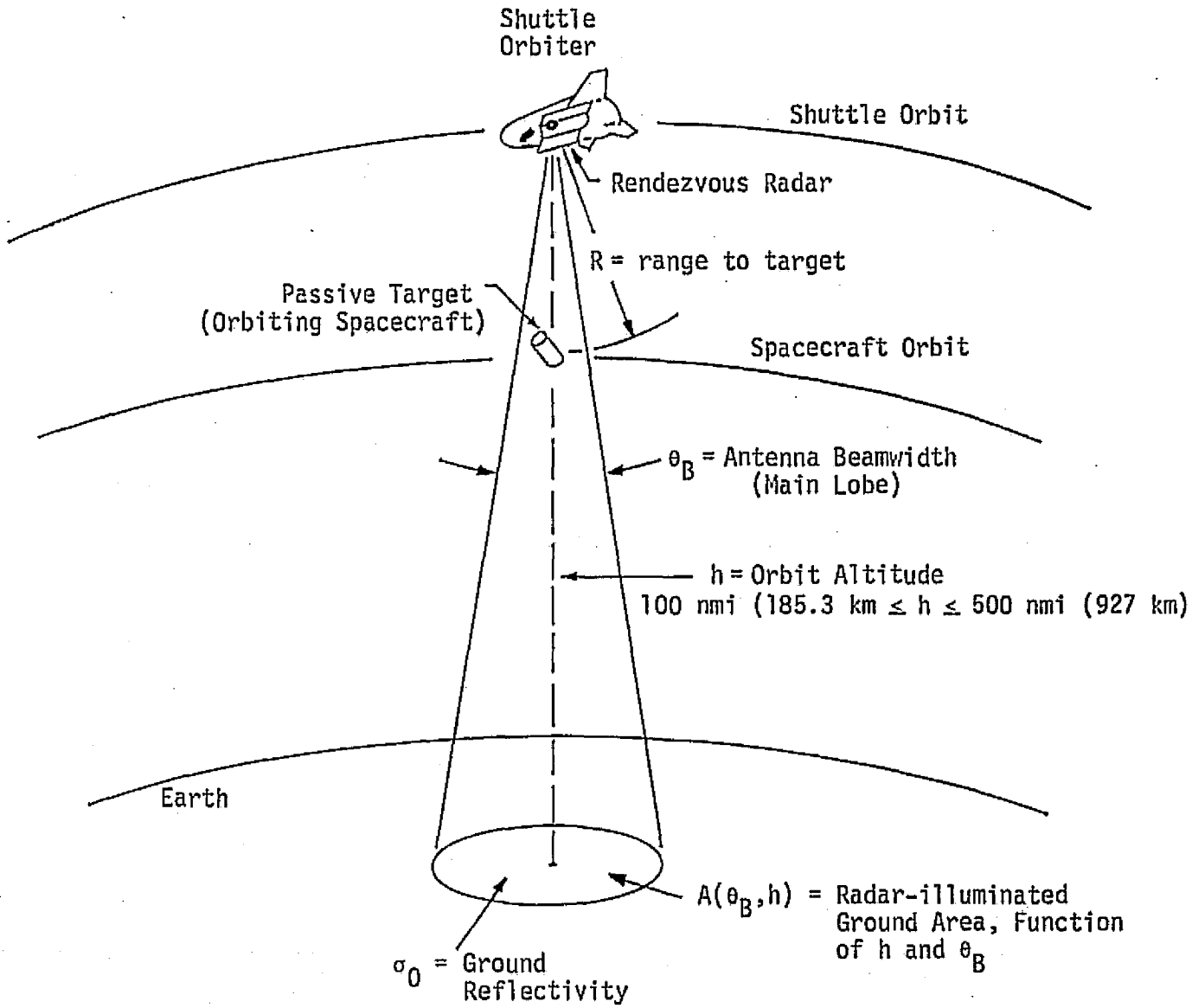

Figure 1. Rendezvous Geometry* With Ground Clutter Return in Main Lobe

*Not to scale

exceeds the round trip time to the ground, the clutter will enter the radar receiver at ambiguous ranges (fold-overs). Consequently, it behooves us to examine the factors which may result in condition (3). We must also examine the possibility of alleviating the effect of ground clutter on system performance by exploring the possibility of adapting the aforementioned clutter rejection techniques to the system under consideration.

2.0 GENERAL CONSIDERATIONS

Before proceeding with the detailed analysis of the ground return and its estimated impact on rendezvous system performance, it is proper to present a few general considerations. These will then determine the specifics of the subsequent analysis.

Consider first the general relationship between the orbit altitude and the target detection ranges. The range of orbital altitudes, h, at which the rendezvous may take place is from 100 nmi (185.3 km) to 500 nmi (927 km), with the lowest altitude presenting a potentially most troublesome rendezvous situation [1]. In comparison, the range, R, for passive target detection and acquisition may vary from about 0.5 nmi (0.927 km) to 12 nmi (22.2 km). However, the range advantage in favor of the passive target may be outweighed by the excessive cross-section area of the ground return. This is particularly true for the passive targets at the extreme of the acquisition range (≈12 nmi) and for antenna line-of-sight (LOS) close to the downward vertical. It must also be pointed out that, for a near vertical incidence, the clutter power falls off as h^{-2} compared to R^{-4} for the passive target return. Therefore, for a rendezvous at any nominal altitude, the target-to-clutter power ratio depends primarily on the target range and is relatively insensitive to altitude changes resulting from the rendezvous manevuers. For example, lowering the orbit altitude from 110 nmi to 100 nmi, as a result of rendezvous "from above," will change the clutter return by 20 log (110/100) or 0.83 dB, assuming a vertical descent on the target. In comparison, the change in target signal strength resulting from reducing the range to the target from 12 nmi to 0.5 nmi is 40 log (12/0.5) or 55.2 dB!

This simple example points to the fact that, at ranges an order of magnitude shorter than the maximum detection range (12 nmi specified

for 1 m^2 target), the signal advantage in favor of the desired passive target outweighs the possible deleterious effects of ground clutter. On the other hand, the potential degradation of system performance must be estimated quantitatively, as is done by the use of the time domain analysis in Section 3.0.

Figure 2 shows, qualitatively, the time domain relationship between the various power levels which influence the performance of the rendezvous radar in the presence of the clutter. As shown in this figure, the pertinent power levels are:

P_T = signal (target) return power

P_C = ground clutter return power

P_n = system noise in detect (or track) bandwidth.

The ratios of importance are then:

P_T/P_C = signal-to-clutter power ratio

P_C/P_n = clutter-to-noise power ratio

P_T/P_n = signal-to-noise power ratio.

It is intuitively obvious that, if the rendezvous geometry is such that $P_C/P_n \ll 1$, the clutter return is completely submerged in the thermal noise and, thus, the system performance is determined, such as in a "clear" mode, by the P_S/P_n ratio. When $P_C/P_n \approx 1$, the clutter may, depending on its nature, begin to degrade the target detection performance and possibly target tracking performance of the system, as well.

For $P_C/P_n > 1$, the radar performance may be affected considerably, but it can be regained by lowering the transmitter power. The reduction of the transmitter power "buries" the clutter in the thermal noise, but it also reduces the received signal power. Therefore, the transmitter power reduction should be carried out only if the available P_S/P_n is high enough so that, when the received signal drops in strength (relative to P_n) along with the clutter, the resulting P_S/P_n is sufficient to perform the appropriate radar function.

Finally, if $P_S/P_C < U$, where U is some minimum ratio required to perform a designated function, the radar becomes inoperative and "fixes" have to be employed. Some of the potentially usable fixes are described in Section 4.0.

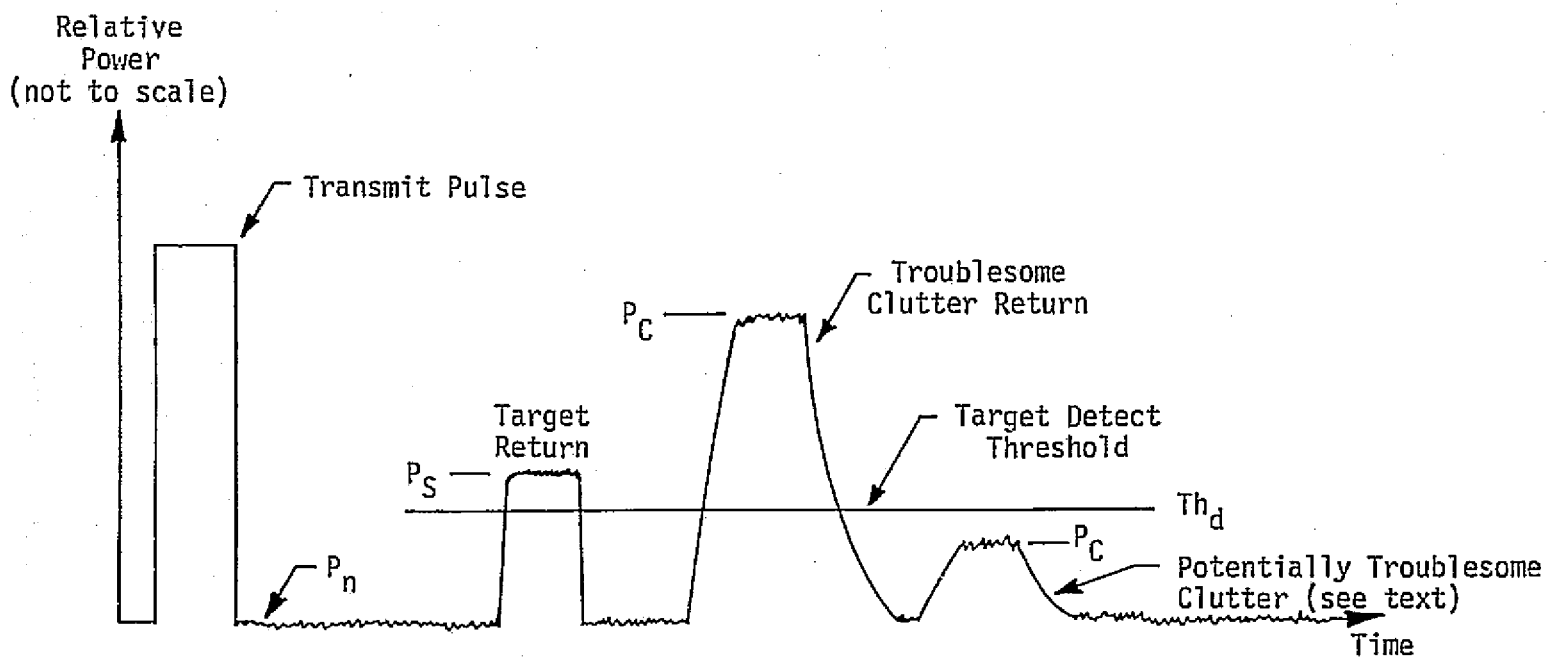

P_T = target return power

P_C = ground clutter return power

P_n = system noise in detect (or track) bandwidth

Figure 2. The Degree of Clutter Interference in Time Domain Depends on the Relative Magnitudes of P_S/P_C and P_C/P_n Ratios

The acceptable value of U depends on the mode in which the radar is operating. We will consider radar operation with clutter in terms of two requirements: (1) a general requirement stated in the original specification [1], and (2) a specific requirement [2] pertaining to the rendezvous for the Skylab reboost mission.

2.1 The General Requirement

The general requirement for radar operation in the presence of the ground clutter is defined by paragraph 3.2.1.3.5.1 of [1]:

> "3.2.1.3.5.1 Ground Clutter. The radar shall meet the performance requirements of this specification in both the detection and tracking phases and in both the passive and active modes of operation in the presence of transmitted power reflected from the surface of the earth. Detection and tracking shall not be degraded by earth-reflected signals (clutter) for any antenna pointing angle which results in a total signal-to-clutter ratio of 20 decibels or greater. The clutter may result from main-beam and sidelobe reflections or sidelobe reflections only. The reference signal level shall be equivalent to that provided by the reflection from a 1-square-meter target. Clutter signal levels shall be computed in accordance with the clutter model given in Appendix VI. . . ."

From the general requirement, it is evident that as long as the P_S/P_C ratio is kept at 20 dB or above, the system operation must be compatible with the nominally specified operation "in the clear." Note that paragraph 3.2.1.3.5.1 does not demand meeting system performance requirements for incidence angles close to vertical; yet there is no relief in either the range or the cross-section specification as a tradeoff for the capability of operating with the targets being within a near-vertical main lobe. The situation is different with the Skylab reboost mission requirements.

2.2 Skylab Reboost Mission Rendezvous Requirement (Preliminary)

In comparison, the preliminary requirements [2] for the radar rendezvous for the Skylab reboost mission are as follows:

Mandatory - Detect, acquire, and track the passive target at a minimum range of 0.5 nmi (0.927 km) with the ground clutter in the main lobe directed downward, including vertical direction.

Highly Desirable - Detect, acquire, and track the passive target at a range of up to 3 nmi (5.56 km) with the ground clutter in the main lobe directed downward, including vertical direction.

The tradeoffs in this case are between the requirement to operate with the ground clutter in the downward-directed main lobe and the range capability of the system. Also, because the nominal cross-section of the Skylab is 10 m^2 (versus 1 m^2 general specification), another tradeoff is offered for the requirement to operate in the presence of the main lobe nadir clutter.

The analysis which follows considers the radar performance in view of both the general system and the Skylab reboost mission requirements.

3.0 GROUND RETURN CALCULATIONS

3.1 Transient Response of Main Lobe Nadir Ground Return

For a relatively flat earth surface, i.e., surface void of topological irregularities, the strongest main lobe ground clutter will be observed at an incidence angle close to vertical. The primary reason for this is that the ground back-scatter coefficient is largest at vertical incidence. Also, because the reflective properties of the incrementally-illuminated areas of the ground change as the radar signal propagates along the ground, the power of the ground clutter, as seen by the radar, also changes with time.

The general nature of a time-varying ground return can be understood in considering the simplified case of vertical incidence illustrated in Figure 3. From this figure it is evident that, as the leading edge of an RF signal hits the ground, progressively larger areas are illuminated and thus, theoretically, the total return increases as the time progresses. For most cases of practical interest, this is not the case, however. The main factors contributing to the "diminishing return" are: (1) the average reflectivity σ_n of the incremental areas decreases with the incidence angle θ_n, and (2) the antenna beam shape attenuates returns at $\theta_n \geq \theta_B$, where θ_B is the nominal antenna beamwidth. The latter condition occurs when the time required for the incident RF wavefront to spread

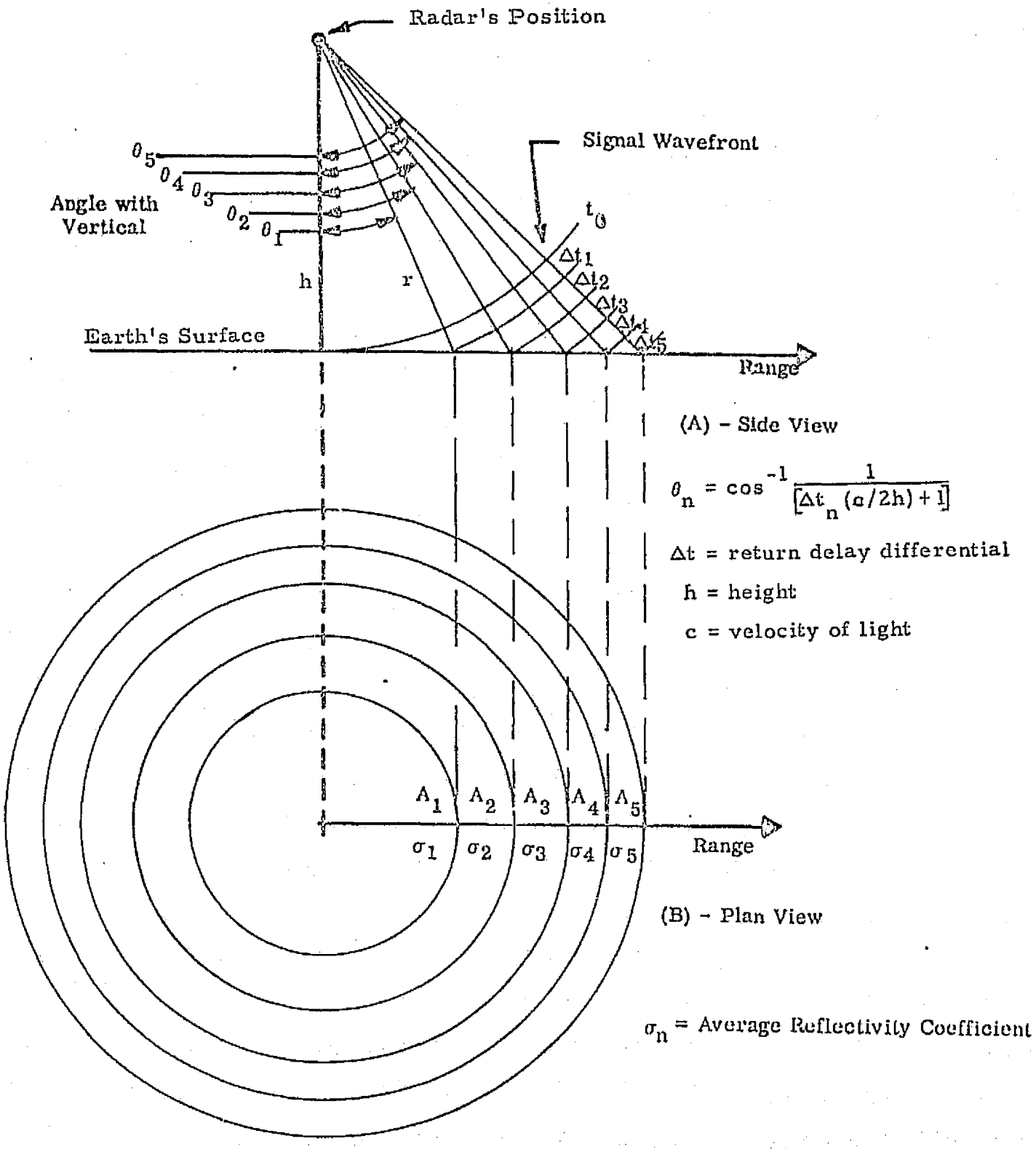

Figure 3. Time-Area Diagram for Transient Analysis of Ground Return

across the ground area, defined by θ_B, is short compared with the duration of the radar pulse. This condition is generally referred to as "beam-width limited" operation.

To obtain a highly accurate representation of the transient behavior of the main lobe ground clutter, one must first obtain an "impulse response" of the ground return by examining the temporal pattern of the power reflected off the incremental areas $\Delta A(\theta)$. Then, to obtain the shape of the ground return for any arbitrary waveform, one must perform the convolution of the transmitted waveform with the impulse response of the ground. The complexity of obtaining the impulse response by the aforementioned method is evident by considering the expression for the power returned from an incremental area $\Delta A(\theta)$:

$$\Delta P_{rec} = \frac{P_t G^2(\theta) \lambda^2}{(4\pi)^3 d^4(\theta)} \sigma_0(\theta,\rho,\lambda') \Delta A(\theta) \qquad (1)$$

where ΔP_{rec} = power received from an incremental surface area $\Delta A(\theta)$

P_t = transmitted power

$G(\theta)$ = antenna gain in the direction of the incremental area

θ = angle from LOS to incremental area

λ = operating wavelength

$d(\theta)$ = distance between radar antenna and incremental area $\Delta A(\theta)$

ρ = surface roughness

λ' = wavelength-dependent losses

$\sigma_0(\theta,\rho,\lambda')$ = average ground reflectivity (referred to as back-scatter coefficient δ in [1])

$\Delta A(\theta)$ = incremental area .

As can be seen from (1), the evaluation of the total return from an extended surface is rather complex and therefore, wherever applicable, various simplifications should be used. One such simplification is that, for a relatively narrow beam (i.e., $\theta_B \leq 3°$), σ_0 may be assumed to be nearly constant over the illuminated area. This is particularly true

for the back-scatter coefficient of the earth, as represented by the RI/SD model described in [1] and in Addendum B.

Another simplifying assumption is that, within the antenna beamwidth, the differences between the ranges to the individual reflectors, i.e., dr, are insignificant compared to the total height, h, above the ground. Specifically, for a near-vertical return, the range $R(\theta)$ to the reflecting areas lying along the perimeter defined by the antenna beamwidth is

$$R(\theta) = \frac{h}{\cos.\theta_B/2}, \tag{2}$$

where h is the altitude and θ_B is the 3 dB antenna beamwidth. The range loss ratio L_R is then

$$L_R(\theta) = \left[\frac{h}{R(\theta)}\right]^4 = \left(\cos\frac{\theta_B}{2}\right)^4. \tag{3}$$

For $\theta_B = 1.6°$,

$$L_R(\theta) = (\cos 1.6°/2)^4 = (0.9999)^4 = 0.9996. \tag{4}$$

Note that the value shown in (4) is independent of altitude h and, obviously, it causes only a negligible reduction in the power levels contributed by the ground areas lying along the periphery defined by θ_B intersecting the ground surface.

Based on these two assumptions, a simplified analytical model for the transient behavior of the near-vertical return can be derived, as explained in Addendum A. Equation (19) of that addendum is of particular importance because it represents the transient response of the ground return to a unit step. Thus, using (19) of Addendum A, we have

$$u_G'(t) = A(\theta_B,h)\, b(1 - e^{-t/t_0}), \tag{5}$$

where

$A(\theta_B,h) = \frac{\pi h^2 \theta_B^2}{4}$ = effective ground area, a function of h and θ_B

b = weighting coefficient, function of beam shape approximation used

h = radar altitude

θ_B = 3 dB antenna beamwidth in radians

t_0 = system "time constant," function of h, θ_B, and antenna beam shape approximation.

Note that both b and t_0 are functions of the beam shape approximation used. For a Gaussian approximation, which we use here for our analysis, we have

$$b = 0.720$$

and

$$t_0 = 0.180\,\theta_B^2(h/c), \tag{6}$$

where θ_B is in radians.

The time varying power level of the vertical ground return can be computed from a range equation into which all the pertinent parameters have been substituted. Thus,

$$P_C(t) = \frac{P_t G^2 \lambda^2 \sigma_0 A(\theta_B,h)\, b(1 - e^{-t/t_0})}{(4\pi)^3 h^4 L_t}, \tag{7}$$

where P_t = peak transmitted power

G = maximum gain of radar antenna

λ = system wavelength

L_t = transmitter losses

σ_0 = ground reflectivity coefficient

and h, $A(\theta_B,h)$, b, and t_0 are as defined previously. The maximum expected vertical ground return power can be found from (7) by letting $t \gg t_0$. The time behavior of $P_C(t)$ can also be found from (7) by examining $P_C(t)$ for all values of t.

Let us compute the maximum values of $P_C(t)$ for vertical return and for typical orbit altitudes, such as 100 nmi, 200 nmi, and 500 nmi. We can also then compute the temporal behavior of $P_C(t)$ to determine the effects of various pulse widths on system performance. Table 1 shows the numbers pertinent to such computations.

The power budgets for computing the value of $P_C(t)_{max}$ are shown in Table 2.

Table 1. Effective Ground Area and System Time Constant as Functions of Orbit Altitude (Antenna beamwidth $\theta_B = 1.6°$ or 0.028 radians. Vertical return)

Orbit Altitude, h nmi (km)	$A(\theta_B,h)$ m^2	$A(\theta_B,h)$ $dB\text{-}m^2$	$t_0(\theta_B,h)$ μsec	$40 \log (h)$ $dB\text{-}m^4$
100 (185.3)	2.10×10^7	73.2	0.087	210.7
200 (370.6)	8.40×10^7	79.2	0.173	222.8
500 (927)	5.25×10^8	87.2	0.434	238.7

The values of $P_C(t)$ shown are the asymptotic values, because they represent the value of $P_C(t)$ for $t >> t_0$. Figure 4 shows how these asymptotic values are approached as the function of time. The responses shown are the result of transmitting either the classic unit step excitation pulse, or a pulse whose rise time is short compared to t_0, but whose duration exceeds t_0 by at least an order of magnitude.

The most important feature shown by the ground response curves of Figure 4 is that, for values of $t > 0.7$ μsec, all of the responses are within about 1 dB of their asymptotic value. Considering the pulse width used in the radar system being built by the Ku-band equipment subcontractor (Hughes Aircraft Company), this means that all pulses equal to or longer than 2.07 μsec will result in the full magnitude of the clutter return for all orbit altitudes of interest.

The importance of transient analysis of ground return is also indicated by the set of curves given in Figure 5. The curves shown there illustrate the effect of orbit altitude on the rise time of the main beam vertical ground return.

It can be seen that the rise time of the return is similar to that of a single-pole RC low-pass circuit responding to either a step or a long pulse input. We also know that the time constant, t_0, which determines the "speed" of the response, is a function of altitude and the antenna beamwidth.

Again, as in Figure 4, one can see that for $t > 0.7$ to 1.0 μsec, the ground return power reaches a level within 5% of the maximum with

Table 2. Power Budget for Computing Maximum Value $P_C(t)$

Term	Value	dB (+)	dB (-)
P_t	50 w	47 dBm	----
G^2	(2)(38.5 dB)	77	----
λ^2	0.0218 m (2.18 cm)	----	33.2
L_t	3.5 dB	----	3.5
$(4\pi)^3$	2000	----	30.0
b	0.720	----	1.4
σ_0	0.80	----	1.0
A_G	Function of h	$10 \log A_G(h)$	----
h^4	Variable	----	$40 \log (h)$
	$P_C(t)_{max}$ =	$124 + 10 \log A_G(h)$	$-69.1 - 40 \log (h)$
	=	$54.9 \text{ dBm} + 10 \log A_G(h) - 40 \log (h)$	

Substituting the values of Table 1 into the equation in Table 2, one obtains:

Altitude	$P_C(t)_{max}$
100 nmi	-82.6 dBm
200 nmi	-88.6 dBm
500 nmi	-96.6 dBm

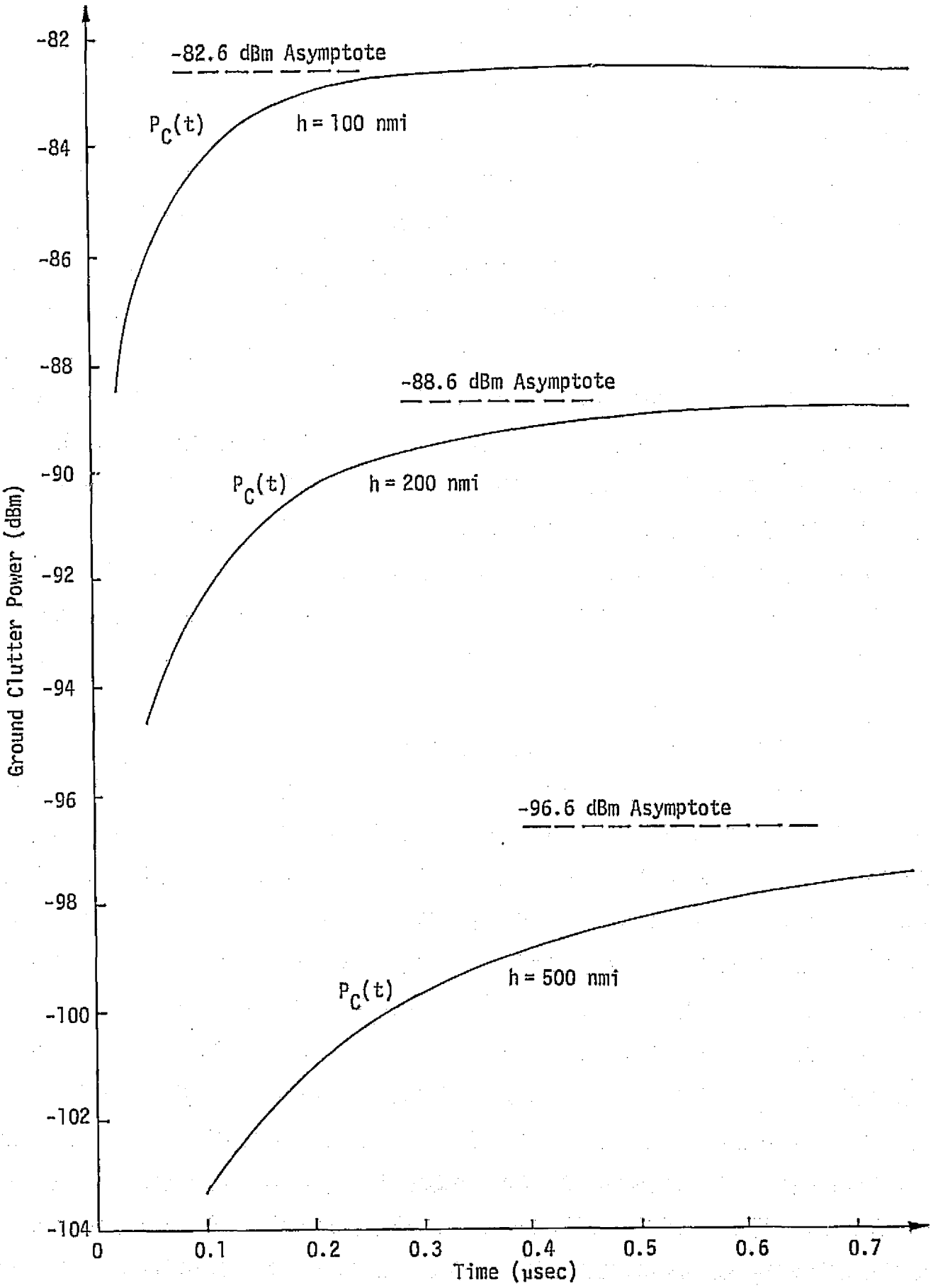

Figure 4. Main Beam Ground Return Clutter Power Level as a Function of Time (Nadir Return)

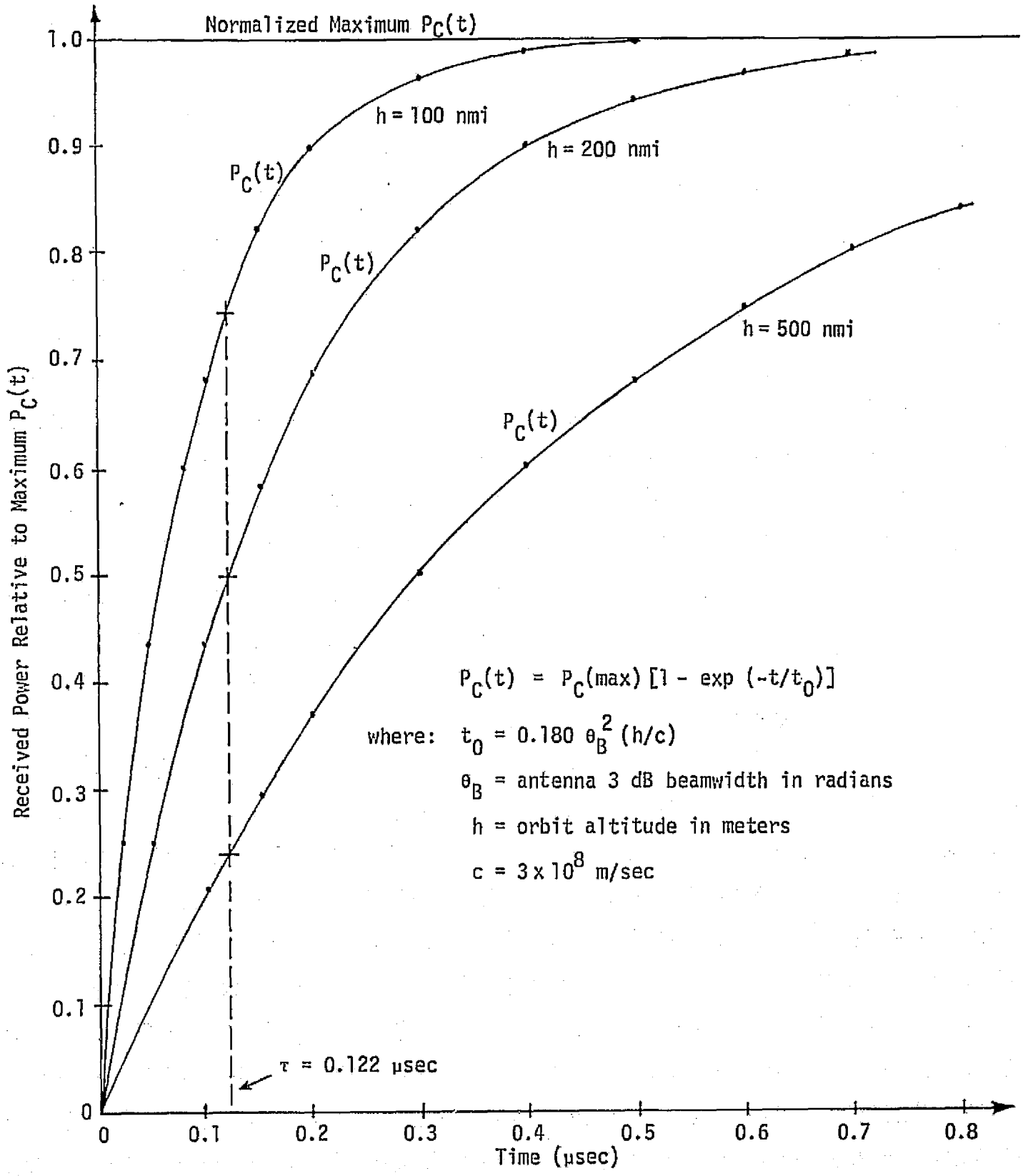

Figure 5. Effect of the Orbit Altitude on the Rise Time of Main Lobe Nadir Ground Return

the exception of the h = 500 nmi curve which has a relatively slow response.

Another interesting fact revealed by the curves of Figures 4 and 5 is that, for t less than about 0.1 μsec, the ground return does not reach its full amplitude. Thus, for the radar mode using a pulse 0.122 μsec wide, the estimated clutter level maxima would be:

Altitude	P_c' (0.122 μsec)	dB Below Maximum
100 nmi	-83.9 dBm	-1.3
200 nmi	-91.7 dBm	-3.1
500 nmi	-102.8 dBm	-6.2

The fact that the clutter power drops as the transmitted pulse is narrowed can be used for improving the target-to-clutter power ratio, P_S/P_C. A close examination of data in Figures 4 and 5 indicates, however, that for the system parameters under consideration to provide worthwhile improvement, say 6 dB or better for the h = 100 nmi case, the pulse width must be about 0.025 μsec. Such a pulse width may be usable only at the short ranges, say less than 3000 feet, at which the P_S/P_C ratio is already sufficient due to range advantage.

Thus, one concludes that the prime purpose of the time analysis of the nadir return is to indicate at which pulse width the system operates in the "beamwidth limited" mode. As shown in Figures 4, 5, and 6, this mode takes place at $\tau \geq 2.02$ μsec and thus clutter return for greater values of τ is the same as for $\tau = 2.02$ μsec.

3.2 Effect of Target Range on Signal-to-Clutter Ratio

Having estimated the absolute values of the main lobe ground clutter for the worst case of nadir return, one can proceed to calculate the signal-to-clutter ratio P_S/P_C as a function of range. The first necessary step for this is, of course, the calculation of absolute level of power return from a passive target of specified cross-section. Table 3 shows the power budget for this calculation.

To make the data available to us complete, we also need to know the absolute noise powers in the system bandwidths associated with the various functions of the rendezvous radar. The noise levels can be obtained by multiplying the system noise density, which includes system

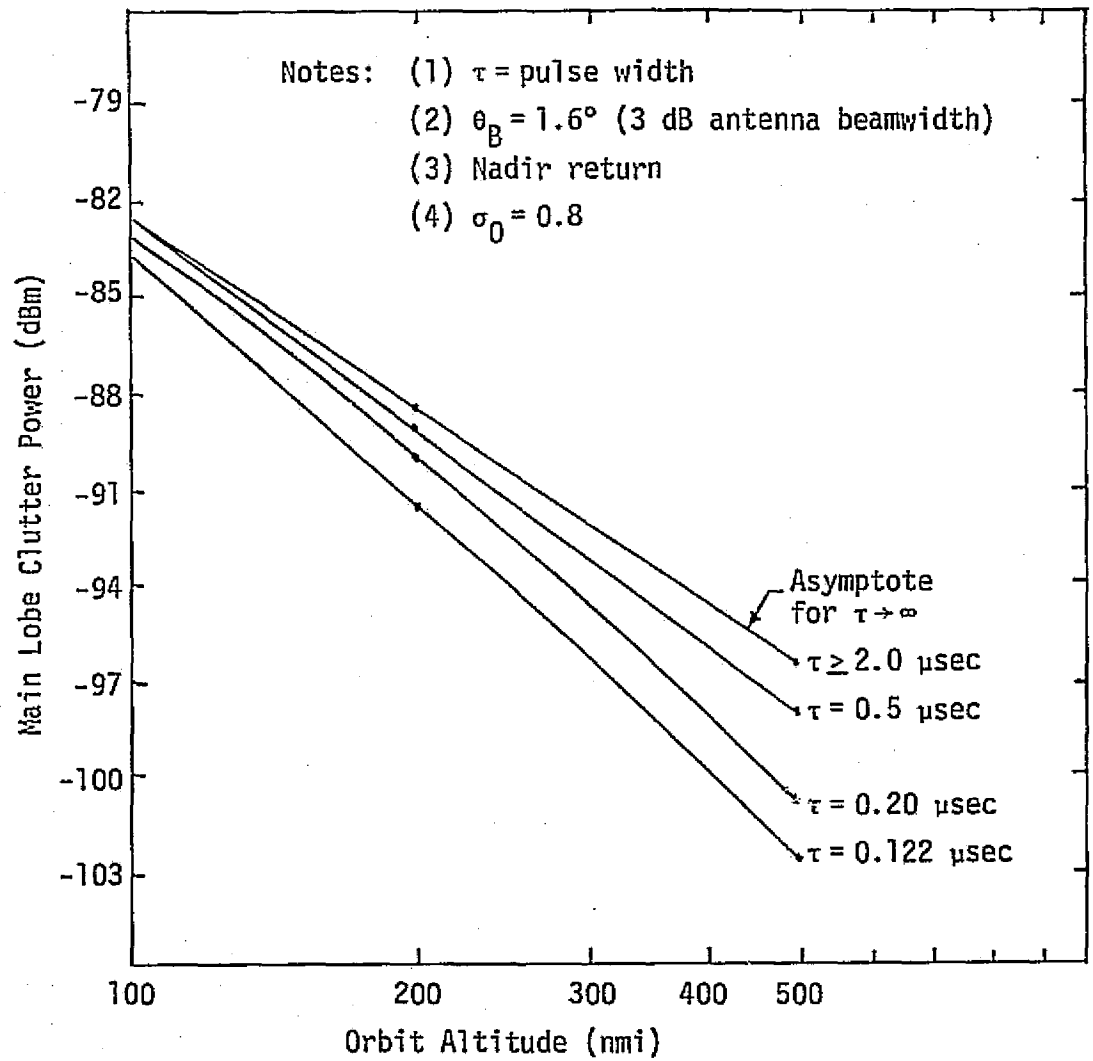

Figure 6. Main Lobe Clutter Power Approaches Asymptotic Value as Pulse Width is Increased to About 2 μsec

noise temperature for the radar mode, with the appropriate system bandwidth. The latter can be assumed to be approximately equal to the inverse of the pulse width utilized during any particular mode. Table 4 shows the noise power levels in dBm as a function of the transmitted pulse width [3].

Note that, for all pulse widths longer than 0.122 μsec, the noise power is referred to the output of the pre-sum circuit, which is essentially a time domain matched filter for pulses longer than 2.07 μsec.

Figure 7 shows the power received from a passive target relative to range, ground clutter and system noise. The data presented in this figure is based on solutions provided in Tables 3, 2 and 4, respectively. From Figure 7, it is evident that the specification requirement [1] for detecting a 1 m^2 passive target at 12 nmi (22.2 km) cannot be met regardless of the orbit altitude if the target is along the downward vertical direction from the Shuttle.* On the other hand, Figure 7 shows that the requirement for the Skylab reboost mission, which calls for 10 m^2 target detection at 0.5 nmi (0.927 km), can be met even at the worst case altitude of 100 nmi. The margin with which this requirement can be met will depend, of course, on the detection method used, but from data in Figure 7 it is evident that P_S/P_C of more than 20 dB is available at 0.5 nmi range for σ of 10 m^2.

From Figure 7, it is also evident that the main lobe nadir clutter exceeds the level of system noise, even for the narrow pulse operation with $\tau = 0.122$ μsec. A 12 dB reduction in transmitter power will bring the 100 nmi altitude clutter approximately to the noise level of the 0.122 μsec pulse operation. Similarly, a 24 dB power-down will bring the 100 nmi clutter level to about the 2.07 μsec pulse operation level. But, surprisingly enough, the operation with the 0.122 μsec pulse will then be thermal noise limited and not clutter limited! Figure 8 shows this phenomenon.

The explanation for data shown in Figure 8 is obtained from Figure 7. Specifically, at a range of about 0.9 km, where the 0.122 μsec pulse mode takes over, P_S/P_C is about 20.5 dB and P_S/P_n is about 35.5 dB

*This statement does not pertain to cases where fixes such as frequency agility can be used to combat clutter.

Table 3. Power Budget for Computing the Absolute Level of Passive Target Return

Term	Value	dB (+)	dB (-)
P_t	50 w	47 dBm	----
G^2	(2)(38.5 dB)	77	----
λ^2	0.0218 m	----	33.2
L_t	3.5 dB	----	3.5
$(4\pi)^3$	2000	----	30.0
σ_0	1 m^2 (specification)	10 log σ	----
R^4	Range (variable)	----	40 log R (in meters)
	$P_S(R)$ =	124 + 10 log σ	-66.7 - 40 log R
	=	57.3 dBm - 10 log σ - 40 log R	

Table 4. Noise Power as a Function of Transmitted Pulse Width [3]

Transmitted Pulse Width τ (μsec)	Pre-sum Ratio (N)	Noise Power (dBm)		
		Video	After Pre-sum	After Doppler Filter
0.122	N/A	-96	N/A	N/A
2.07	1	-108	-108	-120
4.15	2	-108	-109	-121
8.3	4	-108	-112	-124
16.6	8	-108	-115	-127
33.2	16	-108	-118	-130
66.4	32	-108	-121 (-123 in manual)	-133 (-135 in manual)

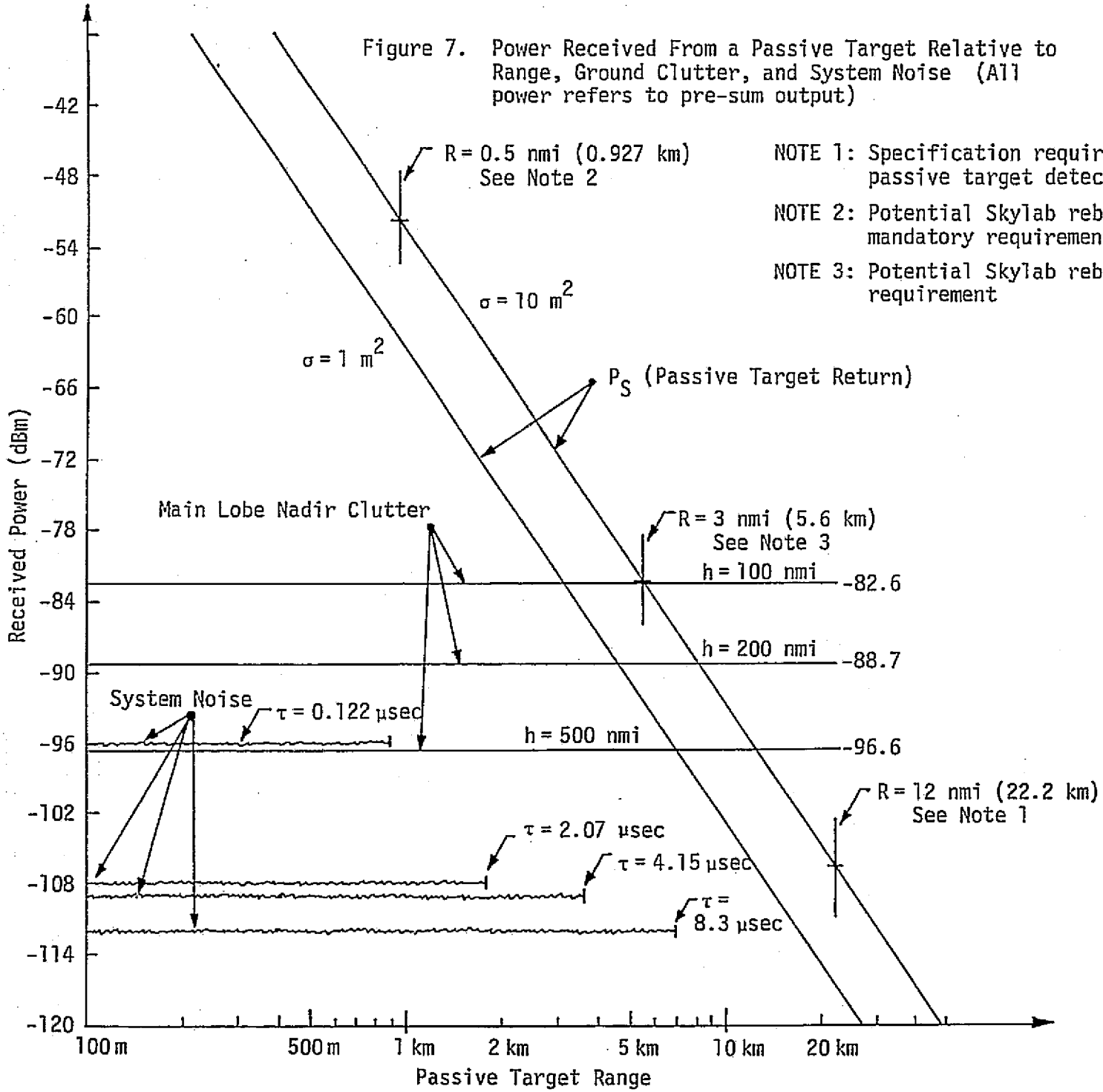

Figure 7. Power Received From a Passive Target Relative to Range, Ground Clutter, and System Noise (All power refers to pre-sum output)

NOTE 1: Specification requirement for passive target detection

NOTE 2: Potential Skylab reboost mission mandatory requirement

NOTE 3: Potential Skylab reboost goal requirement

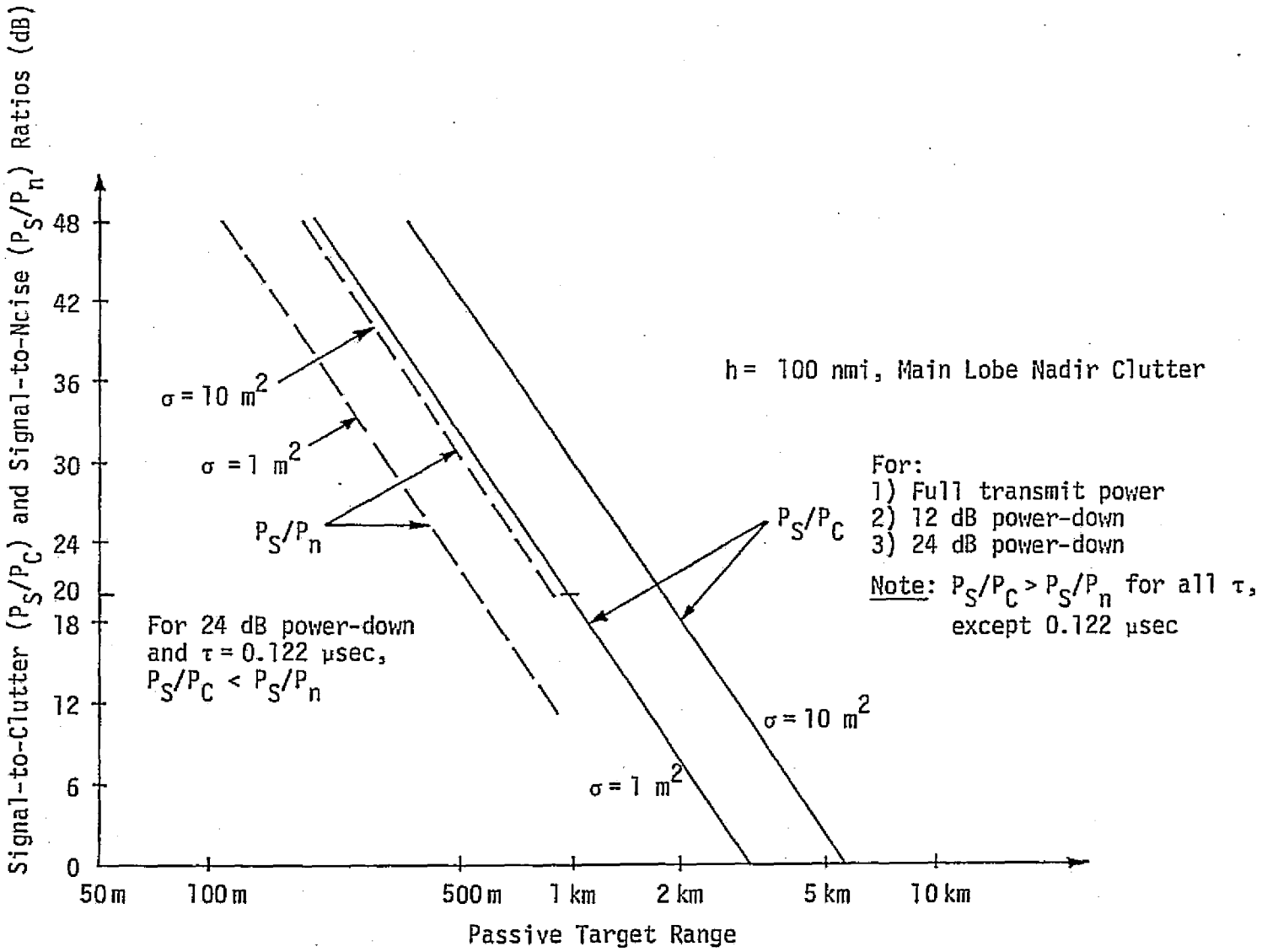

Figure 8. Signal-to-Clutter and Signal-to-Noise Ratios Versus Range

for a $\sigma = 1\ m^2$ target. The clutter signal for h = 100 nmi is about 13.4 dB above system noise for $\tau = 0.122$ μsec. Therefore, reducing the transmitter power by 24 dB places the clutter 10.6 dB below system noise. But the 24 dB power-down also lowers the signal-to-noise ratio by the same amount, thus reducing this ratio from 35.5 dB to only 11.5 dB, a ratio which is far below the signal-to-clutter ratio of 20.5 dB available at this range, i.e., approximately 0.9 km.

Although the results of a 24 dB power-down will not affect the tracking function, because of an increased SNR available owing to tracker integration, the effect of power reduction must be examined in detail, particularly if one is considering acquiring a $10\ m^2$ target at about 0.9 km, a task required by the Skylab reboost mission.

Another issue which must be addressed when considering the effect of clutter is that of providing a 20 dB signal-to-clutter ratio as called out by the specification [1]. From Figure 8, it is evident that, for an orbit altitude of 100 nmi and a $1\ m^2$ target, the 20 dB P_S/P_C ratio will be at about 1 km for the case of main lobe nadir clutter. Consultation of the clutter versus incidence angle curves of Addendum C permit one to construct a set of $P_S/P_C \geq 20$ dB range contours as a function of pulse width and incidence angle. These contours are shown in Figure 9. From this figure, it is evident that the longer pulses provide better clutter immunity at angles of incidence other than vertical. This is evidenced by the fact that, for any particular angle of incidence other than vertical, the ranges included within the $P_S/P_C \geq 20$ dB increases with the pulse length. This is opposite to the aforementioned short pulse at vertical incidence. Note also that, for vertical incidence, the P_S/P_C is the same for all pulse widths.*

The leveling of the contours at the longer ranges is due to thermal noise limitation. In other words, as the incidence angle increases, the $P_S/P_C \leq 20$ dB contour extends further into the range until the condition is reached where $P_S/P_C \geq 20\ \text{dB} = P_S/P_n$.

The ranges at which the thermal noise limitation takes over can be obtained from data in Tables 3 and 4, and also from Figure 7. For example, the $P_S/P_n = 20$ dB for a 2.07 μsec pulse operation is reached at about 4.3 km; for 8.3 μsec, it is reached at about 5 km, etc.

*For $\tau \geq 2$ μsec, the system operates in the beamwidth-limited mode and, hence, the short pulse ($\tau \ll 1$ μsec argument) improvement is not observed.

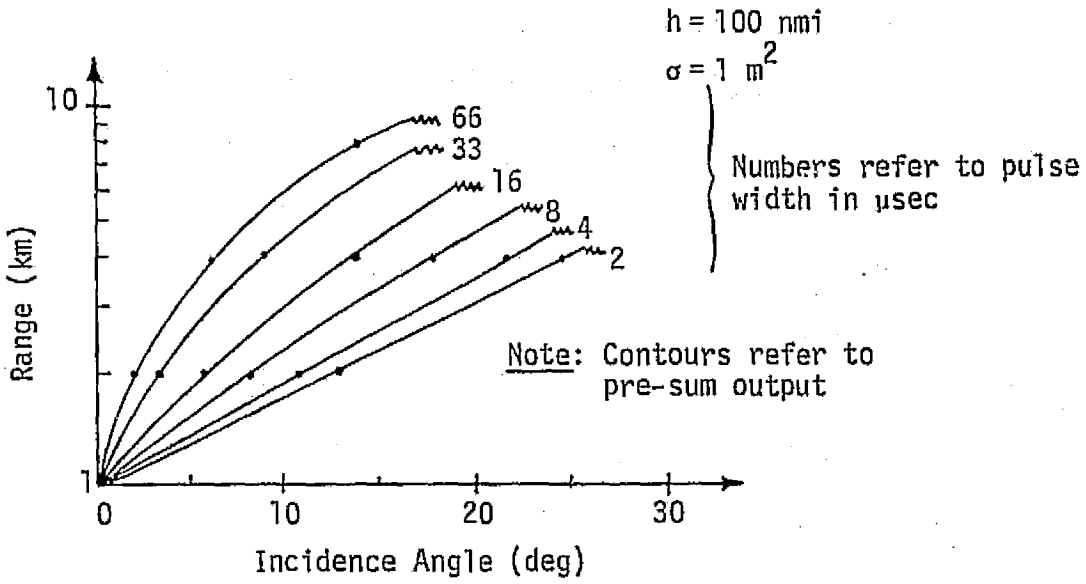

Figure 9. Contours of 20 dB Signal-to-Clutter (P_S/P_n) Ratio Versus Angle of Incidence and Range

It must be emphasized, however, that thermal noise contour limits shown in Figure 9 are determined by the pre-sum output bandwidth, which is approximately equal to the inverse of the pulse width used. But, as shown in Table 4, the doppler filter output noise is 12 dB lower than the pre-sum output noise. Consequently, from the standpoint of thermal noise limitation, the ranges to the noise contours can be doubled. But, because the effect of doppler filters on the clutter level is difficult to predict, the plots of Figure 9 are presented in terms of pre-sum output ratios only. Once the effect of doppler filtering on clutter is established, one can work out the $P_S/P_C \geq 20$ dB contours, referred to as doppler filter output rather than pre-sum output. Considering the complexity of the doppler structure of the ground return as the function of the incidence angle, this task may require analytical modeling and numerical evaluation.

4.0 FREQUENCY AGILITY EFFECTS

As indicated in the previous section, the requirement of the system to detect and acquire a 1 m^2 target at 12 nmi cannot be met at angles close to vertical and at the lowest orbit altitude of 100 nmi. The question to ask is then: What techniques can be used to alleviate the ground clutter problem?

One of the methods which suggests itself is the use of frequency agility. This method is of particular interest because the frequency agility is already employed by the radar system to combat the effects of target return fluctuation. Let us thus consider the numbers involved.

The round trip time, which is the radar time to the nadir ground return is

$$t_{min}(GR) = \frac{2h}{C}, \tag{8}$$

where h is the orbit altitude in meters and $C = 3 \times 10^8$ meters/second. Figure 10 shows the values of $t_{min}(GR)$ for the range of orbit altitudes from 100 nmi to 500 nmi. Now the radar operation, as it is presently defined by the contractor, requires 16 independent pulses at each frequency to form a 16-frequencies Fourier transformation. An additional pulse may be required for initialization, thus making it a 17-pulse group at each of five diversity frequencies. For the acquisition PRF's

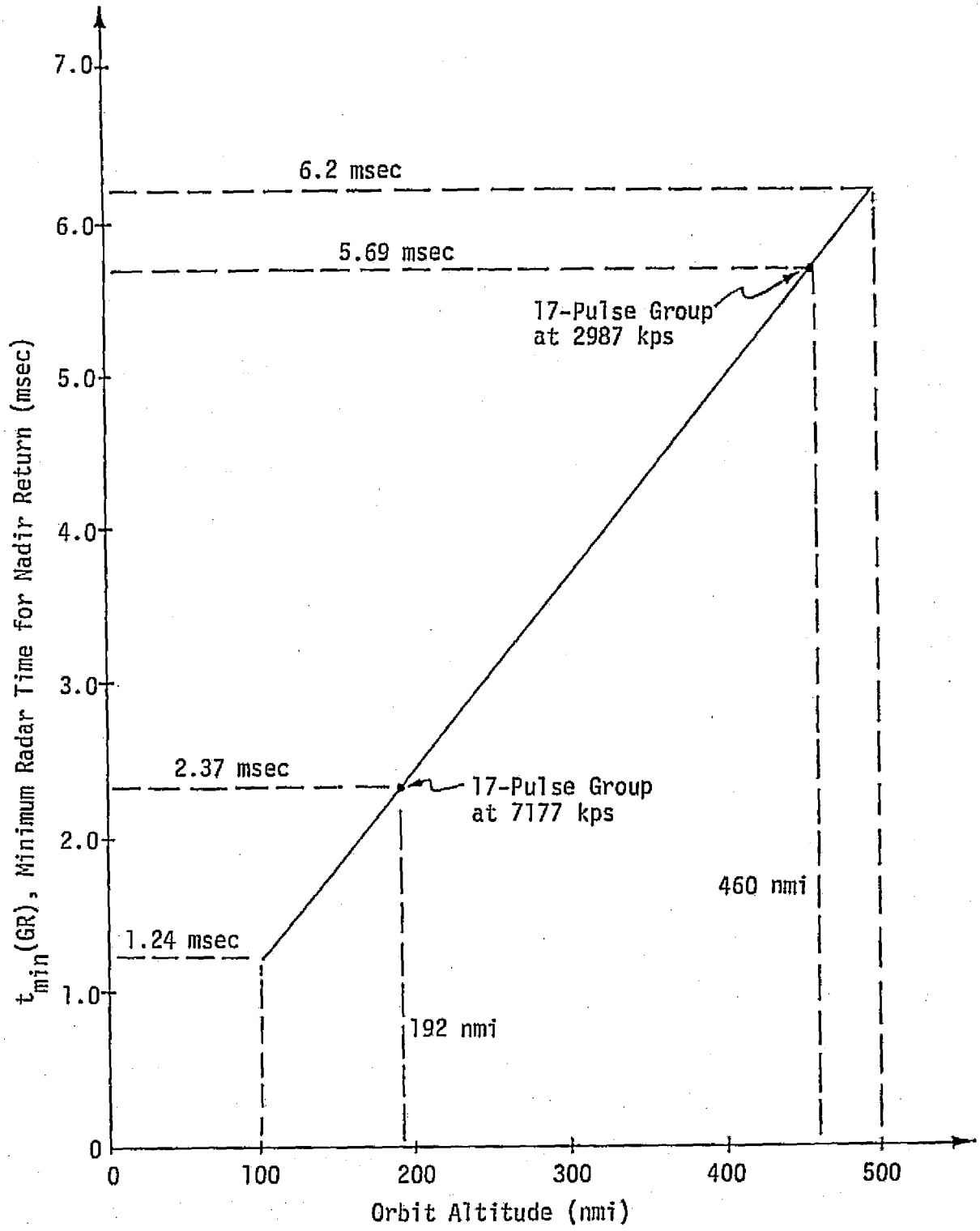

Figure 10. Minimum Radar Time to Nadir Return Versus Orbit Altitude

of 2987 pps and 7177 pps, the durations of the 17-pulse groups are thus

$$T_{17}(2987) = \frac{17}{2987} = 5.69 \text{ msec} \quad (9a)$$

$$T_{17}(7177) = \frac{17}{7177} = 2.37 \text{ msec}. \quad (9b)$$

These delay times transform into 460 nmi and 192 nmi clutter-free altitudes, respectively, provided the operating frequencies are also changed at the same intervals.

Consequently, if we were to construct the maps of altitude versus angle-off-nadir areas where one can expect the clutter-free operation, one would correlate the data of Addendum C with the clutter-free altitudes indicated by (9a) and (9b). Such maps are shown in Figure 11 for the two PRF's under consideration. The corresponding time-frequency patterns are also shown. The significance of the maps is that, within the shaded boundaries, the ground clutter is above thermal noise at the output of the pre-sum device and, consequently, it is a potential threat. It must be noted that, outside the angle barriers (vertical boundaries) the clutter is below the thermal noise, yet it is present at the input to the system. However, above the orbit altitude limits (horizontal boundaries), the clutter is virtually eliminated (except for some very weak multiple time around) at the input to the receiver due to frequency hopping. To distinguish the nature of clutter suppression, the symbols consisting of two orthogonal arrows have been attached to the appropriate boundaries.

Suppose now that one were to consider a time-frequency pattern which would change the frequency at the interval of $t_{min}(GR)$, i.e., every 1.24 msec. The area of clutter interference would then be as shown in Figure 12. From this figure, it is evident that such operation would clear all altitudes up to 500 nmi from primary clutter interference. At 500 nmi, the ground return will be falling with the operating frequency of the system, but it will be attenuated relative to clutter at 100 nmi by

$$\Delta P_C = \left(\frac{500}{100}\right)^2 = 25 \quad (10)$$

or 14 dB. The 14 dB attenuation indicates that system range performance

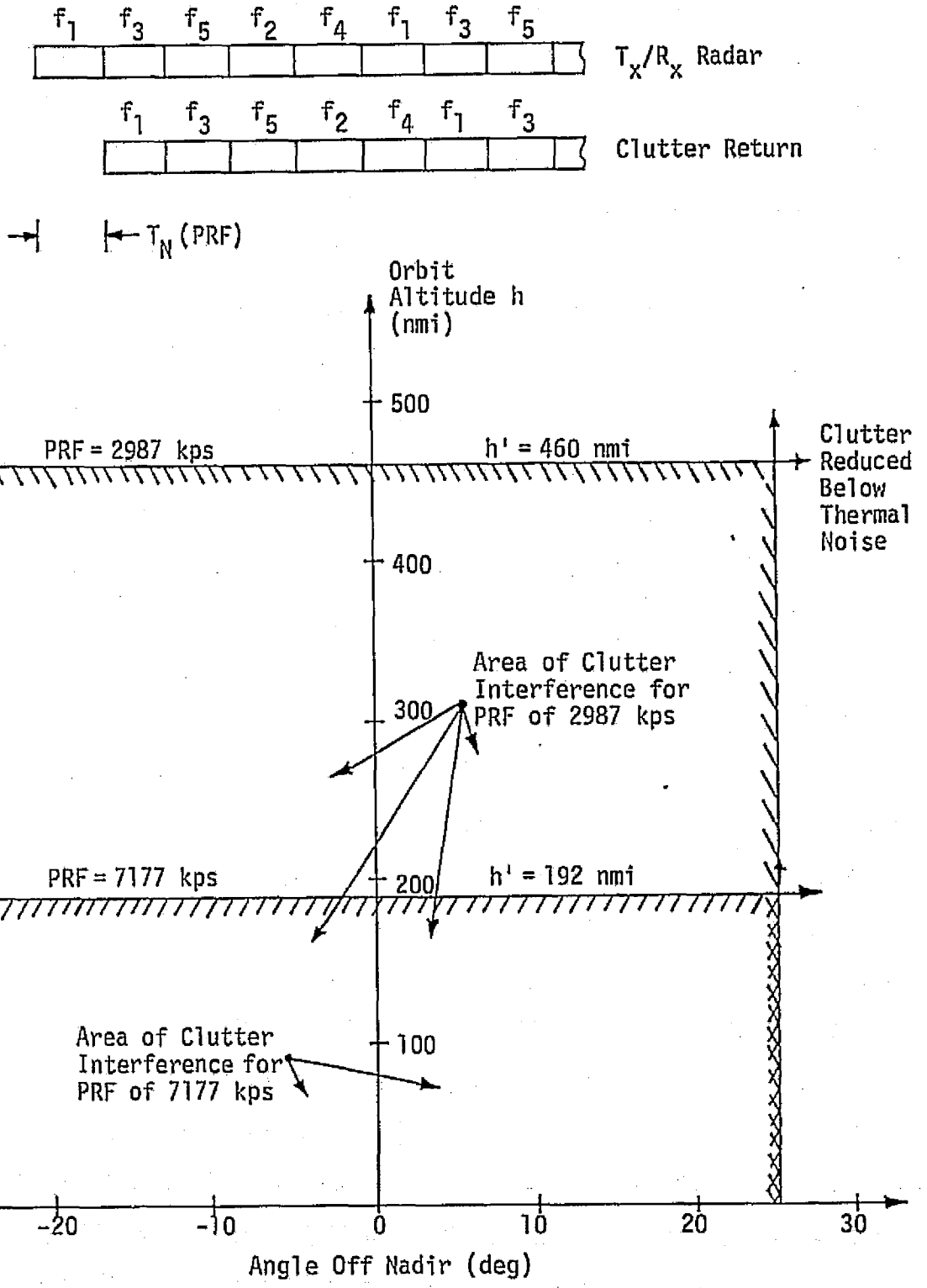

Figure 11. Typical Time-Frequency Pattern of Radar and Corresponding Areas of Clutter Interference

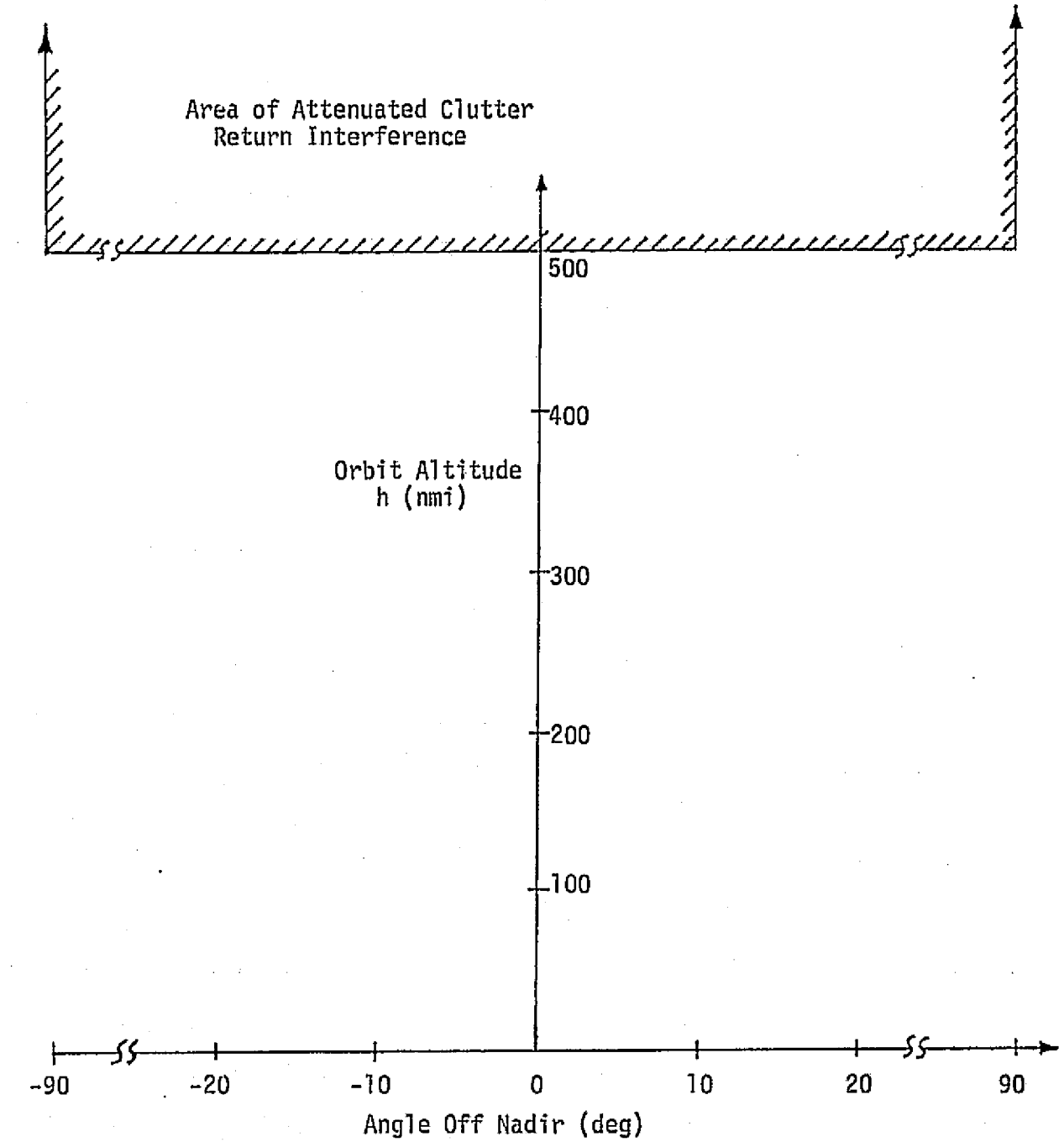

Figure 12. Changing Frequency at Intervals Equal to Radar Time for 100 nmi Clears the 500 nmi Altitude Range of Primary Clutter Interference (5 frequencies used)

can be at least doubled at the 500 nmi altitude. It can be further improved by employing alternating frequency time patterns to avoid the return at 500 nmi. For example, a simple technique would be to introduce à fixed frequency offset to each alternate time-frequency pattern of five frequencies.

Consider now the effect of such "fast" hopping on the number of pulses available for integration at each frequency. Thus,

$$N(7177) = (1.24 \times 10^{-3} \text{ sec})(7177) = 8.9 \quad \text{(11a)}$$

or about 9 pulses;

$$N(2987) = (1.24 \times 10^{-3} \text{ sec})(2987) = 3.7 \quad \text{(11b)}$$

or about 4 pulses.

From (11a) and (11b), we conclude that "fast" frequency hopping will result in an insufficient amount of pulses to be coherently integrated at each frequency. In principle, however, one should consider the possibility of storing the individual small subgroups of pulses until a sufficient number are available to perform a 16-point Fourier transform. If permitted by antenna dwell times and target return coherency, such a method would provide a very promising solution to the clutter return problem at all altitudes.

REFERENCES

1. "Procurement Specification MC409-0025, Ku-Band Integrated Radar and Communications Equipment," Vol. II, Rockwell International/Space Division, March 15, 1976.

2. R. Becker and A. DuPont, "Rendezvous Profile Summary," NASA Presentation at Hughes PDR of April 19-20, 1977.

3. "Performance in Presence of Main Lobe Clutter," Hughes Presentation During PDR of April 19-20, 1977.

ADDENDUM A

TRANSIENT RESPONSE OF THE NEAR-VERTICAL GROUND RETURN

The analysis presented below takes into account the effect of the time dependence, as well as the radar pulse width dependence, of the ground return. It is also shown that the antenna beamwidth is a major factor which influences the target-to-clutter power ratio.

We begin by referring to Figure 1, which shows the relationship between the quasi-stationary and the time-variable parameters which determine the transient behavior of the near-vertical ground return. Specifically, we assume that the altitude h varies slowly compared to other time-dependent parameters, and thus is quasi-stationary. We also assume that the average ground reflectivity σ_0 is virtually uniform within the limits defined by the antenna beamwidths under consideration* and that the illuminated ground patch is level.

Thus, as the RF wavefront hits the ground at nadir point a, the boundary of the reflecting area begins to spread and, at some time t after nadir contact, it spreads to a circle containing point b. Also, as shown in Figure 1, the boundary of the illuminated area is defined by the time-varying angle $\theta(t)$. From the geometry shown, we have

$$\cos \theta(t) = \frac{h}{h + \Delta r(t)} \tag{1}$$

where

$$\Delta r(t) = \frac{2t}{c}, \tag{2}$$

since we are considering only the monostatic radar return.

Substituting (2) into (1), we have

$$\cos \theta(t) = \frac{1}{1 + \frac{t}{(2h/c)}} = \frac{1}{1 + \frac{t}{T}}, \tag{3}$$

where we define

$$T = \frac{2h}{c} = \text{nadir return delay}. \tag{4}$$

---

*See Addendum B.

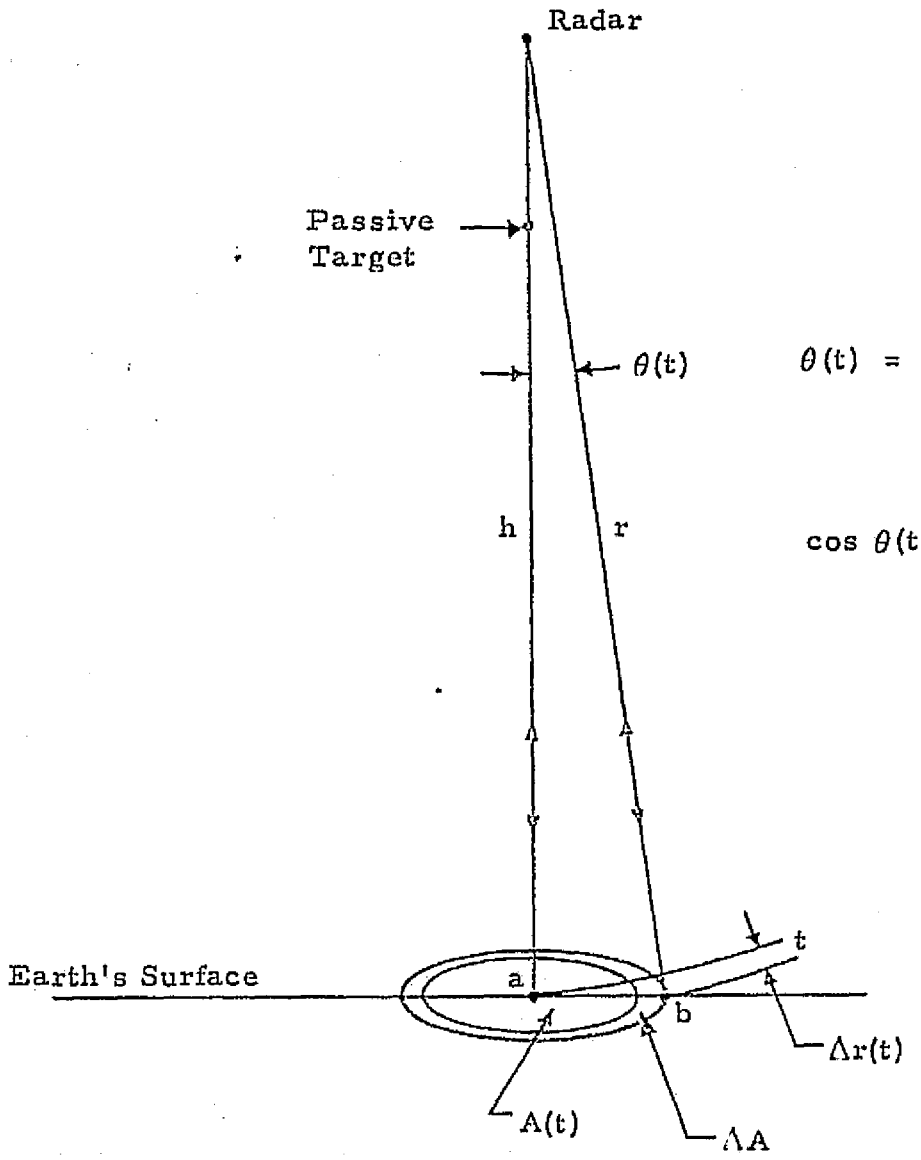

$$\theta(t) = \cos^{-1}\left[\frac{1}{\frac{t}{(2h/c)} + 1}\right]$$

$$\cos\theta(t) = \left[\frac{1}{\frac{t}{(2h/c)} + 1}\right]$$

Figure 1. Near-Vertical Return Geometry

Note that, for the case of h = 185.3 km (100 nmi), T is

$$T = \frac{(2)(185.3 \times 10^3 \text{ m})}{300 \text{ m/}\mu\text{sec}} = 1235.3 \ \mu\text{sec}. \tag{5}$$

Now, since we are considering cases where $t \ll T$ and $\theta \ll 1$ radian, we can expand both sides of (3) into their respective series. Thus, (3) becomes

$$1 - \frac{\theta^2(t)}{2!} + \frac{\theta^4(t)}{4!} - \ldots = 1 - \frac{t}{T} + \frac{2}{2!}\left(\frac{t}{T}\right)^2 - \ldots \tag{6}$$

Retaining only the first lowest order terms of both sides, we have

$$\theta^2(t) \cong 2\frac{t}{T}. \tag{7}$$

Equation (7) establishes a relatively simple relationship between $\theta(t)$ and t, i.e., the time after start of radar return.

Now we will derive the expression for the time-varying area of the ground return. From Figure 1, it is evident that

$$\begin{aligned} A(t) &= \pi h^2 \tan^2 \theta(t) \\ &\cong \pi h^2 \theta^2(t) \quad \text{for } \theta(t) \ll 1 \text{ radian}. \end{aligned} \tag{8}$$

Substituting (7) into (8), we obtain the expression for A(t) explicitly as the function of t:

$$A(t) = \frac{2\pi h^2}{T} t. \tag{9}$$

Equation (9) shows that the illuminated area varies directly as a function of t, provided that we do not consider the effect of the antenna directivity pattern $G(\theta)$. For a Gaussian beam shape approximation, the <u>two-way</u> normalized directivity (gain) pattern is given by

$$G^2(\theta) = \exp\left(-5.552\ \theta^2/\theta_B^2\right), \tag{10}$$

where θ_B is the one-way 3 dB beamwidth and θ is the direction of signal arrival with respect to beam center. But, from (7), we know that θ is a time-varying function $\theta(t)$. Thus, we can rewrite (10) as a time-varying weighing function:

$$w[\theta(t)] = \exp\left[-5.552\ \theta^2(t)/\theta_B^2\right]. \tag{11}$$

The weighing factor expressed by (11) can be applied only to the differential areas defined by an expanding ring having a time "thickness" Δt. In other words, (11) can be applied only to the "impulse response" of the ground. To obtain the expression for such a response, we use (9). Thus, the differential increase in area ΔA due to time increase Δt is computed by subtracting $A(t)$ from $A(t+\Delta t)$:

$$A = A(t+\Delta t) - A(t) = \frac{2\pi h^2}{T}(t+\Delta t - t) = \frac{2\pi h^2}{T}\Delta t . \tag{12}$$

The magnitude of the impulse response is obtained by dividing ΔA by Δt and letting $\Delta t \to 0$. Consequently,

$$\delta_G(t) = \lim_{\Delta t \to 0} \frac{\Delta A}{\Delta t} = \lim_{\Delta t \to 0} \frac{A(t+\Delta t) - A(t)}{\Delta t} = \frac{2\pi h^2}{T} . \tag{13}$$

Because this is a definition of the derivative, we thus obtain:

$$\delta_G(t) = \frac{dA}{dt} = \frac{2\pi h^2}{T} \tag{14}$$

for the unweighted impulse response of the ground. Note that within the assumptions used, i.e., $\theta(t) << 1$ radian and $\theta_B << 1$ radian, this response is constant, which is a characteristic of a perfect integrator. This is also evident from (9), which tells us that the reflecting area increases linearly with time. Since such a ramp-like response is obtained from an integrator when a unit step function is applied to its input, we could have obtained (14) by direct differentiation of (9).

We can now proceed to apply the antenna pattern weighting function (11) to the unweighted impulse response (14):

$$\delta_G'(t) = \frac{2\pi h^2}{T} \exp\left[-5.552\ \theta^2/\theta_B^2\right] , \tag{15}$$

where the prime indicates the weighted response.

Substituting (7) into (15):

$$\delta_G'(t) = \frac{2\pi h^2}{T} \exp\left[-(5.552)(2)\, t/T\right]$$

$$= \frac{2\pi h^2}{T} \exp\left[-t/t_0(\theta_B, h)\right] , \tag{16}$$

where

$$t_0(h,\theta_B) = \frac{\theta_B^2 T}{(2)(5.552)} = \frac{\theta_B^2 (2h)}{(2)(5.552)c} = 0.180\ \theta_B^2 (h/c)\,. \qquad (17)$$

Note that (16) and (17) can be used to obtain the ground return due to any envelope shape of the transmitted radar signal. For this, the envelope of the transmitted radar signal is to be convolved with (16).

But since we are primarily interested in ground response due to rectangular pulses, we can integrate (16) to obtain the weighted ground return waveform due to a unit step. Once we know the response to the unit step, the response to a pulse of any length can be obtained by the conventional method of using positive and delayed negative step functions.

The weighted step response of the ground is the integral of (16). Thus,

$$\begin{aligned} u_G'(t) &= \frac{2\pi h^2}{T} \int_0^t e^{-t'/t_0}\, dt' \\ &= \frac{2\pi h^2}{T} \left[-t_0 e^{-t'/t_0}\right]_0^t = \frac{2\pi h^2}{T} (-t_0 e^{-t/t_0} + t_0) \\ &= \frac{2\pi h^2}{T} t_0 (1 - e^{-t/t_0})\,, \end{aligned} \qquad (18)$$

where T and t_0 have been defined by (4) and (17), respectively. The physical significance of (18) can be understood better if we replace the t_0 factor <u>outside</u> the parentheses by its definition given in (17):

$$\begin{aligned} u_G'(t) &= \frac{2\pi h^2}{T} \times \frac{\theta_B^2 T}{(2)(5.552)} \times (1 - e^{-t/t_0}) \\ &= \frac{\pi h^2 \theta_B^2}{4} \times \frac{1}{1.388} \times (1 - e^{-t/t_0})\,. \end{aligned} \qquad (19)$$

The term $\pi h^2 \theta_B^2/4$ is the area of the ground within the cone defined by the 3 dB beamwidth of the antenna. Furthermore, the factor 1.388 is the weighting factor for this area due to the Gaussian beam shape approximation.* Therefore, we can write (19) in terms of its

*In (19), we deliberately factored the coefficient 5.552 as (4)(1.388).

coefficients as

$$u_G'(t) = A(\theta_B,h)\, b(1 - e^{-t/t_0}) \tag{20}$$

where $A(\theta_B,h) = \dfrac{\pi h^2 \theta_B^2}{4}$ = ground area, function of h and θ_B

b = weighting coefficient, function of beam shape approximation used (b = 1/1.388 for a Gaussian beam)

t_0 = system "time constant," function of h and θ_B.

Note that (20) is rather general and thus can be used along with (16) for various combinations of parameters, provided the assumptions used for expansion (6) are valid.

Figure 2 shows the vertical ground return response to a unit step and to a pulse of finite duration. The latter can be computed from the following:

$$f_G(t) = A(\theta_B,h)\, b(1 - e^{-t/t_0}); \qquad 0 < t \leq \tau \tag{21}$$

$$f_G(t) = A(\theta_B,h)\, b(1 - e^{-\tau/t_0})\, e^{-(t-\tau)/t_0}; \qquad t > \tau \tag{22}$$

where τ is the radar pulse duration in time units compatible with units of t_0.

It is interesting to note that the transient response of the near-vertical ground clutter to a Gaussian beam antenna illumination has the same form as the response of a single-pole low-pass RC filter.

To compute the <u>maximum</u> target-to-ground clutter ratio, P_S/P_C, for any pulse width, one estimates the highest value of $A'(\theta_B,h)$ reached at τ/t_0 and substitutes it into the appropriate range equations. Table 1 shows the expression for P_S/P_C as a function of τ/t_0 and of all other pertinent parameters. Note that substituting (21) and (22) into the equation of Table 1, the transient behavior of P_S/P_C can be obtained for all values of τ/t_0.

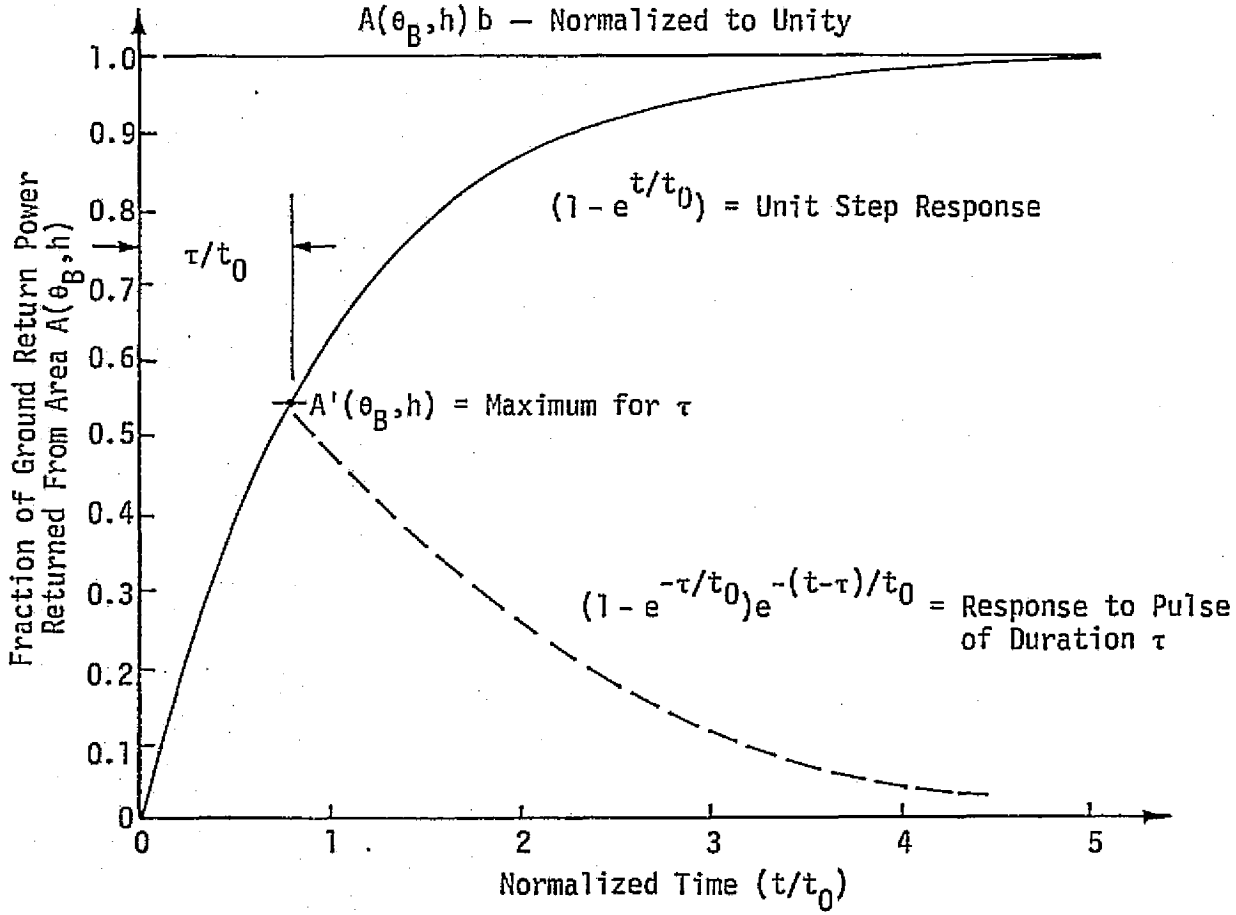

Figure 2. Normalized Near-Vertical Ground Return Response to Unit Step and to Pulse of Finite Duration

Table 1. Maximum Target-to-Ground Clutter Power Ratio for a Boresight Target and Near-Vertical Ground Return

$$\frac{P_S}{P_C}(\tau) = \frac{P_t G^2 \lambda^2 \sigma_t}{(4\pi)^3 R^4 L} \quad \frac{(4\pi)^3 h^4 L}{P_t G^2 \lambda^2 A_G(\theta_B, h, \tau) b \sigma_0} = \frac{\sigma_t h^4}{R^4 A_G(\theta_B, h, \tau) b \sigma_0}$$

$$= \frac{\sigma_t h^4 (4)}{R^4 \pi h^2 \theta_B^2 b(1 - e^{\tau/t_0}) \sigma_0} = \frac{4 \sigma_t h^2}{\pi b R^4 \theta_B^2 (1 - e^{-\tau/t_0}) \sigma_0}$$

where

P_t = peak transmitted power

G = bore axis antenna gain

λ = wavelength

R = target range (meters)

h = altitude (meters)

σ_t = target cross-section (1 m^2)

L = system losses

$A_G(\theta_B, h, \tau)$ = ground return area

b = antenna beam shape factor ($b = 0.72$ for Gaussian approximation)

θ_B = antenna beamwidth (in radians)

τ = pulse width

$t_0 = 0.180\ \theta_B^2\ (h/c)$ for Gaussian beam shape

σ_0 = ground reflectivity

P_S = target power

P_C = ground clutter power

ADDENDUM B

GROUND BACK-SCATTER COEFFICIENT MODEL FOR EARTH'S SURFACE

According to the RI/SD specification [1], the values of the back-scatter coefficient of the earth's surface will be those associated with a smooth sea, i.e., approximately Seastate 1. The value of the back-scatter coefficient σ_0 (a numeric, referred to as δ in the RI/SD specification), according to the specification, ranges from 0.8 for vertical incidence (specular reflection) to 10^{-3} (diffuse reflection) for incidence angles greater than 20 degrees. Furthermore, for clutter estimation purposes, the σ_0 is assumed to be a linear function of the angle off the vertical in accordance with the following:

θ	σ_0
0°	0.8
20°	10^{-1}
40°	10^{-2}
60° or greater	10^{-3}

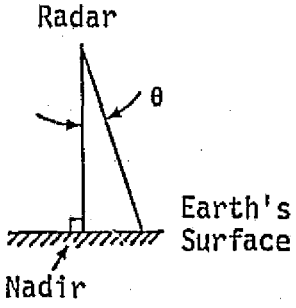

where σ_0 is the back-scatter coefficient and θ is the angle off nadir. Figure 1 shows the σ_0 value as a function of θ for the ranges of θ specified in the table.

Of particular interest is the behavior of σ_0 close to nadir and within the angles commensurate with the radar antenna beamwidth. Figure 2 shows this behavior. From this figure, it is evident that, for calculations of the near-vertical ground return, the value of the ground reflection coefficient may be considered to be constant at 0.8 numeric. Note that, across the 6 dB two-way antenna pattern, the maximum deviation from the 0.8 value is only 0.155 dB.

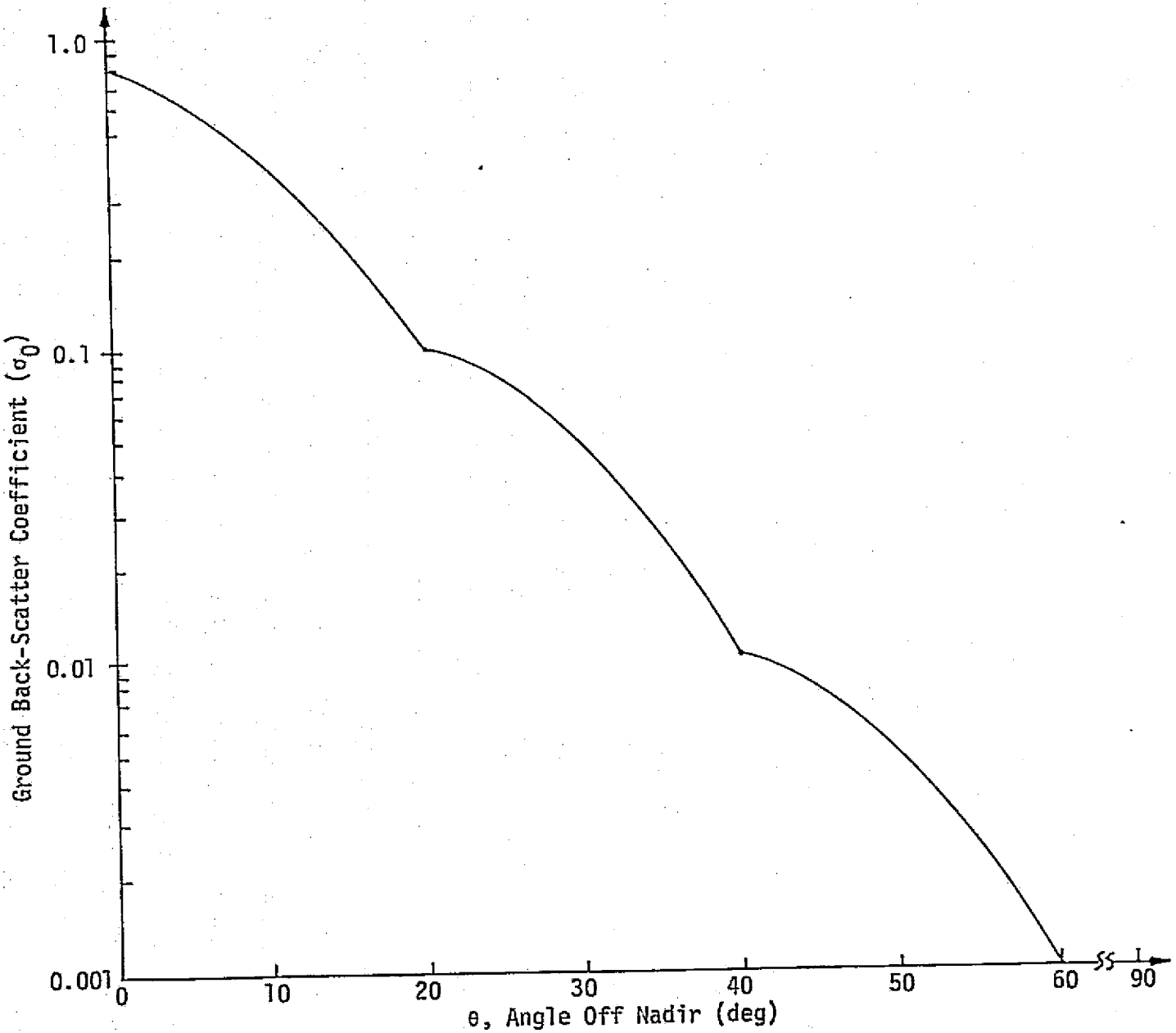

Figure 1. Rockwell Model for Ground Back-Scatter Coefficient (Spec. #357)

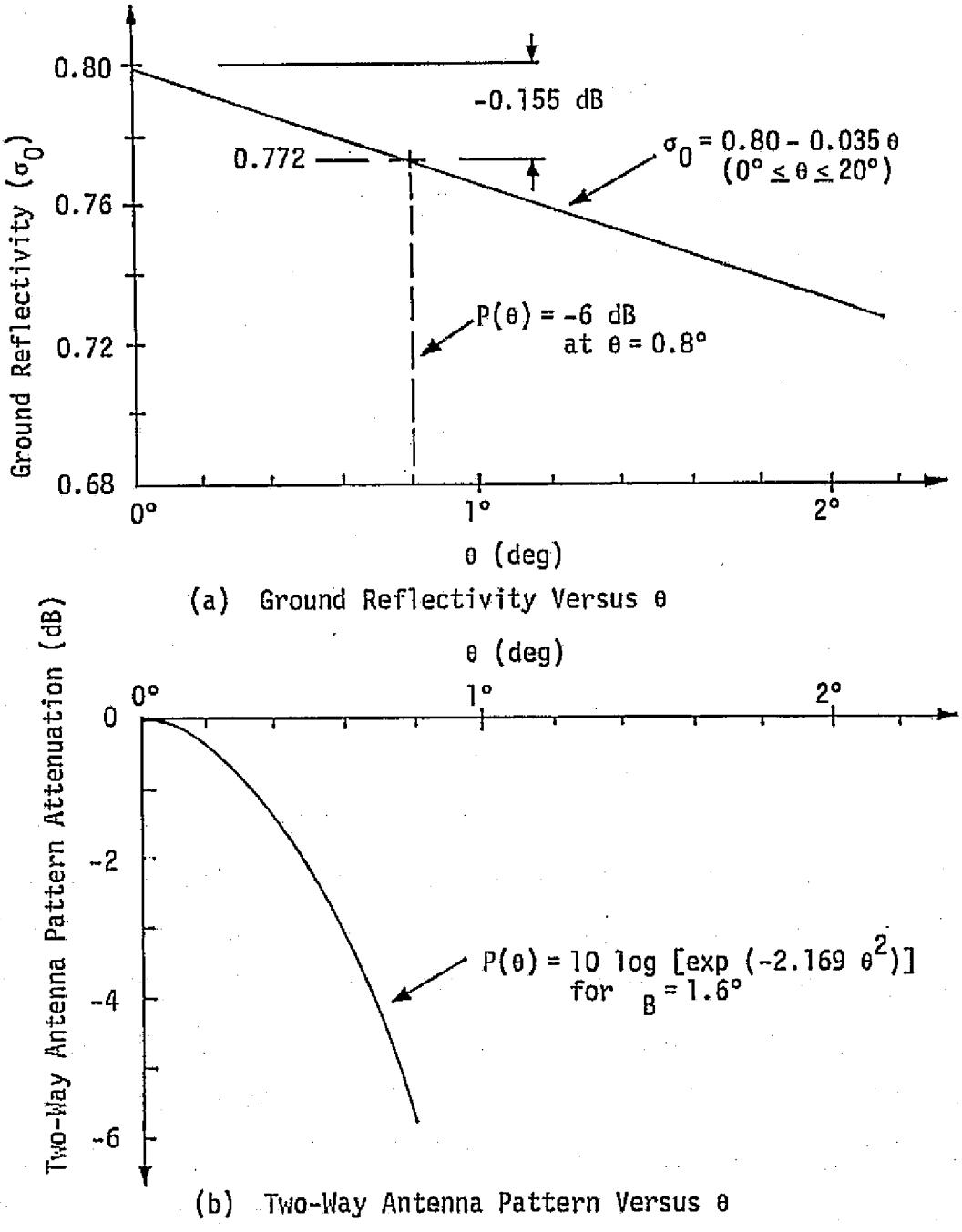

Figure 2. Ground Reflectivity (a) Changes Very Slowly Compared to Two-Way Antenna Pattern Attenuation (b)

ADDENDUM C

MAIN LOBE GROUND CLUTTER VERSUS INCIDENCE ANGLE AND PULSE WIDTH

This addendum presents data on the behavior of the main lobe clutter at incidence angles other than vertical and also as the function of pulse width τ. The data summarized below is based on the technical presentation [3] dealing with this subject. It is included in this report to provide completeness to the discussion of the clutter effects.

The video signal processor model assumed for the clutter and thermal noise calculations prior to doppler processing is shown by the the block diagram of Figure 1.

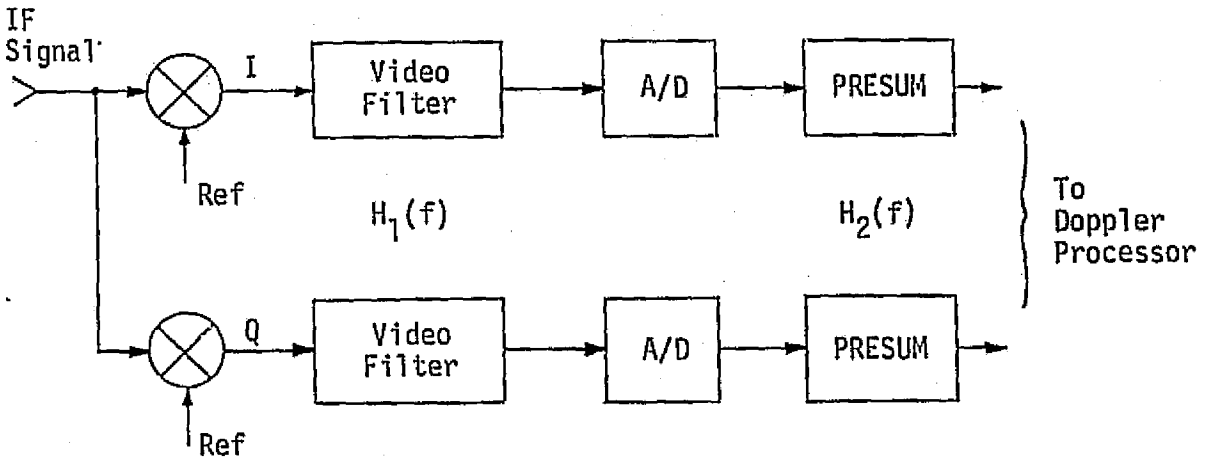

Transfer Functions

Video filter: $|H_1(f)|^2 = \dfrac{1}{1+(f/f_c)^4}$

$f_c = 237$ kHz for $\tau = 2.07$ to 66.4 μsec

$f_c = 4.0$ MHz for $\tau = 0.122$ μsec

Pre-sum: $|H_2(f)|^2 = \dfrac{1}{N}\dfrac{\sin^2 \pi N T_s f}{(\pi T_s f)^2}$

N = number of pulses summed

T_s = sampling interval

$1/T_s = 483$ kHz

Figure 1. Block Diagram and Transfer Function of the Video Signal Processor

The clutter data shown in this addendum is referred to the output of the pre-sum unit and so is the system thermal noise floor. The latter is determined by the bandwidth approximately equal to the inverse of the pulse width and by the system noise temperature in the radar mode.

Table 1 presents the relationship between the pulse width used and the corresponding thermal noise power at the output of the video processor.

Table 1. Thermal Noise Power Versus Pulse Width

Transmitted Pulse Width τ (μsec)	Pre-sum Ratio	Noise Power (dBm)	
		Video	After Pre-sum
0.122	N/A	-96	N/A
2.07	1	-108	-108
4.15	2	-108	-109
8.3	4	-108	-112
16.6	8	-108	-115
33.2	16	-108	-118
66.4	32	-108	-121 (-123 in manual)

Note that, for the short pulse operation, i.e., $\tau = 0.122$ sec, the pre-summer is bypassed. Figures 2 through 8 show the variation of main lobe clutter power P_C as a function of the incidence angle θ (angle off nadir) and pulse width τ. Figure 2 is for video filter output $P_C(\theta)$ and P_n. Figures 3 through 8 refer $P_C(\theta)$ and P_n to the pre-sum output.

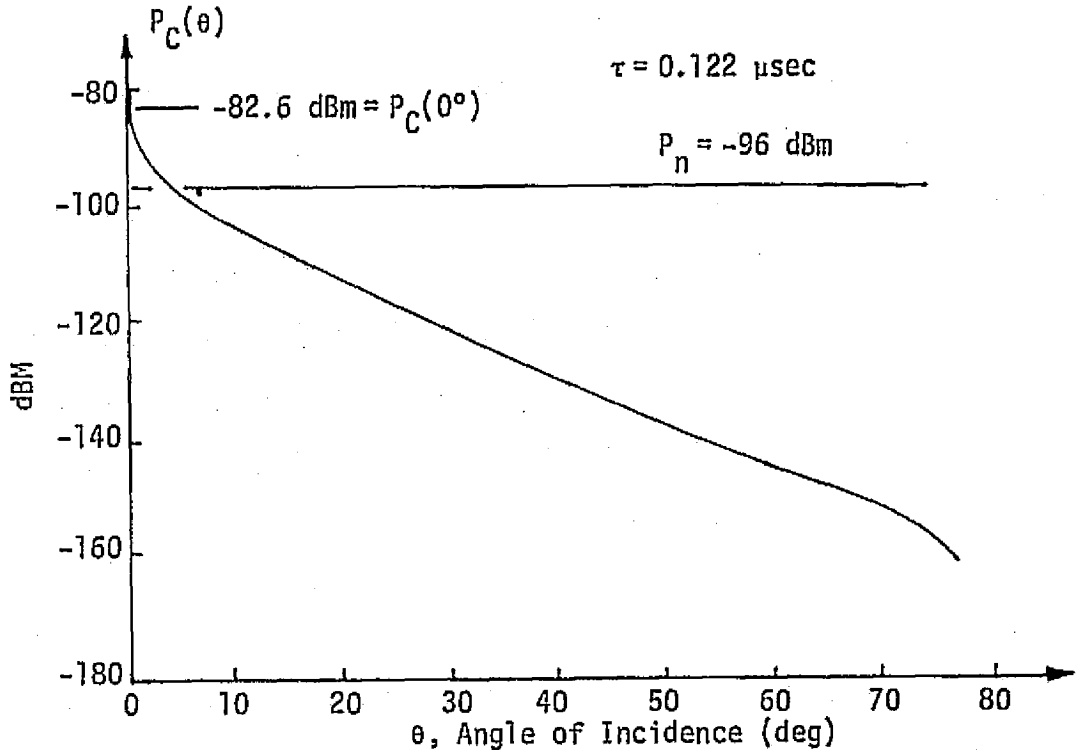

Figure 2. Ground Clutter Versus θ for $\tau = 0.122$ μsec

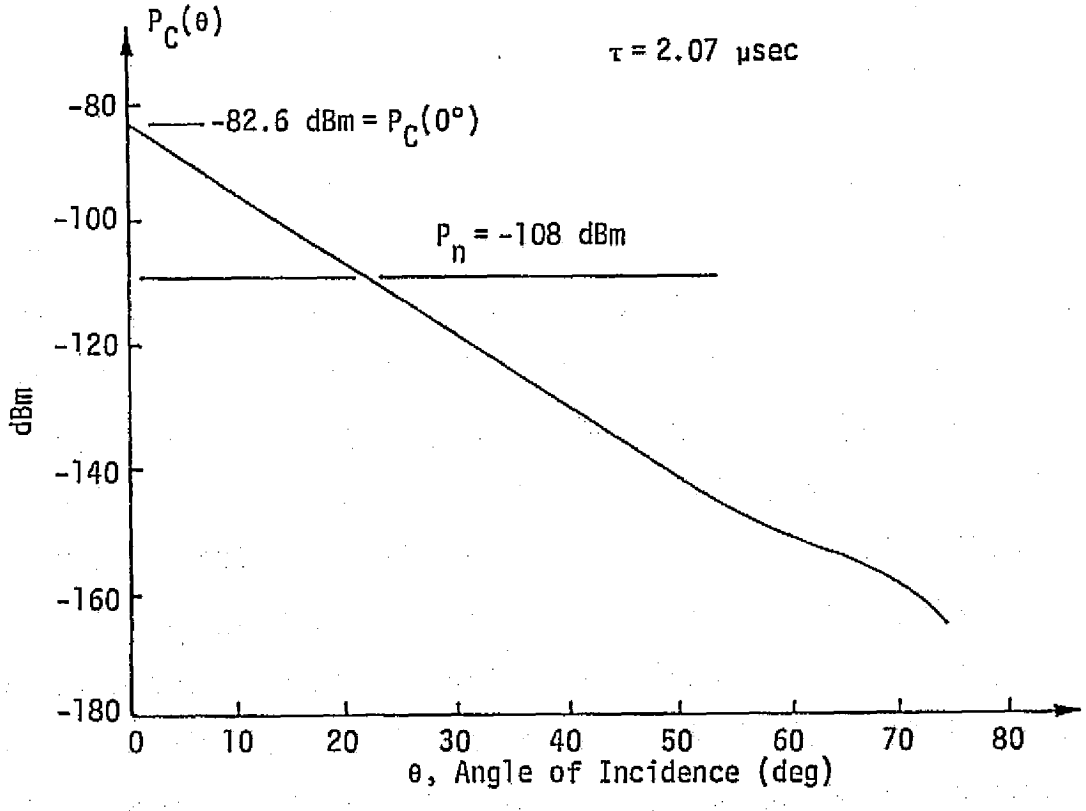

Figure 3. Ground Clutter Versus θ for $\tau = 2.07$ μsec

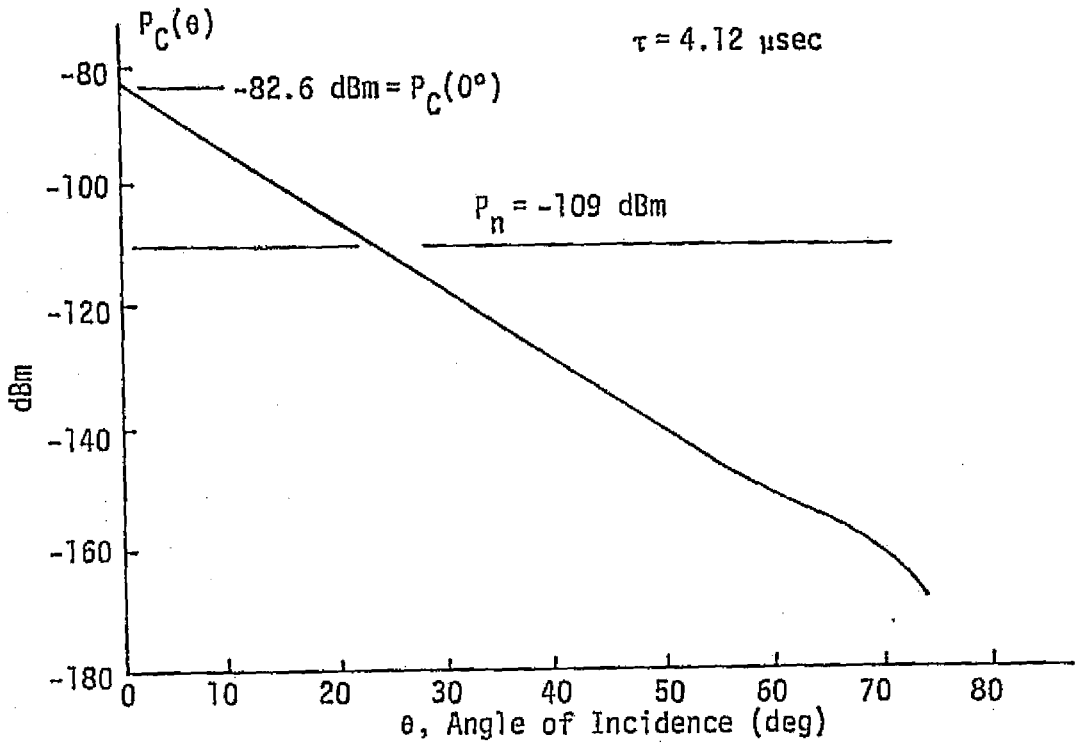

Figure 4. Ground Clutter Versus θ for $\tau = 4.12$ μsec

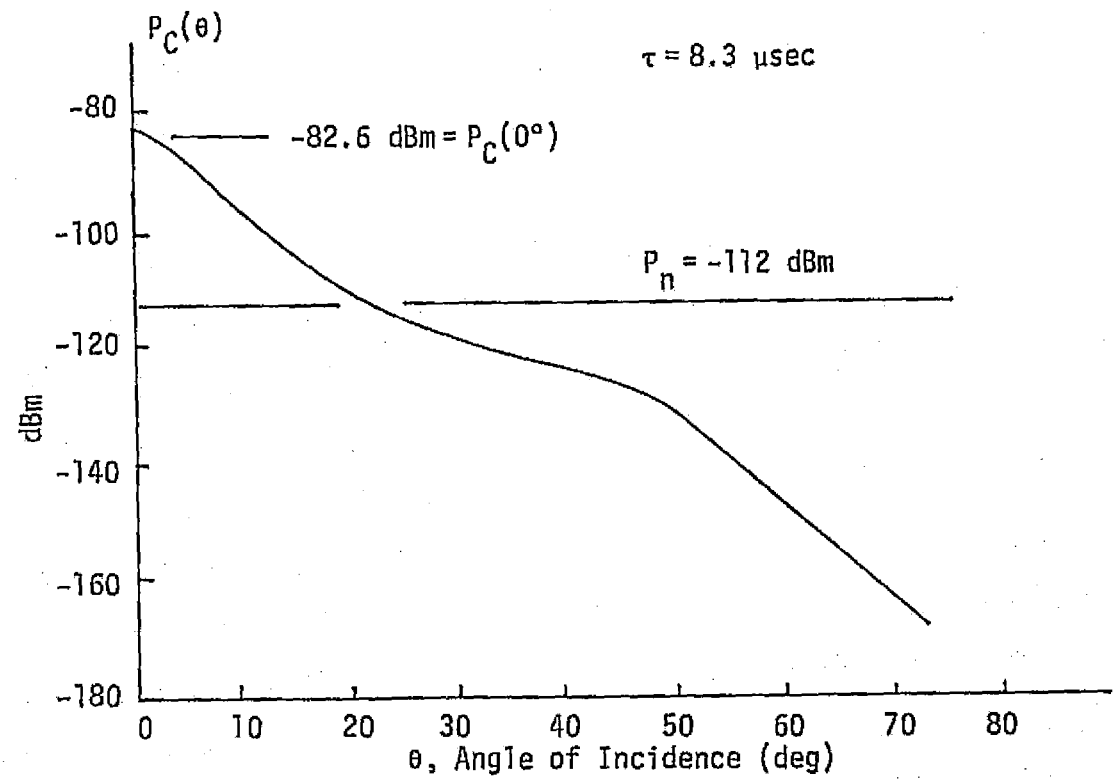

Figure 5. Ground Clutter Versus θ for $\tau = 8.3$ μsec

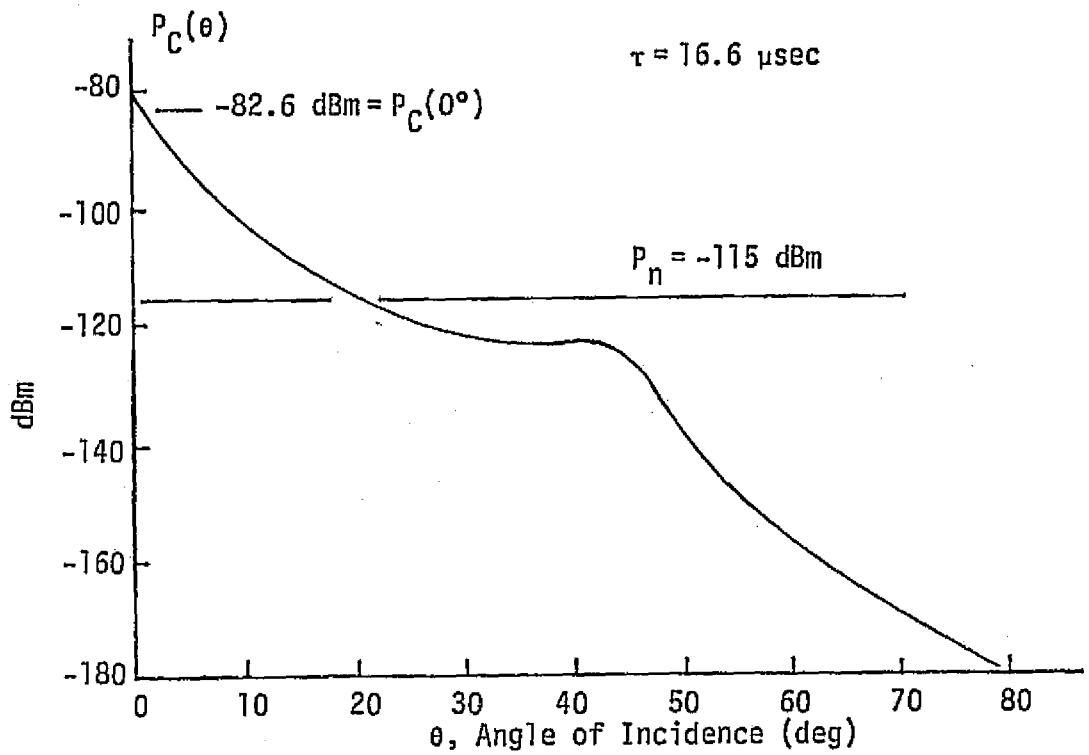

Figure 6. Ground Clutter Versus θ for $\tau = 16.6$ μsec

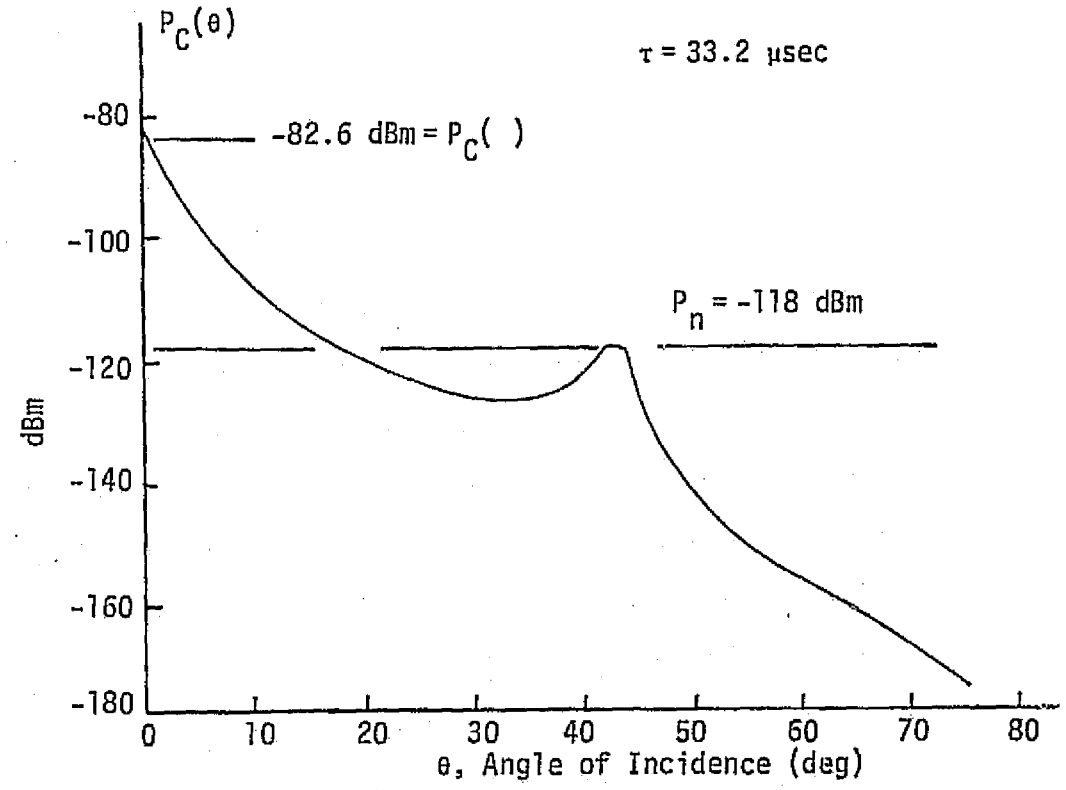

Figure 7. Ground Clutter Versus θ for $\tau = 33.2$ μsec

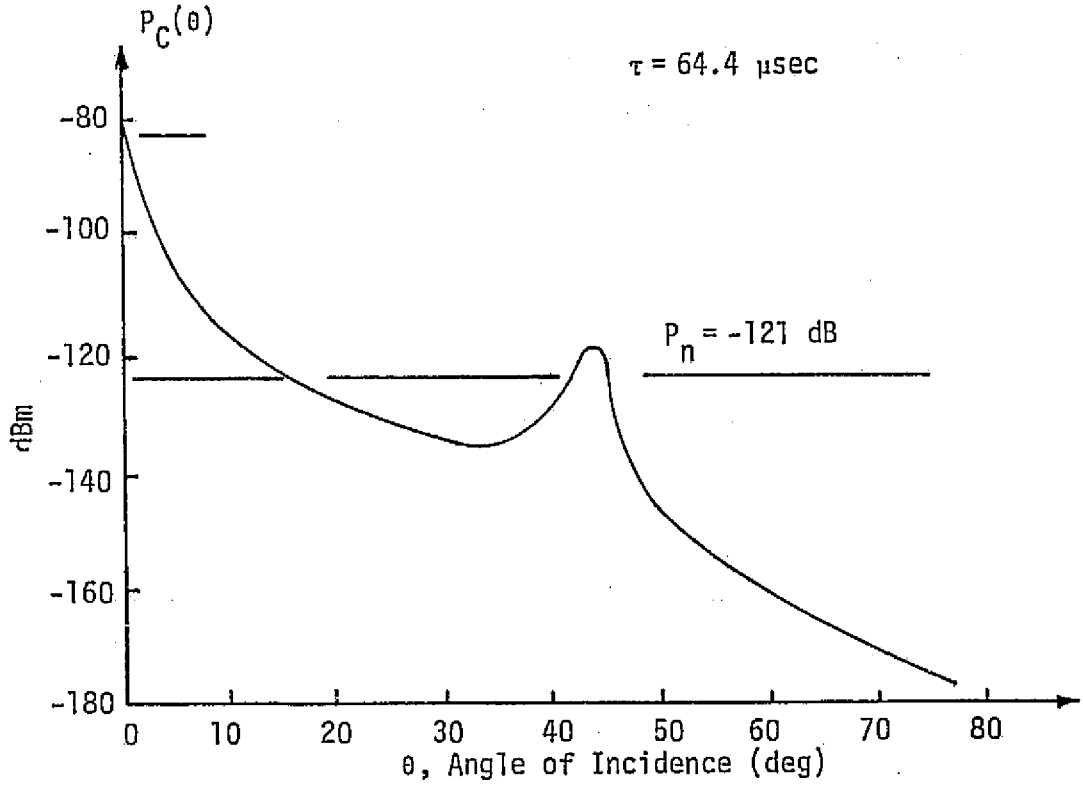

Figure 8. Ground Clutter Versus θ for $\tau = 64.4$ μsec

APPENDIX E

RANGING WAVEFORMS FOR SHORT RANGE OPERATION

APPENDIX E

RANGING WAVEFORMS FOR SHORT RANGE OPERATION

by
Waddah Alem

1.0 INTRODUCTION

Several candidates for short range ($R < 3000$ ft) radar waveforms in the Shuttle Ku-band radar are introduced. The basic requirement in choosing any one of these waveforms is its high range resolution accuracy. The range rate accuracies can be achieved by the use of a bank of doppler filters or via the α-β estimator at these short ranges. The ranging waveforms considered here are (1) linear FM signal, (2) short pulse signal, (3) tone ranging signal, and (4) pulse coded signal. The resolution capabilities, as well as the ambiguity functions, of these waveforms are presented and compared.

2.0 AMBIGUITY FUNCTIONS AND ERROR VARIANCES

The ambiguity function of a radar signal is defined in [1-4] as

$$\chi(\tau,\phi) = \int_{-\infty}^{\infty} u(t)\, u^*(t+\tau) \exp\,[-j\,2\pi\,\phi\,t]\, dt\ , \qquad (1)$$

where $u(t)$ is the complex envelope representation of the transmitted signal $s(t) \exp\,[j\theta(t)]$ (Ref. [1]), τ is the time delay between actual reception and anticipated reception, ϕ is the doppler frequency displacement caused by the target radial motion, and (*) denotes the complex conjugate. The properties of the ambiguity functions are well documented in [1,4]. The minimum error variance of the target range σ_R^2 and the target velocity $\sigma_{\dot{R}}^2$ are given in the literature [1,4] as

$$\sigma_R^2 = \frac{c^2}{4(2E/N_0)\,\beta^2} \qquad (2)$$

$$\sigma_{\dot{R}}^2 = \frac{\lambda^2}{4(2E/N_0)\,\alpha^2} \qquad (3)$$

where β is the rms bandwidth and α is the rms time duration; that is,

$$\beta = \frac{(2\pi)^2}{2E} \int_{-\infty}^{\infty} f^2 U(f)\, U^*(f)\, df \tag{4}$$

and

$$\alpha = \frac{(2\pi)^2}{2E} \int_{-\infty}^{\infty} t^2 u(t)\, u^*(t)\, dt . \tag{5}$$

E denotes the received signal energy, ω_0 is the carrier frequency, U(f) is the Fourier transform of u(t), c is the velocity of light in free space and λ is the wavelength. It is shown in [1] that the system that leads to the realization of these error variances is a maximum likelihood receiver composed of a bank of matched filters so that only range ambiguity is the main concern in designing the radar signal.

As seen from (2) and (3), the values of α and β provide an indication of the measurement accuracies in range and range rate, respectively.

3.0 LINEAR FM SIGNALS

Linear FM is a means of achieving pulse compression. The complex baseband representation can be written as

$$u(t) = \frac{1}{\sqrt{T}} \text{rect}\left[\frac{t}{T}\right] e^{j(kt^2)/2}; \qquad |t| < \frac{T}{2}, \tag{6}$$

where T is the pulse duration, k is a constant determining the slope of the FM. The absolute value of k is given by

$$B = \frac{kT}{2\pi} \text{ Hz},$$

where B is the swept frequency band. The ambiguity function of the linear FM signal introduced in (6) is found in [4] to be

$$X[\tau,\phi] = \begin{cases} e^{j\pi\phi\tau}\left(1 - \frac{|\tau|}{T}\right) \dfrac{\sin\left[\pi T\left(1 - \frac{|\tau|}{T}\right)\left(\phi + \frac{k}{2\pi}\tau\right)\right]}{T\left(1 - \frac{|\tau|}{T}\right)\left(\phi + \frac{k}{2\pi}\tau\right)}; & |\tau| \le T \\ 0; \text{ otherwise} \end{cases} \tag{7}$$

Figure 1 illustrates the ambiguity function of a linear FM pulse for TB = 5. It should be noted that more elaborate schemes exist (e.g., VFM) with improved ambiguity function at the expense of an increase in complexity in both the transmitter and the receiver.

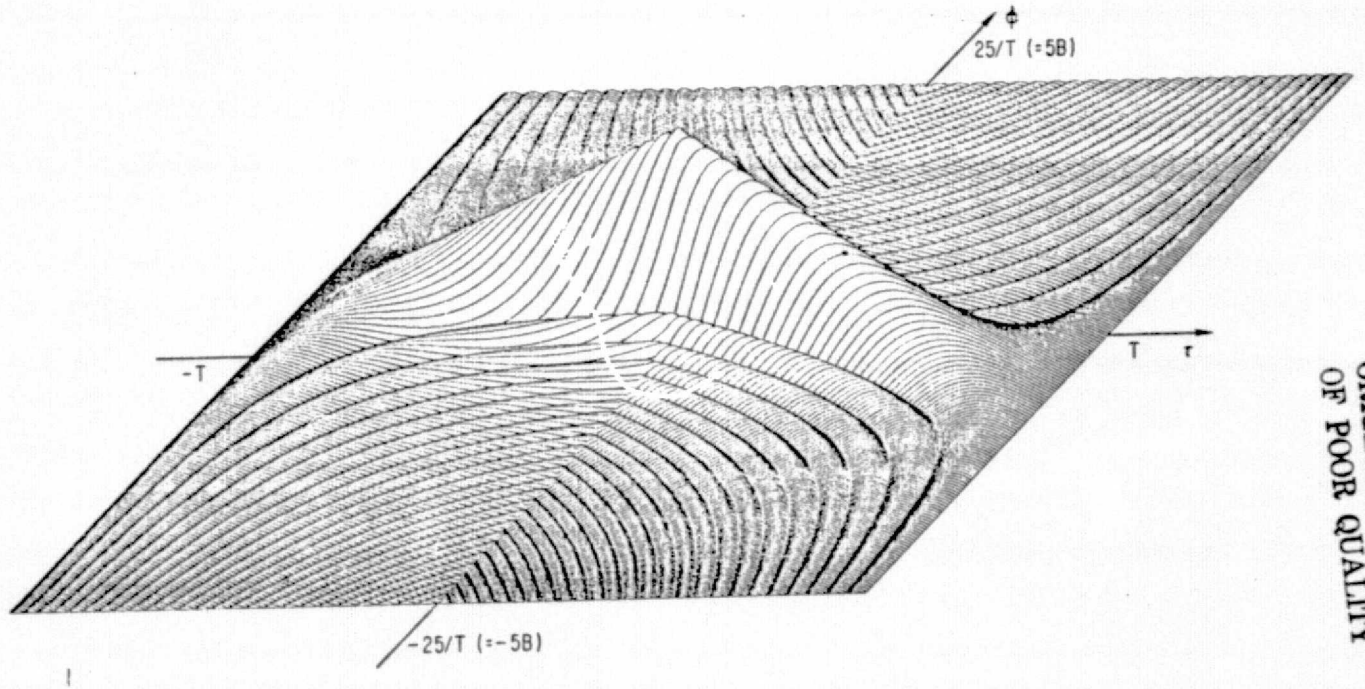

ORIGINAL PAGE IS
OF POOR QUALITY

Figure 1. Linear FM Ambiguity Function for TB = 5

In an actual implementation, a signal

$$s(t) = \cos\left(\omega_0 t + \frac{kt^2}{2}\right); \qquad |t| < \frac{T}{2}, \tag{8}$$

is transmitted and then passed after reception through a matched filter of the form

$$h(t) = A \cos\left[\omega_0 t - \frac{kt^2}{2}\right] \qquad |t| < \frac{T}{2}.$$

If the doppler frequency shift is $\omega_d = 2\pi\phi$, then the output of the filter will be [5]:

$$s_0(\tau,\omega_d) = A \frac{\sin\left[\frac{\omega_d + k\tau}{2}(T - |\tau|)\right]}{\omega_d + k\tau} \cos\left(\omega_0 + \frac{\omega_d}{2}\right)\tau; \quad |\tau| < T. \tag{9}$$

Since at close range the effect of doppler using doppler filters is essentially eliminated, the maximum of $s_0(\tau,0)$ peaks at $\tau = 0$.

Figure 2 compares the response of the output of a matched filter for a rectangular RF pulse and a matched filter for a linear FM rectangular pulse. The compression effect is readily obvious from the figure.*

The only major modification in the Ku-band block diagram is the substitution of the existing pre-summer with a weighted pre-summing. The sample weights are chosen so as to simulate the effect of linear FM matched filtering.

As was indicated in Section 2.0, the rms bandwidth (β) and the rms time duration (α) are indications of range accuracy and doppler accuracy, respectively. For the linear FM signal given in (8), it can be found that the rms bandwidth is given by [6]:

$$\beta^2 = \frac{\frac{k^2}{12} - \frac{k^2 \sin(kT)}{4(kT)} + \frac{k^2 S(kT/2)}{4\pi(kT/\pi)^{3/2}}}{1 + \frac{C(kT/2)}{(kT/\pi)^{1/2}}} \tag{10}$$

*Pulse compression means more energy in a certain time interval which results in more accurate measurement capabilities.

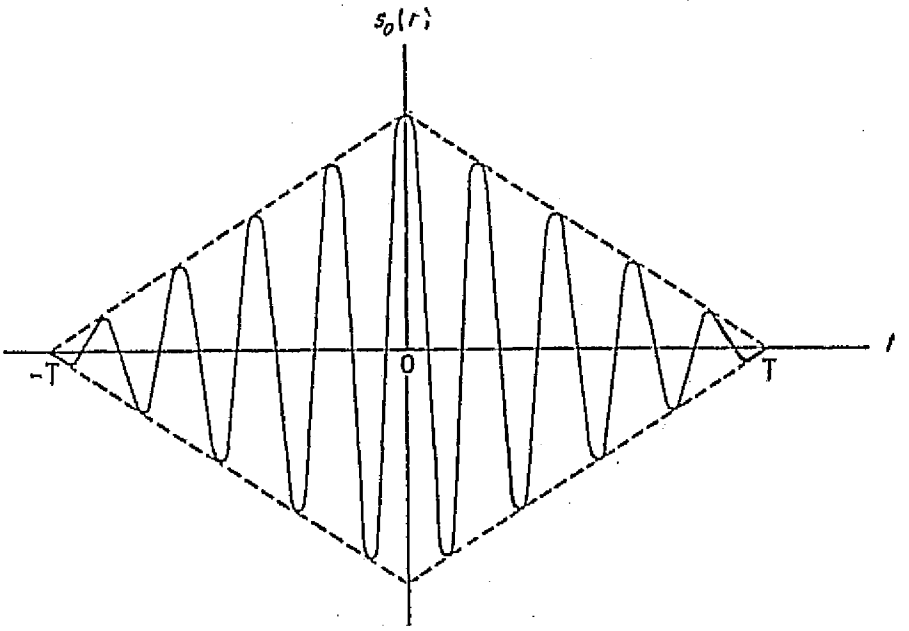

(a) Rectangular Pulse Without FM

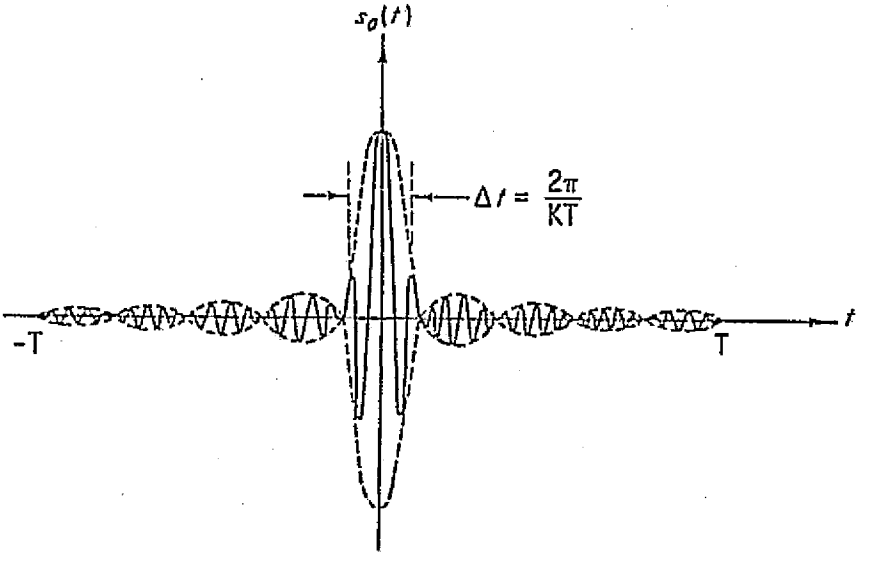

(b) Rectangular Pulse With FM

Figure 2. Compression Effect of Linear FM

where S(t) and C(t) are Fresnel integrals defined as

$$S(z) \triangleq \int_0^z \sin\left(\frac{\pi}{2} t^2\right) dt$$

$$C(z) \triangleq \int_0^z \cos\left(\frac{\pi}{2} t^2\right) dt .$$

For large time-bandwidth product $kT \gg 1$, the value of β^2 is equal to

$$\beta^2 = \frac{k^2}{3} . \tag{11}$$

This results in a minimum mean square error of

$$\sigma_R = \frac{\sqrt{3}\, C}{k(2E/N_0)^{1/2}} . \tag{12}$$

Similarly, for large kT, the minimum mean square velocity error is found to be

$$\sigma_{\dot{R}} = \frac{\lambda}{4} \left(\frac{k}{2\pi T\, E/N_0}\right)^{1/2} .$$

To compare the performance of a linear FM pulse with a rectangular pulse with the same duration T and bandwidth $k/2\pi$, the relation of the rms time errors is computed:

$$\frac{\text{"Rectangular" pulse rms time-error}}{\text{Linear FM pulse rms time-error}} = \frac{\pi}{\sqrt{6}} \left(\frac{kT}{2\pi}\right)^{1/2} . \tag{13}$$

For $kT/2\pi = 400$, the theoretical time error ratio (improvement) is 25.65. When considering a linear FM signal or any other pulse compression as a candidate for close range Shuttle Ku-band radar, the effect of range sidelobes has to be taken into consideration, as well as means of reducing them by various weighting functions [1]. Another effect that should be taken into consideration is the transmitter tube phase ripple (b_t) on the sidelobes. For the TWT used in the Shuttle,

$$b_t = \frac{1}{3} \left(\frac{\Delta V}{V}\right) \theta_\ell ,$$

where $\Delta V/V$ is the voltage ripple ratio and θ_ℓ is the electrical length of the device.

4.0 SHORT PULSE SIGNAL

Since the resolution improves with decreasing the pulse duration, a short pulse should be considered as a candidate at short ranges ($R < 2000$). The main advantage of a short pulse is its simplicity when compared with any other waveform format.

The ambiguity function can be derived from (7) by letting $k = 0$. Thus,

$$\chi(\tau,\phi) = \begin{cases} e^{j\pi\phi\tau} \dfrac{\sin\left[\pi T\left(1 - \dfrac{|\tau|}{T}\right)\right]}{\pi T} ; & |\tau| < T \\ 0 ; \text{ otherwise} \end{cases} \tag{14}$$

The ambiguity function given in (14) is shown in Figure 3.

The output of a matched filter to the RF pulse with zero doppler was shown in Figure 3. Direct application of (4) results in $\beta \to \infty$. This is due to the infinite rise time of the pulse. In actual implementation, the rise time and fall time of the pulse cannot be infinite due to the limited bandwidth; hence, if the bandwidth of the pulse is restricted to be B Hz, while time width is kept approximately equal to T, it is shown in [6] that

$$\beta^2 = \frac{1}{T^2} \frac{\pi B\tau - \sin \pi B\tau}{Si(\pi B\tau) + (\cos \pi B\tau - 1)/\pi B\tau} \tag{15}$$

where

$$Si(z) = \int_0^z \frac{\sin t}{t}\, dt .$$

For large time bandwidth product ($BT >> 1$), the theoretical rms range error can be given as

$$\sigma_R = \frac{C}{4}\left(\frac{T}{B\, E/N_0}\right)^{1/2} . \tag{16}$$

Applying (5) to a perfect squarewave results in a range rate error of

$$\sigma_{\dot{R}} = \frac{\sqrt{3}\,\lambda}{2\pi T\,(2E/N_0)^{1/2}} .$$

For short pulses, the range accuracy improves at the expense of the doppler resolution. However, since in the range rate, resolution is

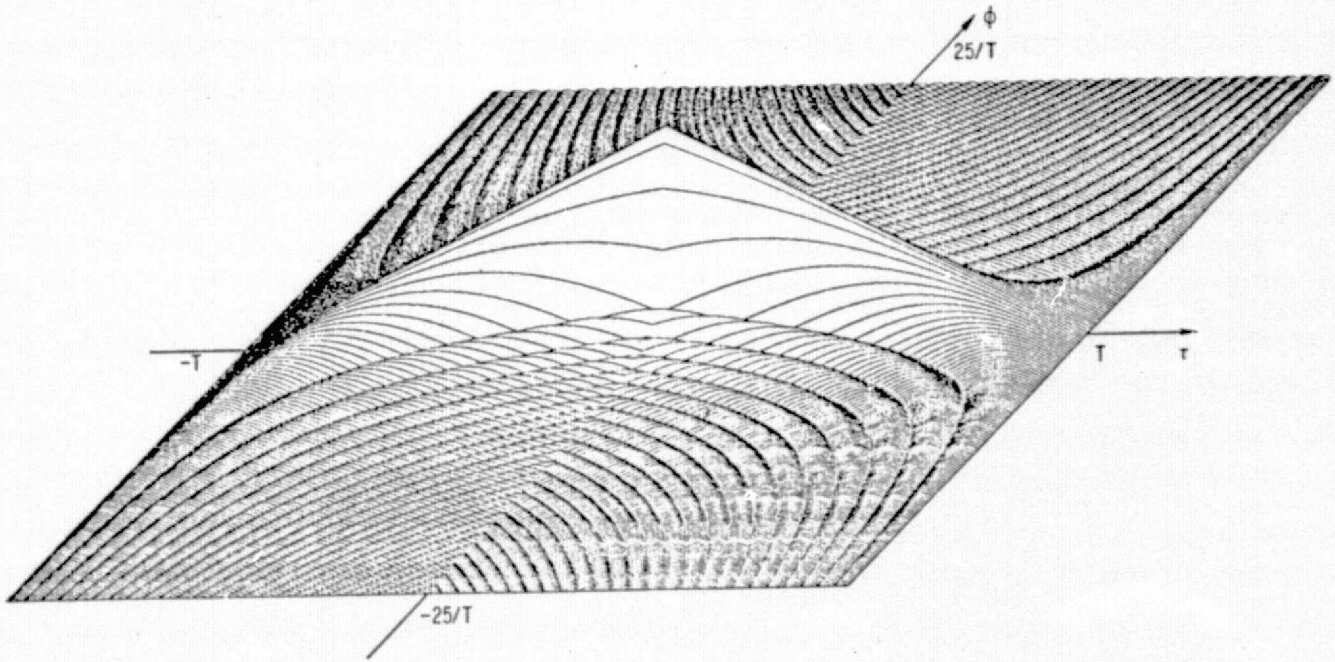

Figure 3. $|\chi(\tau,\phi)|$ of a Constant-Carrier Pulse With a Rectangular Envelope

obtained using a bank of 16 doppler filters and, since the doppler variations are small at close range, a short pulse should be considered as a candidate.

The theoretical rms range error for a pulse with duration T = 0.1 μsec and a time bandwidth product BT = 100 as a function of signal-to-noise ratio per pulse is shown in Table 1.

Table 1. Theoretical RMS Range Error for T = 0.1 μsec, TB = 100

E/N_0 (dB)	-20	-10	0	10	20
σ_R (m)	30	9.49	3	0.95	0.30

5.0 FIXED TONE RANGING SIGNAL

The fixed tone ranging technique consists of transmitting a properly weighted series of N single tone signals so that the lowest tone, which can arbitrarily be called ω_1, satisfies the ambiguity requirement while the accuracy is maintained by the highest tone, ω_N.

The accuracy of fixed tone measurements is derived in [7]. If the average power of the nth tone signal is P_{tn}, then the square of the rms bandwidth β^2 is found to be

$$\beta^2 = \frac{\sum_{n=1}^{N} \omega_n^2 P_{tn}}{P_T} \tag{17}$$

where P_T is the total power in all the N tones.

If the suboptimum receiver shown in Figure 4 is used, then assuming that the period of the lowest tone signal is equal to the maximum expected target delay and that the ratio between two consecutive frequencies is a constant equal to M ($M = \omega_{i+1}/\omega_i > 1$), it is shown [7] that the variance of the range error is given by

$$\sigma_R = \frac{1}{4\pi} \left[\frac{C R_{max}}{P_{tN}/N_0} \frac{2\pi B_N}{\omega_i} \right]^{1/2} \frac{1}{M^{N-1}}, \tag{18}$$

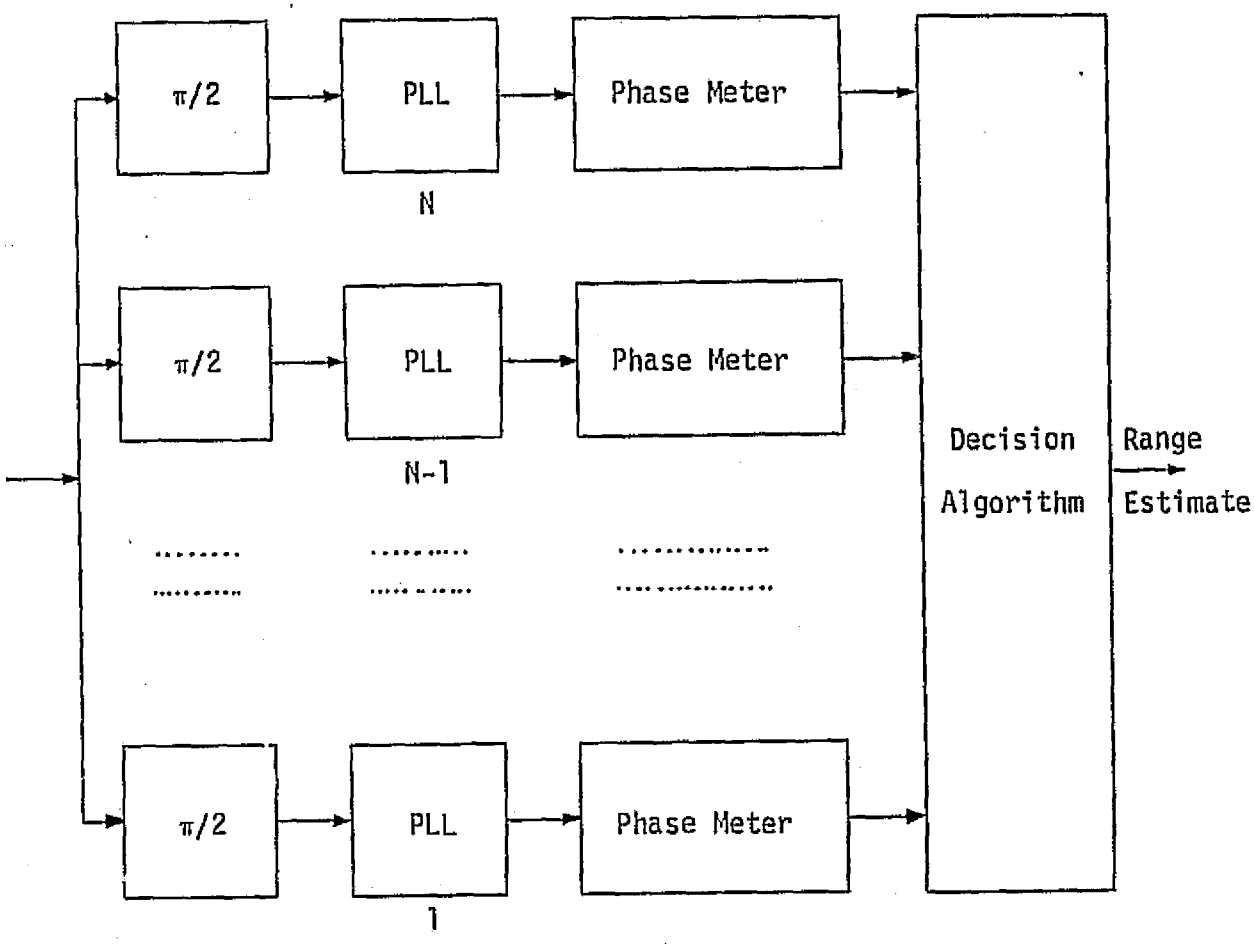

Figure 4. Suboptimal Receiver for Fixed Tone Ranging

where B_N is the loop bandwidth of the highest frequency tone and R_{max} is the maximum expected range.

As is clear from equation (18), the variance of the range is increased with the increase in the number of tones (N) which results in more complicated receivers. The variance also decreases with the increase of the ratio between two consecutive frequencies at the expense of more bandwidth.

The decision algorithm uses all the outputs of the N channels to estimate the range of the target. This is done by tracking the phase of the highest frequency so as to locate the peaks of this sinusoidal waveform within a period of the lowest tone signal. The tracking of the phase of the second highest tone helps eliminate half of the ambiguity of the first measurement by reducing the number of possible ambiguous high frequency peaks by a factor of two. The process is repeated N-1 steps until the ambiguity is completely resolved.

This method is very accurate at the expense of complex hardware implementation. An additional factor that has to be considered if this method is chosen for further study for close range tracking is the necessary acquisition time required by the phase lock loops (PLL) before an estimate can be derived. This might be a major factor in determining the eligibility of this ranging waveform.

6.0 PULSE CODED SIGNAL

Phase coding techniques can be used for pulse compression purposes which, in turn, is a means of improving measurement accuracies. Two candidates are considered, namely, maximal length sequences (pseudonoise) and Barker sequences (perfect sequences). The main purpose of this section is to investigate the possibilities of using these codes and to point out the various problems that have to undergo further study before deciding if a given code can be used as a short ranging waveform.

6.1 Pseudonoise (PN) Sequences

The generation and properties of PN sequences have been discussed in detail in the literature [8,10]. Their application in ranging and radar measurements is found in [1,],7,11]. The most important features about PN sequences from the ranging point of view is that they are easy to generate using linear shift registers with proper tap connections [10]

and their correlation function resembles that of random walk signals for large sequence periods. The period (N) of a PN sequence is given by

$$N = 2^n - 1, \tag{19}$$

where n is the length of the linear shift register.

The autocorrelation function of a PN sequence, averaged over a whole period of the sequence, is shown in Figure 5. The idea behind any PN tracking system is to transmit a PN sequence and then correlate the received target return with a shifted version of the transmitted sequence until the peak in the correlation function is detected. The amount of local PN generator shift is a measure of the range. If the chip time is Δ and the amount of shift is x chips, then the range R is given by

$$R = \frac{c x \Delta}{2}.$$

Since the autocorrelation function of PN sequences is periodic, it is important to have an initial estimate of the range so that the correct peak is detected.

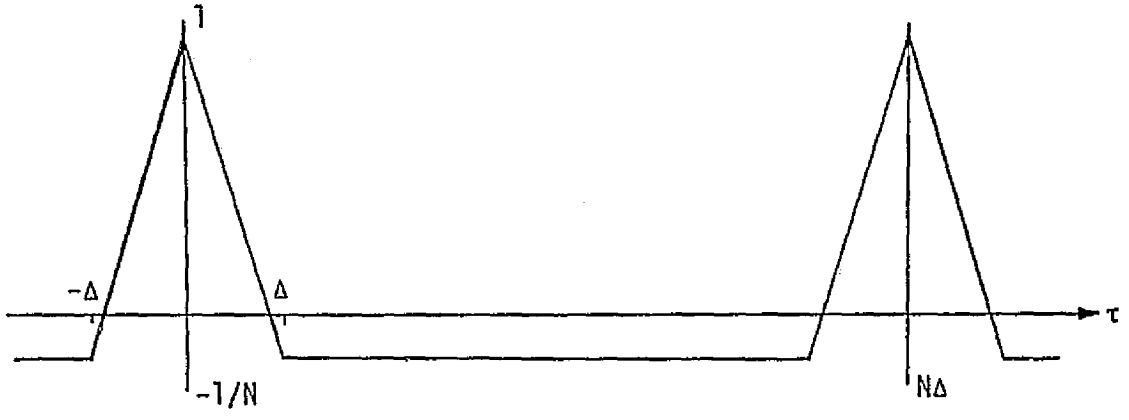

Figure 5. PN Sequence Autocorrelation Function

The ranging capabilities of PN sequences can best be understood by the following analogy. If a CW system is paired to an unmarked yardstick used in measuring distances, then a PN system is paired to a marked yardstick whose marks are the code bits.

The squared magnitude of the ambiguity function of a PN sequence with a period N is given in [11] as

$$|\chi(\tau,\phi)|^2 = \left|\sum_k a_k a_{k+m} \exp\left(\frac{2\pi j}{N}\right)^{k\phi}\right|^2 \qquad (20)$$

$$= N^2 \text{ for } m = 0 \pmod N,\ \phi = 0$$

$$= 1 \text{ for } m \neq 0 \pmod N,\ \phi = 0$$

$$= 0 \text{ for } m = 0 \pmod N,\ \phi \neq 0$$

$$= N+1, \text{ otherwise .}$$

The ambiguity function in (20) peaks at $m = 0 \pmod N$ and $\phi = 0$, which corresponds to accurate range measurement and no doppler.

A possible idealistic block diagram of the tracking system using a PN waveform is shown in Figure 6. In this block diagram, the received signal is mixed down to baseband, then correlated with a delayed version of the same (local) PN code. The delay is adjusted by stepping the local code until a threshold is exceeded, which means that the two codes are brought to within a fraction of a chip time. The switch S is then closed and a tracking loop is used to bring the two codes to within the required range accuracy [12-14]. The range estimate is obtained by recording the amount of delay that the local code has to undergo before it is in complete synchronization with the received code. The thresholds are chosen so as to satisfy certain prespecified probabilities of error along with the examination period [15]. The accuracy in range is related to the mean square error of the tracking system. Expressions for the tracking errors for various systems are given in [12-14]. It is to be noted that, if the chosen examination period is not equal to the code period, the partial autocorrelation function of the code has to be used in the analysis [15].

Two closely related factors have to be considered when analyzing the system in Figure 6:

(1) An initial range estimate (designated range) has to be known to set the initial time delay.

(2) The acquisition time has to be calculated to see if it can be tolerated at close range measurements. This, in turn, is a function of the accuracy of the initial estimate, because as the latter is improved, the amount of possible shifts between the two sequences becomes less and,

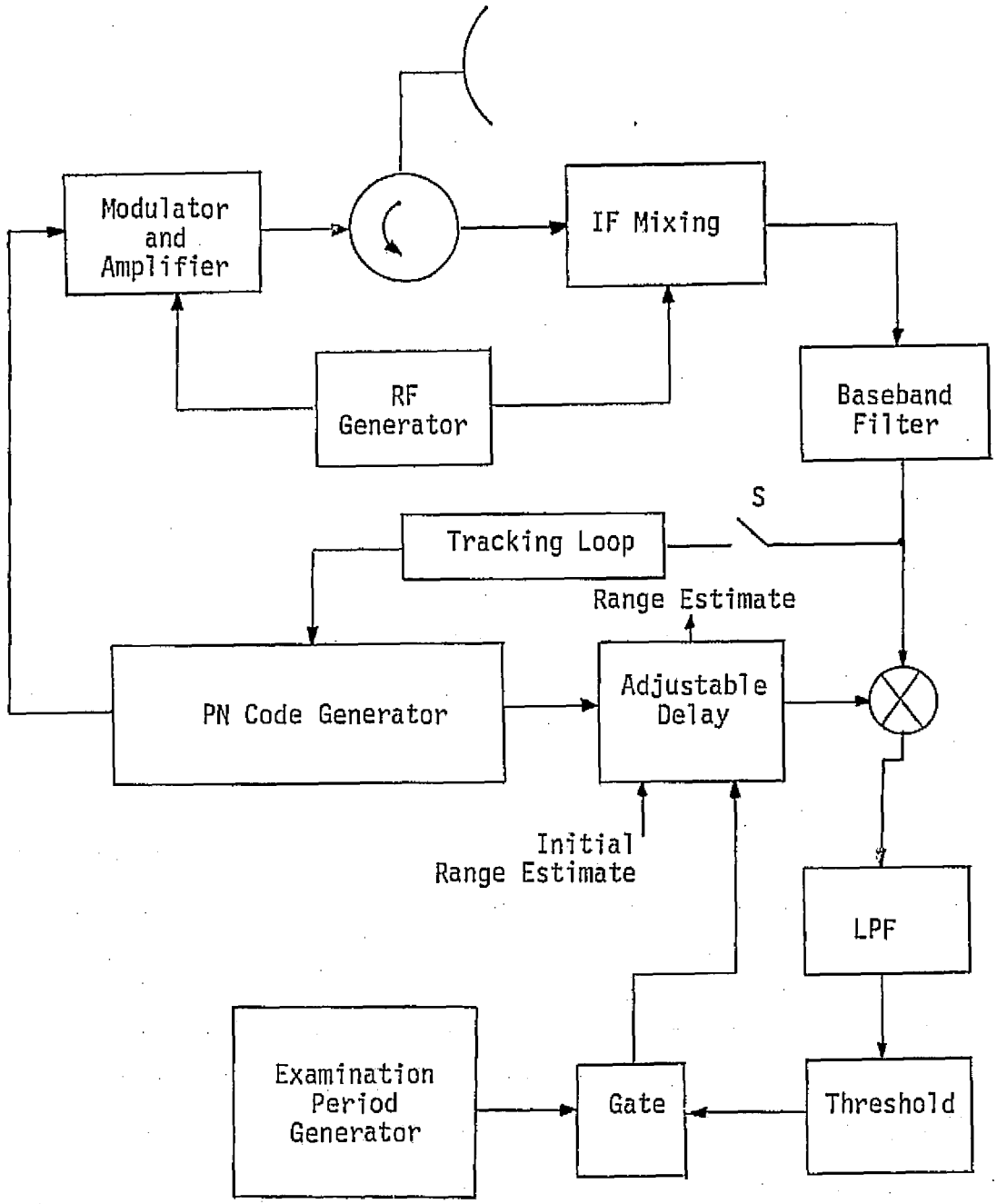

Figure 6. PN Coded Radar Block Diagram

hence, faster acquisition can be expected.

The block diagram in Figure 6 is idealistic. In any actual implementation, the correlation process could be done at the early and late range gates to generate a pair of signals which are fed back after processing to step the local PN generator. Doppler filters have to be used to eliminate the effect of target range rate. Also, the pre-summing has to be modified by proper weights so as to match the PN signal.

As in any other pulse compression system, sidelobe effect has to be analyzed and accounted for. A recursive least square estimate of channel response has been analyzed in [16] to eliminate the sidelobes effect.

6.2 Barker Sequences

The Barker sequences are those whose ambiguity function in the absence of any doppler is characterized by

$$\chi(k,0) = \begin{cases} N; & k = 0 \\ \pm 1, 0; & k \neq 0 \end{cases} \tag{21}$$

There are only 9 Barker sequences known to exist. These sequences are found in the literature [1, 4, 10, 11] and are listed in Table 2 for convenience.

Table 2. Barker Sequences

N	$\{c_n\}$	$\chi(k,0)$; $k = 0,1,\ldots,(N-1)$
2	+ +	2 +
2	- +	2 -
3	+ + -	3 0 -
4	+ + - +	4 - 0 +
4	+ + + -	4 + 0 -
5	+ + + - +	5 0 + 0 +
7	+ + + - - + -	7 0 - 0 - 0 -
11	+ + + - - - + - - + -	11 0 - 0 - 0 - 0 - 0 -
13	+ + + + + - - + + - + - +	13 0 + 0 + 0 + 0 + 0 + 0 +

Barker sequences are called perfect sequences because of the definition of their ambiguity function in absence of doppler. The property that the magnitude of the sidelobes is always less than or equal to unity does not apply when doppler is present [17,18].

Code 13, which is applied in practical systems, has the autocorrelation shown in Figure 7 and the ambiguity function shown in Figure 8 [4].

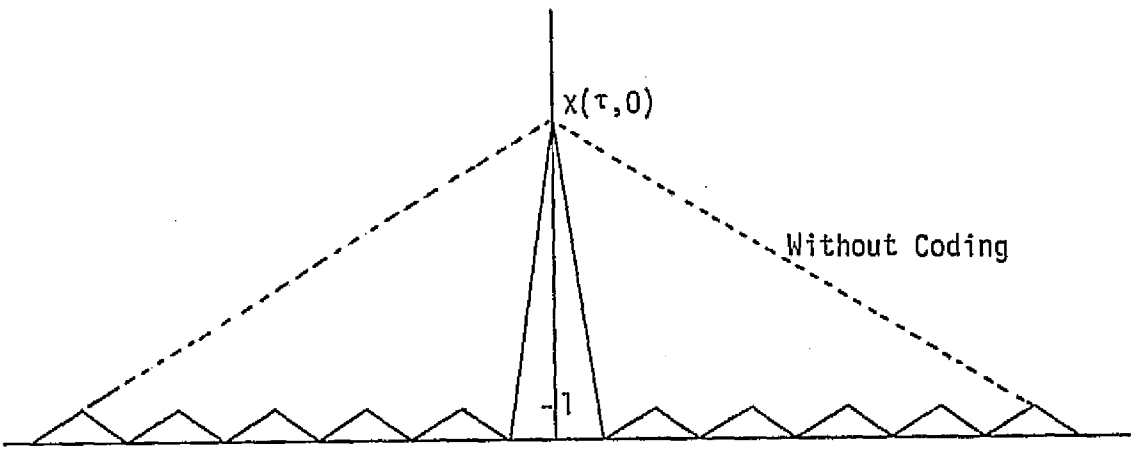

Figure 7. Autocorrelation Function of Barker Code of Length 13

The ambiguity function stresses the fact that the use of phase coding is useless in the presence of excess doppler. However, since in close range tracking, doppler is small and almost negligible, phase coding remains a modulation candidate.

The actual implementation of a Barker code in phase coding a radar signal for tracking purposes is similar to that of PN codes where the received code is correlated with its shifted replica until the peak in the autocorrelation function is detected. The amount by which the local code is shifted is the measure of target range.

7.0 CONCLUSION

In order to choose the best ranging waveform for close range tracking, a rigorous analysis of all the candidates is required. This analysis should take all actual implementation losses into consideration, as well as the resulting complexity of the receiver, before any final selection is made.

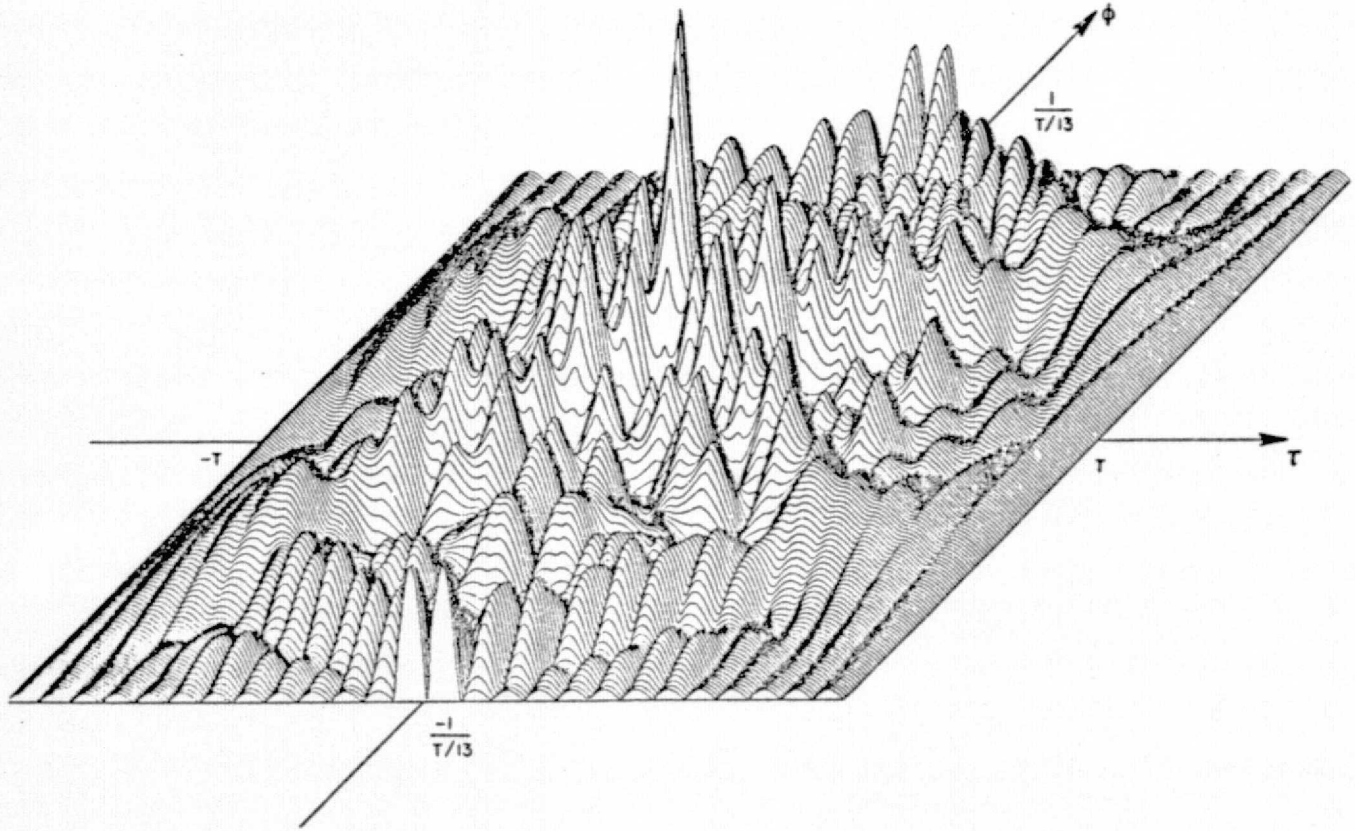

Figure 8. $\chi|(\tau,\phi)|$ for the 13-Element Barker Code

REFERENCES

1. Cook and Bernfeld. Radar Signals, An Introduction to Theory and Applications. Academic Press, New York, 1967.

2. R. S. Berkowitz. Modern Radar - Analysis, Evaluation, and System Design. John Wiley & Sons, New York, 1965.

3. M. Skolnik. Radar Handbook. McGraw-Hill, New York, 1970.

4. A. Rihaczek. Principles of High-Resolution Radar. McGraw-Hill, New York, 1969.

5. J. DiFranco and W. Rubin. Radar Detection. Prentice-Hall, Inc., New Jersey, 1968.

6. M. Skolnik, "Theoretical Accuracy of Radar Measurements," IRE Trans. on Aeronautical and Navigational Electronics, December 1960, pp. 123-129.

7. W. Lindsey and M. Simon. Telecommunication Systems Engineering. Prentice-Hall, Inc., New Jersey, 1973.

8. S. Golomb et al. Digital Communications with Space Applications. Prentice-Hall, Inc., New Jersey, 1964.

9. R. C. Dixon. Spread Spectrum Systems. Wiley, New York, 1976.

10. S. Golomb. Shift Register Sequences. Holden Day, San Francisco, 1967.

11. F. E. Nathanson. Radar Design Principles, Signal Processing and the Environment. McGraw-Hill Co., New York, 1969.

12. W. Alem, "Integrated Source and Channel Encoded Digital Communication System Design Study," Appendixes B, C and D, Axiomatix Report No. R7704-1, April 13, 1977.

13. W. J. Gill, "A Comparison of Binary Delay Lock Loop Implementations," IEEE Trans. Aerospace and Electronic Systems, Vol. AES-2, July 1966, pp. 415-424.

14. H. P. Hartman, "Analysis of Dithering Loop for PN Code Tracking," IEEE Trans. Aerospace and Electronic Systems, Vol. AES-10, No. 1, January 1974.

15. W. Alem, "Advanced Techniques for Direct Sequence Spread Spectrum Acquisition," Ph.D. Dissertation, Department of Electrical Engineering, University of Southern California, February 1977.

16. E. D. Mese and D. Giuli, "Optimal Recursive Processing in Phase-Coded Waveform Radar," IEEE Trans. Aerospace and Electronic Systems, Vol. AES-13, No. 2, March 1977.

17. S. W. Golomb and R. A. Scholtz, "Generalized Barker Sequences," IEEE Trans. Information Theory, Vol. IT-11, 1965, pp. 533-537.

18. R. M. Lerner, "Signals With Uniform Ambiguity Functions," 1958 IRE Intern. Conv. Record, Pt. IV, pp. 27-36.

APPENDIX F

MAXIMUM LIKELIHOOD ESTIMATION OF THE RATIO OF POWERS IN TWO NARROWBAND PROCESSES

APPENDIX F

MAXIMUM LIKELIHOOD ESTIMATION OF THE RATIO OF POWERS IN TWO NARROWBAND PROCESSES

by

Charles L. Weber

ABSTRACT

The maximum likelihood estimate of the ratio of the power in two narrowband processes is developed. Its RMS error is determined.

The estimate of this ratio is used in all radar tracking loops of the Space Shuttle Ku-band integrated rendezvous radar/communication system.

1.0 INTRODUCTION

In this report, we consider the maximum likelihood (M.L.) estimate of the ratio of the power in two narrowband processes. These processes are assumed to be Gaussian and, in general, will be correlated. The in-phase and quadrature-phase components of each process are sampled N times, where the time between samples is assumed to be large enough so that the samples are statistically independent.

The estimate of this ratio and its performance play a fundamental role for all types of tracking in the radar described in [1].

2.0 THE MAXIMUM LIKELIHOOD ESTIMATE OF POWER RATIO

Consider the narrowband Gaussian process u(t), which we describe as

$$u(t) = u_c(t) \cos \omega_0 t + u_s(t) \sin \omega_0 t \ , \tag{1}$$

where $u_c(t)$ and $u_s(t)$ are baseband, zero mean, stationary, and Gaussian random processes.

The in-phase and quadrature-phase samples of u(t) are represented as the real and imaginary components of a sequence of complex Gaussian random variables, namely,

$$U_i = u_{ci} + j u_{si} \ , \qquad i = 1,\ldots,N \ . \tag{2}$$

The expected value of $|U_i|^2$ is denoted by

$$P_U = E[|U_i|^2] = E[u_{ci}^2 + u_{si}^2] \qquad \text{for all } i \ , \tag{3}$$

which is twice the average power in u(t), $u_c(t)$, and $u_s(t)$. Equivalently,

$$E[u^2(t)] = E[u_c^2(t)] = E[u_s^2(t)] = \frac{P_U}{2} \ . \tag{4}$$

The same notation can be established for the other narrowband Gaussian process,

$$v(t) = v_c(t) \cos \omega_0 t + v_s(t) \sin \omega_0 t \ ,$$

with average power $P_V/2$.

With this notation, we can restate the estimation problem as follows:

Let $\underline{U}$ and $\underline{V}$ be N-dimensional complex Gaussian vectors whose N complex components U_i, V_i $(i=1,\ldots,N)$ have magnitudes and phases equal to the magnitudes and phases of a sequence of statistically independent samples of the narrowband processes $u(t)$ and $v(t)$, respectively.

Given these observations, the maximum likelihood estimate of P_U/P_V and $\ln(P_U/P_V)$ are desired, as well as the RMS error of the estimates.

In Addendum A, we show that the M.L. estimate of $\ln(P_U/P_V)$ is given by

$$\widehat{\ln [P_U/P_V]} = \ln \widehat{[P_U/P_V]} = \ln \left[\frac{||\underline{U}||^2}{||\underline{V}||^2} \right] \tag{5}$$

where

$$||\underline{U}||^2 \triangleq \sum_{i=1}^{N} |U_i|^2 \tag{6}$$

and

$$||\underline{V}||^2 \triangleq \sum_{i=1}^{N} |V_i|^2 . \tag{7}$$

The estimator in (5) says that the M.L. estimate of $\ln(P_U/P_V)$ is equal to the natural logarithm of the M.L. estimate of P_U/P_V. In Addendum A, this is shown to be the case for any strictly monotonically increasing function of the estimate.

3.0 STATISTICAL CHARACTERISTICS OF THE OBSERVATIONS

At time t_i, when the $\underline{i}$th sample of $u_c(t)$, $u_s(t)$, $v_c(t)$, and $v_s(t)$ are observed, the covariance matrix of the resulting four-dimensional Gaussian vector will be of the form

$$M_4 = \left[\begin{array}{cc:cc} P_U/2 & a & c & d \\ a & P_U/2 & -d & c \\ \hdashline c & -d & P_V/2 & b \\ d & c & b & P_V/2 \end{array}\right] . \tag{8}$$

In Addendum B, the statistical characteristics of two narrowband Gaussian processes are considered. In particular, it is shown that the

narrowband processes u(t) and v(t) that are observed in each of the tracking modes of the radar are "spherically symmetric." The physical meaning of a spherically symmetric random process is also described in Addendum B. The result is that $a = b = 0$ in (8). In addition, the conditions under which $d = 0$ are also enumerated, and it is noted that these conditions are met by the narrowband processes u(t) and v(t).

The covariance matrix M_4 in (8) therefore simplifies to

$$M_4 = \left[\begin{array}{cc:cc} P_U/2 & 0 & c & 0 \\ 0 & P_U/2 & 0 & c \\ \hdashline c & 0 & P_V/2 & 0 \\ 0 & c & 0 & P_V/2 \end{array}\right] . \tag{9}$$

With this covariance matrix, all in-phase components are statistically independent of all quadrature components. As a result, each complex sample of u(t) and v(t) can be interpreted as two consecutive real samples.

Stated equivalently, the observations can be thought of as 2N independent samples of the real baseband Gaussian processes $u_c(t)$ and $v_c(t)$, where these zero mean processes for each sample have covariance matrix

$$M_2 = \begin{bmatrix} P_U/2 & c \\ c & P_V/2 \end{bmatrix} , \quad i = 1,\ldots,2N . \tag{10}$$

The maximum likelihood estimate of P_U/P_V is now given by

$$\widehat{P_U/P_V} \triangleq x_a^2 = \frac{\sum_{i=1}^{2N} u_{ci}^2}{\sum_{k=1}^{2N} v_{ck}^2} . \tag{11}$$

The performance of this estimator, as well as $z = \ln \widehat{P_U/P_V}$ is developed in the next section.

4.0 PERFORMANCE OF M.L. ESTIMATE OF POWER RATIO

In order to develop most directly the pdf of x_a defined in (11), the following notation is used.

The normalized correlation between u_{ci} and v_{ci} is given by

$$\rho = \frac{2c}{\sqrt{P_U P_V}} , \quad |\rho| \leq 1 . \tag{12}$$

The inverse of the covariance matrix M_2 is denoted as

$$W_2 \triangleq M_2^{-1} = \begin{bmatrix} w_{11} & w_{12} \\ w_{12} & w_{22} \end{bmatrix} . \tag{13}$$

With this notation, the pdf of x_a in (11) is given by ([2, p. 50] or [5]):

$$q(x_a) = \frac{2\,[\det\,(W_2)]^{n/2}\, x_a^{n-1}\, [w_{11}\, x_a^2 + w_{22}]}{B\left(\frac{n}{2}, \frac{n}{2}\right)\left[(w_{11}\, x_a^2 + w_{22})^2 - (2\, x_a\, w_{12})^2\right]^{(n+1)/2}} , \tag{14}$$

where

$$n = \text{total number of independent samples} = 2N \tag{15}$$

$$B(\alpha,\beta) = \text{Beta Function} \triangleq \frac{\Gamma(\alpha)\,\Gamma(\beta)}{\Gamma(\alpha+\beta)} \tag{16}$$

$$\Gamma(\alpha) = \text{Gamma Function} = (\alpha-1)! \text{ if } \alpha \text{ is an integer} \tag{17}$$

$$\det W_2 = \text{determinant of } W_2 . \tag{18}$$

Substituting (12), (13) and (15) through (18) into (14), the pdf of x_a can be written as

$$q(x_a) = \frac{2\left[\sigma_U^2\,\sigma_V^2\,(1-\rho^2)\right]^{-N} x_a^{2N-1}\left[\dfrac{x_a^2}{\sigma_U^2\,(1-\rho^2)} + \dfrac{1}{\sigma_V^2\,(1-\rho^2)}\right]}{\dfrac{[(N-1)!]^2}{(2N-1)!}\left[\left(\dfrac{x_a^2}{\sigma_U^2\,(1-\rho^2)} + \dfrac{1}{\sigma_V^2\,(1-\rho^2)}\right)^2 - \left(\dfrac{2\,x_a\,\rho}{\sigma_U\,\sigma_V\,(1-\rho^2)}\right)^2\right]^{(2N+1)/2}} \tag{19}$$

where $\sigma_U^2 = P_U/2$, $\sigma_V^2 = P_V/2$. (20)

The estimate of P_U/P_V is

$$\widehat{P_U/P_V} \triangleq z_a = x_a^2 \ . \tag{21}$$

Carrying out this transformation,

$$z_a = x_a^2$$

$$d z_a = 2 x_a \, d x_a \ .$$

The Jacobian of the transformation is

$$|J| = \frac{1}{2\sqrt{z_a}}$$

and the pdf of z_a, after some algebraic manipulation, is given by

$$p(z_a) = \frac{(2N-1)! \left[\frac{\sigma_U^2}{\sigma_V^2}\right]^N (1-\rho^2)^N z_a^{N-1} \left(z_a + \frac{\sigma_U^2}{\sigma_V^2}\right)}{[(N-1)!]^2 \left[\left(z_a + (\sigma_U^2/\sigma_V^2)(1-2\rho^2)\right)^2 + 4(\sigma_U/\sigma_V)^4 \rho^2 (1-\rho^2)\right]^{N+\frac{1}{2}}} \ . \tag{22}$$

The form of this pdf can be substantially simplified if we normalize z_a by setting

$$z_a \triangleq \frac{P_U}{P_V} x \ . \tag{23}$$

Then,*

$$p(x) = A \frac{(x+1) x^{N-1}}{[(x+1)^2 - 4\rho^2 x]^{N+\frac{1}{2}}} \ , \tag{24}$$

where

$$A = (1-\rho^2)^N (2N-1)! \Big/ [(N-1)!]^2 \ . \tag{25}$$

The performance of the estimate of

$$\widehat{\ln P_U/P_V} = \ln \widehat{P_U/P_V} = z = \ln z_a \triangleq \ln (P_U/P_V) + \ln x \tag{26}$$

*The pdf of p(x) in (24) agrees exactly with that developed in [1, p. C-9].

is evaluated by determining the RMS error.

The first moment is initially evaluated and is given by

$$E\left[\widehat{\ln (P_U/P_V)}\right] = \ln (P_U/P_V) + E(\ln x) . \tag{27}$$

By making the change of variable $x = e^y$,

$$E\left[(\ln x)^k\right] = A\int_0^\infty \frac{(\ln x)^k (x+1)\, x^{N-1}\, dx}{[(x+1)^2 - 4\rho^2 x]^{N+\frac{1}{2}}}$$

$$= 2A\int_{-\infty}^{\infty} \frac{y^k \cosh (y/2)}{[2\cosh y + 2 - 4\rho^2]^{N+\frac{1}{2}}}\, dy . \tag{28}$$

When $k = 1$ in (28), the integrand is an odd function over even limits and therefore vanishes. Hence,

$$E\left(\widehat{\ln P_U/P_V}\right) = \ln (P_U/P_V) \tag{29}$$

and $\widehat{\ln P_U/P_V}$ is an unbiased estimate of $\ln (P_U/P_V)$.

The variance of error is

$$\text{Var}\left[\widehat{\ln P_U/P_V}\right] \triangleq \sigma_z^2 = E\{[\ln x]^2\}. \tag{30}$$

Letting $k = 2$ in (28),*

$$\sigma_z^2 = E[(\ln x)^2] = 4A\int_0^\infty \frac{y^2 \cosh (y/2)}{[2\cosh y + 2 - 4\rho^2]^{N+\frac{1}{2}}}\, dy$$

$$= 2A\int_0^\infty \frac{y^2 [1 + e^{-y}]\, e^{-Ny}}{[e^{-2y} + (2 - 4\rho^2)\, e^{-y} + 1]^{N+\frac{1}{2}}}\, dy . \tag{31}$$

This integral has been numerically computed. The results are illustrated in Figure 1. The computed values of the rms error, σ_z, agree with the results shown in [1, p. B-4].

*Equation (31) agrees with the performance result in [1, p. C-10].

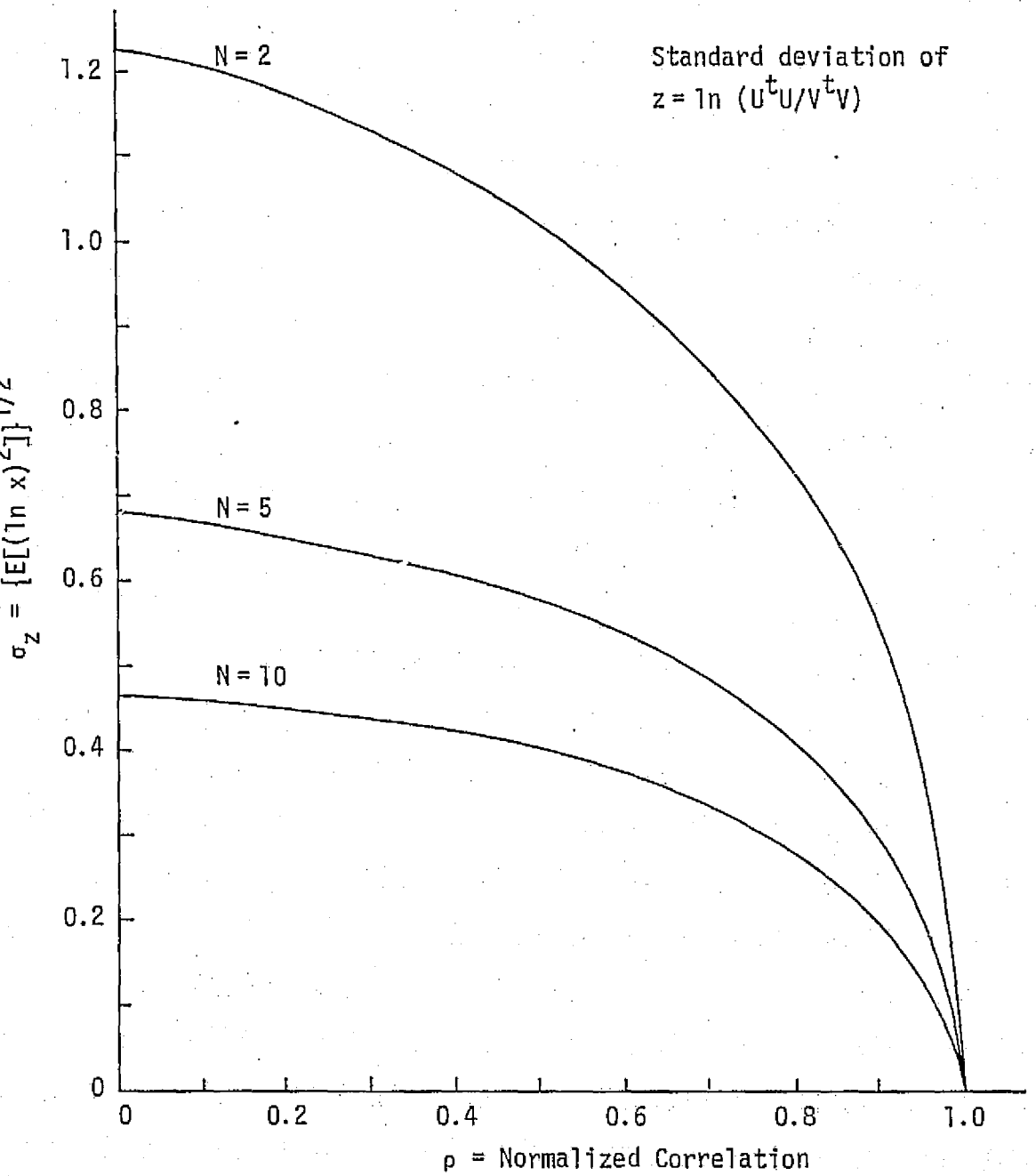

Figure 1. Standard Deviation of the Random Variable z as a Function of Correlation

REFERENCES

1. "Space Shuttle Ku-Band Integrated Rendezvous Radar/Communications System Study," Hughes Aircraft Co., Report No. D4148 SCG60041R, for NASA-JSC under Contract NAS 9-14595, March 1976.

2. K. S. Miller, Multidimensional Gaussian Distributions, Wiley, 1964.

3. K. S. Miller, Complex Stochastic Processes, Addison-Wesley, 1974.

4. T. L. Grettenberg, "A Representation Theorem for Complex Normal Processes," IEEE Trans. on Info. Theory, Vol. IT-11, No. 2, April 1965, pp. 305-306.

5. J. Omura and T. Karlath, "Some Useful Probability Distributions," Stanford Electronics Lab Report 7050-6, September 1965.

6. H. Cramer, Mathematical Methods of Statistics, Princeton Press, 1946.

7. C. M. Thomas, "Maximum Likelihood Estimation of Signal-to-Noise Ratio," Ph.D. Dissertation, Department of Electrical Engineering, University of Southern California, June 1967.

ADDENDUM A

MAXIMUM LIKELIHOOD ESTIMATE OF POWER RATIO

MAXIMUM LIKELIHOOD ESTIMATE

The maximum likelihood estimate of the ratio of power in two complex Gaussian vectors is developed. If $\underline{U}$ and $\underline{V}$ are random vectors and α is a parameter of the probability density function (pdf), $p(\underline{U},\underline{V};\alpha)$, then the M.L. estimate of α is defined as that α which is

$$\max_{\alpha} p(\underline{U},\underline{V};\alpha) \triangleq p(\underline{U},\underline{V};\hat{\alpha}) \quad . \tag{A-1}$$

If the pdf is unimodal, then $\hat{\alpha}$ is that α which is the solution to

$$\frac{\partial\, p\,(\underline{U},\underline{V};\alpha)}{\partial\alpha} = 0 \tag{A-2}$$

or equivalently, that α which is the solution to

$$\frac{\partial \ln p(\underline{U},\underline{V};\alpha)}{\partial\,\alpha} = 0 \; . \tag{A-3}$$

If there is more than one unknown parameter, whether or not it is to be estimated, the M.L. estimate is given by the following. Suppose α and β are unknown parameters and α is to be estimated. The M.L. estimate for α and β is formed by simultaneously solving [6-7] the following:

$$\frac{\partial \ln p(\underline{U},\underline{V};\alpha,\beta)}{\partial\,\alpha} = 0$$

$$\frac{\partial \ln p(\underline{U},\underline{V};\alpha,\beta)}{\partial\,\beta} = 0 \tag{A-4}$$

for α and β. The solutions are the M.L. estimates for α and β. If only one of the parameters is to be estimated, the estimate does not change.

We also note that: <u>The maximum likelihood estimate of any strictly monotonically increasing function of a parameter is equal to that same function of the M.L. estimate of the parameter</u>.

For example, if we have $p(\underline{U};\alpha)$, and we desire the M.L. estimate of

$$\gamma = \ln \alpha , \tag{A-5}$$

then we form

$$\frac{\partial\, p(\underline{U},e^{\gamma})}{\partial\, \gamma} = 0 \tag{A-6}$$

and solve for $\hat{\gamma}$. By the chain scale for differentiation, however,

$$\frac{\partial\, p(\underline{U},e^{\gamma})}{\partial\, \gamma} = \frac{\partial\, p(\underline{U},\alpha)}{\partial\, \alpha}\,\frac{\partial\, \alpha}{\partial\, \gamma} . \tag{A-7}$$

Since

$$\frac{\partial\, \alpha}{\partial\, \gamma} = e^{\gamma} > 0 \quad \text{for all } \gamma , \tag{A-8}$$

the only way (A-7) can equal zero is for

$$\frac{\partial\, p(\underline{U},\alpha)}{\partial\, \alpha} = 0 , \tag{A-9}$$

since e^{γ} never vanishes.

Therefore, when determining the M.L. estimate of $\ln (P_U/P_V)$, we need only consider the M.L. estimate of P_U/P_V.

THE MAXIMUM LIKELIHOOD ESTIMATE OF POWER RATIOS

The M.L. estimate of power ratios is developed in steps. Consider first real uncorrelated Gaussian samples. The pdf $p(\underline{U},\underline{V})$ is given by

$$p(\underline{U},\underline{V}) = \left[\frac{1}{\sqrt{2\pi}\,\sigma_{\underline{U}}}\right]^{N} \exp\left[\frac{-1}{2\,\sigma_{u}^{2}}\,||\underline{U}||^{2}\right]\left[\frac{1}{\sqrt{2\pi}\,\sigma_{\underline{V}}}\right]^{N} \exp\left[\frac{-1}{2\,\sigma_{v}^{2}}\,||\underline{V}||^{2}\right] . \tag{A-10}$$

The M.L. estimate of

$$R \triangleq \left[\frac{\sigma_U}{\sigma_V}\right]^{2} \tag{A-11}$$

is desired. The second parameter in $p(\underline{U},\underline{V})$ is chosen to be σ_U, so that $p(\underline{U},\underline{V})$ can be written as

$$p(\underline{U},\underline{V}) = \left[\frac{1}{2\pi\sigma_u^2}\right]^N R^{N/2} \exp\left\{\frac{-1}{2\sigma_u^2}\left[||\underline{U}||^2 + R||\underline{V}||^2\right]\right\} . \quad \text{(A-12)}$$

The M.L. estimates are solutions to

$$\frac{\partial \ln p(\underline{U},\underline{V})}{\partial R} = 0$$

$$\frac{\partial \ln p(\underline{U},\underline{V})}{\partial \sigma_u} = 0 . \quad \text{(A-13)}$$

Without difficulty, the M.L. estimate for R is shown to be given by

$$\hat{R} = \widehat{\left[\frac{\sigma_u}{\sigma_v}\right]^2} = \frac{||\underline{U}||^2}{||\underline{V}||^2} . \quad \text{(A-14)}$$

Also,

$$\widehat{\sqrt{R}} = \widehat{\left[\frac{\sigma_u}{\sigma_v}\right]} = \frac{||\underline{U}||}{||\underline{V}||} , \quad \text{(A-15)}$$

since the square root is a strictly monotonically increasing function.

In the case of power ratios, it is noted that

$$\widehat{\left[\frac{\sigma_u^2}{\sigma_v^2}\right]} = \frac{\widehat{\sigma_u^2}}{\widehat{\sigma_v^2}} \quad \text{(A-16)}$$

when the random vectors are uncorrelated. We shall see that this is also the case when $u(t_i)$ and $v(t_i)$ are correlated.

CORRELATED SAMPLES

Correlated Gaussian samples are now considered. Since the extension from one sample of u and v to N samples is direct, we restrict attention to one sample of u and v. The joint pdf is given by

$$p(u,v) = \frac{1}{2\pi \sigma_u \sigma_v \sqrt{1-\rho^2}} \exp\left\{\frac{-1}{2(1-\rho^2)}\left[\frac{u^2}{\sigma_u^2} + \frac{v^2}{\sigma_v^2} - \frac{2uv\rho}{\sigma_u \sigma_v}\right]\right\} \quad \text{(A-17)}$$

where ρ is the normalized correlation coefficient between u and v, defined by

$$\rho = \frac{E(uv)}{\sigma_u \sigma_v} . \quad \text{(A-18)}$$

With the definition of R given in (A-11), $p(u,v)$ can be written as

$$p(u,v) = \frac{1}{2\pi \sigma_v^2 [(1-\rho^2) R]^{1/2}} \exp\left\{\frac{-1}{2(1-\rho^2)}\left[\frac{u^2}{\sigma_v^2 R} + \frac{v^2}{\sigma_v^2} - \frac{2uv\rho}{\sigma_v^2 \sqrt{R}}\right]\right\} . \quad \text{(A-19)}$$

There are now three parameters, so that the M.L. estimates are given by the solutions of

$$\frac{\partial \ln p(u,v)}{\partial R} = 0 \quad \text{(A-20)}$$

$$\frac{\partial \ln p(u,v)}{\partial \rho} = 0 \quad \text{(A-21)}$$

$$\frac{\partial \ln p(u,v)}{\partial (\sigma_v^2)} = 0 . \quad \text{(A-22)}$$

Performing the indicated operations, we obtain

$$R = \frac{1}{(1-\rho^2)\sigma_2^2}\left[u^2 - uv\rho\sqrt{R}\right] , \quad \text{(A-23)}$$

$$\sigma_2^2 = \frac{1}{2}\left(\frac{1}{1-\rho^2}\right)\left[\frac{u^2}{R} + v^2 - \frac{2uv\rho}{\sqrt{R}}\right] , \quad \text{(A-24)}$$

and

$$\sigma_2^2 = \left(\frac{1}{1-\rho^2}\right)\left(\frac{u^2}{R} + v^2\right) - \frac{uv}{\sqrt{R}}\left[\frac{1+\rho^2}{\rho(1-\rho^2)}\right] \quad \text{(A-25)}$$

from (A-20), (A-21), and (A-22), respectively.

From (A-23), (A-24), and (A-25), the M.L. estimate of R is

$$\hat{R} = \frac{u^2}{v^2}$$

or equivalently,

$$\widehat{\ln R} = \ln [u^2/v^2] . \qquad \text{(A-26)}$$

The key point is that when the random variables become correlated, the M.L. estimate for σ_u^2/σ_v^2 does not change.

The extension of these results to complex correlated Gaussian vectors is straightforward, although somewhat more cumbersome, with the result as shown in (5). With the simpler development that is shown here, the M.L. estimate in (5) is the expected estimate.

ADDENDUM B

STATISTICAL CONSIDERATIONS OF TWO NARROWBAND GAUSSIAN PROCESSES

Preliminary statistical considerations of the two narrowband Gaussian processes are presented which are necessary before the performance of the maximum likelihood estimate can be determined.

The processes used in this estimation are marginally and jointly "spherically symmetric." Spherically symmetric means that an arbitrary phase shift of the carrier frequency will not change the statistical characteristics of the in-phase and quadrature-phase components of either process.

For spherically symmetric complex Gaussian vector processes, we can invoke Grettenberg's Theorem [3 - 4], an extension of which is quoted for this application.

Grettenberg's Theorem. Let $\underline{W}(t)$ be a complex (column) vector Gaussian process with mean zero. Then a necessary and sufficient condition that

$$E[\underline{W}(t)\,\underline{W}^T(s)] = 0 \tag{B-1}$$

for all s,t is that w(t) and $e^{j\theta}w(t)$ be identically distributed for all real θ (i.e., spherically symmetric). The T in (B-1) means "transpose."

Mutually spherically symmetric for vector complex Gaussian processes implies that the information is in the phase differences, and an arbitrary but same phase shift in all components of the vector process produces no change in the joint statistics.

As pointed out above, the processes u(t) and v(t) are such that they are jointly spherically symmetric. It has already been assumed that the successive samples of {u(t),v(t)} are sufficiently separated in time so as to be independent. The utility of Grettenberg's Theorem here is when s = t, for which

$$E[u^2(t)] = 0 \tag{B-2}$$

$$E[v^2(t)] = 0 \tag{B-3}$$

$$E[u(t)\,v(t)] = 0\ . \tag{B-4}$$

From (B-2),

$$E[u^2(t)] = E(u_{ci}^2) - E(u_{si}^2) + 2j\,E(u_{ci}\,u_{si}) = 0 . \qquad \text{(B-5)}$$

Hence,

$$E(u_{ci}^2) = E(u_{si}^2) \qquad \text{(B-6)}$$

and

$$E(u_{ci}\,u_{si}) = 0 . \qquad \text{(B-7)}$$

Therefore, u_{ci} and u_{si} are statistically independent and identically distributed.

A similar statement can be made about v(t) from (B-3).

From (B-4),

$$0 = E[u(t)\,v(t)] = E[u_{ci}\,v_{ci} - u_{si}\,v_{si}] + j\,E[u_{ci}\,v_{si} + u_{si}\,v_{ci}] . \qquad \text{(B-8)}$$

Hence,

$$E(u_{ci}\,v_{ci}) = E[u_{si}\,v_{si}] \triangleq c \qquad \text{(B-9)}$$

$$E(u_{ci}\,v_{si}) = -E[u_{si}\,v_{ci}] \triangleq d \qquad \text{(B-10)}$$

where c and d are real.

The cross-correlation of u(t) and v(t) is defined as

$$P_{UV} \triangleq E[u^*(t)\,v(t)]$$

$$= E[u_{ci}\,v_{ci} + u_{si}\,v_{si}] + j\,E[u_{ci}\,v_{si} - u_{si}\,v_{ci}] . \qquad \text{(B-11)}$$

For spherically symmetric processes,

$$P_{UV} = 2c \qquad \text{(B-12)}$$

and is real.

The covariance matrix of $[u_{ci}, u_{si}, v_{ci}, v_{si}]^T$ can now be written as

$$M_4 = \left[\begin{array}{cc|cc} P_U/2 & 0 & c & d \\ 0 & P_U/2 & -d & c \\ \hline c & -d & P_V/2 & 0 \\ d & c & 0 & P_V/2 \end{array}\right] . \qquad \text{(B-13)}$$

Next consider u(t) and v(t) expressed in terms of envelope and phase variations:

$$u(t) = R_1(t) \cos [\omega_0 t - \theta_1(t)]$$

$$v(t) = R_2(t) \cos [\omega_0 t - \theta_2(t)] . \qquad \text{(B-14)}$$

Then,

$$E[u_c v_c] = E[R_1 R_2 \cos \theta_1 \cos \theta_2] = c$$

$$E[u_s v_s] = E[R_1 R_2 \sin \theta_1 \sin \theta_2] = c$$

$$E[u_c v_s] = E[R_1 R_2 \cos \theta_1 \sin \theta_2] = d$$

$$E[u_s v_c] = E[R_1 R_2 \sin \theta_1 \cos \theta_2] = -d . \qquad \text{(B-15)}$$

Let $\phi \triangleq \theta_2 - \theta_1$, where ϕ represents the "phase difference information" between u(t) and v(t). Then,

$$E(u_c v_c) = \frac{1}{2} E\left\{R_1 R_2 \left(\cos \phi + \cos (\phi + 2\theta_1)\right)\right\} = c$$

$$E(u_s v_s) = \frac{1}{2} E\left\{R_1 R_2 \left(\cos \phi - \cos (\phi + 2\theta_1)\right)\right\} = c \qquad \text{(B-16)}$$

$$E(u_c v_s) = \frac{1}{2} E\left\{R_1 R_2 \left(\sin \phi + \sin (\phi + 2\theta_1)\right)\right\} = d$$

$$E(u_s v_c) = \frac{-1}{2} E\left\{R_1 R_2 \left(\sin \phi - \sin (\phi + 2\theta_1)\right)\right\} = -d . \qquad \text{(B-17)}$$

For spherically symmetric processes, θ_1 is uniformly distributed over $(-\pi, \pi)$. When this is incorporated into (B-16) and (B-17),

$$E[u_c v_c] = -E[u_s v_s] = \frac{1}{2} E[R_1 R_2 \cos \phi] = c \qquad \text{(B-18)}$$

$$E(u_c v_s) = E(u_s v_c] = \frac{1}{2} E[R_1 R_2 \sin \phi] = d . \qquad \text{(B-19)}$$

Finally, if the phase difference ϕ has a symmetric pdf about 0, then $E(\sin \phi) = 0$, and $d = 0$. In the applications anticipated with this estimator, the statistics of the estimator are independent of phase. In addition, the assumption that ϕ has a symmetric pdf is a very reasonable one for most applications. This assumption is therefore made and, hence, $d = 0$.

The covariance matrix M_4 in (B-13) now simplifies to

$$M_4 = \left[\begin{array}{cc:cc} P_U/2 & 0 & c & 0 \\ 0 & P_U/2 & 0 & c \\ \hdashline c & 0 & P_V/2 & 0 \\ 0 & c & 0 & P_V/2 \end{array}\right] \qquad \text{(B-20)}$$

Inspection of the covariance matrix in (B-20) shows that the only dependence is between the real part of u(t) and the real part of v(t), and the imaginary part of u(t) and the imaginary part of v(t). These correlations are also identical. Since everything else is uncorrelated (and therefore independent, since all processes are Gaussian), the observations could equally well be modeled as 2N samples of two real baseband processes $u_c(t)$ and $v_c(t)$.

When the pdf of the estimator is determined, we assume that 2N samples of $u_c(t)$ and $v_c(t)$ are observed. The resulting pdf of the estimator is identical to that when N complex samples are assumed to be observed from u(t) and v(t) with the covariance matrix given by (B-20).